

Copyright

by

Jurijs Bazilevs

2006

The Dissertation Committee for Jurijs Bazilevs
certifies that this is the approved version of the following dissertation:

Isogeometric Analysis of Turbulence and Fluid-Structure Interaction

Committee:

Thomas J. R. Hughes, Supervisor

Ivo Babuška

John R. Boisseau

Omar Ghattas

Robert D. Moser

J. Tinsley Oden

Isogeometric Analysis of Turbulence and Fluid-Structure Interaction

by

Jurijs Bazilevs, B.S., M.S.

Dissertation

Presented to the Faculty of the Graduate School of

The University of Texas at Austin

in Partial Fulfillment

of the Requirements

for the Degree of

Doctor of Philosophy

The University of Texas at Austin

August 2006

To the memory of Prof. Y. M. Tarnopolskii'

Acknowledgments

This work was made possible by the efforts of many people. In the space provided it would be impossible to thank everyone. Nevertheless, I would like to acknowledge the following contributions:

Prof. Thomas J.R. Hughes, my adviser, is a great mentor in many ways. He taught me not only the technical side of the subject, but also went out of his way to expose me to the cultural aspects of the field. Anna, my wife, was extremely understanding, supportive, and encouraging throughout the whole process. Elena and Sergey, my parents, provided a much needed safety net and encouraged me to achieve as much as possible. Prof. Kenneth E. Jansen, my master's thesis adviser, introduced me to the world of scientific research and taught me the basic "survival" skills. Alessandro, Austin, Giancarlo, Jessica, Lorenzo, and Victor, my colleagues, created an atmosphere conducive to fruitful research. My committee members provided me with many useful comments and suggestions to improve the quality of the work.

JURIJS BAZILEVS

The University of Texas at Austin
August 2006

Isogeometric Analysis of Turbulence and Fluid-Structure Interaction

Publication No. _____

Jurijs Bazilevs, Ph.D.

The University of Texas at Austin, 2006

Supervisor: Thomas J. R. Hughes

This work puts Isogeometric Analysis, a new analysis framework for computational engineering and sciences, on a firm mathematical foundation. FEM-like theory is developed in which optimal in h approximation properties for NURBS spaces with boundary conditions and inverse estimates are shown. This, in turn, grants straightforward extensions of the theory to stabilized formulations of incompressible and advection dominated phenomena.

This work also continues the development of residual-based turbulence models for incompressible fluid flow based on the multiscale paradigm. Novel turbulent closures, inspired by well-known stabilized methods, are derived and tested within the unsteady parallel isogeometric incompressible flow solver that was written as a part of this work.

The latter part of this dissertation focuses on the fluid-structure interaction (FSI) problem. A fully-coupled FSI formulation is proposed and a methodology for deriving shape derivative jacobian matrices is presented, allowing for a monolithic solution of the FSI system at the discrete level, and rendering the fluid and structural computations more robust. These ideas are implemented in the

form of an isogeometric parallel fluid-structure interaction solver. This technology is used to perform computations of contemporary interest and importance in patient-specific vascular simulation and modeling.

Contents

Acknowledgments	v
Abstract	vi
List of Figures	xi
Chapter 1 Introduction	1
1.1 Background and Motivation	1
1.1.1 Isogeometric Analysis	1
1.1.2 Turbulence Modeling and Simulation	2
1.1.3 Fluid-Structure Interaction	5
1.2 Dissertation Outline and Discussion of Major Developments	6
Chapter 2 Isogeometric Analysis Framework and Construction of Analysis-Suitable Geometries	11
2.1 A brief review of isogeometric analysis employing NURBS	11
2.1.1 One-dimensional B-splines	11
2.1.2 Multi-dimensional B-splines and geometrical objects	12
2.1.3 NURBS functions and geometry	13
2.1.4 Analysis framework based on NURBS	15
2.2 Construction of Analysis-Suitable Vascular Models	21
Chapter 3 Isogeometric Analysis: Approximation, stability and error estimates for h-refined meshes	24
3.1 Preliminaries	24
3.1.1 Univariate splines	25
3.1.2 Multivariate tensor product splines	25
3.1.3 NURBS and the geometry of the physical domain	27

3.2	Approximation properties of the NURBS space	29
3.2.1	Approximation with splines on a patch in the parametric domain	31
3.2.2	Approximation with NURBS on a patch in the parametric domain	36
3.2.3	Approximation with NURBS in the physical domain	37
3.2.4	Spaces with boundary conditions	42
3.3	Inverse inequalities for NURBS	43
3.4	Applications to physical problems	44
3.4.1	Elasticity	45
3.4.2	Incompressible and almost incompressible isotropic elasticity – stabilized methods	46
3.4.3	Incompressible and almost incompressible isotropic elasticity – a BB-stable method	50
3.4.4	Advection-diffusion	65
3.5	Numerical Examples	69
3.5.1	Solid elastic circular cylinder subjected to internal pressure loading	70
3.5.2	Infinite elastic plate with circular hole under constant in-plane tension in the x -direction	70
3.5.3	Constrained block subjected to a trigonometric load	75
3.5.4	Driven cavity problem	76
3.5.5	Advection-diffusion in a hollow cylinder	78
Chapter 4	Variationally Consistent Multiscale Turbulence Modeling	86
4.1	Small-scale Green’s operator, small-scale Green’s function, and connection with stabilized methods	86
4.2	Theoretical formulation of residual-based turbulence modeling	91
4.2.1	Continuous formulation of incompressible Navier-Stokes equations	91
4.2.2	Decomposition of spaces	93
4.2.3	The fine-scale problem	94
4.2.4	Derivation of the fine-scale model	95
4.2.5	The coarse-scale problem	97
4.2.6	Approximate closures and connection with stabilized methods	98
4.3	Numerical examples	102
4.3.1	Turbulent channel flow at $Re_\tau = 395$	102
4.3.2	Flow over Eppler 387 airfoil	109

Chapter 5	Isogeometric Fluid-Structure Interaction Analysis with Applications to Arterial Blood Flow	116
5.1	Formulation of the fluid-structure interaction problem	116
5.1.1	The solid problem	117
5.1.2	Motion of the fluid subdomain problem and the ALE mapping	120
5.1.3	The fluid problem	122
5.1.4	The coupled problem	123
5.2	Formulation of the fluid-structure interaction problem at the discrete level	125
5.2.1	Approximation spaces for ALE formulations and enforcement of kinematic compatibility conditions	125
5.2.2	The semi-discrete problem	128
5.2.3	Time integration of the FSI system	129
5.3	Linearization of the discrete FSI system: a methodology for computing shape derivatives	133
5.3.1	Shape derivatives	135
5.4	Numerical examples	142
5.4.1	Wave propagation in an elastic tube	142
5.4.2	Blood flow in an idealized aneurysm	147
5.4.3	Patient-specific abdominal aorta	151
Chapter 6	Conclusions and Future Work	155
	Bibliography	156
	Vita	167

List of Figures

2.1	(a) B-spline, piecewise quadratic curve in \mathbb{R}^2 . Control point locations are denoted by \bullet 's. (b) Toroidal NURBS surface. (c) Control net for toroidal surface.	14
2.2	Knot insertion. Control points are denoted by \bullet 's.	17
2.3	Order elevation. Control points are denoted by \bullet 's.	18
2.4	k -refinement takes advantage of the fact that knot insertion and order elevation do not commute. (a) Base case of one linear element. (b) Classic p -refinement approach: knot insertion followed by order elevation results in seven piecewise quadratic basis functions that are C^0 at internal knots. c) New k -refinement approach: order elevation followed by knot insertion results in five piecewise quadratic basis functions that are C^1 at internal knots.	20
2.5	Stages 3 and 4 of the patient-specific cardiovascular model construction for isogeometric analysis. Left: depiction of a cross-section surface template. Cross-section surface is bounded by a closed quadratic NURBS curve defined in terms of the control polygon consisting of 16 points. Middle: arterial path identified by skeletonization. Right: solid NURBS geometry, ready for refinement and analysis. . . .	22
2.6	The abdominal aorta model is divided into 26 patches, and each color represents one different patch. (a) - volume rendering result; (b) - isocontouring result; (c) - surface model and its path after removing unnecessary components; (d) - control mesh; (e) - solid NURBS mesh after refinement (73,314 elements); (f) - fluid-structure interaction simulation results: contours of the arterial wall velocity (cm/s) during late systole plotted on the current configuration. Only major branches are kept in (d-f).	23

3.1	Example of a quadratic ($p_1 = 2$) B-spline basis in one dimension derived from the knot vector $\Xi = \{0, 0, 0, 0.2, 0.4, 0.6, 0.8, 0.8, 1, 1, 1\}$. Note that due to the open knot vector (i.e., the first and last knots are repeated $p_1 + 1$ times), the first and last basis functions are interpolatory (i.e., they take on the value 1 at the first and last knots). The continuity at interior knots ξ_i is $C^{p_1 - m_i}$, where m_i is the number of repetitions of knot ξ_i . For example, only the interior knot 0.8 is repeated, and the continuity there is $C^{p_1 - 2} = C^0$. At the other knots the continuity is $C^{p_1 - 1} = C^1$, the maximal continuity of quadratic B-splines.	26
3.2	h -refinement with NURBS. In this illustration a NURBS patch is mapped onto a quarter of a square domain with a circular hole in physical space. The minimum degree NURBS required to exactly represent the geometry is quadratic. The open knot vectors are $\Xi_1 = \{0, 0, 0, 0.5, 1, 1, 1\}$ and $\Xi_2 = \{0, 0, 0, 1, 1, 1\}$, as illustrated. The exact geometry is represented at the coarsest level of discretization, and it and its parameterization are unchanged during refinement. In particular, the geometrical map \mathbf{F} and the weighting function w are unchanged during refinement.	30
3.3	Depiction of the support extensions \tilde{K} , \tilde{Q} , and corresponding \hat{Q} . For non-repeated knots, the case illustrated would conform to quadratic B-splines or NURBS (i.e., $p_\alpha = 2$). Quadratic splines and NURBS have support over three knot spans in each direction. That is, each basis function is supported by a 3×3 mesh of elements. The support extensions are confined to individual patches in the multipatch case, assuming the patches are adjoined in C^0 -continuous fashion.	32
3.4	$\Pi_{\mathcal{V}_h} v$ is the push-forward of the NURBS projector $\Pi_{\mathcal{N}_h}(v \circ \mathbf{F})$, where $v \in L^2(\Omega)$ and $v \circ \mathbf{F} \in L^2((0, 1)^d)$	39
3.5	Thick cylinder pressurized internally.	70
3.6	Solid circular cylinder meshes	71
3.7	Solid circular cylinder with varying internal pressure. Convergence of the error in the energy norm for quadratic, cubic, and quartic NURBS discretizations.	72
3.8	Elastic plate with a circular hole: problem definition.	72
3.9	Elastic plate with circular hole. Meshes produced by h -refinement (knot insertion).	73
3.10	Error measured in the L^2 -norm of stress vs. mesh parameter.	74
3.11	Trigonometric load problem setup.	75
3.12	Trigonometric load problem meshes produced by h -refinement (knot insertion).	76

3.13	Trigonometric load problem. Convergence to the analytical solution for displacement and pressure. Top: Douglas-Wang stabilization, equal-order, quadratic, C^1 -continuous bases. Middle: Galerkin's method, cubic displacement, quadratic pressure, C^0 -continuous bases. Bottom: Galerkin's method, cubic displacement, quadratic pressure, C^1 -continuous bases.	77
3.14	Driven cavity problem setup.	79
3.15	Driven cavity problem. Velocity vectors superposed on pressure contours. Left: Galerkin solution with equal-order discretization ($p = 2$). Right: Galerkin solution with unequal-order discretization ($p = 2$ for the pressure and $p = 3$ for the velocity).	79
3.16	Driven cavity problem. Velocity vectors superposed on pressure contours. GLS solution with equal-order discretization. Left: $p = 2$, Right $p = 3$	80
3.17	Advection-diffusion in a hollow cylinder. Problem setup.	81
3.18	Advection-diffusion in a hollow cylinder. Meshes 1-3.	82
3.19	Advection-diffusion in a hollow cylinder. Solution contours on the finest mesh, $\kappa = 0.025$	83
3.20	Advection-diffusion in a hollow cylinder, $\kappa = 0.025$. Convergence rates.	84
3.21	Advection-diffusion in a hollow cylinder, $\kappa = 0.00625$. Convergence rates.	84
3.22	Advection-diffusion in a hollow cylinder, $\kappa = 0.00625$. Convergence rates outside of the boundary layer.	85
4.1	A graphical depiction of a space-time cylinder and a space-time slab.	91
4.2	Turbulent channel. Problem setup.	103
4.3	Turbulent channel flow. Stream-wise velocity contours in different views.	105
4.4	Turbulent channel flow, results using linear elements. Top left: convergence of the mean flow, top right: convergence of u_{rms} , bottom left: convergence of v_{rms} , bottom right: convergence of w_{rms}	106
4.5	Turbulent channel flow, results using quadratic splines. Top left: convergence of the mean flow, top right: convergence of u_{rms} , bottom left: convergence of v_{rms} , bottom right: convergence of w_{rms}	107
4.6	Turbulent channel flow, results using quartic splines. Top left: convergence of the mean flow, top right: convergence of u_{rms} , bottom left: convergence of v_{rms} , bottom right: convergence of w_{rms}	108
4.7	Flow over Eppler airfoil problem setup. Computational domain and boundary conditions.	109

4.8	Flow over Eppler airfoil. NURBS mesh for both two-dimensional and three-dimensional calculations. Span-wise resolution was reduced to one linear element for a two-dimensional calculation.	110
4.9	Flow over Eppler airfoil. Snapshots of stream-wise velocity and pressure fields for a two-dimensional calculation. Note the coherence of the vortical structures and smoothness of pressure contours.	111
4.10	Flow over Eppler airfoil. Snapshots of stream-wise velocity and trailing edge pressure fields for a three-dimensional calculation. Pressure fluctuations are a source of hydrodynamically generated noise.	113
4.11	Flow over Eppler airfoil. Span-wise velocity isosurfaces for a three-dimensional calculation.	114
4.12	Flow over Eppler airfoil. Plot of the pressure coefficient $C_p = \frac{1}{2} \frac{p - p_\infty}{\rho u_\infty^2}$. Excellent agreement between a three-dimensional computation and experimental data is observed.	115
5.1	Abstract setting for the fluid-structure interaction problem. Depiction of the initial and the current configurations related through the ALE mapping. The initial configuration also serves as the reference configuration.	116
5.2	Wave propagation in a fluid-filled elastic tube problem setup. $H(t)$ is the Heaviside function.	143
5.3	Wave propagation in a fluid-filled elastic tube mesh consisting of 6,080 NURBS elements.	144
5.4	Wave propagation in a fluid-filled elastic tube. Contours of fluid pressure at various radial slices. Solution remains pointwise axisymmetric	145
5.5	Wave propagation in a fluid-filled elastic tube. (a) Outer wall radial displacement. (b) Centerline pressure. Computational results of Greenshields and Weller [38] are plotted for comparison.	146
5.6	Idealized aneurysm problem setup.	147
5.7	Idealized aneurysm mesh consisting of 14,630 NURBS elements.	148
5.8	Idealized aneurysm. Velocity vectors superimposed on axial velocity contours at various times. Top right and bottom left correspond to the systolic and diastolic phases, respectively. Note that the flow is axisymmetric.	149
5.9	Idealized aneurysm. Inflow and outflow waveforms. Notice the time lag attributable to the distensibility of the wall.	150
5.10	Patient-specific abdominal aorta geometry.	151

5.11 Patient-specific abdominal aorta mesh consisting of 52,420 quadratic NURBS elements.	152
5.12 Patient-specific abdominal aorta. Isosurfaces of the velocity magnitude plotted on the deformed geometry at various times.	153
5.13 Patient-specific abdominal aorta. Inlet and outlet flow waveforms. Flowrates (cm^3/s) versus time (s).	154

Chapter 1

Introduction

This dissertation makes an attempt to establish Isogeometric Analysis as a bona-fide analysis framework for solving problems of contemporary interest and importance in computational engineering and sciences. It also focuses on the design of novel formulations and numerical procedures for computation of turbulent fluid flow and fluid-structure interaction, using isogeometric analysis as a platform for these developments.

1.1 Background and Motivation

1.1.1 Isogeometric Analysis

Isogeometric analysis based on NURBS (non-uniform rational B-splines) was introduced in [52] and further expanded on in [18]. The objectives of isogeometric analysis are to generalize and improve upon Finite Element Analysis (FEA) in the following ways: 1) To provide more accurate modeling of complex geometries and to exactly represent common engineering shapes such as circles, cylinders, spheres, ellipsoids, etc.; 2) To fix exact geometries at the coarsest level of discretization and eliminate geometrical errors *ab initio*; 3) To vastly simplify mesh refinement of complex industrial geometries by eliminating the necessity to communicate with the CAD description of geometry; 4) To provide systematic refinement procedures, including classical h - and p -refinements analogues, and to develop a new “ k -refinement” procedure that increases the smoothness almost everywhere of element functions beyond the standard C^0 -continuity of finite elements and exhibits improved accuracy and efficiency compared with classical p -refinement. The references [18, 52] provide a comprehensive introduction to the main ideas and procedures, and computational verification of its veracity and potential. In particular, optimal in h convergence rates with respect to the polynomial order were attained for linear elasticity examples and convergence to thin shell solutions was observed. The k -refinement strategy was shown to converge to monotone solutions for linear

advection-diffusion examples with sharp internal and boundary layers. Further study of isogeometric analysis showed that results superior to standard finite elements are obtained in the context of structural vibrations.

In a sense, isogeometric analysis is a superset of FEA. Standard h - and p -methods can be reproduced, but isogeometric analysis includes directions and possibilities not available in standard FEA. Some of these have been explored in [18, 52] and many others identified. At the same time, isogeometric analysis has many features in common with FEA, in particular, it invokes the isoparametric concept in which dependent variables and the geometry share the same basis functions. We note that, despite the geometry being fixed at the coarsest level of discretization, the mesh, and the corresponding basis, can be refined and order-elevated while maintaining the original exact geometry. The isoparametric concept possesses important properties relevant to the analysis of structures (see [44, 52]) and the Lagrangian description of continuous media for which the geometry and mesh need to be updated by the displacement field.

The above developments create an opportunity for a successful application of the isogeometric methodology to computational fluid dynamics, in particular, turbulent flows (the pioneering studies of boundary layer turbulence [62, 63, 65, 89] should be mentioned in this regard), and fluid-structure interaction (FSI), which are primary goals of this dissertation. Both areas present a great challenge to the Computational Mechanics community at large, and are of great interest to Sandia National Laboratories and the Office of Naval Research, whom are primary sponsors of this work.

1.1.2 Turbulence Modeling and Simulation

Classically, and to this day, turbulence modeling and simulation is classified, according to the computational effort involved, into RANS (Reynolds-Averaged Navier-Stokes), LES (Large-Eddy Simulation), and DNS (Direct Numerical Simulation), RANS being the least expensive and DNS being the most costly. In RANS only the very large scales of the flow are retained in the computations and most of the time steady solutions are sought. Because of its inexpensive nature RANS is the most popular technology when it comes to large-scale industrial computations. The major drawback of RANS is the fact that it heavily relies on models which are “tuned” for very specific flow conditions and geometrical configurations. This casts a shadow of doubt on predictive capabilities of RANS technology. For a good comprehensive review of RANS turbulence modeling see Wilcox [113]. DNS, as can be inferred from its name, resolves the flow all the way down to the Kolmogorov scales, the smallest eddies present in the flow (see Pope [80] for details and definitions). The following estimate is widely used in computational fluid dynamics

$$N \approx Re^{9/4}, \quad (1.1)$$

where N is the number of points necessary to fully resolve a turbulent flow in a 3-dimensional cube in the absence of boundary layers. Re appearing in (1.1) is the Reynolds number of the flow, which is typically several thousand or several million for a variety of industrial applications. It is precisely relation (1.1) that makes DNS prohibitively expensive to apply to flows of industrial interest.

While RANS and DNS are on the opposite ends of the spectrum in terms of the computational expense, LES falls somewhere in between the two extremes. Kolmogorov theory of cascade (see Pope [80]) postulates the existence of the so-called *inertial sub-range*. Inertial sub-range refers to the set of scales in the flow which are smaller than the ones directly affected by geometry, boundary conditions, and forcing (here assumed to be confined to the lowest wave numbers) yet larger than the ones dominated by the viscosity. It is believed that scales in the inertial subrange behave in a universal fashion and, on average, transfer energy from large or energy carrying, to small or viscous scales by means of a nonlinear mechanism which is reflected in the structure of the incompressible Navier-Stokes equations (INS). LES places a “cut-off” somewhere in the inertial subrange and aims to represent the energy carrying scales and approximate the effect of the smaller scales on them. Universality of the scales in the inertial sub-range greatly simplifies the modeling task. The above mentioned characteristics render LES more accurate than RANS and much less expensive than DNS.

As a starting point of the classical LES developments a notion of a spatial filter, possessing the properties of homogeneity and symmetry (see the ground breaking paper of Leonard [67]), is introduced. This filter induces the separation of large and small spatial scales in the flow field. Application of this filter to the INS supplemented with a closure model for the resultant “sub-grid” stress (the main difficulty in LES modeling) yields a system of LES equations, now written in terms of the filtered quantities. A variety of closures exist, the most popular ones (for example Smagorinsky type models, see [91], [34]) make use of *ad hoc* nonlinear viscosities to represent the sub-grid stress. LES equations are then approximated numerically with the grid size capable of representing scales in the inertial sub-range. LES is successfully applied to a variety of important turbulent flows, yet the structure of the methods and models often requires explicit application of the so-called test filters and the presence of the homogeneous directions in the flow. This renders classical LES procedures cumbersome to properly extend to complex geometrical configurations. On the theoretical side, very little justification is given to the exact form of the model terms. From the standpoint of numerical analysis, addition of *ad hoc* nonlinear viscosities upsets the consistency of the method rendering higher-order approaches useless, as the consistency error will always dominate the approximation error.

In order to circumvent serious drawbacks of the classical LES framework, Hughes, Mazzei and Jansen [48] proposed the variational multiscale method (VMM or VMS), in which a concept of filtering was abandoned in favor of the a-priori scale separation via variational projections, and

models based on eddy viscosities were included in the small-scale equations only, while consistency was preserved in the large-scale equations. The static eddy viscosity based on the Smagorinsky model version of the VMM was studied in Hughes *et al.* [49], Hughes, Oberai, and Mazzei [50], and Oberai and Hughes [75]. The model was found to work very well for homogeneous isotropic flows and fully developed, equilibrium and non-equilibrium, turbulent channel flows. The dynamic version of the VMM based on the Germano procedure [34] was tested in Holmen *et al.* [42] and Hughes, Wells and Wray [55]. Results superior to the static model were reported. Of note are a series of works by Ramakrishnan and Collis [81–84] who explored VMS in the context of a DG formulation of compressible flow as well as that of Farhat and Koobus [24], and Koobus and Farhat [61], who obtained good results with the unstructured grid finite volume compressible flow code.

While theoretically more sound, the original version of the VMM was found lacking in practical aspects. At least two scales are necessary in the discretization, which can be achieved through discrete projection (see Calo [14], Farhat and Koobus [24]) or hierarchical bases (see Ramakrishnan and Collis [84], Jansen and Tejada-Martinez [57].) This technology, while easily implementable in the case of spectral discretizations and structured meshes, is not readily available in a lot of the unstructured grid codes. Employing an eddy viscosity in the small scales is also viewed as an inefficient mechanism, as the small scales, represented in the computation, are being “sacrificed” to retain full consistency of the large scales. For the case of the spectral discretization in 3D, with a cut-off placed at the half of the wave-number space, consistency is retained only on 12.5 % of the modes, which is strikingly small. One can hardly call such a method consistent.

Recently Calo [14] and Hughes, Calo, and Scovazzi [51] proposed the variationally consistent residual-based turbulence modeling approach, in which all the scales are accounted for consistently and the use of eddy viscosities is avoided completely. All resolved scales are viewed as large scales, hence the efficiency issue is obviated from the outset. The philosophy of this new method is to try and solve for the fine scales, which reside in an infinite dimensional space, analytically, and include their effect in the coarse scale system, which is finite dimensional. Obtaining exact expressions for the fine scale variables is just as daunting as solving the original Navier-Stokes system, hence various approximations are necessary in order to make the method practical. Note that the coarse scale equations are exact, so the only “modeling” component of the present approach is the analytical approximation of the fine scales. Preliminary evidence of the success of the new method were reported in Calo [14]. This approach is pursued further in this work. A parallel, transient, three-dimensional isogeometric flow solver was written for the purposes of validating the new approach.

1.1.3 Fluid-Structure Interaction

A big part of this dissertation is the development of an isogeometric fluid-structure interaction procedures with particular emphasis on arterial modeling and blood flow, which is an area of research currently receiving considerable attention. It is believed that the ability of NURBS to accurately represent smooth exact geometries, that are natural for arterial systems, but unattainable in the faceted finite-element representation, and the high order of approximation of NURBS (shown in this thesis), should render fluid and structural computations more physiologically realistic.

Initial attempts to simulate blood flow in arteries made use of simplified geometries. This approach had limited applicability because of its inability to represent complex flow phenomena occurring in real blood vessels. The concept of patient-specific cardiovascular modeling was first established in [97], where real-life geometries were used to simulate blood flow. This opened the door for designing predictive tools for vascular modeling and treatment planning. Dramatic improvements in the computational results were observed in [97], yet the blood vessel wall was treated as being rigid. As was shown earlier, for example with the flexible and rigid wall computations [105–108], the rigid wall assumption precludes pressure wave propagation and overestimates wall shear stress. There exists a variety of methods to include the effect of the moving wall in computations, the most prevalent being the arbitrary Lagrangian-Eulerian (ALE) approach. For a general discussion of ALE, the reader is referred to [20, 22, 23, 46, 66] and references therein. Applications of ALE to hemodynamics are discussed in [26, 30, 33, 74] and references therein. Some of the other techniques include the coupled momentum method [28], the immersed finite element method [116], and the space-time finite element method [99, 100, 102]. This work adopts the ALE framework. The arterial wall is treated as a nonlinear elastic solid in the Lagrangian description governed by the equations of elastodynamics. Blood is assumed to be a Newtonian viscous fluid governed by the incompressible Navier-Stokes equations written in the ALE form. The fluid velocity is set equal to the velocity of the solid at the fluid-solid interface. The coupled FSI problem is written in the variational form such that the stress compatibility condition at the fluid-solid interface is enforced weakly. The ALE equations require the specification of the fluid region motion. This motion is found by solving an auxiliary static linear-elastic boundary-value problem for which the fluid-solid boundary displacement acts as a Dirichlet boundary condition (see, e.g., [58]).

Fluid-structure coupling has been a topic of discussion in the literature on the subject. In this work, monolithic discretization is employed, meaning that there is one mesh, which embodies both the fluid and the structure. Also, a monolithic solution approach is adopted, namely fluid and solid solution increments are solved for simultaneously. The effect of the mesh motion on the fluid equations is accounted for in the jacobian matrix by means of *discrete shape derivatives*. The latter require derivation, which is one of the contributions of this thesis. As a result, a lot of the coupling issues are obviated from the outset, rendering the method robust.

1.2 Dissertation Outline and Discussion of Major Developments

Chapter 2 of this dissertation gives an overview of the NURBS-based isogeometric analysis framework. We introduce B-spline polynomials and NURBS, focusing only on issues necessary for subsequent developments. For background, the interested reader may consult standard references, such as Rogers [85], Piegl and Tiller [79], and Farin [25]. Basic definitions are given, and construction of solution spaces, refinement algorithms, and geometrical modeling approaches are discussed.

Chapter 3 of this thesis is devoted to the mathematical study of isogeometric analysis with NURBS as a basis. We focus on h -refinement. The geometry of the mapping between a d -cube in the parametric space (d is the number of space dimensions) and its image in physical space requires the introduction of concepts and spaces not utilized in standard FEA. The reason for this is that when the continuity of the interpolant is sufficiently high, one cannot stay in a single element and invoke a standard Bramble-Hilbert estimate. A notion of “support extension” is necessitated, but produces the following complication: If a function u is assumed to be of class H^m in the support extension in the physical domain, its pull-back by the geometrical mapping is no longer an H^m -function in the support extension in the parametric domain. Rather, it is of class H^m on the supports of individual elements comprising the support extension in the parametric domain, but with reduced regularity across the internal element boundaries. This new non-standard space is a Hilbert space, and its approximation properties are key to our developments. It may be thought of as intermediate in continuity between standard Sobolev spaces and the “broken” Sobolev spaces utilized in the analysis of Discontinuous Galerkin Methods [3, 78]. For this reason we refer to these new spaces as “bent” Sobolev spaces.

We establish approximation properties of NURBS within so-called “patches” that is, d -cubes in the parametric domain and their images in physical space under the geometric mapping. The union of patches in physical space comprises the geometry. First, a new Bramble-Hilbert lemma is established that utilizes the concept of support extension developed here and expresses how functions in bent Sobolev spaces, involving the regularity constraints of B-spline spaces, are approximated by B-splines. This result enables us to overcome the difficulties previously mentioned, and we feel it may be of interest in its own right. NURBS are projective transformations of B-splines (Farin [25]) and their approximation properties are established with the aid of the new Bramble-Hilbert lemma. These results depend crucially on the specific structure of NURBS basis functions engendered by the projective transformation. The approximation results are generalized to include strongly imposed Dirichlet boundary data. In Section 4, we establish inverse inequalities for NURBS. These are required, for example, in the convergence analysis of stabilized methods. Our results in are developed for a single patch, however, they may be generalized in a straightforward

way to geometries composed of multiple patches by standard techniques.

We apply the new approximation results obtained to obtain error estimates for problems of interest. We begin with linear elasticity theory. This is a standard symmetric, positive-definite, elliptic problem for which a minimum principle exists and optimal error estimates follow directly from the approximation results. Next we consider stabilized formulations of incompressible and almost incompressible isotropic elasticity. Here, in order to obtain stability and error estimates, we require both the new approximation result and inverse estimates for NURBS. As is usual for stabilized methods, these results pertain to a wide variety of displacement and pressure interpolatory combinations. We follow these developments with the more technically challenging case of inf-sup (i.e., Babuška-Brezzi, or BB) stable Galerkin methods. We focus on the case of C^0 -continuous interpolations across element boundaries and, in particular, on the case of the displacement field one order higher than the pressure. (When we speak of “order” of a NURBS basis, we are thinking of the polynomial order of their B-spline progenitors.) This case is somewhat analogous to known BB-stable finite elements (see, e.g., Brezzi-Fortin [11]). However, geometric aspects of NURBS and isogeometric analysis provide new analytical challenges. In isogeometric analysis, the exact geometry is fixed patch-wise by the coarsest mesh and maintained, along with its parameterization, throughout h -refinement. This is a distinguishing feature of isogeometric analysis and one not shared by FEA. To facilitate analysis, the notion of a “vertex mesh” is introduced, which may be thought of as a coarsening of the “control net” or “control mesh” of NURBS theory. NURBS are not interpolatory and so the coefficients of basis functions (i.e., “control points,” or “generalized coordinates”) in the geometrical mapping do not lie on the geometry and thus do not have a direct physical interpretation. The control net is the piece-wise multilinear interpolant of the control points. In three dimensions it is a mesh of trilinear hexahedral elements. At the coarsest level of discretization it is often quite distinct from the exact geometry. However, as the mesh is h -refined, the control mesh converges to the physical mesh. (In a sense, use of low-order finite elements may be viewed as performing analysis on a particular control mesh rather than an actual geometry.) The theoretical analysis of mixed Galerkin methods for the incompressible problem presented herein utilizes the concept of the vertex mesh. We are able to prove inf-sup stability and establish quasi-optimal error estimates by employing the approximation results for NURBS. In our final application, we consider stabilized methods for scalar advection-diffusion. Utilizing standard arguments, along with the new approximation results and inverse estimates, we establish stability and error estimates analogous to those for finite elements.

We present several numerical calculations to test the mathematical results. In all cases that fall within the hypotheses of the mathematical results, the computed error estimates were found to be consistent with theory. We also tested some cases that do not satisfy our hypotheses. For example, in the analysis of a linear elastic boundary-value problem for a plate with a circular hole, the

geometrical mapping utilized is singular at one corner point of the domain. (This was a choice, not a necessity.) Consequently, the hypotheses of our theory are not satisfied. Nevertheless, optimal rates of convergence were still obtained. In other examples, concerning incompressible elastic analysis by the mixed Galerkin method, we tested displacement-pressure combinations that were smoother than C^0 across element boundaries. Recall, our mathematical results for the BB-stable theory are only applicable in the C^0 case. In particular, we tested cubic displacements combined with quadratic pressure, but both C^1 -continuous across element interfaces. In the examples presented, and some others not shown, we found this combination to be stable and optimally convergent. We conjecture that for additional smoothness, beyond C^0 , across element interfaces, elements of this type, with displacements one order higher than pressure, are mathematically stable and optimally convergent. We did not investigate pressures that are discontinuous across element boundaries, but, inspired by the spectral element work of Maday, Patera, and Ronquist [69], and others, we conjecture that for pressure two orders lower than displacements, error estimates suboptimal by one order can be proven. We did study stabilized methods and mixed Galerkin methods on the driven cavity Stokes flow problem. (The equations of Stokes flow are form-identical to the equations of isotropic incompressible elasticity.) The solution of the driven cavity possesses pressure singularities and represents a stringent stability test. All stabilized methods, and mixed Galerkin methods with displacement (i.e., velocity in this case) one order higher than pressure, proved stable. On the other hand, equal-order interpolations for mixed Galerkin methods were manifestly unstable. Finally, we numerically verified error estimates for Stabilized Methods for an advection-diffusion problem with a boundary layer. By excising the boundary layer domain, we demonstrated optimal “interior estimates” for unresolved cases.

The above developments render NURBS-based isogeometric analysis a bona-fide computational technology.

Chapter 4 of this dissertation focuses on further developing the variationally consistent residual-based turbulence modeling approach, proposed by Calo [14] and Hughes, Calo, and Scovazzi [51], and integrating it with isogeometric analysis. We review the concept of the small-scale Green’s function, introduced in Hughes and Sangalli [54]. The small-scale Green’s function is a fundamental object in the design and analysis of variational multiscale methods.

We make use of the small-scale Green’s function to develop the theoretical formulation of the residual-based turbulence model. It is the philosophy of this document that incompressible Navier-Stokes equation system, with the associated initial and boundary conditions, adequately describes turbulence phenomena. Thus, the goal of turbulence modeling is to accurately approximate solutions to INS. Following the approach of Calo [14] and Hughes and Sangalli [54], we represent the solution space, comprised of velocity and pressure, as the sum decomposition of a

finite-dimensional space of functions, coming from the discretization, and its infinite-dimensional complement in the full space. We then derive the form of the multiscale model for the incompressible Navier-Stokes equations, which explicitly depends on the small-scale Green's operator for both the velocity and pressure. Assuming the localization property of the small-scale Green's function we propose local algebraic models for small-scale velocity and pressure by making use of the large body of experience in stabilized methods theory.

The new formulation is tested on a fully-developed turbulent channel flow at Reynolds number $Re_\tau = 395$ based on friction velocity. This is a standard benchmark test case in the turbulence literature (see, e.g., [72]). As analytical results are not available for this test case, it is customary to verify the computations against DNS, a high-fidelity simulation, which resolves all spatial and temporal scales of the problem. In the computations we used first order NURBS, which are identical to C^0 -continuous tri-linear hexahedral finite elements, and employed k -refinement to obtain discretizations of order $p = 2$ and $p = 3$, maintaining the continuity of the basis functions at the C^{p-1} level. For low order NURBS results of the simulations are competitive with, and even superior to the state-of-the-art eddy-viscosity based approaches popular in the LES community. Dramatic increase in accuracy is observed when going from a C^0 -continuous linear to a C^1 -continuous quadratic discretization. Results are further improved for C^2 -continuous cubics. High-order, high-continuity NURBS results also appear to be competitive with spectral discretizations, which are considered optimal for computing turbulent flows, albeit on very simple geometries. On the basis of these observations one may conclude that the geometric flexibility of NURBS, combined with their high order of approximation, may potentially make them an ideal tool for simulating turbulent flows in complex geometric configurations of industrial interest. As a step in this direction, we also present a computation involving a fully developed three-dimensional turbulent flow over an Eppler 387 wing section at Reynolds number $Re = 100,000$ based on the chord length, and $\alpha = 2^\circ$ angle of attack. Computations of this kind are of interest in the area of hydroacoustics for the purposes of predicting turbulence-induced noise (see, e.g., [76, 77]). Turbulent and laminar regions co-exist in this flow. As a result, a good turbulence model needs to automatically adjust in different parts of the domain to reflect various flow regimes. Our computational results compare very well with the experimental findings.

Chapter 5 of this thesis focuses on the fluid-structure interaction problem. A NURBS-based isogeometric fluid-structure interaction formulation, coupling incompressible fluids with nonlinear elastic solids, and allowing for large structural displacements, is developed. This methodology, encompassing a very general class of applications, is applied to problems of arterial blood flow modeling and simulation. We formulate the FSI problem mathematically at the continuous level, give the discrete formulation, and show the details of the time integration algorithm. Linearization of the discrete

FSI system is discussed in detail. A methodology for deriving shape derivatives is presented, which is one of the main contributions of this thesis. Shape derivatives are tangent operators (tangent matrices in finite dimensions) that reflect changes in the equations of motion with respect to the perturbations of the spatial domain. They are necessary for a consistent linearization of the discrete FSI equations, and, as a consequence, the development of robust fully-coupled solution algorithms. The difficulty in deriving these tangent operators lies in the fact that the fluid integrals of the variational formulation are taken over a spatial configuration that directly depends on the displacement of the fluid domain. To circumvent this difficulty, we change variables and work on the reference element, which allows us to pass the derivatives inside the integral operators. Using identities that are standard in nonlinear continuum mechanics, we arrive at the shape derivative matrices that are form-identical to other tangent matrices in nonlinear finite element and isogeometric analysis, and whose implementation is straightforward.

We test the new formulation on two benchmark problems, and present an application involving flow in a patient-specific abdominal aorta. Our results compare well with the reference computations of other researchers.

Chapter 2

Isogeometric Analysis Framework and Construction of Analysis-Suitable Geometries

2.1 A brief review of isogeometric analysis employing NURBS

This section gives a very brief overview of isogeometric analysis based on NURBS. A more detailed description of the isogeometric approach may be found in [18, 52]. For an introductory text on NURBS, see Rogers [85], while a more detailed treatment is given in the book of Piegl and Tiller [79]. Mathematical theory of isogeometric analysis for h -refined meshes may be found in the recent work of Bazilevs *et al.* [6].

2.1.1 One-dimensional B-splines

A B-spline basis is comprised of piece-wise polynomials joined with prescribed continuity. In order to define a B-spline basis of polynomial order p in one dimension one needs the notion of a *knot vector*. A knot vector in one dimension is a set of coordinates in the parametric space, written as $\Xi = \{\xi_1, \xi_2, \dots, \xi_{n+p+1}\}$, where i is the knot index, $i = 1, 2, \dots, n+p+1$, $\xi_i \in [0, 1]$ is the i^{th} knot, and n is the total number of basis functions. A knot vector is said to be *open* if its first and last knots are repeated $p+1$ times. Basis functions formed from an open knot vector are interpolatory at the end points of the parametric interval, but they are not, in general, interpolatory at the interior knots.

Given Ξ and p , B-spline basis functions are defined recursively starting with piecewise

constants ($p = 0$) :

$$B_{i,0}(\xi) = \begin{cases} 1 & \text{if } \xi_i \leq \xi < \xi_{i+1}, \\ 0 & \text{otherwise.} \end{cases} \quad (2.1)$$

For $p = 1, 2, 3, \dots$, they are defined by

$$B_{i,p}(\xi) = \frac{\xi - \xi_i}{\xi_{i+p} - \xi_i} B_{i,p-1}(\xi) + \frac{\xi_{i+p+1} - \xi}{\xi_{i+p+1} - \xi_{i+1}} B_{i+1,p-1}(\xi). \quad (2.2)$$

Basis functions of order p have $p - 1$ continuous derivatives at knots. If a knot is repeated k times, then the number of continuous derivatives decreases by k . When the multiplicity of a knot is exactly p , the basis function is interpolatory. Basis functions form a partition of unity, each one is compactly supported on the interval $[\xi_i, \xi_{i+p+1}]$, and they are point-wise non-negative. These properties are important and make these functions attractive for use in analysis.

2.1.2 Multi-dimensional B-splines and geometrical objects

Let α be a positive integer such that $1 \leq \alpha \leq d$, where d is the number of space dimensions. Given α knot vectors $\Xi_{\gamma,p_\gamma}, \gamma = 1, \dots, \alpha$, multi-dimensional B-splines are constructed by taking tensor products of their one-dimensional counterparts:

$$B_{i_1, \dots, i_\alpha}(\xi_1, \dots, \xi_\alpha) = \otimes_{\gamma=1}^{\alpha} B_{i_\gamma, p_\gamma}(\xi_\gamma). \quad (2.3)$$

B-spline functions are defined on a parametric domain $(0, 1)^\alpha$, and p_γ is the polynomial order in the parametric direction γ .

Objects of B-spline geometry can be most generally characterized as unions of *patches* in \mathbb{R}^d . A patch is an image under a mapping of the parametric interval $(0, 1)^\alpha$, expressed as a linear combination of spline basis functions (2.3) and points in \mathbb{R}^d , that is,

$$\begin{aligned} \Omega &= \{\mathbf{F}(\boldsymbol{\xi}) \mid \boldsymbol{\xi} \in (0, 1)^\alpha\}, \\ \mathbf{F}(\boldsymbol{\xi}) &= \sum_{i \in I} \mathbf{C}_i B_i(\boldsymbol{\xi}), \end{aligned} \quad (2.4)$$

where I is the index set

$$I = \{i = (i_1, \dots, i_\alpha) \in \mathbb{N}^\alpha \mid 1 \leq i_\gamma \leq n_\gamma + p_\gamma + 1\}, \quad (2.5)$$

Ω represents an object and the \mathbf{C} 's are the so-called *control points*. Various geometrical objects may be obtained by varying α , namely: the case of $\alpha = 1$ corresponds to a *B-spline curve*, $\alpha = 2$

generates a *B-spline surface*, and a *B-spline solid* is obtained by setting $\alpha = 3$. A piece-wise linear interpolation of the control points for curves, and a piece-wise multi-linear interpolation of the control points for surfaces and solids is called a *control mesh*.

2.1.3 NURBS functions and geometry

The geometric framework based on B-splines is limited in that basic elements of engineering design, such as exact circles, ellipses, and other conic sections cannot be obtained by using B-spline functions alone. NURBS were devised to overcome this shortcoming. NURBS geometrical objects in \mathbb{R}^d are precisely *projective transformations* of B-spline geometrical objects in \mathbb{R}^{d+1} (see Farin [25]), that is,

$$\begin{aligned}\Omega &= \{\mathbf{F}(\boldsymbol{\xi}) \mid \boldsymbol{\xi} \in (0, 1)^\alpha\}, \\ \mathbf{F}(\boldsymbol{\xi}) &= \mathcal{P}\left(\sum_{i \in I} \{\hat{\mathbf{C}}_i, w_i\} B_i(\boldsymbol{\xi})\right) = \\ &= \sum_{i \in I} \left(\frac{\hat{\mathbf{C}}_i}{w_i}\right) \left(\frac{w_i B_i(\boldsymbol{\xi})}{\sum_{j \in I} w_j B_j(\boldsymbol{\xi})}\right) = \\ &= \sum_{i \in I} \mathbf{C}_i \frac{w_i B_i(\boldsymbol{\xi})}{w(\boldsymbol{\xi})} = \sum_{i \in I} \mathbf{C}_i R_i(\boldsymbol{\xi}).\end{aligned}\tag{2.6}$$

In the above $\hat{\mathbf{C}}_i, \mathbf{C}_i$ are in \mathbb{R}^d , $w_i \in \mathbb{R}$, strictly positive, is the *weight*, and $w(\boldsymbol{\xi}) = \sum_{i \in I} w_i B_i(\boldsymbol{\xi})$ is the *weighting function*. The weighting function is defined on the geometry and stays unchanged throughout the refinement process. The last line of (2.6) defines NURBS basis functions $\{R_i\}_{i \in I}$:

$$R_i(\boldsymbol{\xi}) = \frac{w_i B_i(\boldsymbol{\xi})}{w(\boldsymbol{\xi})}.\tag{2.7}$$

It is important to note that while a B-spline basis depends only on the structure of the knot vector, construction of a NURBS basis requires information about the geometry. Multi-dimensional NURBS basis functions are no longer tensor products of one-dimensional entities, in contrast with B-splines. Properties such as partition of unity, positivity, and compact support are retained for NURBS bases. Continuity of NURBS functions is also the same as that of B-splines.

Examples of a B-spline curve, a toroidal NURBS surface, and the corresponding control meshes are given in Figure 2.1.

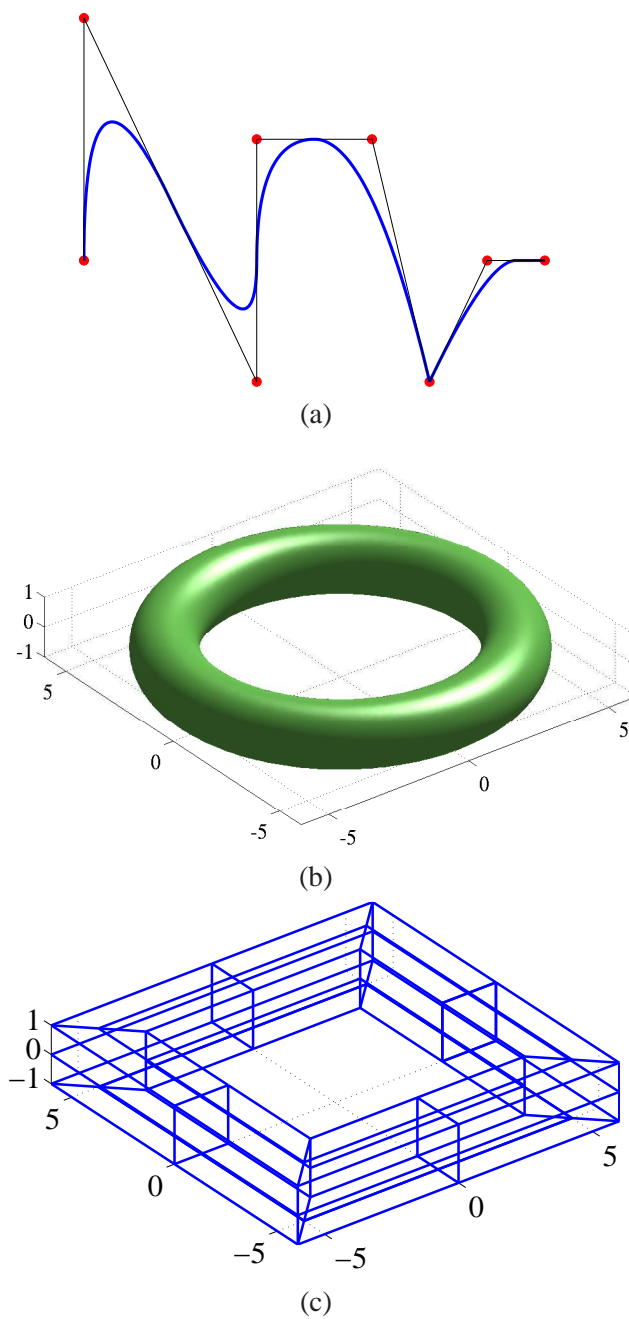


Figure 2.1: (a) B-spline, piecewise quadratic curve in \mathbb{R}^2 . Control point locations are denoted by \bullet 's. (b) Toroidal NURBS surface. (c) Control net for toroidal surface.

2.1.4 Analysis framework based on NURBS

Isogeometric analysis framework consists of the following items and features:

1. A physical domain consists of a union of patches, each defined as an image of the parametric space as

$$\Omega = \{\mathbf{F}(\boldsymbol{\xi}) \mid \boldsymbol{\xi} \in (0, 1)^\alpha\} \quad (2.8)$$

2. A mesh for a NURBS patch is defined by the union of NURBS elements, denoted by K , each one being an image under a NURBS map of a knot span in the parametric space

$$K = \{\mathbf{F}(\boldsymbol{\xi}) \mid \boldsymbol{\xi} \in \mathbf{Q} = \otimes_{\gamma=1}^\alpha (\xi_{i_\gamma, \gamma}, \xi_{i_\gamma + m_{i_\gamma, \gamma}})\}. \quad (2.9)$$

where m_{i_γ} is the multiplicity of knot $\xi_{i_\gamma, \gamma}$.

3. The basis for the solution space in the physical domain is defined through a composite mapping as follows:

$$N_i = R_i \circ \mathbf{F}^{-1}, \quad i \in I. \quad (2.10)$$

This definition gives the isoparametric construction [44], that is, the fields in question (e.g., displacement, velocity, temperature, etc.) are represented in terms of the same basis functions as the geometry. Coefficients of the basis functions, or *control variables*, are the degrees-of-freedom of the discrete system. The isoparametric approach is most convenient for applications involving Lagrangian and ALE descriptions of continuous media where geometry is constantly updated as the physical system evolves in time.

4. Boundaries of NURBS geometrical objects are themselves lower dimensions NURBS objects (e.g., a NURBS solid is bounded by NURBS surfaces, which, in turn, are bounded by NURBS curves). As a result, the easiest way to set Dirichlet boundary conditions on a patch face is to constrain control variables that correspond to that face. Interpolation or projection needs to be employed in cases when the prescribed function is not in the discrete space. This amounts to “strong” satisfaction of the boundary conditions. An alternative formulation of Dirichlet conditions can be based on “weak” satisfaction, a standard feature of the discontinuous Galerkin method. Neumann boundary conditions are satisfied as in the standard finite element method.
5. Mesh refinement strategies are developed from a combination of *knot insertion* and *order elevation* techniques. These enable analogues of classical *h*-refinement and *p*-refinement methods, and the new possibility of *k*-refinement.

***h*-refinement: Knot insertion**

The analogue of *h*-refinement is *knot insertion*. Knots may be inserted without changing a curve geometrically or parametrically. Given a knot vector $\Xi = \{\xi_1, \xi_2, \dots, \xi_{n+p+1}\}$, let $\bar{\xi} \in [\xi_k, \xi_{k+1}[$ be a desired new knot. The new $n + 1$ basis functions are formed recursively, using (2.1) and (2.2), with the new knot vector $\Xi = \{\xi_1, \xi_2, \dots, \xi_k, \bar{\xi}, \xi_{k+1}, \dots, \xi_{n+p+1}\}$. The new $n + 1$ control points, $\{\bar{\mathbf{C}}_1, \bar{\mathbf{C}}_2, \dots, \bar{\mathbf{C}}_{n+1}\}$, are formed from the original control points, $\{\mathbf{C}_1, \mathbf{C}_2, \dots, \mathbf{C}_n\}$, by

$$\bar{\mathbf{C}}_i = \alpha_i \mathbf{C}_i + (1 - \alpha_i) \mathbf{C}_{i-1} \quad (2.11)$$

where

$$\alpha_i = \begin{cases} 1 & 1 \leq i \leq k - p, \\ \frac{\bar{\xi} - \xi_i}{\xi_{i+p} - \xi_i} & k - p + 1 \leq i \leq k, \\ 0 & k + 1 \leq i \leq n + p + 2 \end{cases} \quad (2.12)$$

Knot values already present in the knot vector may be repeated as above but as described earlier, the continuity of the basis will be reduced. Continuity of the curve is preserved by choosing the control points as in (2.11) and (2.12). Each unique internal knot value may appear no more than p times or the curve becomes discontinuous.

An example of knot insertion is presented in Figure 2.2. The original curve consists of quadratic B-splines. The knot vector is $\Xi = \{0, 0, 0, 1, 1, 1\}$. The curve is shown on the left with basis functions below. A new knot is inserted at $\bar{\xi} = 0.5$. The new curve, shown on the right, is geometrically and parametrically identical to the original curve, but the basis functions, below the curve, and control points are changed. There is one more of each. This process may be repeated to enrich the solution space by adding more basis functions of the same order while leaving the curve unchanged. This subdivision strategy is seen to be analogous to the classical *h*-refinement strategy in finite element analysis.

Remark 2.1.1. An *h*-refinement procedure was described for NURBS curves. NURBS surfaces and solids are *h*-refined by inserting knots into each parametric direction sequentially. The same holds for *p*- and *k*-refinements, as described below.

***p*-refinement: Order elevation**

The polynomial order of basis functions may be increased without changing the geometry or parameterization. It is important to note that each unique knot value in Ξ must be repeated to preserve discontinuities in the p^{th} derivative of the curve being elevated. The number of new control points depends on the multiplicities of existing knots. This strategy of *order elevation* is an analogue of *p*-refinement in finite element analysis.

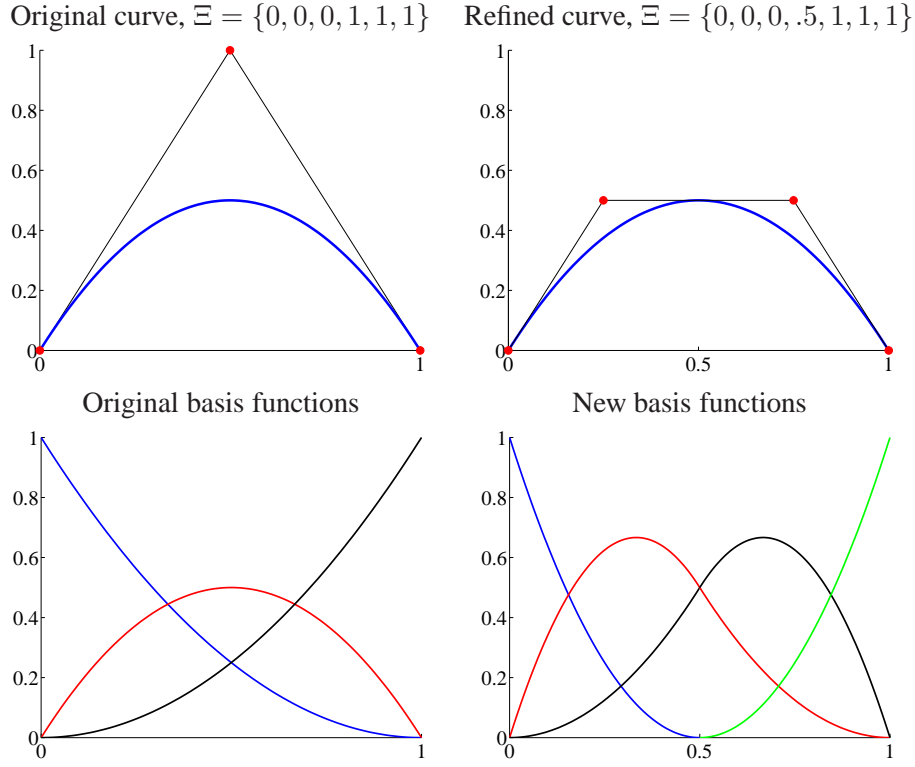


Figure 2.2: Knot insertion. Control points are denoted by \bullet 's.

As is the case of h -refinement by way of knot insertion, the solution space spanned by the order elevated basis functions contains the space spanned by the original functions. Thus, it is possible to order elevate without changing the geometry of the B-spline curve. Less obviously, it can be done so as to leave the parameterization of the curve in tact. The process for doing this involves subdividing the curve into many Bézier curves by knot insertion (see [85] or [79] for a discussion of Bézier curves), order elevating each of these individual segments, and then removing the unnecessary knots to combine the segments into one, order-elevated, B-spline curve. Several efficient algorithms exist which combine the steps so as to minimize the computational cost of the process.

An example of order elevation is depicted in Figure 2.3. The original curve and quadratic basis functions, shown on the left, are the same as considered in the previous example. This time the multiplicity of the knots is increased by one. The numbers of control points and basis functions each increase by one. The locations of the control points change, but the elevated curve is geometrically and parametrically identical to the original curve. There are now four cubic basis functions. The locations of control points for this elevated curve are different than those in the previous example

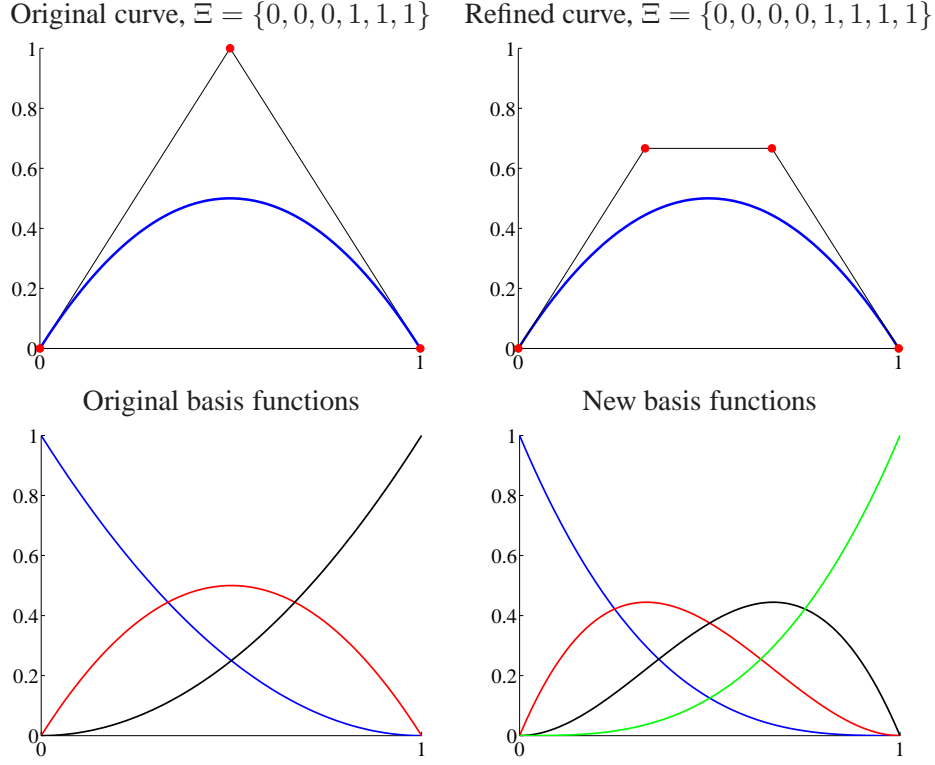


Figure 2.3: Order elevation. Control points are denoted by \bullet 's.

(cf. Fig. 2.2).

***k*-refinement**

An alternative order elevation strategy takes advantage of the fact that the processes of knot insertion and order elevation do not commute. If a unique knot value, $\bar{\xi}$, is inserted between two distinct knots in a curve of order p , the number of continuous derivatives of the basis functions at $\bar{\xi}$ is $p - 1$. As described above, if we subsequently elevate the order to q , the multiplicity of every distinct knot value (including the knot just inserted) is increased so that discontinuities in the p^{th} derivative of the basis are preserved, that is, the basis still has $p - 1$ continuous derivatives at $\bar{\xi}$. If instead we elevated the order of the original curve to q and only then inserted a unique knot value, the basis would have $q - 1$ continuous derivatives at $\bar{\xi}$. This latter procedure is referred to as *k-refinement*. It has no analogue in standard finite element analysis.

It is believed the concept of *k*-refinement is important and potentially a superior approach to high-precision analysis than *p*-refinement. Simple linear advection-diffusion calculations as well as some turbulent flow results, presented later in this document, indicate that this may be the

case. Another advantage of k -refinement is that the increase in the number of degrees of freedom from one refinement to the next is substantially smaller than in the case of p -refinement. It can be shown that in one dimension starting with n basis functions and performing r refinements gives $O(n(r + 1))$ degrees of freedom in the case of p -refinement, and $O(n + r)$ degrees of freedom for the k , which is quite a big difference. Keep in mind, too, that in d dimensions these numbers are raised to the d power. Of course, if the physical situation dictates a certain lower level of continuity at a knot value (e.g., the corners in the geometry, discontinuous material properties, etc.) this can always be incorporated into the process by knot duplication, so no generality is lost.

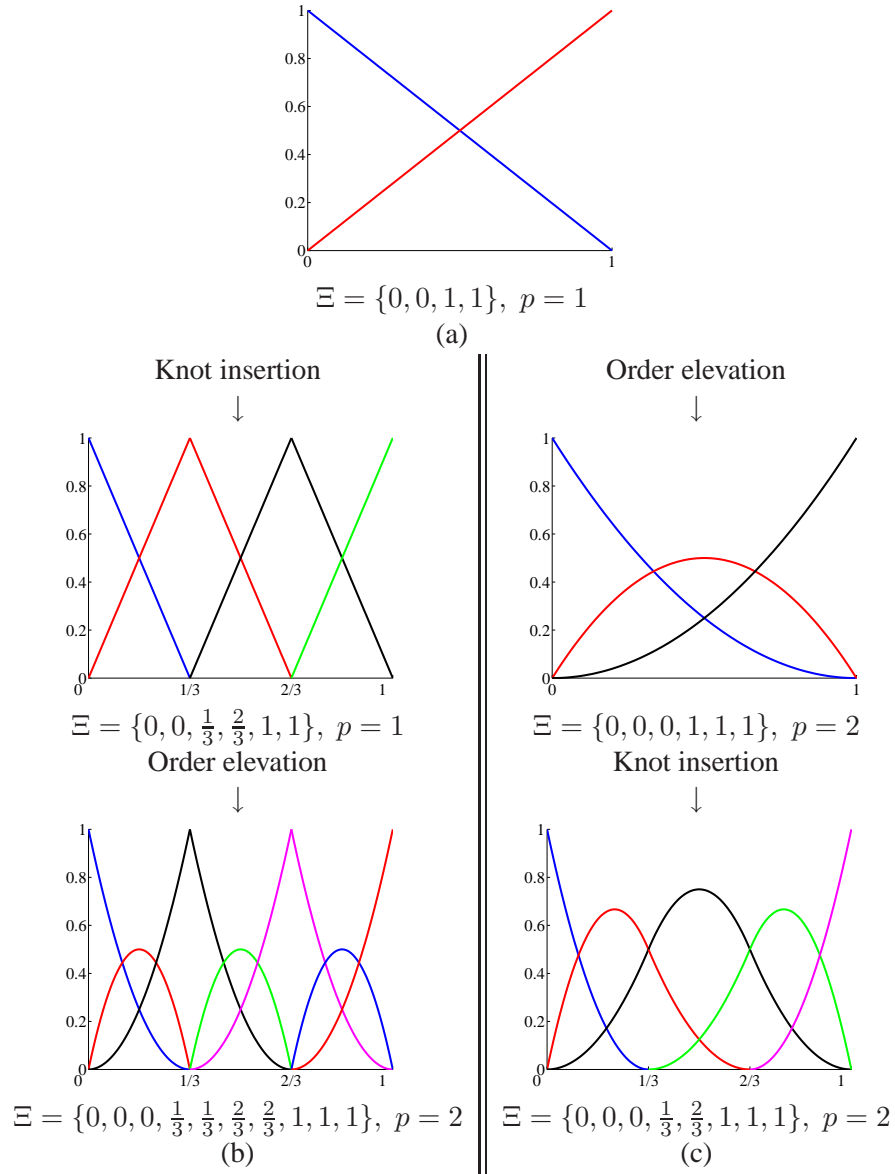


Figure 2.4: k -refinement takes advantage of the fact that knot insertion and order elevation do not commute. (a) Base case of one linear element. (b) Classic p -refinement approach: knot insertion followed by order elevation results in seven piecewise quadratic basis functions that are C^0 at internal knots. (c) New k -refinement approach: order elevation followed by knot insertion results in five piecewise quadratic basis functions that are C^1 at internal knots.

2.2 Construction of Analysis-Suitable Vascular Models

A large part of this work is fluid-structure interaction analysis of vascular flows using patient-specific geometrical configurations. In order to carry out these simulations, one needs to construct analysis-suitable geometrical models from medical imaging data. In Zhang *et al.* [] we have devised a set of procedures which accomplish this task. The summary of these developments is given in this section.

Construction of patient-specific models for isogeometric analysis is a process involving four stages, described below.

1. In scanned Computed Tomography (CT), or Magnetic Resonance Imaging (MRI), of patient-specific data, intensity contrast may not be sufficiently sharp, images are often “noisy”, and the luminal surface is frequently blurred. As a result, preprocessing of the CT/MRI data is necessary to improve its quality. Techniques such as contrast enhancement [115], filtering [5], classification [104], and segmentation [114] are employed for this purpose.
2. The blood vessel surface model can then be constructed from preprocessed imaging data using isocontouring methods. The two main isocontouring methods, that make use of imaging data, are: primal contouring or marching cubes [68], and dual contouring [60]. The latter is chosen in this work for isosurface extraction, as it tends to generate control meshes possessing better aspect ratios. In some cases geometric editing is required to remove unnecessary components and features. Once the luminal surface is identified, skeletonization technique [35] is employed in order to find paths.
3. We have developed a skeleton-based sweeping method to construct hexahedral NURBS control meshes for blood vessels [117]. The template faceted control polygon of a circle, projected onto the true surface, is swept along the arterial path to create a quadrilateral surface control mesh for a given arterial branch. Arterial branches are also arranged in a hierarchy, ranging from the largest to the smallest. Different cross-section templates are applied to different branches in the hierarchy. Templates for various branch intersections, such as bifurcations and trifurcations, are also worked out and applied on a case-by-case basis. See [117] for details.
4. Finally, solid NURBS meshes are constructed by filling in the volumes radially from the outer surface inward. Arterial wall meshes are obtained by extending the outer surface in the normal direction by a user-prescribed amount.

Stages 3 and 4 of the process are demonstrated on a simple example in Figure 2.5. A more complicated example of a patient-specific abdominal aorta is shown in Figure 2.6, where all four

stages of the model generation process, as well as the analysis result using techniques of Chapter 5 of this thesis are depicted.

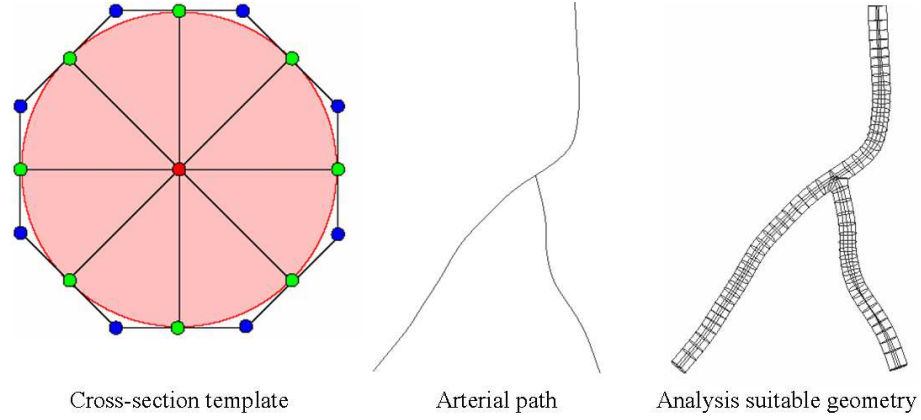


Figure 2.5: Stages 3 and 4 of the patient-specific cardiovascular model construction for isogeometric analysis. Left: depiction of a cross-section surface template. Cross-section surface is bounded by a closed quadratic NURBS curve defined in terms of the control polygon consisting of 16 points. Middle: arterial path identified by skeletonization. Right: solid NURBS geometry, ready for refinement and analysis.

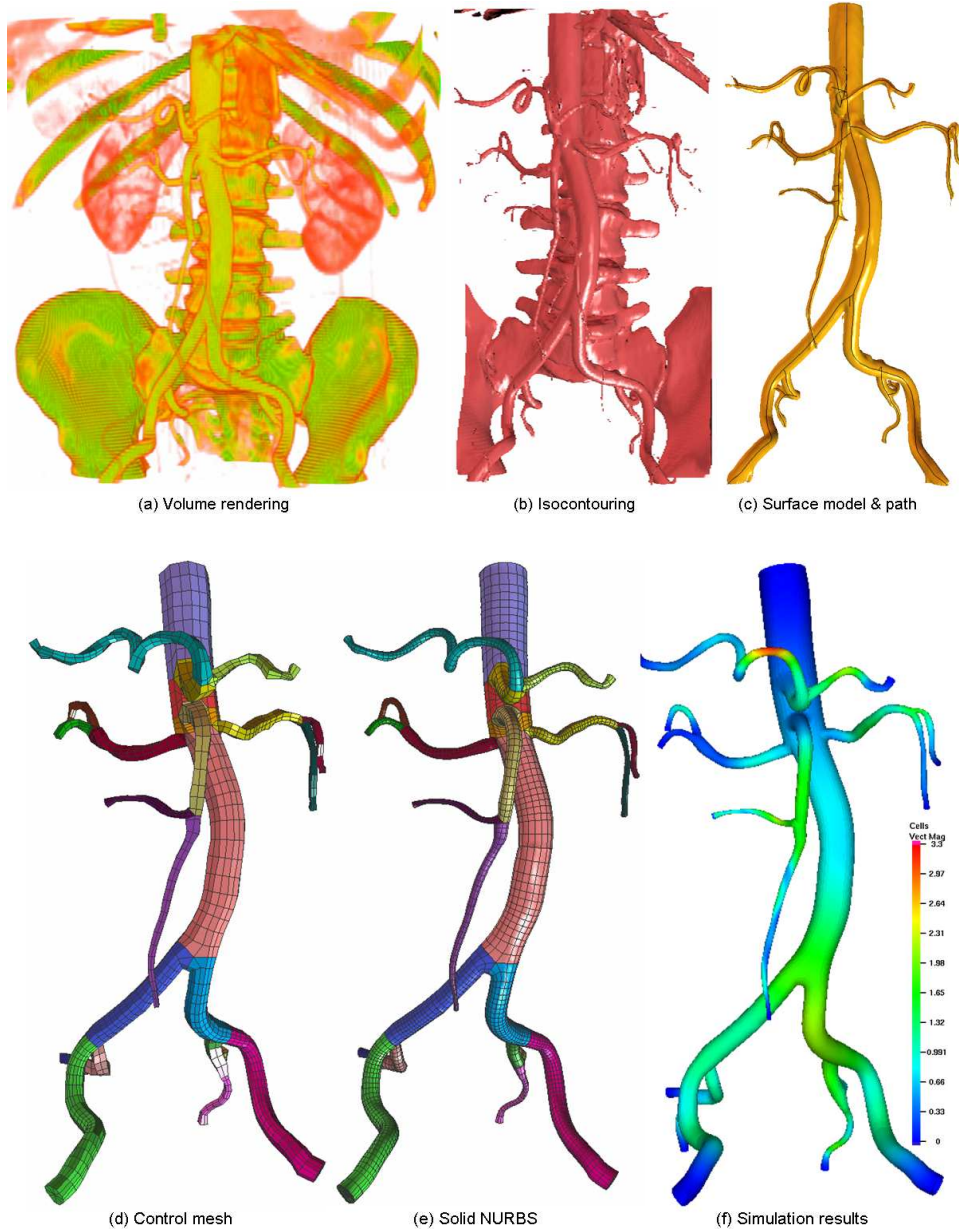


Figure 2.6: The abdominal aorta model is divided into 26 patches, and each color represents one different patch. (a) - volume rendering result; (b) - isocontouring result; (c) - surface model and its path after removing unnecessary components; (d) - control mesh; (e) - solid NURBS mesh after refinement (73,314 elements); (f) - fluid-structure interaction simulation results: contours of the arterial wall velocity (cm/s) during late systole plotted on the current configuration. Only major branches are kept in (d-f).

Chapter 3

Isogeometric Analysis: Approximation, stability and error estimates for h -refined meshes

3.1 Preliminaries

In what follows, let $d \geq 2$ be the dimension of the physical domain of interest. Throughout the analysis, we will make use of the classical Lebesgue spaces $L^p(\Omega)$, endowed with the norm $\|\cdot\|_{L^p(\Omega)}$, where $\Omega \subset \mathbb{R}^d$ is a generic open domain, and $1 \leq p \leq \infty$. We also will need the Sobolev spaces $W^{k,p}(\Omega)$, for k a positive integer and $1 \leq p \leq \infty$, endowed with the usual norm $\|\cdot\|_{W^{k,p}(\Omega)}$ and seminorm $|\cdot|_{W^{k,p}(\Omega)}$, see [1] for details. For the Hilbert spaces $W^{k,2}(\Omega)$ we will switch to the notation $H^k(\Omega)$, and, accordingly, $\|\cdot\|_{H^k(\Omega)}$ and $|\cdot|_{H^k(\Omega)}$ will be used for their norms and seminorms, respectively. We set $H^0(\Omega) := L^2(\Omega)$, and

$$\|\cdot\|_{H^0(\Omega)} \equiv |\cdot|_{H^0(\Omega)} := \|\cdot\|_{L^2(\Omega)}.$$

The spaces of continuous functions on Ω with k^{th} -order continuous derivatives will be denoted by $C^k(\Omega)$.

The rest of this section will be devoted to the introduction of the univariate and the multivariate (tensor product) B-spline basis functions and related spaces, the NURBS (*non-uniform rational B-spline*) basis functions, function space, and the NURBS geometrical map \mathbf{F} . This presentation is quite brief and notationally oriented¹; a more complete introduction to NURBS and isogeometric

¹Be aware that some of the notation and terminology contained here is different from that of [52]. Care should be exercised in comparing the two.

analysis can be found in [52].

3.1.1 Univariate splines

For any α , $1 \leq \alpha \leq d$, given positive integers m_α and n_α , we introduce the (ordered) knot vector

$$\Xi_\alpha := \{0 = \xi_{1,\alpha}, \xi_{2,\alpha}, \dots, \xi_{n_\alpha+m_\alpha,\alpha} = 1\}, \quad (3.1)$$

where we allow repetition of knots, that is, we only assume $\xi_{1,\alpha} \leq \xi_{2,\alpha} \leq \dots \leq \xi_{n_\alpha+m_\alpha,\alpha}$. We assume the Ξ_α 's are *open* knot vectors, that is, the first m_α as well as the last m_α knots are repeated (see [52, §2.1]).

Through the iterative procedure detailed in [87, Theorem 4.15] or in [52, §2.2] one constructs m_α -order B-spline basis functions, which are piecewise polynomials of degree $p_\alpha := m_\alpha - 1$ on the subdivision (3.1)². If a knot $\xi_{i,\alpha}$ is not repeated, then the B-spline basis functions have $p_\alpha - 1$ continuous derivatives at $\xi_{i,\alpha}$. In general, at a knot $\xi_{i,\alpha}$ repeated k times, with $1 \leq k \leq p_\alpha + 1$, the B-spline basis functions have $p_\alpha - k$ continuous derivatives, where $p_\alpha - k = -1$ is allowed and stands for a discontinuity. The B-splines basis functions are denoted by $B_{i,\alpha}$, for $i = 1, \dots, n_\alpha$; each $B_{i,\alpha}$ is non-negative and supported in $(\xi_{i,\alpha}, \xi_{i+m_\alpha,\alpha})$. The interval $(\xi_{i,\alpha}, \xi_{i+1,\alpha})$ is referred to as a knot span. The B-spline basis functions constitute a partition of unity, namely,

$$\sum_{i=1}^{n_\alpha} B_{i,\alpha} = 1 \quad (3.2)$$

A typical example is presented in Figure 3.1. The space of *splines* is denoted by

$$\mathcal{S}_\alpha \equiv \mathcal{S}(\Xi_\alpha, p_\alpha) := \text{span}\{B_{i,\alpha}\}_{i=1,\dots,n_\alpha}. \quad (3.3)$$

3.1.2 Multivariate tensor product splines

Assume that d knot vectors Ξ_α , with $1 \leq \alpha \leq d$, are given. Let $(0, 1)^d \subset \mathbb{R}^d$ be an open *parametric domain*, referred to as a *patch*. Associated with the knot vectors Ξ_α there is a *mesh* \mathcal{Q} , that is, a partition of $(0, 1)^d$ into d -dimensional open knot spans, or elements,

$$\mathcal{Q} \equiv \mathcal{Q}(\Xi_1, \dots, \Xi_d) := \left\{ Q = \otimes_{\alpha=1}^d (\xi_{i_\alpha,\alpha}, \xi_{i_\alpha+1,\alpha}) \mid Q \neq \emptyset, m_\alpha \leq i_\alpha \leq n_\alpha - 1 \right\}. \quad (3.4)$$

²We adhere to the terminology in which the “degree” of a quadratic, cubic, quartic, etc., polynomial is 2, 3, 4, etc., respectively, and the corresponding “order” is 3, 4, 5, etc., respectively. This is not the usual terminology used in the finite element literature, but is frequently used in the splines literature. In [18, 52] we use the finite element terminology to emphasize the similarities with finite elements.

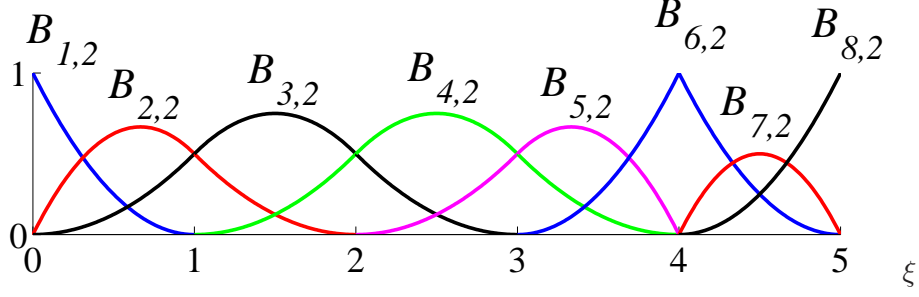


Figure 3.1: Example of a quadratic ($p_1 = 2$) B-spline basis in one dimension derived from the knot vector $\Xi = \{0, 0, 0, 0.2, 0.4, 0.6, 0.8, 0.8, 1, 1, 1\}$. Note that due to the open knot vector (i.e., the first and last knots are repeated $p_1 + 1$ times), the first and last basis functions are interpolatory (i.e., they take on the value 1 at the first and last knots). The continuity at interior knots ξ_i is $C^{p_1 - m_i}$, where m_i is the number of repetitions of knot ξ_i . For example, only the interior knot 0.8 is repeated, and the continuity there is $C^{p_1 - 2} = C^0$. At the other knots the continuity is $C^{p_1 - 1} = C^1$, the maximal continuity of quadratic B-splines.

We denote by h_Q the diameter of the element $Q \in \mathcal{Q}$.

The tensor product B-spline basis functions are defined as

$$B_{i_1 \dots i_d} := B_{i_1,1} \otimes \dots \otimes B_{i_d,d}; \quad (3.5)$$

The tensor-product spline space \mathcal{S} is:

$$\mathcal{S} \equiv \mathcal{S}(\Xi_1, \dots, \Xi_d; p_1, \dots, p_d) := \otimes_{\alpha=1}^d \mathcal{S}(\Xi_\alpha, p_\alpha) = \text{span}\{B_{i_1 \dots i_d}\}_{i_1=1, \dots, i_d=1}^{n_1, \dots, n_d}. \quad (3.6)$$

To a (non empty) element $Q = \otimes_{\alpha=1}^d (\xi_{i_\alpha, \alpha}, \xi_{i_{\alpha+1}, \alpha}) \in \mathcal{Q}$, we associate $\tilde{Q} \subset (0, 1)^d$ defined as

$$\tilde{Q} := \otimes_{\alpha=1}^d (\xi_{i_\alpha - m_\alpha + 1, \alpha}, \xi_{i_\alpha + m_\alpha, \alpha}). \quad (3.7)$$

The set \tilde{Q} will be referred to as the *support extension* of Q , since it is the union of the supports of basis functions whose support intersects Q . An illustration of support extensions is presented later in Figure 3.3.

The functions in \mathcal{S} are piecewise polynomials of degree p_α in the α coordinate. The regularity of each d -dimensional basis function $B_{i_1 \dots i_d}$ across the element boundaries depends on the regularity of the one-dimensional basis functions $B_{i_\alpha, \alpha}$, for $1 \leq \alpha \leq d$, at the corresponding knots. Given two adjacent elements Q_1 and Q_2 we denote by m_{Q_1, Q_2} the number of continuous derivatives across their common $(d - 1)$ -dimensional face $\partial Q_1 \cap \partial Q_2$; $m_{Q_1, Q_2} = -1$ is associated with a discontinuity. For the subsequent analysis, we introduce the following “bent” Sobolev space of

order $m \in \mathbb{N}$

$$\mathcal{H}^m := \left\{ \begin{array}{l} v \in L^2((0, 1)^d) \text{ such that} \\ v|_Q \in H^m(Q), \forall Q \in \mathcal{Q}, \text{ and} \\ \nabla^k(v|_{Q_1}) = \nabla^k(v|_{Q_2}) \text{ on } \partial Q_1 \cap \partial Q_2, \\ \forall k \in \mathbb{N} \text{ with } 0 \leq k \leq \min\{m_{Q_1, Q_2}, m - 1\} \\ \forall Q_1, Q_2 \text{ with } \partial Q_1 \cap \partial Q_2 \neq \emptyset \end{array} \right\}; \quad (3.8)$$

where ∇^k denotes the $(k$ -linear) k^{th} -order partial derivative operator, while $\nabla^0 v = v$. This is a well-defined Hilbert space, endowed with the seminorms

$$|v|_{\mathcal{H}^i}^2 := \sum_{Q \in \mathcal{Q}} |v|_{H^i(Q)}^2, \quad 0 \leq i \leq m \quad (3.9)$$

and norm

$$\|v\|_{\mathcal{H}^m}^2 := \sum_{i=0}^m |v|_{\mathcal{H}^i}^2. \quad (3.10)$$

Indeed, the trace of $\nabla^k v$ is well defined on $\partial Q_1 \cap \partial Q_2$, for $0 \leq k \leq \min\{m_{Q_1, Q_2}, m - 1\}$ (see [1]). We also need the restriction of \mathcal{H}^m to a given support extension \tilde{Q} , which is denoted by $\mathcal{H}^m(\tilde{Q}) := \{v|_{\tilde{Q}} | v \in \mathcal{H}^m\}$, and endowed with the seminorm and norm

$$|v|_{\mathcal{H}^i(\tilde{Q})}^2 := \sum_{\substack{Q' \in \mathcal{Q} \\ Q' \cap \tilde{Q} \neq \emptyset}} |v|_{H^i(Q')}^2 \quad \text{and} \quad \|v\|_{\mathcal{H}^m(\tilde{Q})}^2 := \sum_{i=0}^m |v|_{\mathcal{H}^i(\tilde{Q})}^2. \quad (3.11)$$

The bent Sobolev spaces are intermediate in continuity between standard Sobolev spaces and so-called “broken” Sobolev spaces [78] utilized in the analysis of discontinuous Galerkin methods.

3.1.3 NURBS and the geometry of the physical domain

We associate to each of the tensor-product B-spline basis functions $B_{i_1 \dots i_d}$ a strictly positive constant *weight* $w_{i_1 \dots i_d}$ and a *control point* $\mathbf{C}_{i_1 \dots i_d} \in \mathbb{R}^d$; we also introduce the *weighting function*

$$w := \sum_{i_1=1, \dots, i_d=1}^{n_1, \dots, n_d} w_{i_1 \dots i_d} B_{i_1 \dots i_d}, \quad (3.12)$$

which, due to the partition of unity and non-negativity properties of B-spline bases, is strictly greater than zero and is smooth on each element, along with its reciprocal. The NURBS basis functions on

the patch $(0, 1)^d$ are defined by a projective transformation (see Farin [25]):

$$R_{i_1 \dots i_d} = \frac{w_{i_1 \dots i_d} B_{i_1 \dots i_d}}{w}, \quad (3.13)$$

and, accordingly, the NURBS space on the patch, denoted by \mathcal{N} , is

$$\mathcal{N} \equiv \mathcal{N}(\Xi_1, \dots, \Xi_d; p_1, \dots, p_d; w) := \text{span}\{R_{i_1 \dots i_d}\}_{i_1=1, \dots, i_d=1}^{n_1, \dots, n_d}. \quad (3.14)$$

The NURBS geometrical map \mathbf{F} is given by

$$\mathbf{F} = \sum_{i_1=1, \dots, i_d=1}^{n_1, \dots, n_d} \mathbf{C}_{i_1 \dots i_d} R_{i_1 \dots i_d}; \quad (3.15)$$

\mathbf{F} is a parameterization of the physical domain Ω of interest (see [52]), that is,

$$\mathbf{F} : (0, 1)^d \rightarrow \Omega.$$

We assume that \mathbf{F} is invertible, with smooth inverse, on each element $Q \in \mathcal{Q}$.

Finally, each element $Q \in \mathcal{Q}$ is mapped into an element

$$K = \mathbf{F}(Q) := \{\mathbf{F}(\xi) | \xi \in Q\}, \quad (3.16)$$

and analogously \tilde{Q} , the support extension of Q , is mapped into

$$\tilde{K} = \mathbf{F}(\tilde{Q}). \quad (3.17)$$

We then introduce the mesh \mathcal{K} in the physical domain Ω

$$\mathcal{K} := \{K = \mathbf{F}(Q) | Q \in \mathcal{Q}\}, \quad (3.18)$$

and the space \mathcal{V} of NURBS on Ω (which is the *push-forward* of the space \mathcal{N} of NURBS on the patch)

$$\mathcal{V} \equiv \mathcal{V}(p_1, \dots, p_\alpha) := \text{span}\{R_{i_1 \dots i_d} \circ \mathbf{F}^{-1}\}_{i_1=1, \dots, i_d=1}^{n_1, \dots, n_d} \quad (3.19)$$

NURBS are capable of representing all conic sections, such as circles and ellipses, and consequently cylinders, spheres, tori, ellipsoids, are also exactly representable. See [18, 52] and the standard texts [25, 79, 85] for examples.

3.2 Approximation properties of the NURBS space

We consider now a family of meshes $\{\mathcal{Q}_h\}_h$ on $(0, 1)^d$, where each \mathcal{Q}_h is defined as in Section 2.2, and h denotes the family index, representing the global mesh size

$$h = \max\{h_Q | Q \in \mathcal{Q}_h\}.$$

The family of meshes is assumed to be *shape regular*, that is, the ratio between the smallest edge of $Q \in \mathcal{Q}_h$ and its diameter h_Q is bounded, uniformly with respect to Q and h . This implies that the mesh is *locally quasi-uniform*—the ratio of the sizes of two neighboring elements is uniformly bounded. Following the construction in the previous section, associated with the family of meshes $\{\mathcal{Q}_h\}_h$ we introduce the families of meshes on the physical domain $\{\mathcal{K}_h\}_h$, and the spaces $\{\mathcal{S}_h\}_h$, $\{\mathcal{N}_h\}_h$, $\{\mathcal{V}_h\}_h$, and $\{\mathcal{H}_h^m\}_h$ endowed with their respective norms.

In practical applications, the geometry of the physical domain Ω is frequently described on a mesh of relatively few elements, while the computation of an approximate solution to the problem is performed on a refined mesh (fine enough to achieve desired accuracy). Therefore, we assume that there is a *coarsest mesh* \mathcal{Q}_{h_0} in the family $\{\mathcal{Q}_h\}_h$, of which all the other meshes are a refinement, and that the description of the geometry is fixed at the level of \mathcal{Q}_{h_0} . This means that the weighting function w of (3.12) and the geometrical map \mathbf{F} in (3.15) are assigned in \mathcal{S}_{h_0} and $(\mathcal{N}_{h_0})^d$, respectively, and are the same for every h . When the mesh and the spaces are refined (see [52, §2.4] for details on the refinement procedures), the weights $w_{i_1 \dots i_d}$ are selected so that w stays fixed (see [52, equation (6)]); in a similar way, the control points $\mathbf{C}_{i_1 \dots i_d}$ are adjusted such that \mathbf{F} remains unchanged. Thus the geometry *and* its parameterization are held fixed in the refinement process. See Figure 3.2 for an illustration of this idea.

In what follows, we will denote by C a positive, *dimensionless* constant, possibly different at each occurrence, which depends only on the space dimension d , on the polynomial degrees p_α , $\alpha = 1, 2, \dots, d$, and on the shape regularity of the mesh family $\{\mathcal{Q}_h\}_h$. Observe that the p_α are considered fixed, since we only address h -refinement in this paper (see [52, §2.4], [18]). We will denote by C_s another positive, dimensionless constant, possibly different at each occurrence, which may also depend on the geometry of Ω but still *not* on h . Specifically, C_s depends on the *shape* of Ω , but not on its *size*; therefore C_s is by assumption homogeneous of order 0 with respect to w and $\nabla \mathbf{F}$, where $\nabla \mathbf{F}$ is the matrix of partial derivatives of the coordinate components of \mathbf{F} , that is, C_s is invariant if w and $\nabla \mathbf{F}$ are scaled by a multiplicative factor. Actually, C_s only depends on the dimensionless functions $w/\|w\|_{L^\infty(\Omega)}$ and $\nabla \mathbf{F}/\|\nabla \mathbf{F}\|_{L^\infty(\Omega)}$. Furthermore, if C_s appears in a *local* estimate, then it depends only on the local values of w and $\nabla \mathbf{F}$.

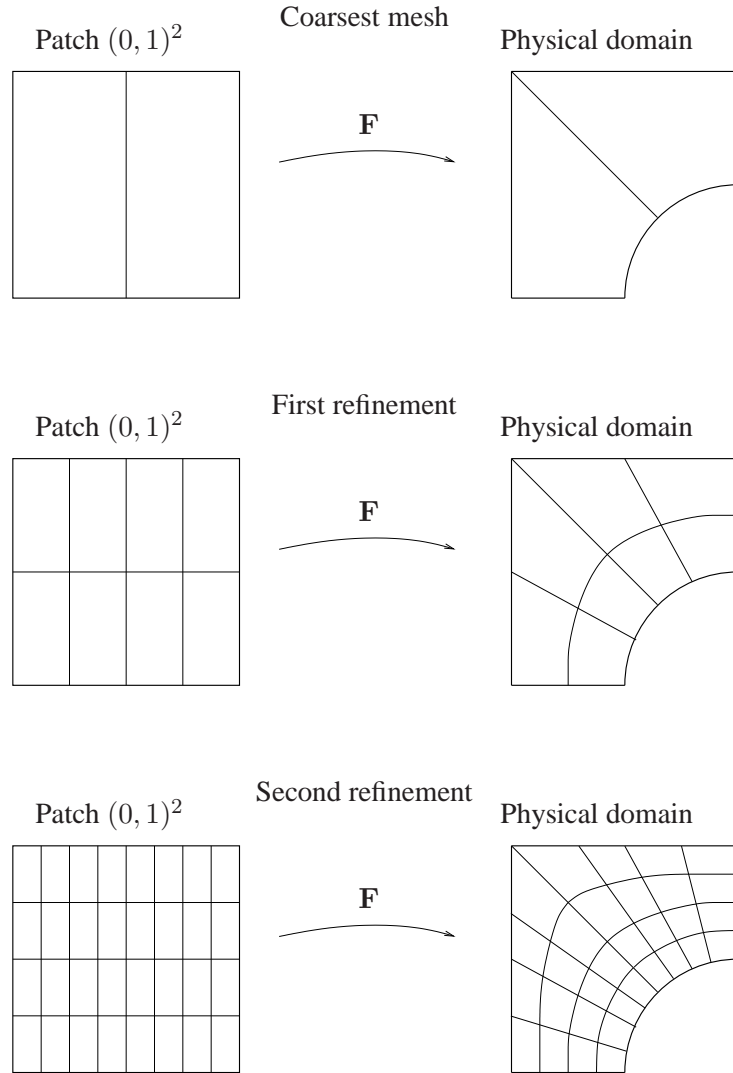


Figure 3.2: h -refinement with NURBS. In this illustration a NURBS patch is mapped onto a quarter of a square domain with a circular hole in physical space. The minimum degree NURBS required to exactly represent the geometry is quadratic. The open knot vectors are $\Xi_1 = \{0, 0, 0, 0.5, 1, 1, 1\}$ and $\Xi_2 = \{0, 0, 0, 1, 1, 1\}$, as illustrated. The exact geometry is represented at the coarsest level of discretization, and it and its parameterization are unchanged during refinement. In particular, the geometrical map \mathbf{F} and the weighting function w are unchanged during refinement.

3.2.1 Approximation with splines on a patch in the parametric domain

Our first lemma states the local approximation properties of the spline space \mathcal{S}_h . It is an extension of the classical result (see Bramble and Hilbert [10]). Our estimate involves bent Sobolev seminorms and spaces (3.8)–(3.9), which will be needed, in the following sections, when dealing with NURBS on the parametric and physical domains. Let p be defined as

$$p := \min_{1 \leq \alpha \leq d} \{p_\alpha\}. \quad (3.20)$$

Lemma 3.2.1. *Let k and l be integer indices with $0 \leq k \leq l \leq p + 1$. Given $Q \in \mathcal{Q}_h$, \tilde{Q} as in (3.7), $v \in \mathcal{H}_h^l$, there exists an $s \in \mathcal{S}_h$ such that*

$$|v - s|_{\mathcal{H}_h^k(\tilde{Q})} \leq Ch_Q^{l-k} |v|_{\mathcal{H}_h^l(\tilde{Q})}. \quad (3.21)$$

Proof. Consider an element $Q \in \mathcal{Q}_h$ and its corresponding support extension \tilde{Q} . The number of elements Q' forming the support extension \tilde{Q} and the degree of regularity of the functions in \mathcal{S}_h or \mathcal{H}_h^l across the internal element boundaries in \tilde{Q} may vary, according to the multiplicities of knots in the underlying knot vectors (see Section 2.2). Nevertheless, it is clear that there is only a finite number of *patterns* for all the possible support extensions \tilde{Q} of any mesh of the family $\{\mathcal{Q}_h\}_h$, and the maximum number of them depends only on p_α and on the space dimension d . It is not restrictive, therefore, to prove (3.21) for a particular \tilde{Q} , with the constant C appearing in (3.21) independent of the size of elements forming \tilde{Q} .

For the proof, we associate to \tilde{Q} a reference support extension \hat{Q} through a piecewise affine map $\mathbf{G} : \hat{Q} \rightarrow \tilde{Q}$ such that each element $Q' \in \tilde{Q}$ is the image of a hypercube $\mathbf{G}^{-1}(Q')$ which has unit edge length, where $\mathbf{G}^{-1}(Q') := \{\mathbf{G}^{-1}(\xi) | \xi \in Q'\}$ (see Figure 3.3).

Let $\hat{\mathcal{H}}_{\mathbf{c}}^m$ be the pullback of $\mathcal{H}_h^m(\tilde{Q})$ through \mathbf{G}

$$\hat{\mathcal{H}}_{\mathbf{c}}^m := \left\{ \hat{v} | \hat{v} = v \circ \mathbf{G}, v \in \mathcal{H}_h^m(\tilde{Q}) \right\}, \quad (3.22)$$

where \mathbf{c} is a vector of positive real numbers with the following meaning: assume that we have an ordering of the internal boundaries e of the elements in \tilde{Q} (e consists of $d - 1$ -dimensional hypercubes, that is, line segments for $d = 2$ or rectangles for $d = 3$) and a corresponding ordering on the internal boundaries \hat{e} in \hat{Q} . Also, define on each e and \hat{e} a unique normal direction \mathbf{n}_e and $\mathbf{n}_{\hat{e}}$. If e is shared between the two adjacent elements Q_1 and Q_2 belonging to \tilde{Q} , then, by construction, a function $v \in \mathcal{H}_h^m(\tilde{Q})$ has *matching* normal derivatives on e , up to the order $\min\{m_{Q_1, Q_2}, m - 1\}$

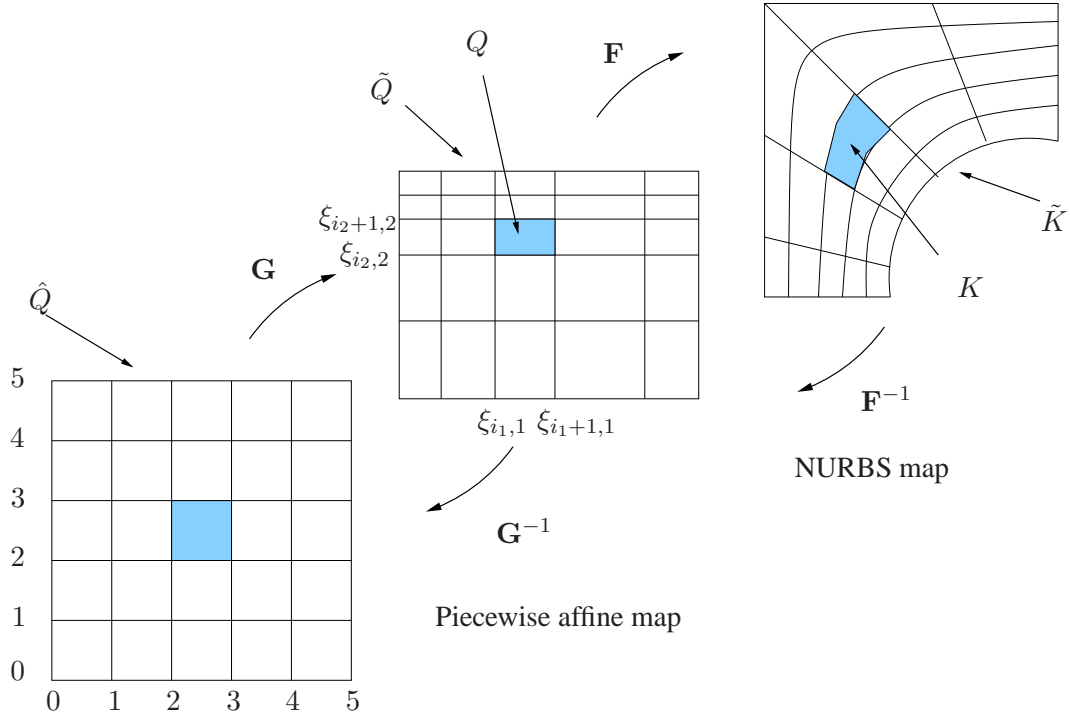


Figure 3.3: Depiction of the support extensions \tilde{K} , \tilde{Q} , and corresponding \hat{Q} . For non-repeated knots, the case illustrated would conform to quadratic B-splines or NURBS (i.e., $p_\alpha = 2$). Quadratic splines and NURBS have support over three knot spans in each direction. That is, each basis function is supported by a 3×3 mesh of elements. The support extensions are confined to individual patches in the multipatch case, assuming the patches are adjoined in C^0 -continuous fashion.

(see definition (3.8))

$$\frac{\partial^i}{\partial \mathbf{n}_e^i} (v|_{Q_1}) = \frac{\partial^i}{\partial \mathbf{n}_e^i} (v|_{Q_2}) \quad \text{on } e = \partial Q_1 \cap \partial Q_2, \quad 0 \leq i \leq \min\{m_{Q_1, Q_2}, m - 1\}. \quad (3.23)$$

When $i = 0$, the equality above expresses continuity of v across $\partial Q_1 \cap \partial Q_2$. For the pullback $\hat{v} = v \circ \mathbf{G}$, condition (3.23) is equivalent to

$$\begin{aligned} \frac{\partial^i}{\partial \mathbf{n}_{\hat{e}}^i} (\hat{v}|_{\mathbf{G}^{-1}(Q_1)}) &= (c_e)^i \frac{\partial^i}{\partial \mathbf{n}_{\hat{e}}^i} (\hat{v}|_{\mathbf{G}^{-1}(Q_2)}) \quad \text{on } \hat{e} = \mathbf{G}^{-1}(e), \\ 0 \leq i &\leq \min\{m_{Q_1, Q_2}, m - 1\}, \end{aligned} \quad (3.24)$$

where the constant c_e equals the ratio of the lengths of the two elements Q_1 and Q_2 in the direction of \mathbf{n}_e . The vector \mathbf{c} collects all of these coefficients. Since all of the meshes are (uniformly) shape regular and locally quasi-uniform, the coefficients c_e belong to a compact set bounded away from

0. Together with the space $\hat{\mathcal{H}}_{\mathbf{c}}^m$, we introduce the usual broken Sobolev space of order m

$$\hat{\mathcal{H}}^m := \left\{ \hat{v} \mid \hat{v} = v \circ \mathbf{G}, v|_{Q'} \in H^m(Q'), \forall Q' \text{ with } Q' \cap \tilde{Q} \neq \emptyset \right\}, \quad (3.25)$$

for which no conditions on the derivatives on the internal boundaries are assumed. We have $\hat{\mathcal{H}}_{\mathbf{c}}^m \subset \hat{\mathcal{H}}^m$, for any \mathbf{c} . We define on $\hat{\mathcal{H}}^m$ the seminorms and norm

$$|\hat{v}|_{\hat{\mathcal{H}}^i}^2 := \sum_{\substack{Q' \in \mathcal{Q}_h \\ Q' \cap \tilde{Q} \neq \emptyset}} |\hat{v}|_{H^i(\mathbf{G}^{-1}(Q'))}^2, \quad 0 \leq i \leq m, \quad \text{and} \quad \|\hat{v}\|_{\hat{\mathcal{H}}^m}^2 := \sum_{i=0}^m |\hat{v}|_{\hat{\mathcal{H}}^i}^2, \quad (3.26)$$

and we recall that

$$\|\hat{v}\|_{\hat{\mathcal{H}}^m}^2 \leq C \left(\|\hat{v}\|_{L^2(\tilde{Q})}^2 + |\hat{v}|_{\hat{\mathcal{H}}^m}^2 \right), \quad \forall \hat{v} \in \hat{\mathcal{H}}^m. \quad (3.27)$$

Let $\hat{\mathcal{P}}$ represent the set of piecewise polynomial functions of degree at most $l-1$ on \tilde{Q} , that is, the set of functions that are polynomials of the prescribed degree on each element forming \tilde{Q} , and define $\hat{\mathcal{P}}_{\mathbf{c}} := \hat{\mathcal{P}} \cap \hat{\mathcal{H}}_{\mathbf{c}}^l$. Observe that

$$\hat{\mathcal{P}}_{\mathbf{c}} \subset \{ \hat{v} \mid \hat{v} = v \circ \mathbf{G}, v \in \mathcal{S}_h \}. \quad (3.28)$$

By (3.27), (3.28), usual scaling arguments, and since $k \leq l$, in order to prove (3.21) it is then sufficient to find, given $\hat{v} \in \hat{\mathcal{H}}_{\mathbf{c}}^l$, a suitable $\hat{s} \in \hat{\mathcal{P}}_{\mathbf{c}}$ such that

$$\|\hat{v} - \hat{s}\|_{L^2(\tilde{Q})} + |\hat{v} - \hat{s}|_{\hat{\mathcal{H}}^l} \leq C |\hat{v}|_{\hat{\mathcal{H}}^l}, \quad (3.29)$$

with C independent of \hat{v} and \mathbf{c} . Let $\hat{\Pi}_{\mathbf{c}} : \hat{\mathcal{H}}^l \rightarrow \hat{\mathcal{P}}_{\mathbf{c}}$ be the $L^2(\tilde{Q})$ -projection onto the space $\hat{\mathcal{P}}_{\mathbf{c}}$. We prove that (3.29) holds true for $\hat{s} := \hat{\Pi}_{\mathbf{c}} \hat{v}$, that is we are going to show that

$$\|\hat{v} - \hat{\Pi}_{\mathbf{c}} \hat{v}\|_{L^2(\tilde{Q})} + |\hat{v} - \hat{\Pi}_{\mathbf{c}} \hat{v}|_{\hat{\mathcal{H}}^l} \leq C |\hat{v}|_{\hat{\mathcal{H}}^l}, \quad \forall \hat{v} \in \hat{\mathcal{H}}_{\mathbf{c}}^l, \quad (3.30)$$

uniformly with respect to \mathbf{c} .

We prove (3.30) by contradiction. Because

$$|\hat{\Pi}_{\mathbf{c}} \hat{v}|_{\hat{\mathcal{H}}^l} = 0, \quad \forall \hat{v} \in \hat{\mathcal{H}}^l, \forall \mathbf{c}, \quad (3.31)$$

assuming that (3.30) is false implies the existence of a sequence $\{\mathbf{c}_j\}_{j \in \mathbb{N}}$ of vectors and a sequence $\{\hat{v}_j\}_{j \in \mathbb{N}}$ of functions in $\hat{\mathcal{H}}_{\mathbf{c}_j}^l$ such that

$$\|\hat{v}_j - \hat{\Pi}_{\mathbf{c}_j} \hat{v}_j\|_{L^2(\tilde{Q})} = 1, \quad (3.32)$$

and

$$|\hat{v}_j|_{\hat{\mathcal{H}}^l} = 1/j. \quad (3.33)$$

As discussed above, the components of \mathbf{c}_j are in a compact set; therefore it is not restrictive to assume that the sequence $\{\mathbf{c}_j\}_{j \in \mathbb{N}}$ converges towards a limit \mathbf{c}_∞ (i.e., the components of \mathbf{c}_j converge to the corresponding components of \mathbf{c}_∞).

Recall that the space $\hat{\mathcal{H}}^l$ is compactly embedded into $L^2(\hat{Q})$. Therefore, defining $\hat{\eta}_j := \hat{v}_j - \hat{\Pi}_{\mathbf{c}_j} \hat{v}_j$, since $\|\hat{\eta}_j\|_{\hat{\mathcal{H}}^l} \leq C\|\hat{v}_j - \hat{\Pi}_{\mathbf{c}_j} \hat{v}_j\|_{L^2(\hat{Q})} + C|\hat{v}_j|_{\hat{\mathcal{H}}^l(\hat{Q})}$ is uniformly bounded, it is not restrictive to assume that the functions $\hat{\eta}_j$ converge towards a limit $\hat{\eta}_\infty$ in $L^2(\hat{Q})$. By (3.31) and (3.33), $\{\hat{\eta}_j\}_{j \in \mathbb{N}}$ is also a Cauchy sequence in $\hat{\mathcal{H}}^l$, hence $\hat{\eta}_j \rightarrow \hat{\eta}_\infty$ in $\hat{\mathcal{H}}^l$. Therefore

$$|\hat{\eta}_\infty|_{\hat{\mathcal{H}}^l} = \lim_{j \rightarrow \infty} |\hat{\eta}_j|_{\hat{\mathcal{H}}^l} = 0,$$

that is,

$$\hat{\eta}_\infty \in \hat{\mathcal{P}}. \quad (3.34)$$

In fact, since $\hat{\eta}_j \in \hat{\mathcal{H}}_{\mathbf{c}_j}^l$, it is easy to see that the conditions of (3.24) pass to the limit, yielding $\hat{\eta}_\infty \in \hat{\mathcal{H}}_{\mathbf{c}_\infty}^l$. This means that $\hat{\eta}_\infty \in \hat{\mathcal{P}}_{\mathbf{c}_\infty}$, and

$$\hat{\eta}_\infty = \hat{\Pi}_{\mathbf{c}_\infty} \hat{\eta}_\infty. \quad (3.35)$$

We have

$$\begin{aligned} & \|\hat{\Pi}_{\mathbf{c}_\infty} \hat{\eta}_\infty\|_{L^2(\hat{Q})} \\ & \leq \left\| \hat{\Pi}_{\mathbf{c}_\infty} \hat{\eta}_\infty - \hat{\Pi}_{\mathbf{c}_j} \hat{\eta}_\infty \right\|_{L^2(\hat{Q})} + \left\| \hat{\Pi}_{\mathbf{c}_j} \hat{\eta}_\infty - \hat{\Pi}_{\mathbf{c}_j} \hat{\eta}_j \right\|_{L^2(\hat{Q})} + \|\hat{\Pi}_{\mathbf{c}_j} \hat{\eta}_j\|_{L^2(\hat{Q})} \\ & = I + II + III. \end{aligned}$$

It is easy to see that $I \rightarrow 0$ when $j \rightarrow \infty$; indeed, we can have bases for $\mathcal{P}_{\mathbf{c}_j}$ that converge to a basis for $\mathcal{P}_{\mathbf{c}_\infty}$. Moreover, since $\hat{\Pi}_{\mathbf{c}_j}$ is uniformly bounded, $II = \|\hat{\Pi}_{\mathbf{c}_j}(\hat{\eta}_\infty - \hat{\eta}_j)\|_{L^2(\hat{Q})} \leq \|\hat{\eta}_\infty - \hat{\eta}_j\|_{L^2(\hat{Q})} \rightarrow 0$. Clearly, $III = 0$. Thus, $\hat{\Pi}_{\mathbf{c}_\infty} \hat{\eta}_\infty = 0$, and so by (3.35), we finally get

$$\hat{\eta}_\infty = 0, \quad (3.36)$$

which is in contradiction with (3.32), which implies

$$\|\hat{\eta}_\infty\|_{L^2(\hat{Q})} = \lim_{j \rightarrow \infty} \|\hat{\eta}_j\|_{L^2(\hat{Q})} = 1.$$

This proves (3.30). □

In [87, Chapter 12] a projector on the spline space \mathcal{S}_h is introduced. The projector, here denoted by $\Pi_{\mathcal{S}_h}$, with the present notation is written as

$$\Pi_{\mathcal{S}_h} v := \sum_{i_1=1, \dots, i_d=1}^{n_1, \dots, n_d} (\lambda_{i_1 \dots i_d} v) B_{i_1 \dots i_d}, \quad \forall v \in L^2((0, 1)^d) \quad (3.37)$$

where the $\lambda_{i_1 \dots i_d}$ are *dual* basis functionals, that is,

$$\begin{aligned} \lambda_{j_1 \dots j_d} B_{i_1 \dots i_d} &= 1 && \text{if } j_\alpha = i_\alpha, \forall 1 \leq \alpha \leq d, \\ \lambda_{j_1 \dots j_d} B_{i_1 \dots i_d} &= 0 && \text{otherwise.} \end{aligned}$$

From [87, Chapter 12], the functionals $\lambda_{i_1 \dots i_d}$ can be represented by functions with local support. This induces local stability properties on $\Pi_{\mathcal{S}_h}$. We summarize the previous properties in the following result, proved in [87, Theorem 12.6]:

Lemma 3.2.2. *We have*

$$\Pi_{\mathcal{S}_h} s = s, \quad \forall s \in \mathcal{S}_h \text{ (spline preserving)}, \quad (3.38)$$

$$\|\Pi_{\mathcal{S}_h} v\|_{L^2(Q)} \leq C \|v\|_{L^2(\tilde{Q})}, \quad \forall v \in L^2((0, 1)^d), \forall Q \in \mathcal{Q}_h \text{ (stability)}. \quad (3.39)$$

Lemma 3.2.3. *Let $\Pi_{\mathcal{S}_h} : L^2((0, 1)^d) \rightarrow \mathcal{S}_h$ satisfy (3.38) and (3.39), and $0 \leq k \leq l \leq p + 1$; then for all $Q \in \mathcal{Q}_h$*

$$|v - \Pi_{\mathcal{S}_h} v|_{H^k(Q)} \leq Ch_Q^{l-k} |v|_{\mathcal{H}^l(\tilde{Q})}, \quad \forall v \in \mathcal{H}_h^l(\tilde{Q}) \cap L^2((0, 1)^d). \quad (3.40)$$

Proof. Let s be as in Lemma 3.2.1; then, using (3.38),

$$\begin{aligned} |v - \Pi_{\mathcal{S}_h} v|_{H^k(Q)} &= |v - s + \Pi_{\mathcal{S}_h}(v - s)|_{H^k(Q)} \\ &\leq |v - s|_{H^k(Q)} + |\Pi_{\mathcal{S}_h}(v - s)|_{H^k(Q)} \\ &= I + II. \end{aligned}$$

Using (3.21) we get straightforwardly

$$I \leq Ch_Q^{l-k} |v|_{\mathcal{H}_h^l(\tilde{Q})}.$$

The usual inverse inequality for polynomials yields

$$|\Pi_{\mathcal{S}_h}(v - s)|_{H^k(Q)} \leq Ch_Q^{-k} \|\Pi_{\mathcal{S}_h}(v - s)\|_{L^2(Q)},$$

whence, making use of (3.39) and (3.21), we get

$$II \leq Ch_Q^{-k} \|v - s\|_{L^2(\tilde{Q})} \leq Ch_Q^{l-k} |v|_{\mathcal{H}_h^l(\tilde{Q})}.$$

□

3.2.2 Approximation with NURBS on a patch in the parametric domain

In this section we derive the approximation properties of the NURBS space on the patch $(0, 1)^d$. We define the projector $\Pi_{\mathcal{N}_h} : L^2((0, 1)^d) \rightarrow \mathcal{N}_h$ as

$$\Pi_{\mathcal{N}_h} v := \frac{\Pi_{\mathcal{S}_h}(wv)}{w}, \quad \forall v \in L^2((0, 1)^d), \quad (3.41)$$

where w is defined by (3.12).

Lemma 3.2.4. *Let k and l be integer indices with $0 \leq k \leq l \leq p + 1$; we have*

$$|v - \Pi_{\mathcal{N}_h} v|_{H^k(Q)} \leq C_s h_Q^{l-k} \|v\|_{\mathcal{H}_h^l(\tilde{Q})}, \quad \forall v \in \mathcal{H}_h^l, \forall Q \in \mathcal{Q}_h \quad (3.42)$$

Proof. Recalling that $w \in \mathcal{S}_{h_0} \subset \mathcal{S}_h$, it follows easily that, if $v \in \mathcal{H}^l(\tilde{Q})$, then also $wv \in \mathcal{H}^l(\tilde{Q})$. Therefore, making use of the definition (3.41), the Hölder inequality, and (3.40), we have

$$\begin{aligned} |v - \Pi_{\mathcal{N}_h} v|_{H^k(Q)} &= \left| \frac{1}{w} (wv - \Pi_{\mathcal{S}_h} wv) \right|_{H^k(Q)} \\ &\leq C \sum_{i=0}^k \left| \frac{1}{w} \right|_{W^{i,\infty}(Q)} |wv - \Pi_{\mathcal{S}_h} wv|_{H^{k-i}(Q)} \\ &\leq Ch_Q^{l-k} \sum_{i=0}^k \left| \frac{1}{w} \right|_{W^{i,\infty}(Q)} |wv|_{\mathcal{H}_h^{l-i}(\tilde{Q})} \\ &\leq Ch_Q^{l-k} \sum_{i=0}^k \left| \frac{1}{w} \right|_{W^{i,\infty}(Q)} \sum_{j=0}^{l-i} \sum_{\substack{Q' \in \mathcal{Q}_h \\ Q' \cap \tilde{Q} \neq \emptyset}} |w|_{W^{j,\infty}(Q')} |v|_{H^{l-(i+j)}(Q')}. \end{aligned}$$

Since $0 \leq i + j \leq l$ in the last summations, we get (3.42), with a constant C_s that depends on $|1/w|_{W^{i,\infty}(Q)} |w|_{W^{j,\infty}(Q')}$, that is, only depends on the weight function w and its reciprocal $1/w$ on \tilde{Q} , and is uniformly bounded with respect to the mesh size. □

3.2.3 Approximation with NURBS in the physical domain

The following lemma gives estimates for the change of variable from the patch to the physical domain.

Lemma 3.2.5. *Let m be a non-negative integer, $Q \in \mathcal{Q}_h$ and $K = \mathbf{F}(Q)$. For all functions $v \in H^m(K)$, it holds that*

$$|v \circ \mathbf{F}|_{H^m(Q)} \leq C_{\mathfrak{s}} \|\det \nabla \mathbf{F}^{-1}\|_{L^\infty(K)}^{1/2} \sum_{j=0}^m \|\nabla \mathbf{F}\|_{L^\infty(Q)}^j |v|_{H^j(K)} \quad (3.43)$$

$$|v|_{H^m(K)} \leq C_{\mathfrak{s}} \|\det \nabla \mathbf{F}\|_{L^\infty(Q)}^{1/2} \|\nabla \mathbf{F}\|_{L^\infty(Q)}^{-m} \sum_{j=0}^m |v \circ \mathbf{F}|_{H^j(Q)} \quad (3.44)$$

Proof. We will address the case $m \geq 1$, the case $m = 0$ being trivial. We start by introducing the function

$$\check{\mathbf{F}} = \frac{\mathbf{F}}{\|\nabla \mathbf{F}\|_{L^\infty(Q)}} : Q \rightarrow \check{K} \quad (3.45)$$

A direct derivation gives

$$\nabla^k \mathbf{F} = \|\nabla \mathbf{F}\|_{L^\infty(Q)} \nabla^k \check{\mathbf{F}} \quad (3.46)$$

where here and in what follows k indicates an integer with $1 \leq k \leq m$. From (3.46) we get

$$\|\nabla^k \mathbf{F}\|_{L^\infty(Q)} \leq \|\nabla \mathbf{F}\|_{L^\infty(Q)} \|\nabla^k \check{\mathbf{F}}\|_{L^\infty(Q)}. \quad (3.47)$$

Let now ξ be any point in Q and $x = \mathbf{F}(\xi)$. We then have by definition

$$x = \|\nabla \mathbf{F}\|_{L^\infty(Q)} \check{\mathbf{F}}(\xi), \quad (3.48)$$

$$\xi = \check{\mathbf{F}}^{-1} \left(\frac{x}{\|\nabla \mathbf{F}\|_{L^\infty(Q)}} \right). \quad (3.49)$$

As a consequence we have

$$\mathbf{F}^{-1}(x) = \xi = \check{\mathbf{F}}^{-1} \left(\frac{x}{\|\nabla \mathbf{F}\|_{L^\infty(Q)}} \right). \quad (3.50)$$

which, by derivation, gives

$$\nabla^k \mathbf{F}^{-1}(x) = \nabla^k \check{\mathbf{F}}^{-1} \left(\frac{x}{\|\nabla \mathbf{F}\|_{L^\infty(Q)}} \right) \|\nabla \mathbf{F}\|_{L^\infty(Q)}^{-k}. \quad (3.51)$$

Taking the L^∞ norm, identity (3.51) gives

$$\|\nabla^k \mathbf{F}^{-1}\|_{L^\infty(K)} \leq \|\nabla^k \check{\mathbf{F}}^{-1}\|_{L^\infty(\check{K})} \|\nabla \mathbf{F}\|_{L^\infty(Q)}^{-k}. \quad (3.52)$$

By Lemma 3 in [16], there exists a constant C depending only on m such that, for all $\xi \in Q$,

$$\|\nabla^m(v \circ \mathbf{F})(\xi)\| \leq C \sum_{j=1}^m \|\nabla^j v(x)\| \sum_{\mathbf{i} \in I(j,m)} \|\nabla \mathbf{F}(\xi)\|^{i_1} \|\nabla^2 \mathbf{F}(\xi)\|^{i_2} \dots \|\nabla^m \mathbf{F}(\xi)\|^{i_m}, \quad (3.53)$$

where

$$I(j, m) = \{\mathbf{i} = (i_1, i_2, \dots, i_m) \in \mathbb{N}^m : i_1 + i_2 + \dots + i_m = j, i_1 + 2i_2 + \dots + mi_m = m\}. \quad (3.54)$$

A change of variables, bound (3.53) and the Hölder inequality give

$$\begin{aligned} |v \circ \mathbf{F}|_{H^m(Q)} & \\ & \leq C \|\det \nabla \mathbf{F}^{-1}\|_{L^\infty(K)}^{1/2} \sum_{j=1}^m |v|_{H^j(K)} \sum_{\mathbf{i} \in I(j,m)} \|\nabla \mathbf{F}\|_{L^\infty(Q)}^{i_1} \|\nabla^2 \mathbf{F}\|_{L^\infty(Q)}^{i_2} \dots \|\nabla^m \mathbf{F}\|_{L^\infty(Q)}^{i_m}. \end{aligned} \quad (3.55)$$

Using (3.47) and recalling (3.54), the above bound easily gives

$$\begin{aligned} |v \circ \mathbf{F}|_{H^m(Q)} & \leq C \|\det \nabla \mathbf{F}^{-1}\|_{L^\infty(K)}^{1/2} \sum_{j=1}^m |v|_{H^j(K)} \|\nabla \mathbf{F}\|_{L^\infty(Q)}^j \\ & \cdot \sum_{\mathbf{i} \in I(j,m)} \|\nabla \check{\mathbf{F}}\|_{L^\infty(Q)}^{i_1} \|\nabla^2 \check{\mathbf{F}}\|_{L^\infty(Q)}^{i_2} \dots \|\nabla^m \check{\mathbf{F}}\|_{L^\infty(Q)}^{i_m} \\ & \leq C'(m, \|\nabla \check{\mathbf{F}}\|_{W^{m,\infty}(Q)}) \|\det \nabla \mathbf{F}^{-1}\|_{L^\infty(K)}^{1/2} \sum_{j=1}^m \|\nabla \mathbf{F}\|_{L^\infty(Q)}^j |v|_{H^j(K)}. \end{aligned} \quad (3.56)$$

Applying Lemma 3 of [16] to the inverse function \mathbf{F}^{-1} , similar arguments give

$$\begin{aligned} |v|_{H^m(K)} & \leq C \|\det \nabla \mathbf{F}\|_{L^\infty(Q)}^{1/2} \\ & \sum_{j=1}^m |v \circ \mathbf{F}|_{H^j(Q)} \sum_{\mathbf{i} \in I(j,m)} \|\nabla \mathbf{F}^{-1}\|_{L^\infty(K)}^{i_1} \|\nabla^2 \mathbf{F}^{-1}\|_{L^\infty(K)}^{i_2} \dots \|\nabla^m \mathbf{F}^{-1}\|_{L^\infty(K)}^{i_m}. \end{aligned}$$

Applying (3.52) to bound (3.57), following the same steps as already performed in (3.56) it finally

follows that

$$|v|_{H^m(K)} \leq C''(m, \|\nabla \check{\mathbf{F}}^{-1}\|_{W^{m,\infty}(\check{K})}) \|\det \nabla \mathbf{F}\|_{L^\infty(Q)}^{1/2} \|\nabla \mathbf{F}\|_{L^\infty(Q)}^{-m} \sum_{j=1}^m |v \circ \mathbf{F}|_{H^j(Q)}. \quad (3.57)$$

Bounds (3.43) and (3.44) are proven, provided we show that C' and C'' behave as *shape* dependent constants $C_{\mathfrak{s}}$ (see Section 3). From the above calculations it immediately follows that C' and C'' are continuous functions of $\|\nabla \check{\mathbf{F}}\|_{W^{m,\infty}(Q)}$ and $\|\nabla \check{\mathbf{F}}^{-1}\|_{W^{m,\infty}(\check{K})}$, respectively. Observe that $\nabla \check{\mathbf{F}}$ and $\nabla \check{\mathbf{F}}^{-1}$ are 0-homogeneous with respect to $\nabla \mathbf{F}$, and so are C' and C'' . Furthermore, from (3.46) and (3.51)

$$\|\nabla \check{\mathbf{F}}\|_{W^{m,\infty}(Q)} = \frac{\|\nabla \mathbf{F}\|_{W^{m,\infty}(Q)}}{\|\nabla \mathbf{F}\|_{L^\infty(Q)}} \leq \|\nabla \mathbf{F}\|_{W^{m,\infty}(Q)} \inf_{x \in K} \|\nabla \mathbf{F}^{-1}(x)\| \quad (3.58)$$

$$\|\nabla \check{\mathbf{F}}^{-1}\|_{W^{m,\infty}(\check{K})} \leq \sum_{j=0}^m \|\nabla^j \mathbf{F}^{-1}\|_{L^\infty(K)} \|\nabla \mathbf{F}\|_{L^\infty(Q)}^j; \quad (3.59)$$

recalling that the NURBS map \mathbf{F} is fixed, uniform boundedness with respect to the mesh-size easily follows. □

We define the projector $\Pi_{\mathcal{V}_h} : L^2(\Omega) \rightarrow \mathcal{V}_h$ as

$$\Pi_{\mathcal{V}_h} v := (\Pi_{\mathcal{N}_h}(v \circ \mathbf{F})) \circ \mathbf{F}^{-1}, \quad \forall v \in L^2(\Omega). \quad (3.60)$$

We refer to (3.60) as the push-forward of the NURBS projector. It is defined in Figure 3.4 and its approximation properties are stated in the next result.

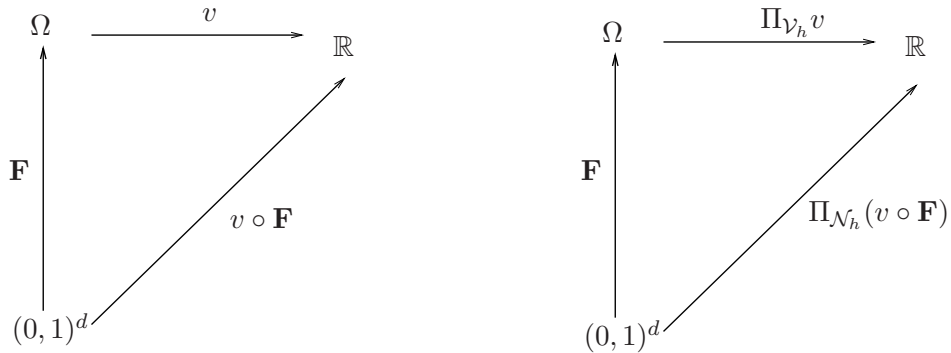


Figure 3.4: $\Pi_{\mathcal{V}_h} v$ is the push-forward of the NURBS projector $\Pi_{\mathcal{N}_h}(v \circ \mathbf{F})$, where $v \in L^2(\Omega)$ and $v \circ \mathbf{F} \in L^2((0,1)^d)$.

Theorem 3.2.1. *Let k and l be integer indices with $0 \leq k \leq l \leq p+1$; let $Q \in \mathcal{Q}_h$, $K = \mathbf{F}(Q)$, \tilde{Q} and \tilde{K} as in (3.7) and (3.17), respectively; we have*

$$|v - \Pi_{\mathcal{V}_h} v|_{H^k(K)} \leq C_s h_K^{l-k} \sum_{i=0}^l \|\nabla \mathbf{F}\|_{L^\infty(\tilde{Q})}^{i-l} |v|_{H^i(\tilde{K})}, \quad \forall v \in L^2(\Omega) \cap H^l(\tilde{K}), \quad (3.61)$$

where h_K is the element size in the physical domain defined as

$$h_K = \|\nabla \mathbf{F}\|_{L^\infty(Q)} h_Q. \quad (3.62)$$

Proof. Using (3.60), and then (3.44), we have

$$\begin{aligned} |v - \Pi_{\mathcal{V}_h} v|_{H^k(K)} &= |v - (\Pi_{\mathcal{N}_h}(v \circ \mathbf{F})) \circ \mathbf{F}^{-1}|_{H^k(K)} \\ &\leq C_s \|\det \nabla \mathbf{F}\|_{L^\infty(Q)}^{1/2} \|\nabla \mathbf{F}\|_{L^\infty(Q)}^{-k} \sum_{i=0}^k |v \circ \mathbf{F} - \Pi_{\mathcal{N}_h}(v \circ \mathbf{F})|_{H^i(Q)} \end{aligned} \quad (3.63)$$

Notice that since $v \in H^l(\tilde{K})$, we have $v \circ \mathbf{F} \in \mathcal{H}_h^l(\tilde{Q})$ and we can use the estimate of (3.42) on each term $|v \circ \mathbf{F} - \Pi_{\mathcal{N}_h}(v \circ \mathbf{F})|_{H^i(Q)}$, obtaining

$$\begin{aligned} |v \circ \mathbf{F} - \Pi_{\mathcal{N}_h}(v \circ \mathbf{F})|_{H^i(Q)} &\leq C_s h_Q^{l-k} \|v \circ \mathbf{F}\|_{\mathcal{H}_h^{l+i-k}(\tilde{Q})} \\ &\leq C_s h_Q^{l-k} \sum_{j=0}^{l+i-k} |v \circ \mathbf{F}|_{\mathcal{H}_h^j(\tilde{Q})}. \end{aligned} \quad (3.64)$$

Since $0 \leq i \leq k$ in (3.63) and $0 \leq j \leq l+i-k$ in (3.64), the two sums over the indices collapse into one and we have

$$\begin{aligned} |v - \Pi_{\mathcal{V}_h} v|_{H^k(K)} &\leq C_s \|\det \nabla \mathbf{F}\|_{L^\infty(Q)}^{1/2} \|\nabla \mathbf{F}\|_{L^\infty(Q)}^{-k} h_Q^{l-k} \sum_{i=0}^l |v \circ \mathbf{F}|_{\mathcal{H}_h^i(\tilde{Q})} \\ &= C_s \|\det \nabla \mathbf{F}\|_{L^\infty(Q)}^{1/2} \|\nabla \mathbf{F}\|_{L^\infty(Q)}^{-k} h_Q^{l-k} \sum_{i=0}^l \sum_{\substack{Q' \in \mathcal{Q}_h \\ Q' \cap \tilde{Q} \neq \emptyset}} |v \circ \mathbf{F}|_{H^i(Q')}. \end{aligned} \quad (3.65)$$

Using (3.43) on each term $|v \circ \mathbf{F}|_{\mathcal{H}_h^i(Q')}$ of the last summation of (3.65) we get

$$|v \circ \mathbf{F}|_{H^i(Q')} \leq C_s \|\det \nabla \mathbf{F}^{-1}\|_{L^\infty(K')}^{1/2} \sum_{j=0}^i \|\nabla \mathbf{F}\|_{L^\infty(Q')}^j |v|_{H^j(K')}, \quad (3.66)$$

where, as before, $\mathbf{F}(Q') = K'$. From (3.65) and (3.66), since $0 \leq i \leq l$ and $0 \leq j \leq i$, by

coalescing the double summation onto a single sum, we have

$$\begin{aligned}
|v - \Pi_{\mathcal{V}_h} v|_{H^k(K)} &\leq C_s \|\nabla \mathbf{F}\|_{L^\infty(Q)}^{-k} h_Q^{l-k} \sum_{i=0}^l \sum_{\substack{K' \in \mathcal{K}_h \\ K' \cap \tilde{K} \neq \emptyset}} \|\nabla \mathbf{F}\|_{L^\infty(Q')}^i |v|_{H^i(K')} \\
&\leq C_s \|\nabla \mathbf{F}\|_{L^\infty(\tilde{Q})}^{-k} h_Q^{l-k} \sum_{i=0}^l \|\nabla \mathbf{F}\|_{L^\infty(\tilde{Q})}^i |v|_{H^i(\tilde{K})},
\end{aligned} \tag{3.67}$$

where we also used $\|\det \nabla \mathbf{F}\|_{L^\infty(Q)}^{1/2} \|\det \nabla \mathbf{F}^{-1}\|_{L^\infty(K)}^{1/2} \leq C_s$. Multiplying and dividing the right-hand side of (3.67) by $\|\nabla \mathbf{F}\|_{L^\infty(\tilde{Q})}^l$, and using the definition of the element size in the physical domain (3.62) we obtain

$$|v - \Pi_{\mathcal{V}_h} v|_{H^k(K)} \leq C_s \frac{\|\nabla \mathbf{F}\|_{L^\infty(\tilde{Q})}^{l-k}}{\|\nabla \mathbf{F}\|_{L^\infty(Q)}^{l-k}} h_K^{l-k} \sum_{i=0}^l \|\nabla \mathbf{F}\|_{L^\infty(\tilde{Q})}^{i-l} |v|_{H^i(\tilde{K})}. \tag{3.68}$$

Subsuming the fraction in the above inequality into C_s , we finally get (3.61). \square

As a corollary we have the global error estimate stated below.

Theorem 3.2.2. *Let k and l be integer indices with $0 \leq k \leq l \leq p+1$, we have*

$$\sum_{K \in \mathcal{K}_h} |v - \Pi_{\mathcal{V}_h} v|_{\mathcal{H}_h^k(K)}^2 \leq C_s \sum_{K \in \mathcal{K}_h} h_K^{2(l-k)} \sum_{i=0}^l \|\nabla \mathbf{F}\|_{L^\infty(\mathbf{F}^{-1}(K))}^{2(i-l)} |v|_{H^i(K)}^2, \forall v \in H^l(\Omega). \tag{3.69}$$

Remark 3.2.1. *We note from Theorem 3.2.1 and Theorem 3.2.2 that the NURBS space \mathcal{V}_h on the physical domain Ω delivers the optimal rate of convergence, as for the classical finite element spaces of degree p . Note that a bound on the k^{th} -order seminorm of the error $v - \Pi_{\mathcal{V}_h} v$ requires a control on the full l^{th} -order norm of v , unlike for finite elements (or splines, as in (3.40)) where only the l^{th} -order seminorm of v is involved in the right-hand side of the estimate. This is due to the role played by the weighting function w and the geometrical map \mathbf{F} .*

Note moreover that the estimates stated in Theorem 3.2.1 and 3.2.2 are dimensionally consistent. Indeed C_s is a dimensionless constant, while both h_K and $\|\nabla \mathbf{F}\|_{L^\infty(\mathbf{F}^{-1}(K))}$ have dimensions of length; the patch $(0,1)^d$ is dimensionless while the physical space Ω is a dimensional space, which implies that $\nabla \mathbf{F}$ has the dimensions of length. The coefficients $\|\nabla \mathbf{F}\|_{L^\infty(\mathbf{F}^{-1}(K))}^{i-l}$ compensate for the different dimensions of the seminorms $|v|_{H^i}$ inside the summation of (3.61) and (3.69).

3.2.4 Spaces with boundary conditions

Dealing with boundary conditions in the variational formulation of continuum mechanics problems requires Sobolev spaces of functions satisfying boundary constraints. The analysis developed in the previous sections can be adapted to this context with only minor modifications, as sketched below.

We focus our attention on the case of Dirichlet boundary conditions for second-order differential operators of the type discussed later in Section 5-6. Let $\partial\Omega$ be the boundary of $\Omega \subset \mathbb{R}^d$, with $d = 2, 3$, and $\Gamma_D \subset \partial\Omega$ the part of the boundary where the Dirichlet conditions hold. Moreover assume, for the sake of simplicity, that Γ_D is the union of element faces (for $d = 3$) or edges (for $d = 2$), and let $\gamma_D = \mathbf{F}^{-1}(\Gamma_D)$. For the purposes of analysis of the numerical methods, we need a projector from $H^k(\Omega)$ into \mathcal{V}_h which preserves the nullity of the traces on Γ_D and with the same approximation properties as stated in Theorem 3.2. Let

$$H_{\Gamma_D}^1(\Omega) = \{v \in H^1(\Omega) \mid v = 0 \text{ on } \Gamma_D\},$$

and accordingly

$$H_{\gamma_D}^1((0, 1)^d) = \left\{v \in H^1((0, 1)^d) \mid v = 0 \text{ on } \gamma_D\right\},$$

Assume, for the sake of simplicity, that $\mathcal{S}_h \subset C^0((0, 1)^d)$. It is easy to verify (see [52] or [87]) that the tensor product B-spline basis functions give

$$\mathcal{S}_h \cap H_{\gamma_D}^1((0, 1)^d) = \text{span}\{B_{i_1 \dots i_d} \mid B_{i_1 \dots i_d} \in H_{\gamma_D}^1((0, 1)^d), 1 \leq i_\alpha \leq n_\alpha, 1 \leq \alpha \leq d\}. \quad (3.70)$$

It seems natural therefore to modify the definition of (3.37), restricting to such a basis in (3.70). Therefore we set

$$\Pi_{\mathcal{S}_h}^0 v := \sum_{\substack{i_\alpha=1, \dots, n_\alpha \\ B_{i_1 \dots i_d} \in H_{\gamma_D}^1((0, 1)^d)}} (\lambda_{i_1 \dots i_d} v) B_{i_1 \dots i_d}, \quad \forall v \in H_{\gamma_D}^1((0, 1)^d), \quad (3.71)$$

where, since (3.70), $\Pi_{\mathcal{S}_h}^0 : H_{\gamma_D}^1((0, 1)^d) \rightarrow \mathcal{S}_h \cap H_{\gamma_D}^1((0, 1)^d)$.

The projectors $\Pi_{\mathcal{N}_h}^0 : H_{\gamma_D}^1((0, 1)^d) \rightarrow \mathcal{N}_h \cap H_{\gamma_D}^1((0, 1)^d)$ and $\Pi_{\mathcal{V}_h}^0 : H_{\Gamma_D}^1(\Omega) \rightarrow \mathcal{V}_h \cap H_{\Gamma_D}^1(\Omega)$ can be defined accordingly:

$$\begin{aligned} \Pi_{\mathcal{N}_h}^0 v &:= \frac{\Pi_{\mathcal{S}_h}^0(wv)}{w}, \quad \forall v \in H_{\gamma_D}^1((0, 1)^d), \\ \Pi_{\mathcal{V}_h}^0 v &:= (\Pi_{\mathcal{N}_h}^0(v \circ \mathbf{F})) \circ \mathbf{F}^{-1}, \quad \forall v \in H_{\Gamma_D}^1(\Omega); \end{aligned}$$

The key tool of our analysis, Lemma 3.2.1, admits the following extension.

Lemma 3.2.6. *Let k and l be integer indices with $0 \leq k < l \leq p + 1$ and $l \geq 1$; given $Q \in \mathcal{Q}_h$, \tilde{Q} as in (3.7), $v \in \mathcal{H}_h^l(\tilde{Q}) \cap H_{\gamma_D}^1((0, 1)^d)$, there exists an $s \in \mathcal{S}_h \cap H_{\gamma_D}^1((0, 1)^d)$ such that*

$$|v - s|_{\mathcal{H}_h^k(\tilde{Q})} \leq C h_Q^{l-k} |v|_{\mathcal{H}_h^l(\tilde{Q})}. \quad (3.72)$$

The proof is similar. From Lemma 3.2.6, the rest of the analysis follows in a straight forward manner as in the previous sections, leading to the result below.

Theorem 3.2.3. *Let k and l be integer indices with $0 \leq k < l \leq p + 1$, we have*

$$\begin{aligned} & \sum_{K \in \mathcal{K}_h} |v - \Pi_{\mathcal{V}_h}^0 v|_{\mathcal{H}_h^k(K)}^2 \\ & \leq C_{\mathfrak{s}} \sum_{K \in \mathcal{K}_h} h_K^{2(l-k)} \sum_{i=0}^l \|\nabla \mathbf{F}\|_{L^\infty(\mathbf{F}^{-1}(K))}^{2(i-l)} |v|_{H^i(K)}^2, \forall v \in H^l(\Omega) \cap H_{\Gamma_D}^1(\Omega). \end{aligned} \quad (3.73)$$

3.3 Inverse inequalities for NURBS

In this section, we prove some inverse inequalities which resemble the ones for finite elements spaces.

Theorem 3.3.1. *We have*

$$|v|_{H^2(K)} \leq C_{\mathfrak{s}} h_K^{-1} |v|_{H^1(K)} \quad \forall K \in \mathcal{K}_h, \forall v \in \mathcal{V}_h, \quad (3.74)$$

Proof. Lemma 3.2.5 yields

$$|v|_{H^2(K)} \leq C_{\mathfrak{s}} \|\det \nabla \mathbf{F}\|_{L^\infty(Q)}^{1/2} \|\nabla \mathbf{F}\|_{L^\infty(Q)}^{-2} \|v \circ \mathbf{F}\|_{H^2(Q)} \quad (3.75)$$

where, as before, $\mathbf{F}(Q) = K$. Moreover

$$\|v \circ \mathbf{F}\|_{H^2(Q)} \leq C \left\| \frac{1}{w} \right\|_{W^{2,\infty}(Q)} \|w(v \circ \mathbf{F})\|_{H^2(Q)} \quad (3.76)$$

Since $w(v \circ \mathbf{F})$ is a polynomial of global degree $p_1 \cdot \dots \cdot p_d$, for a usual inverse inequality we have

$$\|v \circ \mathbf{F}\|_{H^2(Q)} \leq C h_Q^{-1} \left\| \frac{1}{w} \right\|_{W^{2,\infty}(Q)} \|w(v \circ \mathbf{F})\|_{H^1(Q)} \quad (3.77)$$

We now have, again using Lemma 3.2.5,

$$\begin{aligned} \|w(v \circ \mathbf{F})\|_{H^1(Q)} &\leq C \|w\|_{W^{1,\infty}(Q)} \|v \circ \mathbf{F}\|_{H^1(Q)} \\ &\leq C_s \|w\|_{W^{1,\infty}(Q)} \|\det \nabla \mathbf{F}^{-1}\|_{L^\infty(K)}^{1/2} \sum_{j=0}^1 \|\nabla \mathbf{F}\|_{L^\infty(Q)}^j |v|_{H^j(K)}. \end{aligned} \quad (3.78)$$

Joining all of the above bounds, we finally get

$$|v|_{H^2(K)} \leq C_s h_Q^{-1} \sum_{j=0}^1 \|\nabla \mathbf{F}\|_{L^\infty(Q)}^{j-2} |v|_{H^j(K)} \quad (3.79)$$

Let now v_K represent the constant function equal to the average of v on K ; note that $v_K \in \mathcal{V}_h$. Therefore, applying (3.79), classical polynomial interpolation results, and recalling that $\|\nabla \mathbf{F}\|_{L^\infty(Q)}^{-1} h_K = h_Q$, it easily follows that

$$\begin{aligned} |v|_{H^2(K)} &= |v - v_K|_{H^2(K)} \\ &\leq C_s h_Q^{-1} \sum_{j=0}^1 \|\nabla \mathbf{F}\|_{L^\infty(Q)}^{j-2} |v - v_K|_{H^j(K)} \\ &\leq C_s h_K^{-1} |v|_{H^1(K)}. \end{aligned}$$

□

More general inverse inequalities can be easily derived following the approach given above. In particular, the following result holds.

Theorem 3.3.2. *Let k and l be integer indices with $0 \leq k \leq l$; we have*

$$\|v\|_{H^l(K)} \leq C_s h_K^{k-l} \sum_{i=0}^k \|\nabla \mathbf{F}\|_{L^\infty(\mathbf{F}^{-1}(K))}^{i-k} |v|_{H^i(K)} \quad \forall K \in \mathcal{K}_h, \forall v \in \mathcal{V}_h. \quad (3.80)$$

3.4 Applications to physical problems

In this section we obtain error estimates for NURBS applied to some linear physical problems. The basis of the analyses is the approximation and inverse estimates of the previous sections. After considering classical Galerkin methods for elliptic problems, we consider application of stabilized and BB-stable methods to saddle-point problems, and finally we study stabilized methods for advective-diffusive problems.

3.4.1 Elasticity

We start by considering the classical two- and three-dimensional linear elastic problem. We assume that the boundary $\partial\Omega$ is decomposed into a Dirichlet part Γ_D and a Neumann part Γ_N ; as usual, Γ_D and Γ_N are the unions of element edges (for $d = 2$) and faces (for $d = 3$), respectively. Moreover, let $\mathbf{f} : \Omega \rightarrow \mathbb{R}^d$ be the given body force and $\mathbf{g} : \Gamma_N \rightarrow \mathbb{R}^d$ the given traction on Γ_N .

Then, the mixed boundary-value problem for $\Omega \subset \mathbb{R}^3$, supported on Γ_D and free on Γ_N , reads

$$\begin{cases} \nabla \cdot \mathbb{C}\varepsilon(\mathbf{u}) + \mathbf{f} = \mathbf{0} & \text{in } \Omega \\ \mathbf{u} = \mathbf{0} & \text{on } \Gamma_D \\ \mathbb{C}\varepsilon(\mathbf{u}) \cdot \mathbf{n} = \mathbf{g} & \text{on } \Gamma_N, \end{cases} \quad (3.81)$$

where $(\nabla \cdot)$ is the divergence, \mathbf{n} is the unit outward normal at each point of the boundary and the fourth-order tensor \mathbb{C} is defined by

$$\mathbb{C}\mathbf{w} = 2\mu \left[\mathbf{w} + \frac{\nu}{1-2\nu} \text{tr}(\mathbf{w})\mathbf{I} \right] \quad (3.82)$$

for all second-order tensors \mathbf{w} , where tr represents the trace operator and $\mu > 0$, $0 \leq \nu < 1/2$ are, respectively, the shear modulus and Poisson's ratio. The case of inhomogeneous Dirichlet data can be reduced to (3.81) by standard means. The stress, $\boldsymbol{\sigma}$, is given by Hooke's law, $\boldsymbol{\sigma} = \mathbb{C}\varepsilon$.

Assuming for simplicity a regular loading $\mathbf{f} \in [L^2(\Omega)]^d$ and $\mathbf{g} \in [L^2(\Gamma_N)]^d$, we introduce also

$$\langle \boldsymbol{\psi}, \mathbf{v} \rangle = (\mathbf{f}, \mathbf{v})_\Omega + (\mathbf{g}, \mathbf{v})_{\Gamma_N} \quad \forall \mathbf{v} \in [H^1(\Omega)]^d, \quad (3.83)$$

where $(\cdot, \cdot)_\Omega$, $(\cdot, \cdot)_{\Gamma_N}$ indicate, as usual, the L^2 scalar products on Ω and Γ_N , respectively. The variational form of problem (3.81) then reads: find $\mathbf{u} \in [H_{\Gamma_D}^1(\Omega)]^d$ such that

$$(\mathbb{C}\varepsilon(\mathbf{u}), \varepsilon(\mathbf{v}))_\Omega = \langle \boldsymbol{\psi}, \mathbf{v} \rangle \quad \forall \mathbf{v} \in [H_{\Gamma_D}^1(\Omega)]^d \quad (3.84)$$

As is well known, this is an elliptic problem. In order to solve it using NURBS, we follow the same Galerkin approach adopted for classical finite elements, that is, we restrict the original problem to the finite-dimensional NURBS space: find $\mathbf{u}_h \in V_h$ such that

$$(\mathbb{C}\varepsilon(\mathbf{u}_h), \varepsilon(\mathbf{v}))_\Omega = \langle \boldsymbol{\psi}, \mathbf{v} \rangle \quad \forall \mathbf{v} \in V_h, \quad (3.85)$$

where

$$V_h = [\mathcal{V}_h]^d \cap [H_{\Gamma_D}^1(\Omega)]^d, \quad (3.86)$$

with \mathcal{V}_h a NURBS space built as described in the previous sections.

The stability and consistency of the discrete problem (3.85) follow immediately. Therefore, a classical convergence analysis easily gives

$$|\mathbf{u} - \mathbf{u}_h|_{H^1} \leq C(\nu) \inf_{\mathbf{v}_h \in V_h} |\mathbf{u} - \mathbf{v}_h|_{H^1(\Omega)}. \quad (3.87)$$

As a consequence, the interpolation properties of the past section give the optimal convergence of the method with respect to the norm and degree used: assuming quasi-uniform mesh refinement, $h_K \simeq h$, and $\min_\alpha p_\alpha = k$, $\mathbf{u} \in [H^{k+1}(\Omega)]^d$ we have

$$|\mathbf{u} - \mathbf{u}_h|_{H^1(\Omega)} \leq C(\nu, \mathbf{u}) C_s h^k; \quad (3.88)$$

moreover, assuming the regularity of the problem, i.e.

$$\|\mathbf{u}\|_{H^2(\Omega)} \leq C \|\mathbf{f}\|_{L^2(\Omega)} \quad (3.89)$$

for all $\mathbf{f} \in L^2(\Omega)$, whenever $\mathbf{g} = 0$, the following L^2 estimate easily follows using an Aubin-Niestche argument

$$\|\mathbf{u} - \mathbf{u}_h\|_{L^2(\Omega)} \leq C(\nu, \mathbf{u}) C_s h^{k+1}. \quad (3.90)$$

3.4.2 Incompressible and almost incompressible isotropic elasticity – stabilized methods

It is well known that the constant C in bound (3.87) tends to $+\infty$ as the Poisson ratio $\nu \rightarrow 1/2$. As it happens for classical finite elements, in such cases the NURBS discretization (3.85) is expected to give non-satisfactory approximation results. In order to treat both this (almost incompressible) case and the limit (incompressible) case, we rewrite problem (3.84) in the standard mixed form.

For notation simplicity we now set the shear modulus $2\mu = 1$, and define the positive constant

$$\varepsilon = \frac{1 - 2\nu}{\nu} \quad (3.91)$$

The incompressible case is represented by $\varepsilon = 0$.

The mixed variational formulation of (3.81) then reads: find $(\mathbf{u}, p) \in H_{\Gamma_D}^1(\Omega) \times L^2(\Omega)$ such that

$$\begin{cases} (\varepsilon(\mathbf{u}), \varepsilon(\mathbf{v}))_\Omega - (\nabla \cdot \mathbf{v}, p)_\Omega = \langle \boldsymbol{\psi}, \mathbf{v} \rangle & \forall \mathbf{v} \in [H_{\Gamma_D}^1(\Omega)]^d \\ (\nabla \cdot \mathbf{u}, q)_\Omega + \varepsilon(p, q)_\Omega = 0 & \forall q \in L^2(\Omega). \end{cases} \quad (3.92)$$

Throughout this section and the next, we assume that $\Gamma_D \neq \partial\Omega$. If $\Gamma_D = \partial\Omega$ and $\varepsilon = 0$,

the space for the pressure needs to be replaced by

$$L_0^2(\Omega) = \left\{ q \in L^2(\Omega) \mid \int_{\Omega} q = 0 \right\} \quad (3.93)$$

in order for the problem to have a unique solution.

Whenever $\varepsilon > 0$, the stability of the problem and the good properties of the NURBS space guarantee optimal error bounds for Galerkin's method applied to (3.92). On the other hand, similarly to classical finite elements, we expect the Galerkin discretization with NURBS to suffer from lack of stability as $\varepsilon \rightarrow 0$. In general, unless certain combination of spaces (V_h, P_h) are found (see next section), the approximation properties of the numerical method are well known to deteriorate as $\varepsilon \rightarrow 0$; even worse, the limit case $\varepsilon = 0$ can suffer from complete lack of stability and spurious modes. One way to avoid this is to adopt a stabilized formulation of (3.92).

We start by introducing the discrete spaces for displacements and pressures

$$V_h = [\mathcal{V}_h]^d \cap [H_{\Gamma_D}^1(\Omega)]^d \quad (3.94)$$

$$P_h = \mathcal{V}_h \cap H^1(\Omega) \quad (3.95)$$

Note that we are requiring continuity also on the pressures and, for the moment, we are assuming equal-order displacement and pressure fields. Following [45], [32, 53], and [21] we introduce the following stabilized formulations:

SUPG:

$$\begin{aligned} B^{SUPG}(\mathbf{u}, p; \mathbf{v}, q) &= (\varepsilon(\mathbf{u}), \varepsilon(\mathbf{v}))_{\Omega} - (\nabla \cdot \mathbf{v}, p)_{\Omega} + (\nabla \cdot \mathbf{u}, q)_{\Omega} + \varepsilon(p, q)_{\Omega} \\ &\quad + \alpha \sum_{K \in \mathcal{K}_h} h_K^2 (-\nabla \cdot \varepsilon(\mathbf{u}) + \nabla p, \nabla q)_K \end{aligned} \quad (3.96)$$

$$F^{SUPG}(\mathbf{v}) = \langle \psi, \mathbf{v} \rangle + \alpha \sum_{K \in \mathcal{K}_h} h_K^2 (\mathbf{f}, \nabla q)_K \quad (3.97)$$

GLS:

$$\begin{aligned} B^{GLS}(\mathbf{u}, p; \mathbf{v}, q) &= (\varepsilon(\mathbf{u}), \varepsilon(\mathbf{v}))_{\Omega} - (\nabla \cdot \mathbf{v}, p)_{\Omega} - (\nabla \cdot \mathbf{u}, q)_{\Omega} - \varepsilon(p, q)_{\Omega} \\ &\quad - \alpha \sum_{K \in \mathcal{K}_h} h_K^2 (-\nabla \cdot \varepsilon(\mathbf{u}) + \nabla p, -\nabla \cdot \varepsilon(\mathbf{v}) + \nabla q)_K \end{aligned} \quad (3.98)$$

$$F^{GLS}(\mathbf{v}) = \langle \psi, \mathbf{v} \rangle - \alpha \sum_{K \in \mathcal{K}_h} h_K^2 (\mathbf{f}, -\nabla \cdot \varepsilon(\mathbf{v}) + \nabla q)_K \quad (3.99)$$

DW (Douglas-Wang):

$$B^{DW}(\mathbf{u}, p; \mathbf{v}, q) = (\boldsymbol{\varepsilon}(\mathbf{u}), \boldsymbol{\varepsilon}(\mathbf{v}))_{\Omega} - (\nabla \cdot \mathbf{v}, p)_{\Omega} - (\nabla \cdot \mathbf{u}, q)_{\Omega} - \varepsilon(p, q)_{\Omega} \\ - \alpha \sum_{K \in \mathcal{K}_h} h_K^2 (-\nabla \cdot \boldsymbol{\varepsilon}(\mathbf{u}) + \nabla p, \nabla \cdot \boldsymbol{\varepsilon}(\mathbf{v}) + \nabla q)_K \quad (3.100)$$

$$F^{DW}(\mathbf{v}) = \langle \boldsymbol{\psi}, \mathbf{v} \rangle - \alpha \sum_{K \in \mathcal{K}_h} h_K^2 (\boldsymbol{\psi}, -\nabla \cdot \boldsymbol{\varepsilon}(\mathbf{v}) + \nabla q)_K \quad (3.101)$$

where α is a positive constant at our disposal. The discrete NURBS problem then reads: find $(\mathbf{u}_h, p_h) \in V_h \times P_h$ such that

$$B(\mathbf{u}_h, p_h; \mathbf{v}, q) = F(\mathbf{v}) \quad \forall (\mathbf{v}, q) \in V_h \times P_h \quad (3.102)$$

where the bilinear form $B(\cdot, \cdot)$ and the functional $F(\cdot)$ depend on which of the three methods above is adopted.

For the three methods here presented, there hold optimal and ε -uniform error bounds in the natural norms of the problem. Given the interpolation and inverse inequality results of the previous sections, the proof of this result follows in step-by-step fashion its finite element counterpart. For the SUPG method, see Theorem 4.1 in [45], while for the GLS and DW methods see respectively Theorem 3.1, case (ii), and Theorem 3.2, case (ii), in [32]. For completeness we include, in the next lemma, a very brief sketch of the proof of the stability result for the GLS case, the other two cases being very similar; we will make use of the notation

$$|||(\mathbf{v}, q)|||^2 := \|\boldsymbol{\varepsilon}(\mathbf{v})\|_{L^2(\Omega)}^2 + (1 + \varepsilon)\|q\|_{L^2(\Omega)}^2. \quad (3.103)$$

We recall the Korn inequality

$$\text{diam}(\Omega)^{-2} \|\mathbf{v}\|_{L^2(\Omega)}^2 + |\mathbf{v}|_{H^1(\Omega)}^2 \leq C_{korn} \|\boldsymbol{\varepsilon}(\mathbf{v})\|_{L^2(\Omega)}^2.$$

Lemma 3.4.1. *Let the constant $0 < \alpha < C_{inv}^{-1}$, where C_{inv} is the (shape dependent) constant of the inverse inequality stated in Lemma 3.3.1. Then, there exists $C_s > 0$, independent of the mesh size, such that*

$$\sup_{(\mathbf{v}, q) \in V_h \times P_h} \frac{B^{GLS}(\mathbf{u}, p; \mathbf{v}, q)}{|||(\mathbf{v}, q)|||} \geq C_s |||(\mathbf{u}, p)|||. \quad (3.104)$$

Proof. We follow the approach of [32]. The inf-sup condition (3.104) is equivalent to the following: given any $(\mathbf{u}, p) \in V_h \times P_h$, there exists a $(\mathbf{v}, q) \in V_h \times P_h$ and two positive constants C_s, C'_s such

that

$$\begin{aligned} B^{GLS}(\mathbf{u}, p; \mathbf{v}, q) &\geq C_s |||(\mathbf{u}, p)|||^2 \\ |||(\mathbf{v}, q)|||^2 &\leq C'_s |||(\mathbf{u}, p)|||^2. \end{aligned} \quad (3.105)$$

Inequalities (3.105) allow one to establish the uniform stability condition by selecting the appropriate test function for the bilinear form. We start by recalling an argument given in Verfürth [109] that gives the existence of two positive constants C_s and C'_s such that

$$\sup_{0 \neq \mathbf{v} \in V_h} \frac{(\nabla \cdot \mathbf{v}, q)_\Omega}{|\mathbf{v}|_{H^1(\Omega)}} \geq C_s \|q\|_{L^2(\Omega)} - C'_s \left(\sum_{K \in \mathcal{K}_h} h_K^2 \|\nabla q\|_{L^2(K)}^2 \right)^{1/2}, \quad \forall q \in P_h. \quad (3.106)$$

The above inequality relies solely on the interpolation estimate, which for the NURBS approximation space was established in Theorem 3.2.3. The following bound is immediate, provided the inverse estimate (Theorem 3.3.2) holds together with the bound on α ($0 < \alpha < C_{inv}^{-1}$):

$$\begin{aligned} B^{GLS}(\mathbf{u}, p; \mathbf{u}, -p) &\geq C_s |\mathbf{u}|_{H^1(\Omega)}^2 + \varepsilon \|p\|_{L^2(\Omega)}^2 \\ &\quad + \alpha \sum_{K \in \mathcal{K}_h} h_K^2 \|\nabla p\|_{L^2(K)}^2 \quad \forall (\mathbf{u}, p) \in V_h \times P_h, \end{aligned} \quad (3.107)$$

with $C_s = C_{korn}(1 - \alpha C_{inv})$.

Consider $\mathbf{w} \in V_h$ which achieves the supremum in (3.106) for $q = p$ (\mathbf{w} can be rescaled such that $|\mathbf{w}|_{H^1(\Omega)} = \|p\|_{L^2(\Omega)}$, which is what is assumed in the sequel). Then the following bound holds:

$$\begin{aligned} B^{GLS}(\mathbf{u}, p; \mathbf{w}, 0) &\geq -C_s |\mathbf{u}|_{H^1(\Omega)}^2 + C'_s \|p\|_{L^2(\Omega)}^2 \\ &\quad - C''_s \sum_{K \in \mathcal{K}_h} h_K^2 \|\nabla p\|_{L^2(K)}^2, \end{aligned} \quad (3.108)$$

where C_s , C'_s , and C''_s are positive and $(\mathbf{u}, p) \in V_h \times P_h$. Denoting $(\mathbf{v}, q) = (\mathbf{u} - \delta \mathbf{w}, -p)$ and combining (3.107) and (3.108) we arrive at

$$B^{GLS}(\mathbf{u}, p; \mathbf{v}, q) \geq C_s (|\mathbf{u}|_{H^1(\Omega)}^2 + (1 + \varepsilon) \|p\|_{L^2(\Omega)}^2), \quad (3.109)$$

with a suitable choice for a positive parameter δ . On the other hand we have

$$|\mathbf{v}|_{H^1(\Omega)}^2 + (1 + \varepsilon) \|q\|_{L^2(\Omega)}^2 \leq C_s (|\mathbf{u}|_{H^1(\Omega)}^2 + (1 + \varepsilon) \|p\|_{L^2(\Omega)}^2). \quad (3.110)$$

which, in conjunction with (3.109), completes the proof of the uniform stability (3.104). \square

The uniform stability result of Lemma 3.4.1 combined with the inverse inequalities of Section 3.3 and the interpolation estimates of Section 3.2.3 leads to error estimates which are optimal. Let $k = \min(p_1, p_2, \dots, p_d)$ where p_1, p_2, \dots, p_d are as the anisotropic polynomial degrees of \mathcal{V}_h . Then, if $\mathbf{u} \in H^{k+1}(\Omega)$ and $p \in H^k(\Omega)$,

$$|\mathbf{u} - \mathbf{u}_h|_{H^1(\Omega)} + \|p - p_h\|_{L^2(\Omega)} \leq C(\mathbf{u}, p) C_{\mathfrak{s}} h^k. \quad (3.111)$$

Moreover, assuming as in Section 5.1 the regularity of the problem and making use of the Aubin-Niestche argument, we get

$$\|\mathbf{u} - \mathbf{u}_h\|_{L^2(\Omega)} \leq C(\mathbf{u}, p) C_{\mathfrak{s}} h^{k+1}. \quad (3.112)$$

Remark 3.4.1. *Similar results can be obtained for any pair of continuous NURBS spaces V_h, P_h . It is not required that the displacement and pressure spaces be based on the same knot vectors and polynomial degree. If $\mathbf{u} \in H^{s+1}(\Omega)$ and $p \in H^s(\Omega)$, then*

$$|\mathbf{u} - \mathbf{u}_h|_{H^1(\Omega)} + \|p - p_h\|_{L^2(\Omega)} + h^{-1} \|\mathbf{u} - \mathbf{u}_h\|_{L^2(\Omega)} \leq C(\mathbf{u}, p) C_{\mathfrak{s}} h^k, \quad (3.113)$$

$$k = \min\{s, k_u, k_p + 1\}$$

where k_u and k_p are the minimal anisotropic polynomial degrees used for displacements and pressures, respectively.

3.4.3 Incompressible and almost incompressible isotropic elasticity – a BB-stable method

In this section we introduce pairs of displacement and pressure NURBS spaces suitable for the approximation of problem (3.92) without the necessity of adding stabilizing terms. Given a positive isotropic degree k , we introduce the spaces of displacements and pressures

$$V_h = [\mathcal{V}_h(k+1, \dots, k+1)]^d \cap [H_{\Gamma_D}^1(\Omega)]^d, \quad (3.114)$$

$$P_h = \mathcal{V}_h(k, \dots, k) \cap H^1(\Omega), \quad (3.115)$$

where $\mathcal{V}_h(k+1, \dots, k+1)$ and $\mathcal{V}_h(k, \dots, k)$ denote the NURBS spaces introduced in (3.19), of degree $k+1$ and k , respectively. We assume that in V_h no continuity of derivatives is enforced across the element boundaries, that is, in each coordinate direction, the internal knots are repeated $k+1$ times. By construction, there is a basis function that is interpolatory at each vertex of the mesh. The control point associated with each vertex is physically located at that vertex. These control points are a subset of the control points comprising the control net. For this subset, the control points are

identical to the nodal points of finite elements.

We are now able to introduce the discrete problem: find $(\mathbf{u}_h, p_h) \in V_h \times P_h$ such that

$$\begin{cases} (\varepsilon(\mathbf{u}_h), \varepsilon(\mathbf{v}))_\Omega - (\nabla \cdot \mathbf{v}, p_h)_\Omega = \langle \boldsymbol{\psi}, \mathbf{v} \rangle & \forall \mathbf{v} \in V_h \\ (\nabla \cdot \mathbf{u}_h, q)_\Omega + \varepsilon(p_h, q)_\Omega = 0 & \forall q \in P_h \end{cases} \quad (3.116)$$

We recall that

$$h = \max_{Q \in \mathcal{Q}_h} h_Q.$$

Moreover, in what follows we denote by h_{max} a quantity, representing a mesh-size, which depends only on the problem domain, mesh family shape-regularity, and polynomial degree k . We have the following a priori error estimate.

Theorem 3.4.1. *There exists $h_{max} > 0$ such that for $h \leq h_{max}$,*

$$|\mathbf{u} - \mathbf{u}_h|_{H^1(\Omega)} + \|p - p_h\|_{L^2(\Omega)} \leq C_s \left(\inf_{\mathbf{v}_h \in V_h} |\mathbf{u} - \mathbf{v}_h|_{H^1(\Omega)} + \inf_{q_h \in P_h} \|p - q_h\|_{L^2(\Omega)} \right). \quad (3.117)$$

where (\mathbf{u}, p) is the solution of problem (3.92) and (\mathbf{u}_h, p_h) is the solution of problem (3.116).

Theorem 3.4.1 and the interpolation estimates of Section 3.2.3 lead to error estimates which are optimal: if $\mathbf{u} \in H^{k+1}(\Omega)$ and $p \in H^k(\Omega)$,

$$|\mathbf{u} - \mathbf{u}_h|_{H^1(\Omega)} + \|p - p_h\|_{L^2(\Omega)} \leq C(\mathbf{u}, p) C_s h^k. \quad (3.118)$$

The proof of Theorem 3.4.1 follows directly from the Babuška-Brezzi inf-sup (stability) condition stated in the next theorem, and the classical theory of mixed finite element methods (see [11]).

Theorem 3.4.2. *There exists $h_{max} > 0$ and $C_s > 0$ such that the inf-sup condition*

$$\sup_{\mathbf{v} \in V_h} \frac{(\nabla \cdot \mathbf{v}, q)}{|\mathbf{v}|_{H^1(\Omega)}} \geq C_s \|q\|_{L^2(\Omega)}, \quad \forall q \in P_h, \quad (3.119)$$

holds provided that

$$h \leq h_{max}. \quad (3.120)$$

The proof of Theorem 3.4.2 requires some preliminary results and Lemma 3.2.3. We denote by $\bar{\mathbf{F}}_h$ the (piecewise multilinear) nodal interpolant of \mathbf{F} , and by $\bar{\Omega}_h$ the image of $\bar{\mathbf{F}}_h$, that is

$$\bar{\mathbf{F}}_h : (0, 1)^d \longrightarrow \bar{\Omega}_h. \quad (3.121)$$

Note that the domain $\bar{\Omega}_h$ depends on the mesh \mathcal{Q}_h . We also introduce finite-dimensional spaces on the patch $(0, 1)^d$,

$$\hat{V}_h = \left\{ \hat{\mathbf{v}} : (0, 1)^d \rightarrow \mathbb{R}^d \mid \hat{\mathbf{v}} = \mathbf{v} \circ \mathbf{F}, \mathbf{v} \in V_h \right\}, \quad (3.122)$$

$$\hat{P}_h = \left\{ \hat{q} : (0, 1)^d \rightarrow \mathbb{R} \mid \hat{q} = q \circ \mathbf{F}, q \in P_h \right\}, \quad (3.123)$$

and on $\bar{\Omega}_h$:

$$\bar{V}_h = \left\{ \bar{\mathbf{v}} : \bar{\Omega}_h \rightarrow \mathbb{R}^d \mid \bar{\mathbf{v}} = \hat{\mathbf{v}} \circ \bar{\mathbf{F}}_h^{-1}, \hat{\mathbf{v}} \in \hat{V}_h \right\}, \quad (3.124)$$

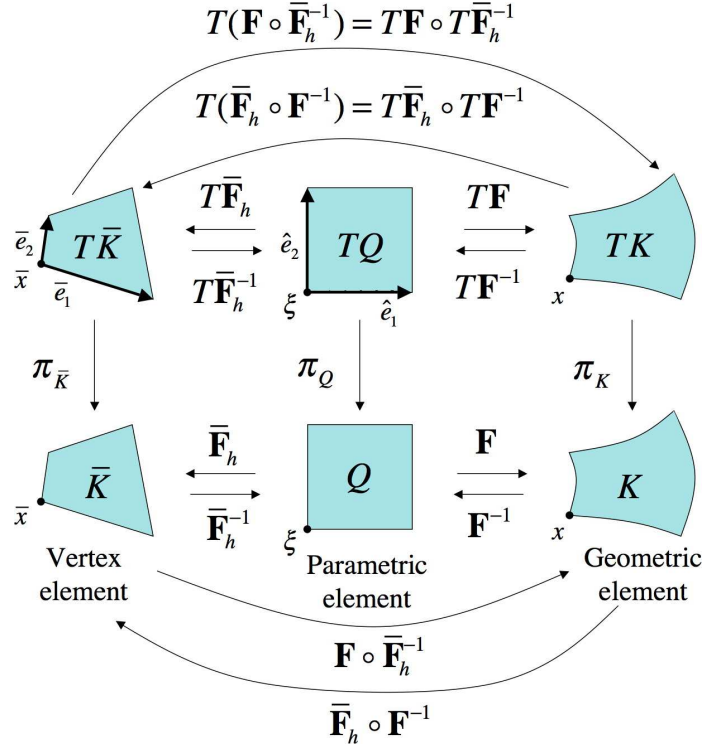
$$\bar{P}_h = \left\{ \bar{q} : \bar{\Omega}_h \rightarrow \mathbb{R} \mid \bar{q} = \hat{q} \circ \bar{\mathbf{F}}_h^{-1}, \hat{q} \in \hat{P}_h \right\}, \quad (3.125)$$

Given $K \in \mathcal{K}_h$, we define the corresponding *vertex element* \bar{K} as

$$\bar{K} = \bar{\mathbf{F}}_h(\mathbf{F}^{-1}(K)) = \{x \in \bar{\Omega}_h \mid x = \bar{\mathbf{F}}_h(\mathbf{F}^{-1}(y)), y \in K\} \quad (3.126)$$

The mesh of all \bar{K} 's is referred to as the *vertex mesh* $\bar{\mathcal{K}}_h$. The union of all $\bar{K} \in \bar{\mathcal{K}}_h$ gives $\bar{\Omega}_h$; also note that the \bar{K} 's are bilinear quadrilaterals and trilinear hexahedra in \mathbb{R}^2 and \mathbb{R}^3 , respectively. $\bar{\mathcal{K}}_h$ may be thought of as a coarsening of the *control net*, or *control mesh*, in NURBS theory (see [18, 52]). The control net facilitates a geometric interpretation of the control points as it is a piecewise multilinear interpolation of *all* the control points. We recall that \mathbf{F}_h interpolates only a subset of the control points. See Box 1 for a schematic illustration of the setup and the relation between mappings.

Box 1. Geometrical setup.



Q is a parametric element, K is a geometric element, and \bar{K} is a vertex element. K and \bar{K} are the images of Q under the mappings \mathbf{F} and $\bar{\mathbf{F}}_h$, respectively. The tangent bundles TQ , TK and $T\bar{K}$ consist of base points and d -dimensional vector spaces emanating from the base points. Corresponding to the mappings \mathbf{F} and $\bar{\mathbf{F}}_h$ are the tangent maps $T\mathbf{F}$ and $T\bar{\mathbf{F}}_h$ (and likewise their inverses). For example, we write $T\mathbf{F} = (\mathbf{F}, \nabla\mathbf{F})$ and thus the tangent maps base points, $\xi \mapsto \mathbf{F}(\xi)$, and vectors by the linear transformation $\hat{e}(\xi) \mapsto \nabla\mathbf{F}(\xi)\hat{e}(\xi)$. Composite tangent maps transform by the chain rule, as illustrated in the figure. Vertex elements are multilinear maps of parametric elements. Thus $\bar{\mathbf{F}}_h$ is bilinear in two dimensions and trilinear in three. Geometric elements are portions of the exact geometry defined by NURBS. Under h -refinement, the vertex elements converge to the geometric elements. π_Q , π_K and $\pi_{\bar{K}}$ are the canonical projections onto the base elements.

Taking ξ at a corner of Q , we have $x = \mathbf{F}(\xi)$ and $\bar{x} = \bar{\mathbf{F}}_h(\xi)$, as shown, and $T\bar{\mathbf{F}}_h(\xi) = (\bar{\mathbf{F}}_h(\xi), \nabla\bar{\mathbf{F}}_h(\xi))$ and $T\bar{\mathbf{F}}_h^{-1}(\bar{x}) = (\bar{\mathbf{F}}_h^{-1}(\bar{x}), \nabla\bar{\mathbf{F}}_h^{-1}(\bar{x}))$. The edge lengths are given by $h_{\hat{e}_\alpha} = \|\hat{e}_\alpha\|$ and $h_{\bar{e}_\alpha} = \|\bar{e}_\alpha\|$, $1 \leq \alpha \leq d$. Furthermore, $\bar{e}_\alpha(\bar{x}) = \nabla\bar{\mathbf{F}}_h(\xi)\hat{e}_\alpha(\xi)$ and $\hat{e}_\alpha(\xi) = \nabla\bar{\mathbf{F}}_h^{-1}(\bar{x})\bar{e}_\alpha(\bar{x})$, from which easily follows $h_{\bar{e}_\alpha} \leq \|\nabla\bar{\mathbf{F}}_h\|_{L^\infty(Q)} h_{\hat{e}_\alpha}$ and $h_{\hat{e}_\alpha} \leq \|\nabla\bar{\mathbf{F}}_h^{-1}\|_{L^\infty(\bar{K})} h_{\bar{e}_\alpha}$, and in turn (3.137).

Let $x = \mathbf{F}(\xi)$ where $\xi \in Q$ is arbitrary. Likewise, $\xi = \mathbf{F}^{-1}(x)$. Since $\mathbf{F} \circ \mathbf{F}^{-1}(x) = x$, $\nabla\mathbf{F}(\xi)\nabla\mathbf{F}^{-1}(x) = \mathbf{I}$, the identity matrix, and so $\nabla\mathbf{F}(\xi)^{-1} = \nabla\mathbf{F}^{-1}(x)$. We write this as $(\nabla\mathbf{F})^{-1} = \nabla\mathbf{F}^{-1} \circ \mathbf{F}$. It is necessary to be careful with compositions and base points in the analysis. Similar results may be derived for the other mappings.

Lemma 3.4.2. *There exists $h'_{max} > 0$ (only dependent on the shape regularity of the mesh \mathcal{Q}_h and on the shape of Ω), such that given $Q \in \mathcal{Q}_h$, $K = \mathbf{F}(Q)$, \bar{K} as in (3.126) and assuming that $h_Q \leq h'_{max}$, then $\bar{\mathbf{F}}_h$ is a one-to-one mapping from Q into \bar{K} and we have*

$$\|\nabla \bar{\mathbf{F}}_h\|_{L^\infty(Q)} \leq C_{\mathfrak{s}} \|\nabla \mathbf{F}\|_{L^\infty(Q)} \quad (3.127)$$

$$\|\nabla \bar{\mathbf{F}}_h^{-1}\|_{L^\infty(\bar{K})} \leq C_{\mathfrak{s}} \|\nabla \mathbf{F}^{-1}\|_{L^\infty(K)} \quad (3.128)$$

$$\|\det \nabla \bar{\mathbf{F}}_h\|_{L^\infty(Q)} \leq C_{\mathfrak{s}} \|\nabla \mathbf{F}\|_{L^\infty(Q)}^d \quad (3.129)$$

$$\|\det \nabla \bar{\mathbf{F}}_h^{-1}\|_{L^\infty(\bar{K})} \leq C_{\mathfrak{s}} \|\nabla \mathbf{F}^{-1}\|_{L^\infty(K)}^d \quad (3.130)$$

Proof. We introduce the map \mathbf{E} and its derivative³

$$\mathbf{E} = \bar{\mathbf{F}}_h - \mathbf{F}, \quad \nabla \mathbf{E} = \nabla \bar{\mathbf{F}}_h - \nabla \mathbf{F} \quad (3.131)$$

Note that a classical result gives the estimate for the interpolation error

$$\|\nabla \mathbf{E}\|_{L^\infty(Q)} \leq C_{ie} h_Q \|\nabla^2 \mathbf{F}\|_{L^\infty(Q)}; \quad (3.132)$$

therefore, we have⁴

$$\|\nabla \mathbf{F}^{-1} \nabla \mathbf{E}\|_{L^\infty(Q)} \leq \|\nabla \mathbf{F}^{-1}\|_{L^\infty(Q)} \|\nabla \mathbf{E}\|_{L^\infty(Q)} \leq C_{ie} \|\nabla \mathbf{F}^{-1}\|_{L^\infty(K)} h_Q \|\nabla^2 \mathbf{F}\|_{L^\infty(Q)}.$$

In particular, if

$$h_Q \|\nabla^2 \mathbf{F}\|_{L^\infty(Q)} \|\nabla \mathbf{F}^{-1}\|_{L^\infty(K)} \leq C_{ie}^{-1}/2, \quad (3.133)$$

then

$$\|\nabla \mathbf{F}^{-1} \nabla \mathbf{E}\|_{L^\infty(Q)} \leq \frac{1}{2}. \quad (3.134)$$

We set

$$h'_{max} := \max_{\substack{Q \in \mathcal{Q}_h \\ K = \mathbf{F}(Q)}} \left\{ \frac{C_{ie}^{-1}}{2 \|\nabla^2 \mathbf{F}\|_{L^\infty(Q)} \|\nabla \mathbf{F}^{-1}\|_{L^\infty(K)}} \right\};$$

³If linear NURBS are utilized, \mathbf{F} and $\bar{\mathbf{F}}_h$ are the same and thus $\mathbf{E} = \mathbf{0}$.

⁴We need to elaborate on the geometric meaning of $\nabla \mathbf{F}^{-1} \nabla \mathbf{E}$. $\nabla \mathbf{F}^{-1}(x)$ is a linear map from the tangent space $T_x K$ to $T_\xi Q$, where $x = \mathbf{F}(\xi)$. Likewise, $\nabla \mathbf{F}(\xi): T_\xi Q \rightarrow T_x K$ is its inverse. However, $\nabla \bar{\mathbf{F}}_h(\xi): T_\xi Q \rightarrow T_{\bar{x}} \bar{K}$, where $\bar{x} = \bar{\mathbf{F}}_h(\xi)$. Thus, the images of $\nabla \mathbf{F}(\xi)$ and $\nabla \bar{\mathbf{F}}_h(\xi)$ reside in different tangent spaces, namely, $T_x K$ and $T_{\bar{x}} \bar{K}$, respectively. To make sense of $\nabla \mathbf{F}^{-1} \nabla \mathbf{E}$, we need to identify the linear space $T_{\bar{x}} \bar{K}$ with $T_x K$ so that $\nabla \mathbf{E}(\xi) = \nabla \bar{\mathbf{F}}_h(\xi) - \nabla \mathbf{F}(\xi)$ may be viewed as a linear map from $T_\xi Q$ to $T_x K$. In other words, if $\hat{e}(\xi) \mapsto \nabla \bar{\mathbf{F}}_h(\xi) \hat{e}(\xi) \in T_{\bar{x}} \bar{K}$, then $\nabla \bar{\mathbf{F}}_h(\xi) \hat{e}(\xi)$ is parallel transported to $T_x K$.

condition (3.133) can be stated as $h \leq h'_{max}$, which we assume in what follows. Observe that

$$\nabla \bar{\mathbf{F}}_h(\xi) = \nabla \mathbf{F}(\xi) + \nabla \mathbf{E}(\xi) = \nabla \mathbf{F}(\xi) (\bar{I} + (\nabla \mathbf{F})^{-1}(\xi) \nabla \mathbf{E}(\xi)) \quad \forall \xi \in Q, \quad (3.135)$$

whence

$$\|\nabla \bar{\mathbf{F}}_h\|_{L^\infty(Q)} \leq \frac{3}{2} \|\nabla \mathbf{F}\|_{L^\infty(Q)}, \quad (3.136)$$

that is, $C_s = \frac{3}{2}$ in (3.127). Furthermore, fixing $\xi \in Q$, the right hand side of (3.135) is a non-singular matrix, and, in particular,

$$\|(\bar{I} + (\nabla \mathbf{F})^{-1}(\xi) \nabla \mathbf{E}(\xi))^{-1}\| \leq (1 - \|(\nabla \mathbf{F})^{-1}(\xi) \nabla \mathbf{E}(\xi)\|)^{-1} \leq 2.$$

Therefore, $\nabla \bar{\mathbf{F}}_h$ is nonsingular and

$$\begin{aligned} \|(\nabla \bar{\mathbf{F}}_h)^{-1}\|_{L^\infty(Q)} &= \|(\bar{I} + (\nabla \mathbf{F})^{-1} \nabla \mathbf{E})^{-1} (\nabla \mathbf{F})^{-1}\|_{L^\infty(Q)} \\ &\leq \|(\bar{I} + (\nabla \mathbf{F})^{-1} \nabla \mathbf{E})^{-1}\|_{L^\infty(Q)} \|(\nabla \mathbf{F})^{-1}\|_{L^\infty(Q)} \\ &\leq 2 \|\nabla \mathbf{F}^{-1}\|_{L^\infty(K)}. \end{aligned}$$

Since $\|\nabla \bar{\mathbf{F}}_h^{-1}\|_{L^\infty(\bar{K})} = \|(\nabla \bar{\mathbf{F}}_h)^{-1}\|_{L^\infty(Q)}$, we get (3.128). The estimates (3.129) and (3.130) follow easily from (3.127) and (3.128), respectively. \square

Given an element $Q \in \mathcal{Q}_h$, let \hat{e}_1 and \hat{e}_2 be tangent vectors associated with any two adjacent edges having lengths $h_{\hat{e}_1} = \|\hat{e}_1\|$ and $h_{\hat{e}_2} = \|\hat{e}_2\|$, respectively. Let \bar{e}_1 and \bar{e}_2 denote the corresponding edges of \bar{K} , of lengths $h_{\bar{e}_1}$ and $h_{\bar{e}_2}$, respectively. Then, we have (see Box 1)

$$\frac{h_{\bar{e}_1}}{h_{\bar{e}_2}} \leq \|\nabla \bar{\mathbf{F}}_h^{-1}\|_{L^\infty(\bar{K})} \|\nabla \bar{\mathbf{F}}_h\|_{L^\infty(Q)} \frac{h_{\hat{e}_1}}{h_{\hat{e}_2}} \leq C_s. \quad (3.137)$$

where we also used the shape regularity of \mathcal{Q}_h in the last bound.

We have indeed more, as stated in the next result.

Lemma 3.4.3. *Under the assumption of Lemma 3.4.2, the family of vertex meshes $\{\bar{\mathcal{K}}_h\}_h$ is shape-regular.*

Proof. Since a uniform bound on the edge lengths ratio follows immediately from (3.137), we are only left to prove a minimum angle condition for $\{\bar{\mathcal{K}}_h\}_h$. We will start addressing the case $d = 2$. In addition to the notation introduced above, denote by $\bar{\theta}$ the angle shared by the two adjacent edges \bar{e}_1 and \bar{e}_2 of \bar{K} . We will prove that

$$|\sin \bar{\theta}| \geq C_s > 0. \quad (3.138)$$

Denoting by \hat{e}_1 and \hat{e}_2 the two corresponding edges of Q , and $\xi \in Q$ the common vertex, then basic geometrical arguments give

$$|\sin \bar{\theta}| = \frac{\|\bar{e}_1 \times \bar{e}_2\|}{\|\bar{e}_1\| \|\bar{e}_2\|} = \frac{\|\nabla \bar{\mathbf{F}}_h(\xi) \hat{e}_1 \times \nabla \bar{\mathbf{F}}_h(\xi) \hat{e}_2\|}{\|\nabla \bar{\mathbf{F}}_h(\xi) \hat{e}_1\| \|\nabla \bar{\mathbf{F}}_h(\xi) \hat{e}_2\|} \quad (3.139)$$

where “ \times ” stands for the cross product. Since \hat{e}_1 and \hat{e}_2 are orthogonal, then $\|A\hat{e}_1 \times A\hat{e}_2\| = |\det A| \|\hat{e}_1\| \|\hat{e}_2\|$ for all matrices $A \in \mathbb{R}^{2 \times 2}$. Therefore, from (3.139), we have

$$|\sin \bar{\theta}| \geq \frac{|\det \nabla \bar{\mathbf{F}}_h(\xi)|}{\|\nabla \bar{\mathbf{F}}_h(\xi)\|^2}. \quad (3.140)$$

The uniform lower bound (3.138) now follows from (3.140) and Lemma 3.4.2.

The case $d = 3$ follows similarly, the main difference being that now the inequality

$$\begin{aligned} |\det A| \|\hat{e}_1\| \|\hat{e}_2\| \|\hat{e}_3\| &= |(A\hat{e}_1 \times A\hat{e}_2) \cdot A\hat{e}_3| \\ &\leq \|A\hat{e}_1 \times A\hat{e}_2\| \|A\| \|\hat{e}_3\|, \end{aligned} \quad (3.141)$$

which holds for any orthogonal vectors \hat{e}_1, \hat{e}_2 and \hat{e}_3 , is used to bound $\|\nabla \bar{\mathbf{F}}_h(\xi) \hat{e}_1 \times \nabla \bar{\mathbf{F}}_h(\xi) \hat{e}_2\|$ from below. \square

In order to prove Theorem 3.4.1 we use a *macroelement* technique (see [95],[94]). A macroelement \bar{M} is a connected set of elements $\bar{K} \in \bar{\mathcal{K}}_h$ (precisely, \bar{M} is the interior of the union of the closure of adjacent elements \bar{K}), therefore a subset of $\bar{\Omega}_h$. In two dimensions we consider macroelements made of two quadrilaterals that share an edge, while in three dimensions we consider macroelements made of four adjacent hexahedra such that each shares two faces with other two hexahedra and one edge with the last hexahedron. We denote by $h_{\bar{M}}$ the diameter of \bar{M} . We assume that the mesh \mathcal{Q}_h is made at least of 2×1 or of $2 \times 2 \times 1$ elements when $d = 2$ or $d = 3$ respectively, so that a macroelement partitioning $\bar{\mathcal{M}}_h$ of $\bar{\Omega}_h$ can be found (with possibly overlapping macroelements) such that each $\bar{K} \in \bar{\mathcal{K}}_h$ is contained in at least one and no more than two (if $d = 2$) or four (if $d = 3$) macroelements \bar{M} of $\bar{\mathcal{M}}_h$.

We associate to a macroelement $\bar{M} \in \bar{\mathcal{M}}_h$ the set

$$\hat{M} = \bar{\mathbf{F}}_h^{-1}(\bar{M}) = \left\{ \xi \in (0, 1)^d \text{ such that } \bar{\mathbf{F}}_h(\xi) \in \bar{M} \right\}.$$

\hat{M} is a macroelement on $(0, 1)^d$.

For a macroelement \bar{M} we define the spaces

$$\bar{V}_{0,\bar{M}} = \bar{V}_{h|\bar{M}} \cap H_0^1(\bar{M}), \quad (3.142)$$

$$\bar{P}_{\bar{M}} = \bar{P}_{h|\bar{M}}; \quad (3.143)$$

moreover, for brevity we denote by $(\cdot, \cdot)_{\bar{M}}$ the $L^2(\bar{M})$ scalar product.

The next step is to obtain a local inf-sup condition, for the spaces $\bar{V}_{0,\bar{M}}$ and $\bar{P}_{\bar{M}}$.

Lemma 3.4.4. *Under the assumption of Lemma 3.4.2, there exists a constant $C_s > 0$ such that, given $\bar{M} \in \bar{\mathcal{M}}_h$ and given any $\bar{q} \in \bar{P}_{\bar{M}}$, there exists a $\bar{v} \in \bar{V}_{0,\bar{M}}$ for which*

$$\begin{aligned} (\nabla \cdot \bar{v}, \bar{q})_{\bar{M}} &\geq C_s h_{\bar{M}} |\bar{q}|_{H^1(\bar{M})} - C'_s h_{\bar{M}} \|\nabla \bar{\mathbf{F}}_h^{-1}\|_{L^\infty(\bar{M})} \|\bar{q}\|_{L^2(\bar{M})}, \\ |\bar{v}|_{H^1(\bar{M})} &\leq 1. \end{aligned} \quad (3.144)$$

Proof. In [94], a similar inf-sup condition for quadrilateral Taylor-Hood type elements, which in our context correspond to the case when w is constant and $d = 2$, is proven. The purely polynomial case for $d = 3$ is an easy extension of that result. We take it as a starting point for our analysis: specifically, from [94] one can easily obtain:

$$w = \text{constant} \quad \Rightarrow \quad \sup_{\bar{v} \in \bar{V}_{0,\bar{M}}} \frac{(\nabla \cdot \bar{v}, \bar{q})_{\bar{M}}}{|\bar{v}|_{H^1(\bar{M})}} \geq C_s h_{\bar{M}} |\bar{q}|_{H^1(\bar{M})}, \quad \forall \bar{q} \in \bar{P}_{\bar{M}}. \quad (3.145)$$

Note that a key ingredient of the proof in [94] (and therefore of (3.145)) is the regularity of the mesh, here given by Lemma 3.4.3.

The inf-sup condition (3.145) implies that, when w is not a constant and introducing $\bar{w} = w \circ \bar{\mathbf{F}}_h^{-1}$, we have

$$\sup_{\bar{v} \in \bar{V}_{0,\bar{M}}} \frac{(\nabla \cdot (\bar{w}\bar{v}), \bar{w}\bar{q})_{\bar{M}}}{|\bar{w}\bar{v}|_{H^1(\bar{M})}} \geq C_s h_{\bar{M}} |\bar{w}\bar{q}|_{H^1(\bar{M})}, \quad \forall \bar{q} \in \bar{P}_{\bar{M}}. \quad (3.146)$$

Given $\bar{q} \in \bar{P}_{\bar{M}}$, we denote by $\bar{v}^* \in \bar{V}_{0,\bar{M}}$ a function which realizes maximum of the quantity $(\nabla \cdot (\bar{w}\bar{v}), \bar{w}\bar{q})_{\bar{M}} / |\bar{w}\bar{v}|_{H^1(\bar{M})}$. We want to show that

$$\frac{(\nabla \cdot \bar{v}^*, \bar{q})_{\bar{M}}}{|\bar{v}^*|_{H^1(\bar{M})}} \geq C_s h_{\bar{M}} |\bar{q}|_{H^1(\bar{M})} - C'_s h_{\bar{M}} \|\nabla \bar{\mathbf{F}}_h^{-1}\|_{L^\infty(\bar{M})} \|\bar{q}\|_{L^2(\bar{M})}, \quad (3.147)$$

which gives (3.144).

Denoting by \bar{w}_{mv} the mean value of \bar{w} on \bar{M} , we have

$$\begin{aligned}
(\nabla \cdot (\bar{w} \bar{\mathbf{v}}^*), \bar{w} \bar{q})_{\bar{M}} &= (\bar{w} \nabla \bar{w} \cdot \bar{\mathbf{v}}^*, \bar{q})_{\bar{M}} + (\bar{w}^2 \nabla \cdot \bar{\mathbf{v}}^*, \bar{q})_{\bar{M}} \\
&= (\bar{w} \nabla \bar{w} \cdot \bar{\mathbf{v}}^*, \bar{q})_{\bar{M}} + ((\bar{w}^2 - \bar{w}_{mv}^2) \nabla \cdot \bar{\mathbf{v}}^*, \bar{q})_{\bar{M}} + (\bar{w}_{mv}^2 \nabla \cdot \bar{\mathbf{v}}^*, \bar{q})_{\bar{M}} \\
&= I + II + III.
\end{aligned} \tag{3.148}$$

Recalling that $\bar{\mathbf{F}}_h(\hat{M}) = \bar{M}$ and making use of the chain rule, we have

$$\begin{aligned}
\|\bar{w}\|_{L^\infty(\bar{M})} &= \|w\|_{L^\infty(\hat{M})}, \\
\|\nabla \bar{w}\|_{L^\infty(\bar{M})} &\leq \|\nabla w\|_{L^\infty(\hat{M})} \|\nabla \bar{\mathbf{F}}_h^{-1}\|_{L^\infty(\bar{M})},
\end{aligned} \tag{3.149}$$

while, from the Friedrich-Poincaré inequality,

$$\begin{aligned}
\|\bar{w} - \bar{w}_{mv}\|_{L^\infty(\bar{M})} &\leq Ch_{\bar{M}} \|\nabla \bar{w}\|_{L^\infty(\bar{M})} \\
&\leq Ch_{\bar{M}} \|\nabla w\|_{L^\infty(\hat{M})} \|\nabla \bar{\mathbf{F}}_h^{-1}\|_{L^\infty(\bar{M})}
\end{aligned} \tag{3.150}$$

and

$$\|\bar{\mathbf{v}}^*\|_{L^2(\bar{M})} \leq Ch_{\bar{M}} \|\nabla \bar{\mathbf{v}}^*\|_{L^2(\bar{M})}. \tag{3.151}$$

Notice also that, from the definition of C_s and recalling that \bar{w}_{mv} is positive, we can write

$$\begin{aligned}
\|w\|_{L^\infty(\hat{M})} &\leq C_s \bar{w}_{mv} \\
\|\nabla w\|_{L^\infty(\hat{M})} &\leq C_s \bar{w}_{mv}.
\end{aligned} \tag{3.152}$$

Therefore, using the Cauchy-Schwarz inequality, (3.149), (3.151), and (3.152), we have

$$\begin{aligned}
I &= (\bar{w} \nabla \bar{w} \cdot \bar{\mathbf{v}}^*, \bar{q})_{\bar{M}} \\
&\leq \|\bar{w}\|_{L^\infty(\bar{M})} \|\nabla \bar{w}\|_{L^\infty(\bar{M})} \|\bar{\mathbf{v}}^*\|_{L^2(\bar{M})} \|\bar{q}\|_{L^2(\bar{M})} \\
&\leq Ch_{\bar{M}} \|w\|_{L^\infty(\hat{M})} \|\nabla w\|_{L^\infty(\hat{M})} \|\nabla \bar{\mathbf{F}}_h^{-1}\|_{L^\infty(\bar{M})} |\bar{\mathbf{v}}^*|_{H^1(\bar{M})} \|\bar{q}\|_{L^2(\bar{M})} \\
&\leq h_{\bar{M}} C_s \bar{w}_{mv}^2 \|\nabla \bar{\mathbf{F}}_h^{-1}\|_{L^\infty(\bar{M})} |\bar{\mathbf{v}}^*|_{H^1(\bar{M})} \|\bar{q}\|_{L^2(\bar{M})}.
\end{aligned} \tag{3.153}$$

Furthermore, using the Cauchy-Schwarz inequality, (3.149), (3.150), and (3.152), we have

$$\begin{aligned}
II &= ((\bar{w}^2 - \bar{w}_{mv}^2) \nabla \cdot \bar{\mathbf{v}}^*, \bar{q})_{\bar{M}} \\
&\leq \|\bar{w} - \bar{w}_{mv}\|_{L^\infty(\bar{M})} \|\bar{w} + \bar{w}_{mv}\|_{L^\infty(\bar{M})} |\bar{\mathbf{v}}^*|_{H^1(\bar{M})} \|\bar{q}\|_{L^2(\bar{M})} \\
&\leq Ch_{\bar{M}} \|\nabla w\|_{L^\infty(\hat{M})} \|w\|_{L^\infty(\hat{M})} \|\nabla \bar{\mathbf{F}}_h^{-1}\|_{L^\infty(\bar{M})} |\bar{\mathbf{v}}^*|_{H^1(\bar{M})} \|\bar{q}\|_{L^2(\bar{M})} \\
&\leq h_{\bar{M}} C_s \bar{w}_{mv}^2 \|\nabla \bar{\mathbf{F}}_h^{-1}\|_{L^\infty(\bar{M})} |\bar{\mathbf{v}}^*|_{H^1(\bar{M})} \|\bar{q}\|_{L^2(\bar{M})},
\end{aligned} \tag{3.154}$$

while, of course,

$$III = \bar{w}_{mv}^2 (\nabla \cdot \bar{\mathbf{v}}^*, \bar{q})_{\bar{M}}. \quad (3.155)$$

Using again the chain rule and (3.149), we have

$$\begin{aligned} |\bar{q}|_{H^1(\bar{M})} &= \left| \frac{\bar{w}\bar{q}}{\bar{w}} \right|_{H^1(\bar{M})} \\ &\leq \left\| \frac{\nabla(\bar{w}\bar{q})}{\bar{w}} \right\|_{L^2(\bar{M})} + \left\| \bar{w}\bar{q} \nabla \frac{1}{\bar{w}} \right\|_{L^2(\bar{M})} \\ &\leq \left\| \frac{1}{\bar{w}} \right\|_{L^\infty(\bar{M})} \left\| \nabla(\bar{w}\bar{q}) \right\|_{L^2(\bar{M})} + \left\| \nabla \frac{1}{\bar{w}} \right\|_{L^\infty(\bar{M})} \|\bar{w}\|_{L^\infty(\bar{M})} \|\bar{q}\|_{L^2(\bar{M})} \\ &\leq \left\| \frac{1}{\bar{w}} \right\|_{L^\infty(\hat{M})} |\bar{w}\bar{q}|_{H^1(\bar{M})} + \left\| \nabla \bar{\mathbf{F}}_h^{-1} \right\|_{L^\infty(\bar{M})} \left\| \nabla \frac{1}{\bar{w}} \right\|_{L^\infty(\hat{M})} \|w\|_{L^\infty(\hat{M})} \|\bar{q}\|_{L^2(\bar{M})}, \end{aligned} \quad (3.156)$$

which implies, using $\left\| \frac{1}{\bar{w}} \right\|_{L^\infty(\bar{M})}^{-1} \geq C_s \bar{w}_{mv}$, as well as $\left\| \nabla \frac{1}{\bar{w}} \right\|_{L^\infty(\hat{M})} \|w\|_{L^\infty(\hat{M})} \leq C_s$,

$$\begin{aligned} |\bar{w}\bar{q}|_{H^1(\bar{M})} &\geq \left\| \frac{1}{\bar{w}} \right\|_{L^\infty(\bar{M})}^{-1} \left(|\bar{q}|_{H^1(\bar{M})} - \left\| \nabla \bar{\mathbf{F}}_h^{-1} \right\|_{L^\infty(\bar{M})} \left\| \nabla \frac{1}{\bar{w}} \right\|_{L^\infty(\hat{M})} \|w\|_{L^\infty(\hat{M})} \|\bar{q}\|_{L^2(\bar{M})} \right) \\ &\geq C_s \bar{w}_{mv} \left(|\bar{q}|_{H^1(\bar{M})} - \left\| \nabla \bar{\mathbf{F}}_h^{-1} \right\|_{L^\infty(\bar{M})} \|\bar{q}\|_{L^2(\bar{M})} \right). \end{aligned} \quad (3.157)$$

In a similar way, using also the Poincaré inequality $\|\bar{w}\bar{\mathbf{v}}^*\|_{L^2(\bar{M})} \leq Ch_{\bar{M}} |\bar{w}\bar{\mathbf{v}}^*|_{H^1(\bar{M})}$, we have

$$\begin{aligned} |\bar{\mathbf{v}}^*|_{H^1(\bar{M})} &\leq \left\| \frac{1}{\bar{w}} \right\|_{L^\infty(\hat{M})} |\bar{w}\bar{\mathbf{v}}^*|_{H^1(\bar{M})} + \left\| \nabla \bar{\mathbf{F}}_h^{-1} \right\|_{L^\infty(\bar{M})} \left\| \nabla \frac{1}{\bar{w}} \right\|_{L^\infty(\hat{M})} \|\bar{w}\bar{\mathbf{v}}^*\|_{L^2(\bar{M})} \\ &\leq \left(\left\| \frac{1}{\bar{w}} \right\|_{L^\infty(\hat{M})} + Ch_{\bar{M}} \left\| \nabla \bar{\mathbf{F}}_h^{-1} \right\|_{L^\infty(\bar{M})} \left\| \nabla \frac{1}{\bar{w}} \right\|_{L^\infty(\hat{M})} \right) |\bar{w}\bar{\mathbf{v}}^*|_{H^1(\bar{M})}. \end{aligned} \quad (3.158)$$

Moreover, following the steps as in (3.156)–(3.157) and using $h_{\bar{M}} \leq h_{\hat{M}} \left\| \nabla \bar{\mathbf{F}}_h \right\|_{L^\infty(\hat{M})} \leq \left\| \nabla \bar{\mathbf{F}}_h \right\|_{L^\infty(\hat{M})}$ together with $\left\| \nabla \bar{\mathbf{F}}_h^{-1} \right\|_{L^\infty(\bar{M})} \left\| \nabla \bar{\mathbf{F}}_h \right\|_{L^\infty(\hat{M})} \leq C_s \left\| \nabla \mathbf{F}^{-1} \right\|_{L^\infty(\mathbf{F}(\hat{M}))} \left\| \nabla \mathbf{F} \right\|_{L^\infty(\hat{M})} \leq C_s$, we have

$$|\bar{w}\bar{\mathbf{v}}^*|_{H^1(\bar{M})} \geq C_s \bar{w}_{mv} |\bar{\mathbf{v}}^*|_{H^1(\bar{M})} \quad (3.159)$$

Recalling that $\bar{\mathbf{v}}^*$ attains the supremum in (3.146), we can now collect the estimates (3.157),

(3.159) and (3.153)–(3.155), getting

$$\begin{aligned}
& h_{\bar{M}} \bar{w}_{mv} \left(|\bar{q}|_{H^1(\bar{M})} - \|\nabla \bar{\mathbf{F}}_h^{-1}\|_{L^\infty(\bar{M})} \|\bar{q}\|_{L^2(\bar{M})} \right) \\
& \leq C_s h_{\bar{M}} |\bar{w} \bar{q}|_{H^1(\bar{M})} \\
& \leq C_s \frac{(\nabla \cdot (\bar{w} \bar{\mathbf{v}}^*), \bar{w} \bar{q})}{|\bar{w} \bar{\mathbf{v}}^*|_{H^1(\bar{M})}} \\
& \leq C_s \frac{I + II + III}{\bar{w}_{mv} |\bar{\mathbf{v}}^*|_{H^1(\bar{M})}} \\
& \leq C_s \left(h_{\bar{M}} \bar{w}_{mv} \|\nabla \bar{\mathbf{F}}_h^{-1}\|_{L^\infty(\bar{M})} \|\bar{q}\|_{L^2(\bar{M})} + \frac{\bar{w}_{mv} (\nabla \cdot \bar{\mathbf{v}}^*, \bar{q})}{|\bar{\mathbf{v}}^*|_{H^1(\bar{M})}} \right),
\end{aligned} \tag{3.160}$$

which is, after dividing by \bar{w}_{mv} , (3.147). This concludes the proof. \square

We can get now a global inf-sup condition for the spaces $\bar{V}_h \cap H_0^1(\bar{\Omega}_h)$ and \bar{P}_h . We set

$$\bar{h} = \max_{\bar{K} \in \bar{\mathcal{K}}_h} h_{\bar{K}}. \tag{3.161}$$

Lemma 3.4.5. *Under the assumption of Lemma 3.4.2, there exists a constant $C_s > 0$ such that, given any $\bar{q} \in \bar{P}_h$, there exists a $\bar{\mathbf{v}} \in \bar{V}_h \cap H_0^1(\bar{\Omega}_h)$ for which*

$$\begin{aligned}
(\nabla \cdot \bar{\mathbf{v}}, \bar{q}) & \geq C_s \left(\sum_{\bar{K} \in \bar{\mathcal{K}}_h} h_{\bar{K}}^2 |\bar{q}|_{H^1(\bar{K})}^2 \right)^{1/2} - C'_s \bar{h} \|\nabla \bar{\mathbf{F}}_h^{-1}\|_{L^\infty(\bar{\Omega}_h)} \|\bar{q}\|_{L^2(\bar{\Omega}_h)}, \\
|\bar{\mathbf{v}}|_{H^1(\bar{\Omega}_h)} & \leq 1.
\end{aligned} \tag{3.162}$$

Proof. For each macroelement $\bar{M} \in \mathcal{M}_h$, let $\bar{\mathbf{w}}_{\bar{M}} \in \bar{V}_h \cap H_0^1(\bar{\Omega}_h)$ such that $\bar{\mathbf{w}}_{\bar{M}} = 0$ in $\bar{\Omega}_h/\bar{M}$ and, according to Lemma 3.4.4,

$$\begin{aligned}
(\nabla \cdot \bar{\mathbf{w}}_{\bar{M}}, \bar{q})_{\bar{M}} & \geq C_s h_{\bar{M}} |\bar{q}|_{H^1(\bar{M})} - C'_s h_{\bar{M}} \|\nabla \bar{\mathbf{F}}_h^{-1}\|_{L^\infty(\bar{M})} \|\bar{q}\|_{L^2(\bar{M})}, \\
|\bar{\mathbf{w}}_{\bar{M}}|_{H^1(\bar{M})} & \leq 1.
\end{aligned}$$

Setting

$$\bar{\mathbf{w}} = \sum_{\bar{M} \in \mathcal{M}_h} h_{\bar{M}} |\bar{q}|_{H^1(\bar{M})} \bar{\mathbf{w}}_{\bar{M}},$$

it is easy to see that (3.162) holds true for the rescaled vector field $\bar{\mathbf{v}} = \bar{\mathbf{w}}/|\bar{\mathbf{w}}|_{H^1(\bar{\Omega}_h)}$. \square

We are now ready to show the following proposition, which is the counterpart of Lemma 3.4.5 for the NURBS spaces V_h, P_h .

Proposition 3.4.1. *Under the assumption of Lemma 3.4.2, there exists a constant $C_s > 0$ such that, given any $q \in P_h$, there exists a $\mathbf{v} \in V_h \cap H_0^1(\Omega)$ for which*

$$(\nabla \cdot \mathbf{v}, q) \geq C_s \left(\sum_{K \in \mathcal{K}_h} h_K^2 |q|_{H^1(K)}^2 \right)^{1/2} - C'_s h \|q\|_{L^2(\Omega)}, \quad (3.163)$$

$$|\mathbf{v}|_{H^1(\Omega)} \leq 1.$$

Proof. Given any function q in P_h , we define $\hat{q} \in \hat{P}_h$ and $\bar{q} \in \bar{P}_h$

$$\hat{q} = q \circ \mathbf{F} \quad \bar{q} = \hat{q} \circ \bar{\mathbf{F}}_h^{-1} \quad (3.164)$$

Due to Lemma 3.4.5, we have the existence of a function $\bar{\mathbf{v}} \in \bar{V}_h$ such that (3.162) holds true. We introduce the functions $\hat{\mathbf{v}} \in \hat{V}_h$ and $\mathbf{v} \in V_h$ as

$$\hat{\mathbf{v}} = \bar{\mathbf{v}} \circ \bar{\mathbf{F}}_h \quad \mathbf{v} = \hat{\mathbf{v}} \circ \mathbf{F}^{-1} \quad (3.165)$$

Recalling Lemma 3.4.2 and that $\|\nabla \mathbf{F}^{-1}\|_{L^\infty(\Omega)} \|\nabla \mathbf{F}\|_{L^\infty((0,1)^d)} \leq C_s$, change of variables leads to the bounds

$$\|\hat{q}\|_{L^2((0,1)^d)} \leq C_s \|\nabla \mathbf{F}^{-1}\|_{L^\infty(\Omega)}^{d/2} \|q\|_{L^2(\Omega)}, \quad (3.166)$$

$$|\hat{\mathbf{v}}|_{H^1((0,1)^d)} \leq C_s \|\nabla \mathbf{F}^{-1}\|_{L^\infty(\Omega)}^{d/2-1} |\bar{\mathbf{v}}|_{H^1(\bar{\Omega}_h)}, \quad (3.167)$$

$$\|\bar{q}\|_{L^2(\bar{\Omega}_h)} \leq C_s \|q\|_{L^2(\Omega)}, \quad (3.168)$$

$$h_K |q|_{H^1(K)} \leq C_s h_{\bar{K}} |\bar{q}|_{H^1(\bar{K})} \quad \forall \bar{K} \in \bar{\mathcal{K}}_h, \quad (3.169)$$

$$|\mathbf{v}|_{H^1(\Omega)} \leq C_s |\bar{\mathbf{v}}|_{H^1(\bar{\Omega}_h)}. \quad (3.170)$$

A direct change of variables and simple algebra now give

$$\begin{aligned} (\nabla \cdot \mathbf{v}, q) &= \int_{\Omega} (\nabla \cdot \mathbf{v}) q \\ &= \int_{(0,1)^d} \text{tr}(|\det \nabla \mathbf{F}| \nabla \mathbf{F}^{-T} \nabla \hat{\mathbf{v}}^T) \hat{q} \\ &= \int_{(0,1)^d} \text{tr}([|\det \nabla \mathbf{F}| \nabla \mathbf{F}^{-T} - |\det \nabla \bar{\mathbf{F}}_h| \nabla \bar{\mathbf{F}}_h^{-T}] \nabla \hat{\mathbf{v}}^T) \hat{q} \\ &\quad + \int_{(0,1)^d} \text{tr}(|\det \nabla \bar{\mathbf{F}}_h| \nabla \bar{\mathbf{F}}_h^{-T} \nabla \hat{\mathbf{v}}^T) \hat{q} \\ &= I + II. \end{aligned} \quad (3.171)$$

We now note that

$$(\det A)A^{-T} = \text{Cof}(A) \quad \forall A \in \mathbb{R}^{d \times d}, \det A \neq 0 \quad (3.172)$$

where $\text{Cof}(\mathbb{A})$ is the cofactor matrix of \mathbb{A} . Therefore, from the definition of $\bar{\mathbf{F}}_h$ and classical interpolation results, it follows

$$\| |\det \nabla \mathbf{F}| \nabla \mathbf{F}^{-T} - |\det \nabla \bar{\mathbf{F}}_h| \nabla \bar{\mathbf{F}}_h^{-T} \|_{L^\infty((0,1)^d)} \leq C_{\mathfrak{s}} \|\nabla \mathbf{F}\|_{L^\infty((0,1)^d)}^{d-1} h \quad (3.173)$$

where a factor $\|\nabla^2 \mathbf{F}\|_{L^\infty((0,1)^d)} / \|\nabla \mathbf{F}\|_{L^\infty((0,1)^d)}$ was included in $C_{\mathfrak{s}}$. Note that this estimate requires the use of NURBS of at least quadratic level. If linear NURBS are utilized the actual geometry is the vertex mesh. Inequality (3.173) is an estimate of the difference between the actual geometry and the corresponding vertex mesh.

As a consequence, using first the Holder inequality and (3.173), then (3.167) and (3.166), and recalling that $|\bar{v}|_{H^1(\bar{\Omega}_h)} \leq 1$ and $\|\nabla \mathbf{F}^{-1}\|_{L^\infty(\Omega)} \|\nabla \mathbf{F}\|_{L^\infty((0,1)^d)} \leq C_{\mathfrak{s}}$, we obtain

$$\begin{aligned} I &\geq -C_{\mathfrak{s}} \|\nabla \mathbf{F}\|_{L^\infty((0,1)^d)}^{d-1} h \|\hat{q}\|_{L^2((0,1)^d)} |\hat{v}|_{H^1((0,1)^d)} \\ &\geq -C_{\mathfrak{s}} h \|q\|_{L^2(\Omega)}. \end{aligned} \quad (3.174)$$

For term II , first a change of variables and then using (3.162) we get

$$II = \int_{\bar{\Omega}_h} \text{tr}(\nabla \bar{v}) \bar{q} \geq C_{\mathfrak{s}} \left(\sum_{\bar{K} \in \bar{\mathcal{K}}_h} h_{\bar{K}}^2 |\bar{q}|_{H^1(\bar{K})}^2 \right)^{1/2} - C_{\mathfrak{s}}' \bar{h} \|\nabla \bar{\mathbf{F}}_h^{-1}\|_{L^\infty(\bar{\Omega}_h)} \|\bar{q}\|_{L^2(\bar{\Omega}_h)} \quad (3.175)$$

Without showing the details, using the bounds (3.168), (3.169), using Lemma 3.4.2 and recalling that $\bar{h} \leq h \|\nabla \mathbf{F}\|_{L^\infty((0,1)^d)}$, we easily have

$$\begin{aligned} &C_{\mathfrak{s}} \left(\sum_{\bar{K} \in \bar{\mathcal{K}}_h} h_{\bar{K}}^2 |\bar{q}|_{H^1(\bar{K})}^2 \right)^{1/2} - C_{\mathfrak{s}}' \bar{h} \|\nabla \bar{\mathbf{F}}_h^{-1}\|_{L^\infty(\bar{\Omega}_h)} \|\bar{q}\|_{L^2(\bar{\Omega}_h)} \\ &\geq C_{\mathfrak{s}} \left(\sum_{K \in \mathcal{K}_h} h_K^2 |q|_{H^1(K)}^2 \right)^{1/2} - C_{\mathfrak{s}}' h \|q\|_{L^2(\Omega)}. \end{aligned} \quad (3.176)$$

Bounds (3.175) and (3.176) now give

$$II \geq C_{\mathfrak{s}} \left(\sum_{K \in \mathcal{K}_h} h_K^2 |q|_{H^1(K)}^2 \right)^{1/2} - C_{\mathfrak{s}}' h \|q\|_{L^2(\Omega)}. \quad (3.177)$$

After rescaling of \mathbf{v} , the identity (3.171) with the bounds (3.174) and (3.177), (3.162) and (3.170), finally give (3.163). \square

Replacing q with $q - q_{mv}$ in (3.163), where q_{mv} is the mean value of q on Ω , we get the following obvious corollary.

Corollary 3.4.1. *As in Proposition 3.4.1, given any $q \in P_h$, there exists a $\mathbf{v} \in V_h \cap H_0^1(\Omega)$ such that*

$$(\nabla \cdot \mathbf{v}, q) \geq C_s \left(\sum_{K \in \mathcal{K}_h} h_K^2 |q|_{H^1(K)}^2 \right)^{1/2} - C'_s h \|q\|_{L^2(\Omega)/\mathbb{R}}, \quad (3.178)$$

$$|\mathbf{v}|_{H^1(\Omega)} \leq 1.$$

We are now able to show the proof of Theorem 3.4.2.

Proof. (Theorem 3.4.2) We will use an argument from Verfürth (see [109]). Due to the validity of the continuous inf-sup condition on Ω and recalling that $P_h \in L^2(\Omega)$, we have the existence of a fixed positive constant C_{shape}^* such that for all $q \in P_h$ there exists a $\mathbf{w} \in H_0^1(\Omega)$ such that

$$(\nabla \cdot \mathbf{w}, q) \geq C_{shape}^* \|q\|_{L^2(\Omega)/\mathbb{R}} \quad (3.179)$$

$$|\mathbf{w}|_{H^1(\Omega)} \leq 1 \quad (3.180)$$

where we introduced the notation C_{shape}^* in order to keep track of the constants in what follows. Using the scaled Poincaré inequality

$$\|\mathbf{w}\|_{L^2(\Omega)} \leq \text{diam}(\Omega) |\mathbf{w}|_{H^1(\Omega)},$$

bound (3.180) is equivalent to

$$\left(\sum_{K \in \mathcal{K}_h} \|\nabla \mathbf{F}\|_{L^\infty(\mathbf{F}^{-1}(K))}^{-2} \|\mathbf{w}\|_{L^2(K)}^2 \right)^{1/2} + |\mathbf{w}|_{H^1(\Omega)} \leq C_s \quad (3.181)$$

From Theorem 3.2.3 there exists a NURBS function $\mathbf{w}_I \in H_0^1(\Omega)$ such that, for all $K \in \mathcal{K}_h$,

$$\|\mathbf{w} - \mathbf{w}_I\|_{L^2(K)}^2 \leq C_s h_K^2 \left(\|\nabla \mathbf{F}\|_{L^\infty(\mathbf{F}^{-1}(K))}^{-2} \|\mathbf{w}\|_{L^2(\tilde{K})}^2 + |\mathbf{w}|_{H^1(\tilde{K})}^2 \right), \quad (3.182)$$

and, using also (3.181)

$$|\mathbf{w}_I|_{H^1(\Omega)} \leq C_s \left[\left(\sum_{K \in \mathcal{K}_h} \|\nabla \mathbf{F}\|_{L^\infty(\mathbf{F}^{-1}(K))}^{-2} \|\mathbf{w}\|_{L^2(K)}^2 \right)^{1/2} + |\mathbf{w}|_{H^1(\Omega)} \right] \leq C_s. \quad (3.183)$$

First integrating by parts, then using the Cauchy-Schwarz inequality and (3.179), finally applying (3.182) and (3.181), it follows

$$\begin{aligned}
(\nabla \cdot \mathbf{w}_I, q) &= (\nabla \cdot (\mathbf{w}_I - \mathbf{w}), q) + (\nabla \cdot \mathbf{w}, q) \\
&\geq - \sum_{K \in \mathcal{K}_h} \|\mathbf{w}_I - \mathbf{w}\|_{L^2(K)} |q|_{H^1(K)} + C_{shape}^* \|q\|_{L^2(\Omega)/\mathbb{R}} \\
&\geq -C_{\mathfrak{s}} \left(\sum_{K \in \mathcal{K}_h} \|\nabla \mathbf{F}\|_{L^\infty(\mathbf{F}^{-1}(K))}^{-2} \|\mathbf{w}\|_{L^2(\tilde{K})}^2 + |\mathbf{w}|_{H^1(\tilde{K})}^2 \right)^{1/2} \left(\sum_{K \in \mathcal{K}_h} h_K^2 |q|_{H^1(K)}^2 \right)^{1/2} \\
&\quad + C_{shape}^* \|q\|_{L^2(\Omega)/\mathbb{R}} \\
&\geq -C_{shape,1} \left(\sum_{K \in \mathcal{K}_h} h_K^2 |q|_{H^1(K)}^2 \right)^{1/2} + C_{shape}^* \|q\|_{L^2(\Omega)/\mathbb{R}} \tag{3.184}
\end{aligned}$$

Now, due to Corollary 3.4.1 and integrating by parts, we have the existence of a $\mathbf{v} \in V_h \cap H_0^1(\Omega)$ such that

$$(\nabla \cdot \mathbf{v}, q) \geq C_{shape,2} \left(\sum_{K \in \mathcal{K}_h} h_K^2 |q|_{H^1(K)}^2 \right)^{1/2} - C_{shape,3} h \|q\|_{L^2(\Omega)/\mathbb{R}} \tag{3.185}$$

$$|\mathbf{v}|_{H^1(\Omega)} \leq 1 \tag{3.186}$$

We now introduce $\mathbf{v}' = \mathbf{w}_I + \alpha \mathbf{v}$ with $\alpha = C_{shape,1} / C_{shape,2}$. From (3.184) and (3.185) it follows

$$\begin{aligned}
(\nabla \cdot \mathbf{v}', q) &\geq (\alpha C_{shape,2} - C_{shape,1}) \left(\sum_{K \in \mathcal{K}_h} h_K^2 |q|_{H^1(K)}^2 \right)^{1/2} \\
&\quad + (C_{shape}^* - \alpha C_{shape,3} h) \|q\|_{L^2(\Omega)/\mathbb{R}} \\
&= (C_{shape}^* - \frac{C_{shape,1} C_{shape,3}}{C_{shape,2}} h) \|q\|_{L^2(\Omega)/\mathbb{R}} \tag{3.187}
\end{aligned}$$

From (3.183) and (3.186) it is immediate to show that

$$|\mathbf{v}'|_{H^1(\Omega)} \leq C_{\mathfrak{s}} \tag{3.188}$$

Assume now that the mesh \mathcal{Q}_h satisfies

$$h \leq h_{max}'' := \frac{1}{2} \frac{C_{shape}^* C_{shape,2}}{C_{shape,1} C_{shape,3}} \tag{3.189}$$

Then from (3.187) it follows

$$(\nabla \cdot \mathbf{v}', q) \geq \frac{C_{shape}^*}{2} \|q\|_{L^2(\Omega)/\mathbb{R}} \quad (3.190)$$

for all meshes in the family.

Therefore, joining (3.190) and (3.188), we have found a positive constant C_{shape}^* such that for all $q \in P_h$ we have the existence of a $\mathbf{v}' \in V_h$ that satisfies

$$(\nabla \cdot \mathbf{v}', q) \geq \frac{C_{shape}^*}{2} \|q\|_{L^2(\Omega)/\mathbb{R}} \quad (3.191)$$

$$\|\mathbf{v}'\|_{H^1(\Omega)} \leq C_s \quad (3.192)$$

Finally, note that the control on the globally constant pressures follows easily due to the fact that $\Gamma_D \neq \partial\Omega$. The proposition is proved. \square

Remark 3.4.2. *Note that, in order for Theorem 3.4.1 to be valid, both the bound (3.189) and the assumptions of Lemma 3.4.2 must be satisfied. Therefore the h_{max} in Theorem 3.4.1 is given by*

$$h_{max} = \min(h'_{max}, h''_{max})$$

Remark 3.4.3. *The numerical tests of the last section seem to show that the method is stable and convergent for practical values of the mesh size. Then, the condition $h \leq h_{max}$, which is needed in the present theoretical analysis, does not seem to be restrictive in the practical case we have considered.*

Remark 3.4.4. *The analysis of this section can be extended straightforwardly to the anisotropic case where the displacement space is of polynomial degree $p_1 + 1, p_2 + 1, \dots, p_d + 1$ and the pressure space p_1, p_2, \dots, p_d . The only point which differs is the starting polynomial inf-sup condition (3.145), while the rest remains identical. The extension of such inf-sup condition to the anisotropic case can be obtained with an easy modification of Lemma 3.2 in [94].*

3.4.4 Advection-diffusion

As before, let Ω be the physical domain, and let $\Gamma_D \equiv \partial\Omega$. Let $f : \Omega \rightarrow \mathbb{R}$ be the given body force; $\mathbf{a} : \Omega \rightarrow \mathbb{R}^d$ is the spatially varying velocity vector and $\mathbf{K} : \Omega \rightarrow \mathbb{R}^{d \times d}$ is the diffusivity tensor, assumed symmetric positive definite; homogeneous Dirichlet boundary conditions on Γ_D are

prescribed. The boundary value problem consists of solving the following equation for $u : \overline{\Omega} \rightarrow \mathbb{R}$:

$$\mathcal{L}u = f \quad \text{in } \Omega, \quad (3.193)$$

$$u = 0 \quad \text{on } \Gamma_D, \quad (3.194)$$

where

$$\mathcal{L}u = \mathbf{a} \cdot \nabla u - \nabla \cdot (\mathbf{K} \nabla u). \quad (3.195)$$

For the purposes of analysis we assume divergence-free advective velocity field and isotropic diffusion:

$$\nabla \cdot \mathbf{a} = 0, \quad (3.196)$$

$$\mathbf{K} = \kappa \mathbf{I}, \quad (3.197)$$

where κ is a positive constant. The weak formulation of (3.193) is: find $u \in H_{\Gamma_D}^1(\Omega)$ such that $\forall v \in H_{\Gamma_D}^1(\Omega)$:

$$B(u, v) = F(v) \quad \text{in } \Omega, \quad (3.198)$$

where

$$B(u, v) = (v, \mathbf{a} \cdot \nabla u)_\Omega + (\nabla v, \kappa \nabla u)_\Omega, \quad (3.199)$$

$$F(v) = (v, f)_\Omega. \quad (3.200)$$

We wish to approximate (3.198) numerically in the NURBS space \mathcal{V}_h defined in Section 3.1 of this document. Galerkin's method is known to be unstable for (3.198) when advection dominates, so we choose to concentrate on the set of techniques known as “stabilized methods”, namely SUPG, GLS and Multiscale (dubbed MS for brevity). The MS version is also referred to as the adjoint, or “unusual,” stabilized method in the literature. These methods were designed to enhance stability of Galerkin's approach without compromising its accuracy. For background and early literature on these formulations we refer the reader to [12], while the state-of-the-art literature on the subject may be found in [2, 8, 9, 13, 17, 19, 37, 39, 40, 61, 70, 101]. Defining $\tilde{\Omega} = \cup K, K \in \mathcal{K}_h$ (i.e., the union of element interiors) and $V_h = \mathcal{V}_h \cap H_{\Gamma_D}^1(\Omega)$, stabilized methods are stated as follows:

SUPG: find $u_h \in V_h$ such that $\forall v_h \in V_h$

$$B^{SUPG}(u_h, v_h) = F^{SUPG}(v_h) \quad \text{in } \Omega, \quad (3.201)$$

with

$$B^{SUPG}(u, v) = B(u, v) + (\mathbf{a} \cdot \nabla v \tau, \mathcal{L}u)_{\tilde{\Omega}}, \quad (3.202)$$

$$F^{SUPG}(v) = F(v) + (\mathbf{a} \cdot \nabla v \tau, f)_{\tilde{\Omega}}. \quad (3.203)$$

GLS: find $u_h \in V_h$ such that $\forall v_h \in V_h$

$$B^{GLS}(u_h, v_h) = F^{GLS}(v_h) \quad \text{in } \Omega, \quad (3.204)$$

with

$$B^{GLS}(u, v) = B(u, v) + (\mathcal{L}v \tau, \mathcal{L}u)_{\tilde{\Omega}}, \quad (3.205)$$

$$F^{GLS}(v) = F(v) + (\mathcal{L}v \tau, f)_{\tilde{\Omega}}. \quad (3.206)$$

MS: find $u_h \in V_h$ such that $\forall v_h \in V_h$

$$B^{MS}(u_h, v_h) = F^{MS}(v_h) \quad \text{in } \Omega, \quad (3.207)$$

with

$$B^{MS}(u, v) = B(u, v) - (\mathcal{L}^*v \tau, \mathcal{L}u)_{\tilde{\Omega}}, \quad (3.208)$$

$$F^{MS}(v) = F(v) - (\mathcal{L}^*v \tau, f)_{\tilde{\Omega}}, \quad (3.209)$$

where \mathcal{L}^* is an adjoint of \mathcal{L} and is given as

$$\mathcal{L}^*v = -\mathbf{a} \cdot \nabla v - \kappa \Delta v. \quad (3.210)$$

In expressions (3.201)-(3.207) a stabilization parameter τ appears, its definition is critical for accuracy, stability and convergence characteristics of the above methods. We adopt expressions presented in Franca, Frey and Hughes [31] and give them here for completeness:

$$\tau(x, \mathbf{Pe}_K(x)) = \frac{h_K}{2\|\mathbf{a}(x)\|} \xi(\mathbf{Pe}_K(x)) \quad (3.211)$$

$$\mathbf{Pe}_K(x) = \frac{\|\mathbf{a}(x)\| h_K}{2\kappa} \quad (3.212)$$

$$\xi(\mathbf{Pe}_K(x)) = \min\{m_K \mathbf{Pe}_K(x), 1\} \quad (3.213)$$

$$m_K = \min\left\{\frac{1}{3}, \frac{2}{C_{inv}}\right\} \quad (3.214)$$

The above expressions are defined from error analysis considerations. K is any element in the partition \mathcal{K}_h of Ω , C_{inv} is the smallest constant satisfying the local inverse estimate of Theorem 3.3.1 with a corresponding definition of h_K .

We briefly show analysis of stabilized formulations for advection-diffusion employing NURBS approximation spaces. The approach we use is very similar to that of the stabilized formulations of incompressible elasticity. In what follows we concentrate on SUPG, other methods are analyzed in a similar fashion.

Lemma 3.4.6. *The bilinear form defined in (3.201) inherits the following stability property:*

$$B^{SUPG}(w, w) \geq C|||w|||^2 \quad \forall w \in V_h, \quad (3.215)$$

where

$$|||w|||^2 = \kappa \|\nabla w\|_{L^2(\Omega)}^2 + \|\tau^{1/2} \mathbf{a} \cdot \nabla w\|_{L^2(\Omega)}^2. \quad (3.216)$$

The above result, which can be easily verified (see, for example, Franca, Frey and Hughes [31]), is a consequence of boundary conditions, definition of the stabilization parameter τ , and the inverse estimate of Theorem 3.3.1. Continuity properties of $B^{SUPG}(\cdot, \cdot)$ are stated in the following lemma.

Lemma 3.4.7. *The bilinear form defined in (3.201) is continuous in the following sense:*

$$B^{SUPG}(w, v) \leq C|||w||| |||v||| \quad \forall w \in V_h, \quad \forall v \in H_{\Gamma_D}^1(\Omega) \cap H^2(\tilde{\Omega}), \quad (3.217)$$

with the norm above is defined as

$$\begin{aligned} |||v|||^2 &= \kappa \|\nabla v\|_{L^2(\Omega)}^2 + \|\tau^{-1/2} v\|_{L^2(\Omega)}^2 \\ &+ \|\tau^{1/2} \mathbf{a} \cdot \nabla v\|_{L^2(\Omega)}^2 + \|\tau^{1/2} \kappa \Delta v\|_{L^2(\tilde{\Omega})}^2. \end{aligned} \quad (3.218)$$

This result follows by a direct computation. Having established coercivity and continuity, we proceed with the error estimate as follows. Define the following quantities

$$e = u - u_h \quad (\text{numerical error}) \quad (3.219)$$

$$\eta = u - \Pi_{\mathcal{V}_h}^0 u \quad (\text{interpolation error}) \quad (3.220)$$

$$e_h = \Pi_{\mathcal{V}_h}^0 u - u_h = \Pi_{\mathcal{V}_h}^0 e \quad (\text{discrete error}), \quad (3.221)$$

and compute:

$$\begin{aligned}
|||e_h|||^2 &\leq C B(e_h, e_h) \quad (\text{coercivity}) \\
&= C B(e_h, -\eta) \quad (\text{Galerkin orthogonality}) \\
&\leq C |||e_h||| |||\eta||| \quad (\text{continuity}).
\end{aligned} \tag{3.222}$$

Relation (3.222) combined with the triangle inequality gives a bound on the numerical error in the solution in terms of the interpolation error

$$|||e||| \leq C |||\eta|||. \tag{3.223}$$

The following theorem establishes convergence rates of the methods in question posed over NURBS spaces.

Theorem 3.4.3. *Assuming $u \in H^{p+1}$, there exists $C_s > 0$ such that*

$$|||u - u_h|||^2 \leq C \sum_K (\|\mathbf{a}\|_{L^\infty(K)} h_K^{2p+1} + \kappa h_K^{2p}) \sum_{i=0}^{p+1} \|\nabla \mathbf{F}\|_{L^\infty(\mathbf{F}^{-1}(K))}^{2(i-p-1)} |u|_{H^i(K)}^2 \tag{3.224}$$

Proof. Given the definition of τ , the following bounds are easily established (see, for example, Franca, Frey and Hughes [31]):

$$\|\tau^{-1/2} \eta\|_{L^2(K)}^2 \leq C(\kappa/h_K^2 + \|\mathbf{a}\|_{L^\infty(K)}/h_K) \|\eta\|_{L^2(K)}^2, \tag{3.225}$$

$$\|\tau^{1/2} \mathbf{a} \cdot \nabla \eta\|_{L^2(K)}^2 \leq C(\kappa + \|\mathbf{a}\|_{L^\infty(K)} h_K) \|\nabla \eta\|_{L^2(K)}^2, \tag{3.226}$$

$$\|\tau^{1/2} \kappa \Delta \eta\|_{L^2(K)}^2 \leq C(\kappa h_K^2 + \|\mathbf{a}\|_{L^\infty(K)} h_K^3) \|\Delta \eta\|_{L^2(K)}^2. \tag{3.227}$$

Using inequality (3.223) together with the above bounds, the local error estimate (3.61), and summing over all the elements in \mathcal{K}_h yields the final result. \square

3.5 Numerical Examples

In this section we report on the results of numerical computations performed with NURBS. We consider examples from compressible and incompressible linear elasticity as well as advection-diffusion. The first two examples were already presented in [52], we repeat them here as evidence in support of convergence theory put forth in the preceding sections of this document. On all the convergence plots the error quantity plotted on the ordinate axis is absolute. In all cases computational results are in agreement with the theoretical findings.

3.5.1 Solid elastic circular cylinder subjected to internal pressure loading

This problem falls within the framework of Section 3.4.1. The problem specification is shown in Figure 3.5. It is a simple matter to obtain an exact solution assuming the pressure varies at most circumferentially (see Gould [36], pp. 117-119). The internal pressure was assumed to vary as $\cos(2\theta)$ and the exact solution is thus of class C^∞ . Meshes developed from h -refinement are shown in Figure 3.6. Quadratic, cubic, and quartic NURBS were employed. As in all of the examples considered herein, the exact geometry is incorporated in the coarsest mesh and is maintained throughout the refinement process. A rational quadratic basis is the minimum order capable of exactly representing the cylindrical geometry. The cubic and quartic cases were obtained from the quadratic case by k -refinement [18, 52], in which case the degree of continuity was increased to C^2 and C^3 , respectively. The rates of convergence of the error measured in the energy norm (the natural norm for the problem, equivalent to the H^1 -norm) are presented in Figure 3.7. The rates of convergence for quadratic, cubic, and quartic NURBS elements are optimal, that is, 2, 3, and 4, respectively. This problem falls within the hypotheses of our theoretical framework and the optimal convergence rates are consistent with the results of Section 3.4.1.

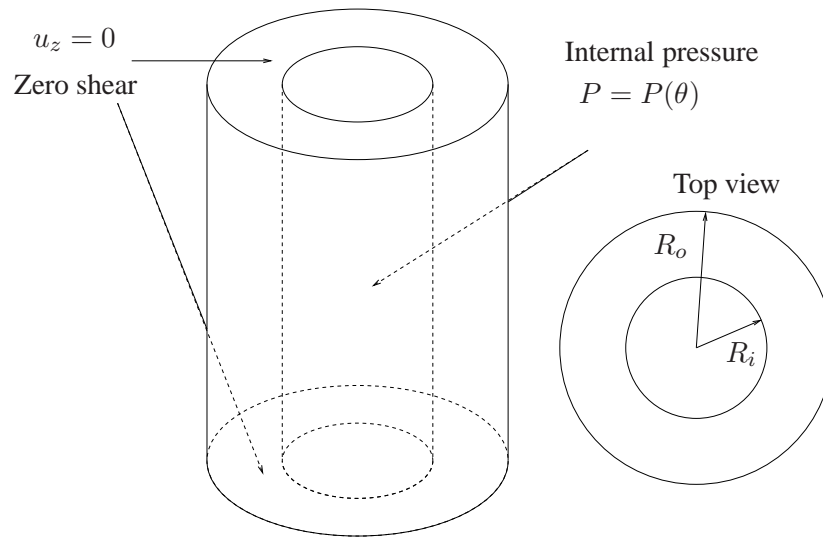
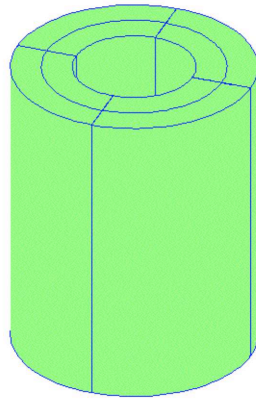


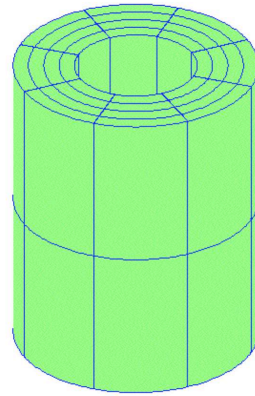
Figure 3.5: Thick cylinder pressurized internally.

3.5.2 Infinite elastic plate with circular hole under constant in-plane tension in the x -direction

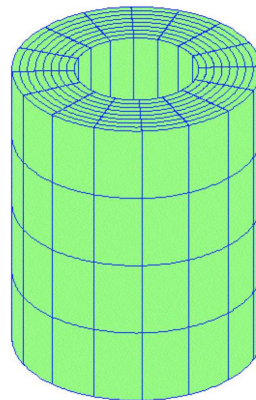
This is a two-dimensional problem of linear elasticity, falling within the framework of section 5.1. The infinite plate is modeled by a finite quarter plate. The exact solution (Gould [36], pp. 120-123),



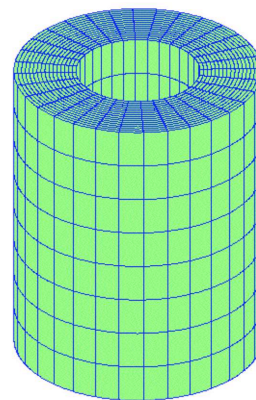
Mesh 1



Mesh 2



Mesh 3



Mesh 4

Figure 3.6: Solid circular cylinder meshes

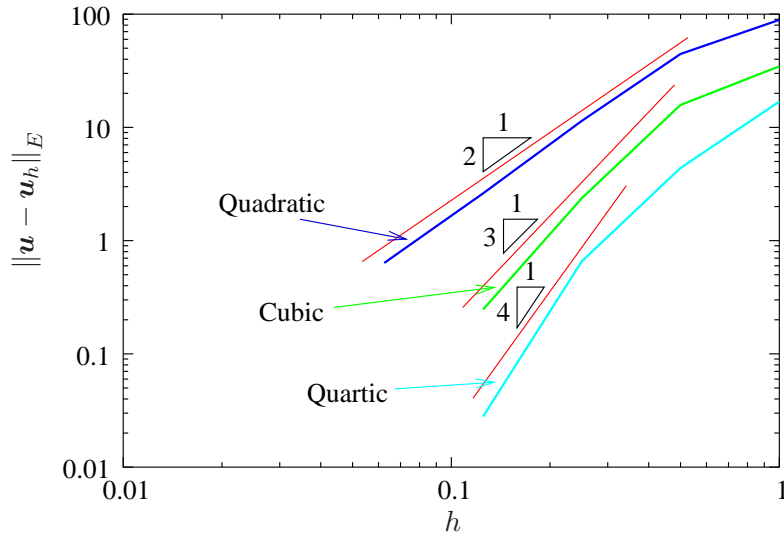


Figure 3.7: Solid circular cylinder with varying internal pressure. Convergence of the error in the energy norm for quadratic, cubic, and quartic NURBS discretizations.

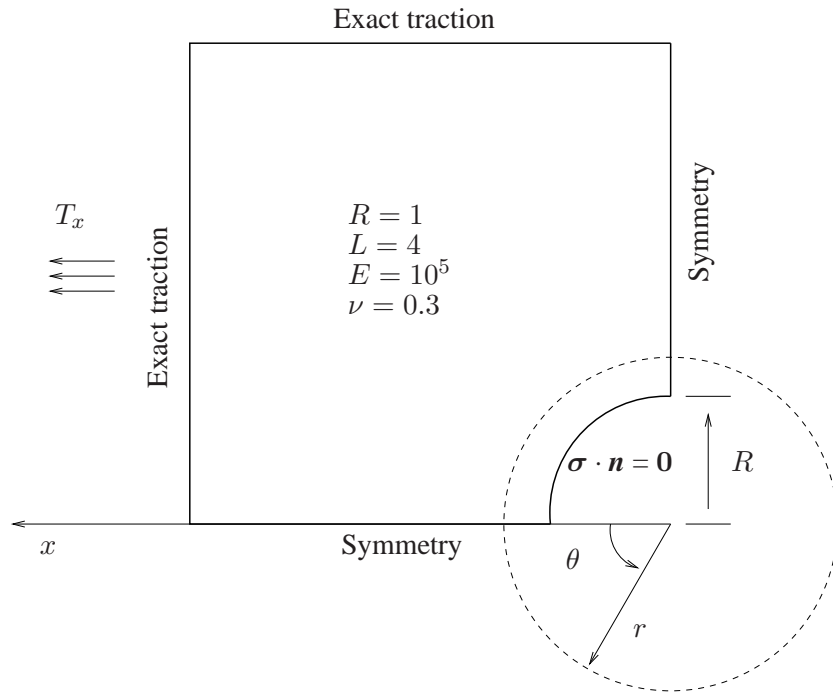


Figure 3.8: Elastic plate with a circular hole: problem definition.

evaluated at the boundary of the finite quarter plate, is applied as a Neumann boundary condition. The setup is illustrated in Figure 3.8. T_x is the magnitude of the applied stress at infinity, R is the radius of the traction-free hole, L is the length of the finite quarter plate, E is Young's modulus, and ν is Poisson's ratio. As in the previous example, a rational quadratic basis is the minimum order capable of exactly representing a circle.

The first six meshes used in the analysis are shown in Figure 3.9. The cubic and quartic NURBS are obtained by order elevation of the quadratic NURBS on the coarsest mesh (for details of the geometry and mesh construction, see [52]). Continuity of the basis is C^{p-1} everywhere, except along the line which joins the center of the circular edge with the upper left-hand corner of the domain. There it is C^1 as is dictated by the coarsest mesh employing rational quadratic parameterization. Convergence results in the L^2 -norm of stresses (which is equivalent to the H^1 -seminorm of the displacements) are shown in Figure 3.10. As can be seen, the L^2 -convergence rates of stress for quadratic, cubic, and quartic NURBS are 2, 3, and 4, respectively. The geometrical mapping used in this example does not conform to the assumptions of the theory, namely, in the elements adjacent to the upper left-hand corner of the domain $\|\mathbf{F}^{-1}\|_{W^{1,\infty}}$ is not uniformly bounded. This was a choice, not a necessity. Nevertheless, optimal convergence rates are still attained.

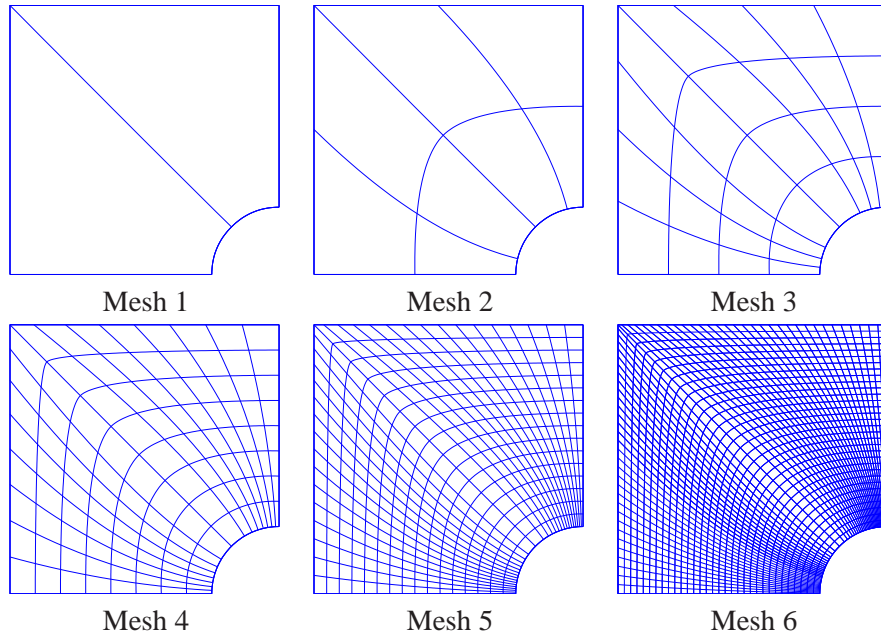


Figure 3.9: Elastic plate with circular hole. Meshes produced by h -refinement (knot insertion).

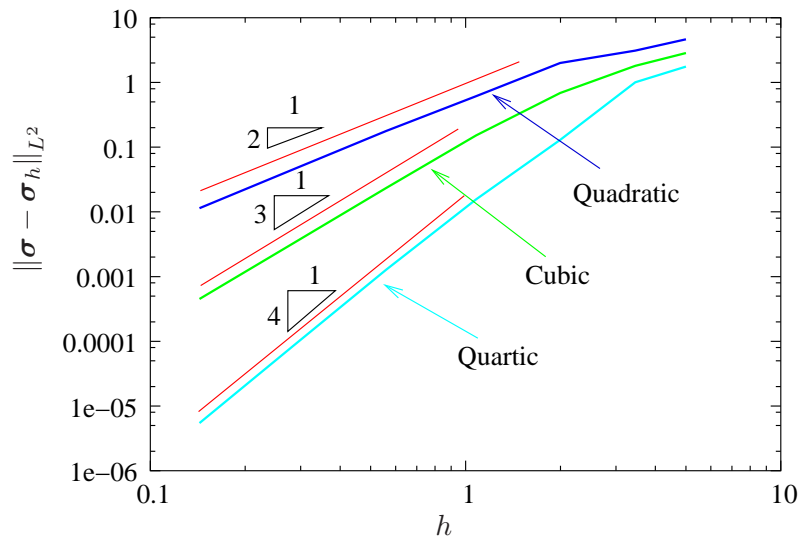


Figure 3.10: Error measured in the L^2 -norm of stress vs. mesh parameter.

3.5.3 Constrained block subjected to a trigonometric load

In this two-dimensional example we consider a fully constrained square of incompressible elastic material loaded externally. This problem falls within the framework of Sections 3.4.2 and 3.4.3. It was designed by Auricchio *et al.* [4], and the setup is illustrated in Figure 3.11, where $\mathbf{u} = (u, v)$ is a displacement vector, μ is the shear modulus and L is the edge half-length. Note that in this case pressure is determined up to an arbitrary constant, so for the purposes of computing an L^2 error of the pressure field, the constant mode is removed from the pressure solution. The load and boundary conditions are selected in such a way that the analytical solution is easily obtained. We give them here for completeness:

$$\begin{aligned}
 u &= -\frac{\cos^2 x \cos y \sin y}{2} \\
 v &= \frac{\cos^2 y \cos x \sin x}{2} \\
 p &= \sin(x^2 y) \\
 f_1 &= \mu \cos y \sin y (1 - 4 \cos^2 x) - 2xy \cos(x^2 y) \\
 f_2 &= -\mu \cos x \sin x (1 - 4 \cos^2 y) - x^2 \cos(x^2 y)
 \end{aligned} \tag{3.228}$$

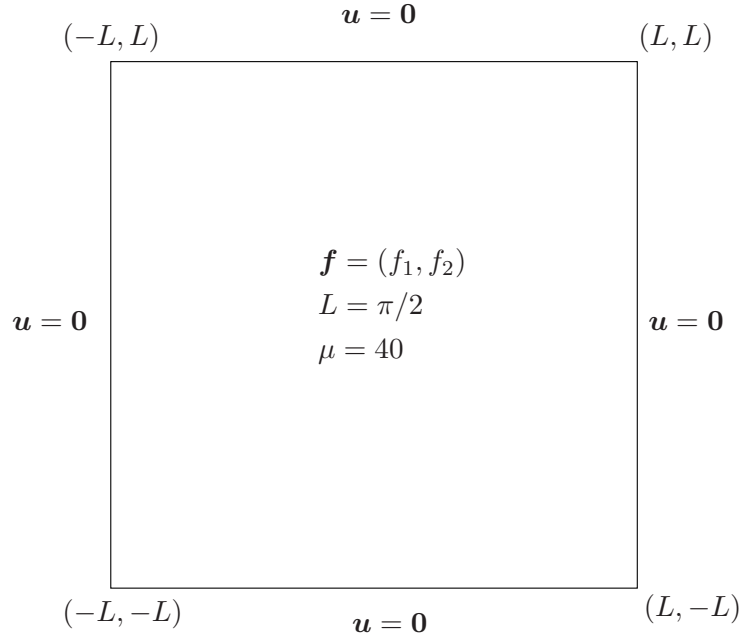


Figure 3.11: Trigonometric load problem setup.

Meshes 1, 3, and 5 used in the computations are shown in Figure 3.12. Distortion of the mesh was introduced at the coarsest level of discretization and maintained throughout the refinement. Three studies were performed for this problem. In the first study we used a C^1 -continuous rational quadratic basis for both \mathbf{u} and p and employed the Douglas-Wang stabilized formulation. The results of this study are shown on the top plot of Figure 3.13. The other stabilized methods behaved in the same fashion and thus the results are not shown. Optimal convergence of the L^2 -norm and the H^1 -seminorm of the displacement error and the L^2 -norm of the pressure error is obtained. The results are consistent with the theoretical predictions of Section 3.4.2. In the second study we used BB-compatible spaces: a C^0 rational quadratic basis for p and C^0 rational cubic basis for \mathbf{u} obtained from the former by degree elevation. These spaces are stable and convergent within Galerkin's method according to the results of Section 3.4.3. The first four of the five meshes were used in the calculations and the results are presented in the middle plot of Figure 3.13. All results converge optimally, in agreement with the theory in Section 3.4.3. In the third study we again used quadratic pressure and cubic displacement, but C^1 -continuity was enforced. This case is not covered in the theory of Section 3.4.3, yet optimal convergence is again obtained, as shown in the bottom plot of Figure 3.13. We conjecture that this type of discretization is BB-stable.

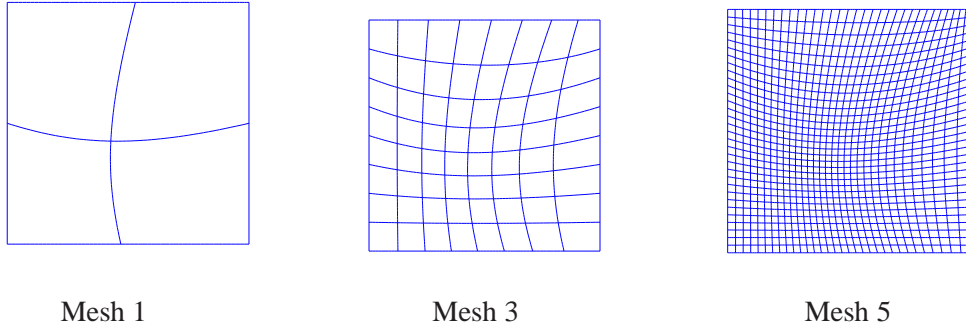


Figure 3.12: Trigonometric load problem meshes produced by h -refinement (knot insertion).

3.5.4 Driven cavity problem

The driven cavity problem is a two-dimensional Stokes flow calculation that is often used as a test of numerical stability. The equations of Stokes flow are identical to the equations of linear, isotropic, incompressible elasticity, only the interpretation is different. In Stokes flow $\mathbf{u} = (u, v)$ is the velocity vector and μ is the dynamic viscosity (see, e.g., [44]). In the exact specification of this problem, the velocity boundary condition is discontinuous at the upper two corners, that is, at $(0, L)$ and (L, L) ; see Figure 3.14 for the problem setup. This produces singular pressures in

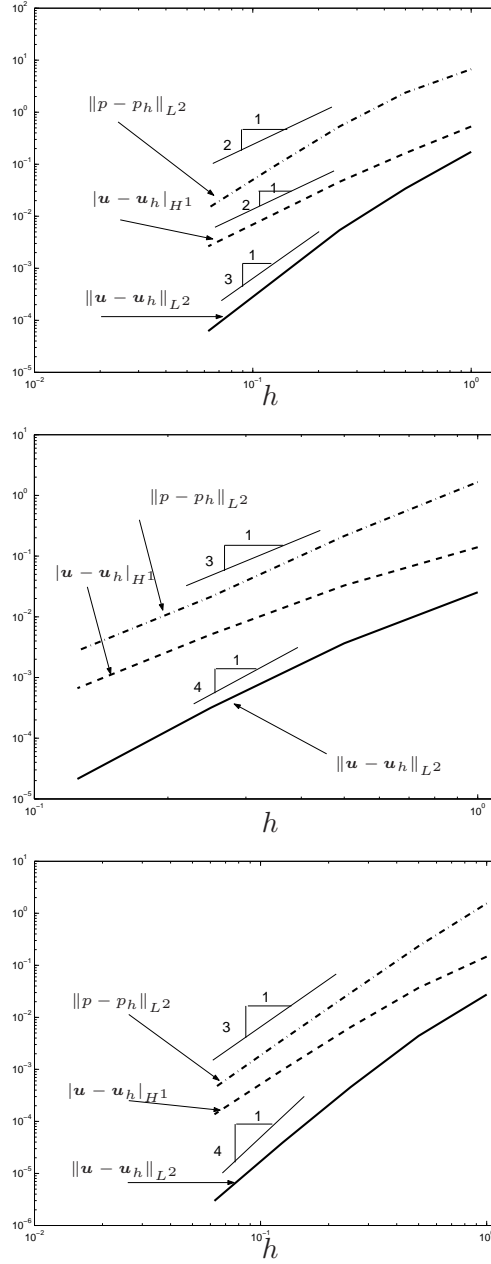


Figure 3.13: Trigonometric load problem. Convergence to the analytical solution for displacement and pressure. Top: Douglas-Wang stabilization, equal-order, quadratic, C^1 -continuous bases. Middle: Galerkin's method, cubic displacement, quadratic pressure, C^0 -continuous bases. Bottom: Galerkin's method, cubic displacement, quadratic pressure, C^1 -continuous bases.

both corners which tend to cause unstable formulations to fail in dramatic fashion. The mesh is comprised of 16×16 square elements. In the first two examples, the pressure discretization is taken to be C^1 quadratic splines. The velocity space is the same in the first example and consists of C^1 -cubic splines in the second. Figure 3.15 compares solutions obtained with the Galerkin formulation. As expected, the equal-order combination produces an unstable result, as is especially apparent for pressure, while the mixed interpolation case appears to be quite stable. The solution is very similar to that presented in Franca, Frey and Hughes [31]. Figure 3.16 shows a stabilized GLS computation for equal-order cases. Both the $p = 2$ and $p = 3$ results appear stable and are again in general agreement with [31]. As may be gleaned from Figures 3.15 and 3.16, the velocity at the upper corners is set to $\mathbf{u} = (1, 0)$. This is referred to as the “leaky” boundary condition treatment (see [44] for further elaboration).

Remark 3.5.1. *Three-dimensional computations of other boundary-value problems (not shown) with the same bases used in this study yielded consistent results, namely, the stabilized methods produced stable calculations with equal-order NURBS whereas the Galerkin formulation did not, and the Galerkin method with velocity one order higher than pressure produced stable results when both velocity and pressure had the same order of continuity across element boundaries. Our theoretical results in Section 3.4.3 only pertain to C^0 -continuous interpolations, but there is considerable evidence that the higher-order uniformly continuous cases are stable as well.*

3.5.5 Advection-diffusion in a hollow cylinder

The problem geometry and parameters are given on Figure 3.17. The axisymmetric analytical solution behaves logarithmically in the radial direction and exponentially in the axial direction, viz.,

$$u(r, z) = \frac{(e^{az/\kappa} - e^{aL/\kappa}) \log(r)}{(1 - e^{aL/\kappa}) \log(2)} \quad (3.229)$$

Four meshes, composed of 32, 256, 2,048 and 16,384 elements, were used. The first three are depicted in Figure 3.18. The meshes are “biased” toward the outflow where a boundary layer occurs. Two values of the diffusivity were considered. In the first case, κ was chosen to be 0.025, which produces a solution than can be fairly well resolved by meshes 2-4. In the second case, κ was selected to be 0.00625, and the boundary layer is fairly well resolved only by the finest mesh. A rational quadratic basis is employed in each parametric direction and no symmetry was assumed, yet a pointwise axisymmetric response was obtained in all cases as can be seen in Figure 3.19. All three stabilized formulations were implemented and compared with the Galerkin solution. In the case of the larger value of κ , all methods produced an optimally convergent solution in both the L^2 -norm and H^1 -seminorm as can be seen in Figure 3.20. This is consistent with the theory of Section 3.4.4.

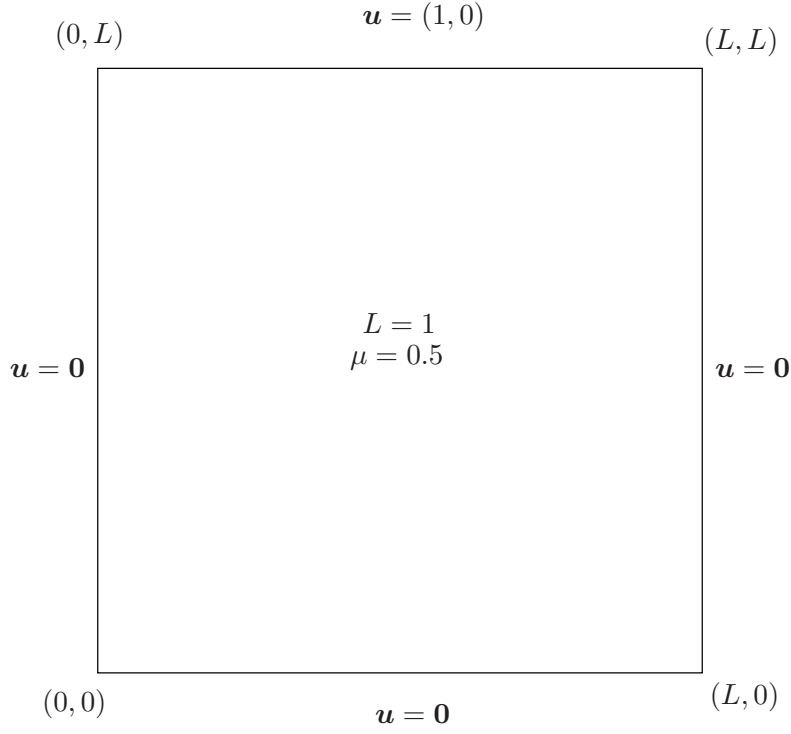


Figure 3.14: Driven cavity problem setup.

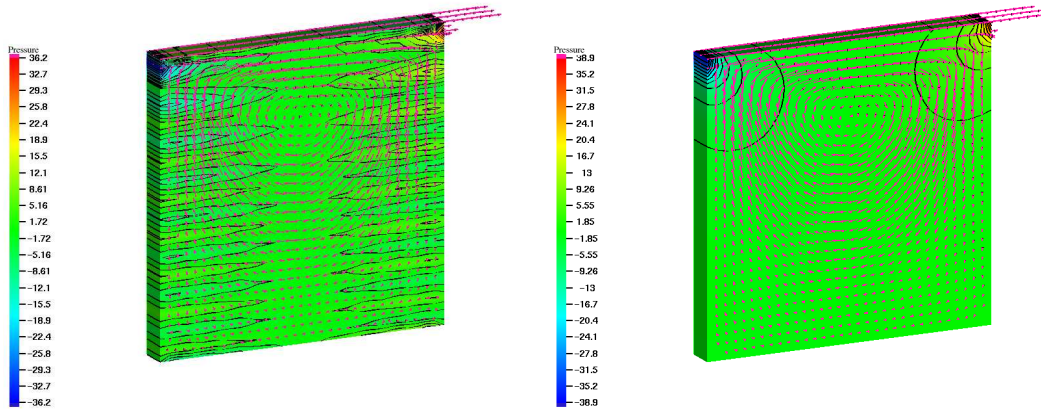


Figure 3.15: Driven cavity problem. Velocity vectors superposed on pressure contours. Left: Galerkin solution with equal-order discretization ($p = 2$). Right: Galerkin solution with unequal-order discretization ($p = 2$ for the pressure and $p = 3$ for the velocity).

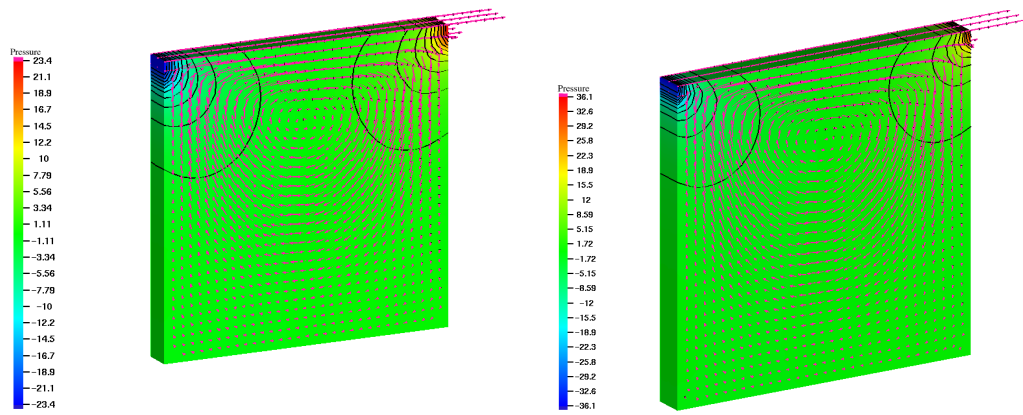


Figure 3.16: Driven cavity problem. Velocity vectors superposed on pressure contours. GLS solution with equal-order discretization. Left: $p = 2$, Right $p = 3$.

The same error norms were computed for the case of smaller diffusivity ($\kappa = 0.00625$). Galerkin's method produced a globally oscillatory solution on coarser meshes, which resulted in a large global L^2 -error compared with the stabilized solutions (see Figure 3.21). The H^1 -error for all methods was suboptimal, which is not surprising, as the major contribution comes from the very thin, unresolved, outflow boundary layer. In order to remove the effect of the boundary layer, we computed the error on the part of the domain which excludes it (i.e., $\{0 < z < 4.95\} \times \{1 < r < 2\}$). The H^1 -error is much better behaved for the stabilized methods. The optimal order of convergence is observed for both H^1 - and L^2 -norms in these cases. The results are typical of stabilized finite element methods in that “localization” or “interior” estimates can be proven (see, e.g., Johnson, Nävert and Pitkäranta [59] and Wahlbin [111]). These estimates are also known *not* to hold for Galerkin finite element methods, for which unresolved layers result in global pollution. This phenomenon is also evident here in Figure 3.21. On the finest mesh, error measures for the Galerkin and stabilized methods seem to coincide, which suggests that the asymptotic regime has been reached.

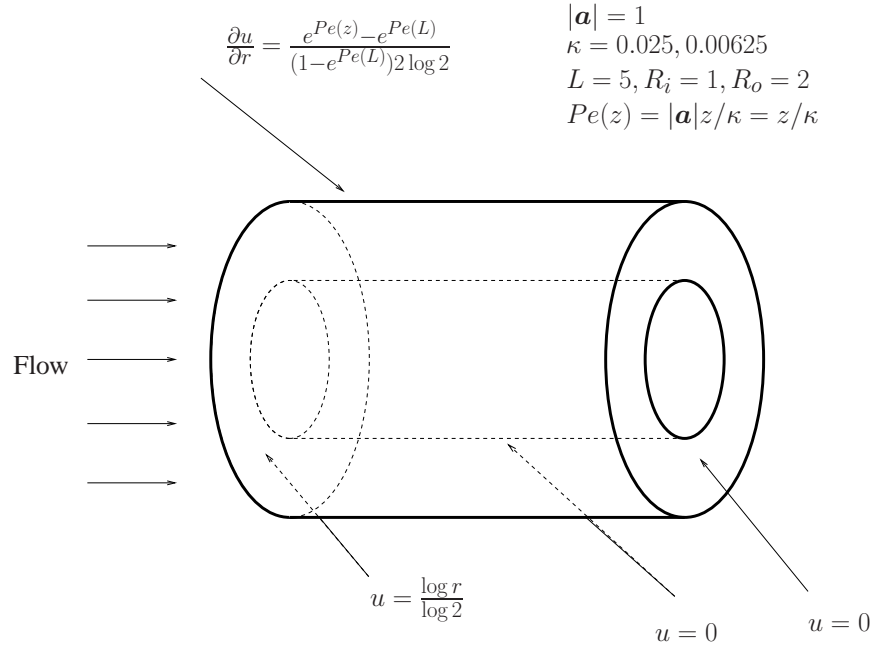


Figure 3.17: Advection-diffusion in a hollow cylinder. Problem setup.

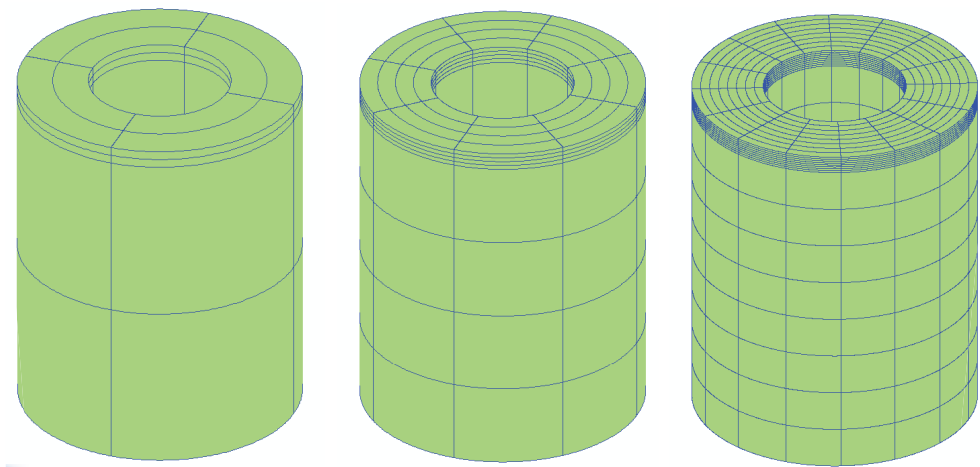
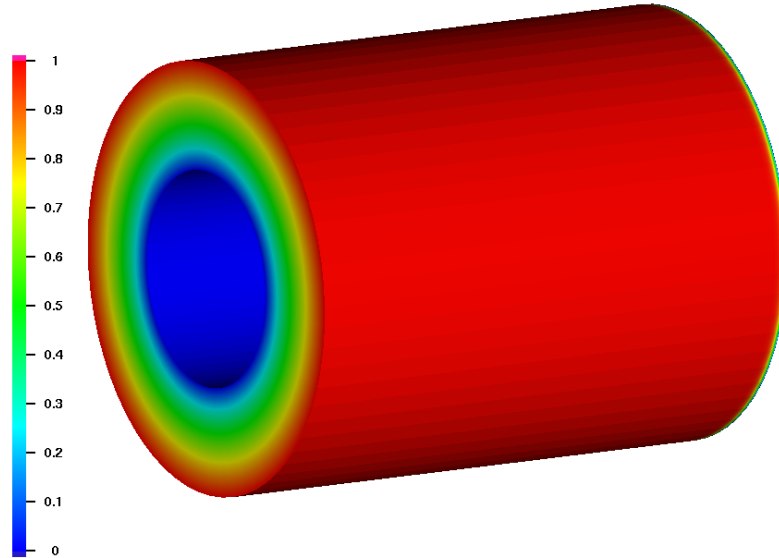
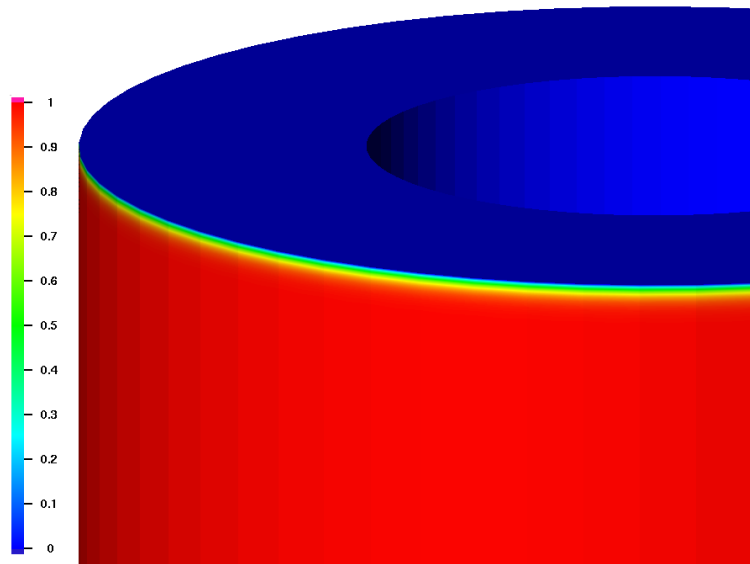


Figure 3.18: Advection-diffusion in a hollow cylinder. Meshes 1-3.



Solution on the whole domain



Zoom on the outflow boundary layer

Figure 3.19: Advection-diffusion in a hollow cylinder. Solution contours on the finest mesh, $\kappa = 0.025$.

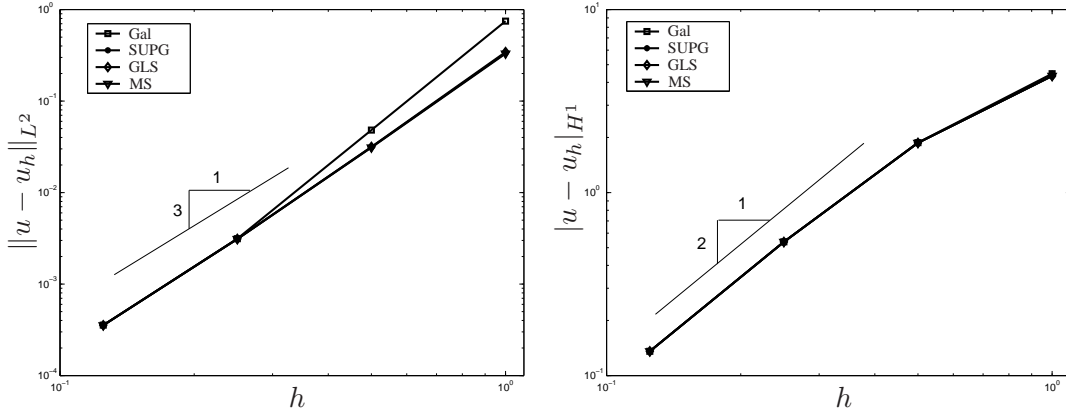


Figure 3.20: Advection-diffusion in a hollow cylinder, $\kappa = 0.025$. Convergence rates.

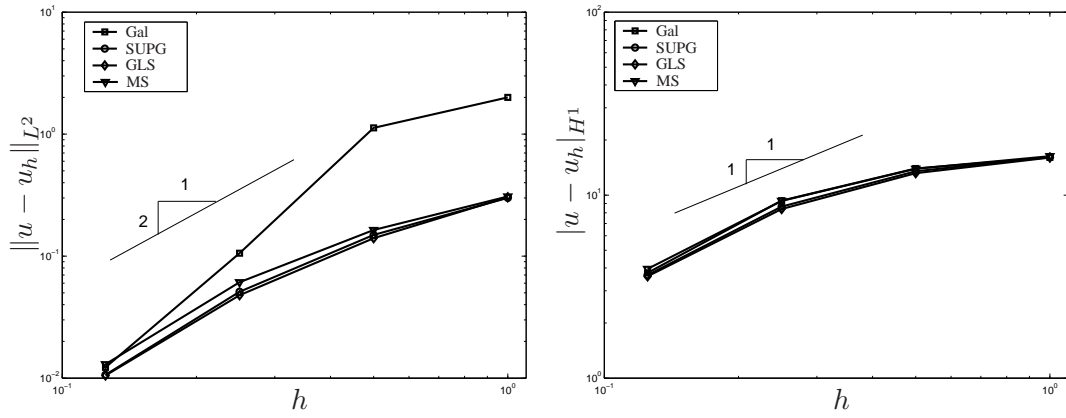


Figure 3.21: Advection-diffusion in a hollow cylinder, $\kappa = 0.00625$. Convergence rates.

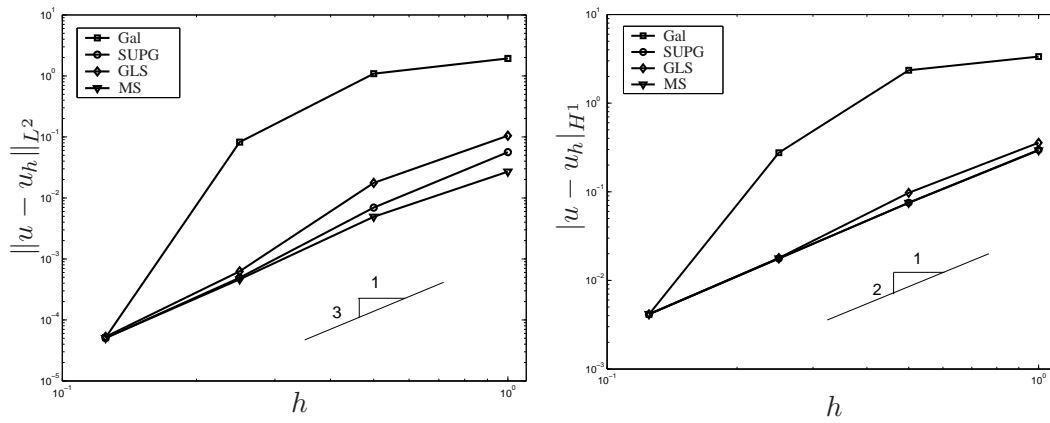


Figure 3.22: Advection-diffusion in a hollow cylinder, $\kappa = 0.00625$. Convergence rates outside of the boundary layer.

Chapter 4

Variationally Consistent Multiscale Turbulence Modeling

4.1 Small-scale Green's operator, small-scale Green's function, and connection with stabilized methods

In this section we review the concepts of the small-scale Green's operator and the small-scale Green's function introduced in Hughes and Sangalli [54]. These objects play a fundamental role in the design and analysis of numerical methods based on the variational multiscale approach. Further in this chapter we will apply the VMS ideas to turbulence modeling.

Let V be a Hilbert space, endowed with the inner-product $(\cdot, \cdot)_V$, and the norm $\|\cdot\|_V = (\cdot, \cdot)_V^{1/2}$. Let V^* be its dual and let $\langle \cdot, \cdot \rangle_{V^*, V}$ denote a duality pairing between V and V^* . Let $\mathcal{L} : V \rightarrow V^*$ represent a linear isomorphism, and let $f \in V^*$.

Consider the following abstract variational problem: Find v such that $\forall w \in V^*$

$$\langle w, \mathcal{L}v \rangle_{V^*, V} = \langle w, f \rangle_{V^*, V}. \quad (4.1)$$

Formally, solution of (4.1) may be expressed by means of a Green's operator $\mathcal{G} : V^* \rightarrow V$ as

$$v = \mathcal{G}f. \quad (4.2)$$

Let \bar{V} be a closed subspace of V . We will refer to \bar{V} as the space of coarse or large scales. Let $\mathcal{P} : V \rightarrow \bar{V}$ be a linear projector onto \bar{V} , with $\mathcal{P}^2 = \mathcal{P}$, and $\bar{V} = \text{Range } \mathcal{P}$. We define $V' = \text{Ker } \mathcal{P}$ and refer to it as the space of small or fine scales. It is also a closed subspace of V .

With this construction, the space V engenders a decomposition

$$V = \bar{V} \oplus V'. \quad (4.3)$$

The above decomposition means that any $u \in V$ has a unique representation $u = \bar{u} + u'$, where $\bar{u} \in \bar{V}$, $u' \in V'$, $\bar{u} = \mathcal{P}u$, and $u' = u - \mathcal{P}u$.

The aim of the VMS approach is to approximate (4.1) in \bar{V} and obtain the solution $\bar{v} = \mathcal{P}v$, where v solves the full problem (4.1). It is shown in Hughes and Sangalli [54] that the above design condition is met when the following variational formulation is employed: Find $\bar{v} \in \bar{V}$ such that $\forall \bar{w} \in \bar{V}$

$$\langle \bar{w}, \mathcal{L}\bar{v} \rangle_{V^*,V} - \langle \bar{w}, \mathcal{L}\mathcal{G}'\mathcal{L}\bar{v} \rangle_{V^*,V} = \langle \bar{w}, f \rangle_{V^*,V} - \langle \bar{w}, \mathcal{L}\mathcal{G}'f \rangle_{V^*,V}. \quad (4.4)$$

\mathcal{G}' above is the small-scale Green's operator, it is defined as

$$\mathcal{G}' = \mathcal{G} - \mathcal{G}\mathcal{P}^T(\mathcal{P}\mathcal{G}\mathcal{P}^T)^{-1}\mathcal{P}\mathcal{G}, \quad (4.5)$$

where $\mathcal{P}^T : \bar{V}^* \rightarrow V^*$ is the transpose of \mathcal{P} .

Approximate solutions to (4.1) are typically constructed in finite-dimensional spaces. For \bar{V} finite-dimensional, one has the following characterization of the fine scales: there exists a set of functionals $\{\mu_i\}_{i=1}^N \in V^*$, such that

$$\langle \mu_i, u \rangle_{V^*,V} = 0 \quad \forall i = 1, \dots, N \iff \mathcal{P}u = 0, \quad (4.6)$$

where N is the dimension of \bar{V} . In this case, the small-scale Green's operator (4.5) becomes

$$\mathcal{G}' = \mathcal{G} - \mathcal{G}\boldsymbol{\mu}^T(\boldsymbol{\mu}\mathcal{G}\boldsymbol{\mu}^T)^{-1}\boldsymbol{\mu}\mathcal{G}, \quad (4.7)$$

where

$$\boldsymbol{\mu}\mathcal{G}(\nu) = \begin{bmatrix} \langle \mu_1, \mathcal{G}\nu \rangle_{V^*,V} \\ \vdots \\ \langle \mu_N, \mathcal{G}\nu \rangle_{V^*,V} \end{bmatrix} \quad \forall \nu \in V^*, \quad (4.8)$$

$$\mathcal{G}\boldsymbol{\mu}^T = \begin{bmatrix} \mathcal{G}\mu_1 & \dots & \mathcal{G}\mu_N \end{bmatrix}, \quad (4.9)$$

and

$$\boldsymbol{\mu} \mathcal{G} \boldsymbol{\mu}^T = \begin{bmatrix} \langle \mu_1, \mathcal{G} \mu_1 \rangle_{V^*, V} & \cdots & \langle \mu_1, \mathcal{G} \mu_N \rangle_{V^*, V} \\ \vdots & \ddots & \vdots \\ \langle \mu_N, \mathcal{G} \mu_1 \rangle_{V^*, V} & \cdots & \langle \mu_N, \mathcal{G} \mu_N \rangle_{V^*, V} \end{bmatrix} \in \mathbb{R}^{N \times N}. \quad (4.10)$$

The above abstract framework extends to the case when \mathcal{L} in (4.1) is a second-order linear partial differential operator, $V = H_0^1(\Omega)$, $V^* = H^{-1}(\Omega)$, and $\Omega \in \mathbb{R}^d$ is the spatial domain. In this case the solution operator \mathcal{G} in (4.2) is represented by a Green's function, $g : \Omega \times \Omega \rightarrow \mathbb{R}$, as

$$v(\mathbf{x}) = \int_{\Omega} g(\mathbf{x}, \mathbf{y}) f(\mathbf{y}) d\Omega. \quad (4.11)$$

\bar{V} is identified with a finite-dimensional subspace of V . It is defined as a span of a set of basis functions, such as trigonometric polynomials, standard polynomial finite element functions, or NURBS. A linear projector may be defined through a scalar product $(\cdot, \cdot) : V \times V \rightarrow \mathbb{R}$ on V , possibly different from $(\cdot, \cdot)_V$, as

$$(\bar{w}, \mathcal{P}u) = (\bar{w}, u) \quad \forall \bar{w} \in \bar{V}, u \in V. \quad (4.12)$$

This construction leads to an orthogonal projector, that is, \bar{u} is orthogonal to u' with respect to the scalar product (\cdot, \cdot) , where, as before, $\bar{u} = \mathcal{P}u$ and $u' = u - \bar{u}$. In the case when the scalar product is taken to be the $H_0^1(\Omega)$ inner product, \mathcal{P} becomes the H_0^1 -projector. An L^2 -projector is obtained when the scalar product is the $L^2(\Omega)$ inner product. Just as before, the space of fine scales, V' , may be characterized by

$$\int_{\Omega} \mu_i(\mathbf{x}) u(\mathbf{x}) d\Omega = 0 \quad \forall i = 1, \dots, N \iff \mathcal{P}u = 0, \quad (4.13)$$

where $\mu_i(\mathbf{x})$ are distributions and the integral is interpreted in the distributional sense. For example, when \bar{V} is a standard finite element space comprised of piece-wise polynomial functions and H_0^1 projector is used, from (4.12) one obtains

$$0 = \int_{\Omega} \nabla N_i(\mathbf{x}) \cdot \nabla u'(\mathbf{x}) d\Omega = \int_{\tilde{\Omega}} -\Delta N_i(\mathbf{x}) u'(\mathbf{x}) d\Omega + \int_{\tilde{\Gamma}} \llbracket \nabla N_i(\mathbf{x}) \cdot \mathbf{n} \rrbracket u'(\mathbf{x}) d\Gamma, \quad (4.14)$$

where $\{N_i(\mathbf{x})\}_{i=1}^N$ is a basis for \bar{V} , \mathbf{n} is the element boundary outward unit normal vector, $\llbracket \cdot \rrbracket$ is the standard “jump” operator, and $\tilde{\Gamma}$ and $\tilde{\Omega}$ denote the union of element boundaries and interiors,

respectively. Comparing the above expression with (4.14), one may think of μ_i 's as:

$$\mu_i(\mathbf{x}) = -\Delta N_i(\mathbf{x}) \text{ on } \tilde{\Omega}, \text{ and } \mu_i(\mathbf{x}) = \llbracket \nabla N_i(\mathbf{x}) \cdot \mathbf{n} \rrbracket \text{ on } \tilde{\Gamma}. \quad (4.15)$$

In the case of L^2 projection, one can set $\mu_i(\mathbf{x}) = N_i(\mathbf{x})$.

Let $B(\cdot, \cdot) : V \times V \rightarrow \mathbb{R}$ represent the bi-linear form associated with \mathcal{L} . Then the VMS formulation (4.4) becomes: Find $\bar{v} \in \bar{V}$, such that $\forall \bar{w} \in \bar{V}$

$$B(\bar{w}, \bar{v}) - \int_{\Omega} \mathcal{L}^* \bar{w}(\mathbf{x}) v'(\mathbf{x}) d\Omega = \int_{\Omega} \bar{w}(\mathbf{x}) f(\mathbf{x}) d\Omega, \quad (4.16)$$

where

$$v'(\mathbf{x}) = \int_{\Omega} g'(\mathbf{x}, \mathbf{y}) (\mathcal{L} \bar{v} - f)(\mathbf{y}) d\Omega, \quad (4.17)$$

\mathcal{L}^* is the adjoint of \mathcal{L} , and the above integrals are interpreted in the sense of distributions. $g'(\mathbf{x}, \mathbf{y})$ in (4.17) is the small-scale Green's function, which in direct analogy with (4.7), takes on the following definition

$$\begin{aligned} g'(\mathbf{x}, \mathbf{y}) = g(\mathbf{x}, \mathbf{y}) - & \left[\int_{\Omega} g(\mathbf{x}, \tilde{\mathbf{y}}) \mu_1(\tilde{\mathbf{y}}) d\tilde{\mathbf{y}} \quad \dots \quad \int_{\Omega} g(\mathbf{x}, \tilde{\mathbf{y}}) \mu_N(\tilde{\mathbf{y}}) d\tilde{\mathbf{y}} \right] \\ & \times \left[\begin{array}{ccc} \int_{\Omega \times \Omega} g(\tilde{\mathbf{x}}, \tilde{\mathbf{y}}) \mu_1(\tilde{\mathbf{x}}) \mu_1(\tilde{\mathbf{y}}) d\tilde{\mathbf{x}} d\tilde{\mathbf{y}} & \dots & \int_{\Omega \times \Omega} g(\tilde{\mathbf{x}}, \tilde{\mathbf{y}}) \mu_1(\tilde{\mathbf{x}}) \mu_N(\tilde{\mathbf{y}}) d\tilde{\mathbf{x}} d\tilde{\mathbf{y}} \\ \vdots & \ddots & \vdots \\ \int_{\Omega \times \Omega} g(\tilde{\mathbf{x}}, \tilde{\mathbf{y}}) \mu_N(\tilde{\mathbf{x}}) \mu_1(\tilde{\mathbf{y}}) d\tilde{\mathbf{x}} d\tilde{\mathbf{y}} & \dots & \int_{\Omega \times \Omega} g(\tilde{\mathbf{x}}, \tilde{\mathbf{y}}) \mu_N(\tilde{\mathbf{x}}) \mu_N(\tilde{\mathbf{y}}) d\tilde{\mathbf{x}} d\tilde{\mathbf{y}} \end{array} \right]^{-1} \\ & \times \left[\begin{array}{c} \int_{\Omega} g(\tilde{\mathbf{x}}, \mathbf{y}) \mu_1(\tilde{\mathbf{x}}) d\tilde{\mathbf{x}} \\ \vdots \\ \int_{\Omega} g(\tilde{\mathbf{x}}, \mathbf{y}) \mu_N(\tilde{\mathbf{x}}) d\tilde{\mathbf{x}} \end{array} \right]. \end{aligned} \quad (4.18)$$

Small-scale Green's function in (4.18) depends on the full Green's function for the continuous problem as well as on the functionals μ_i , which define the relationship between the solution of the continuous problem and its discrete counterpart. As a result, different numerical methods are obtained for different choices of the linear projector \mathcal{P} . Dependence on the particular discretization is also reflected in μ_i 's.

It is argued in Hughes and Sangalli [54] that while $g(\mathbf{x}, \mathbf{y})$ is globally supported over $\Omega \times \Omega$, $g'(\mathbf{x}, \mathbf{y})$ is highly localized for the right choice of the projector. The latter property opens the door for the design of efficient numerical methods which deliver near optimal discrete solutions. Indeed,

inserting (4.17) into (4.16), one obtains the formulation: Find $\bar{v} \in \bar{V}$ such that $\forall \bar{w} \in \bar{V}$

$$B(\bar{w}, \bar{v}) - \int_{\Omega \times \Omega} \mathcal{L}^* \bar{w}(\mathbf{x}) g'(\mathbf{x}, \mathbf{y}) \mathcal{L} \bar{v}(\mathbf{y}) d\mathbf{x} d\mathbf{y} = \int_{\Omega} \bar{w}(\mathbf{x}) f(\mathbf{x}) d\Omega - \int_{\Omega \times \Omega} \mathcal{L}^* \bar{w}(\mathbf{x}) g'(\mathbf{x}, \mathbf{y}) f(\mathbf{y}) d\mathbf{x} d\mathbf{y}. \quad (4.19)$$

Localization property of the small-scale Green's function implies that integrals over $\Omega \times \Omega$ may be restricted to much smaller subdomains, and are conducive to efficient implementations.

For the case of a 1-D steady advection-diffusion equation, if one approximates the solution with C^0 -continuous finite elements and demands H^1 optimality of the discrete solution with respect to its continuous counterpart, integrals over $\Omega \times \Omega$ reduce to the sum of the integrals over $\Omega_e \times \Omega_e$, where Ω_e is an individual element. Furthermore, only moments of g' are required as the element-level residuals reside in polynomial spaces. For the case of linear elements and element-wise constant forcing, average of the element-level Green's function is sufficient to obtain an H^1 -optimal method, which is SUPG [12]. The situation is different in multi-dimensions. Since fine scales are not confined to element interiors, support of g' escapes $\Omega_e \times \Omega_e$. Moments of element-level Green's function are no longer enough to construct an H^1 -optimal method and one needs to resort to approximation. One such approximation embodies a family of well-known stabilized methods, which mimic the structure of the VMS formulation by replacing (4.19) with: Find $\bar{v} \in \bar{V}$ such that $\forall \bar{w} \in \bar{V}$

$$B(\bar{w}, \bar{v}) - \sum_e \int_{\Omega_e} \mathcal{L}^* \bar{w}(\mathbf{x}) \tau(\mathbf{x}) \mathcal{L} \bar{v}(\mathbf{x}) d\mathbf{x} = \int_{\Omega} \bar{w}(\mathbf{x}) f(\mathbf{x}) d\Omega - \sum_e \int_{\Omega_e} \mathcal{L}^* \bar{w}(\mathbf{x}) \tau(\mathbf{x}) f(\mathbf{x}) d\mathbf{x}, \quad (4.20)$$

where an element-wise function $\tau(\mathbf{x})$ is a stabilization parameter that reflects the properties of the small-scale Green's function. Despite their simplicity, stabilized methods perform remarkably well for incompressible and advection-dominated phenomena as can be inferred from the previous chapter. This is a direct consequence of the localization property of the fine-scale Green's function. Stabilized methods of the form (4.20) can also be viewed as VMS methods with local algebraic approximations to the fine scales. Namely,

$$v'(\mathbf{x}) = \int_{\Omega} g'(\mathbf{x}, \mathbf{y}) (\mathcal{L} \bar{v} - f)(\mathbf{y}) d\Omega \approx \tau(\mathbf{x}) (\mathcal{L} \bar{v} - f)(\mathbf{x}). \quad (4.21)$$

This approximation will be employed in the next section in which we derive a class of residual-based turbulence models based on the VMS approach.

4.2 Theoretical formulation of residual-based turbulence modeling

In this section we present the theoretical formulation of the the variationally consistent residual-based turbulence model. We begin with the incompressible Navier-Stokes problem posed over continuous spaces and apply the VMS methodology in order to derive a class of residual-based turbulence models. Time dependent, incompressible Navier-Stokes partial differential equations are taken as a departure point for the upcoming developments. It is believed that a suitable class of weak solutions of INS are in fact turbulent solutions. For the purposes of the numerical treatment of INS, existence and sufficient regularity of solutions is assumed a priori. For details of the mathematical theory of the INS the reader is referred to Foias *et al.* [29], and references therein.

4.2.1 Continuous formulation of incompressible Navier-Stokes equations

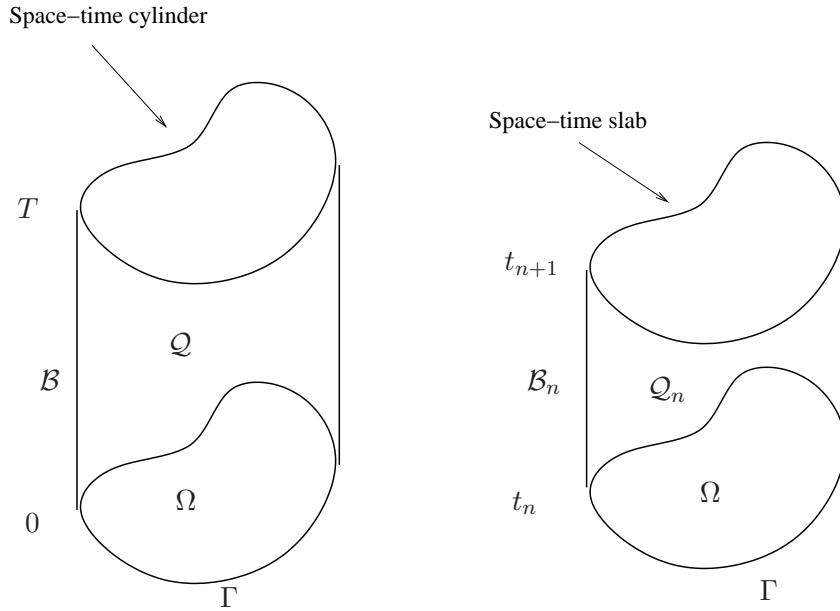


Figure 4.1: A graphical depiction of a space-time cylinder and a space-time slab.

Let $\Omega \in \mathbb{R}^d$ be the physical domain of the problem, $\Gamma = \partial\Omega$ is its boundary and $(0, T)$ is a time interval of interest. Let $\mathcal{Q} = \Omega \times (0, T)$ be the space-time cylinder obtained by extruding the spatial domain Ω along the time axis, and $\mathcal{B} = \Gamma \times (0, T)$ be its lateral boundary. Let $(0, T)$ be decomposed into n_{\max} time intervals such that $(0, T) = \cup_{n=1}^{n=n_{\max}} (t_n, t_{n+1})$. As a result \mathcal{Q} is decomposed into space-time slabs $\mathcal{Q}_n = \Omega \times (t_n, t_{n+1})$, with lateral boundaries $\mathcal{B}_n = \Gamma \times (t_n, t_{n+1})$, where $n = 1, \dots, n_{\max}$. For an illustration of these concepts see Figure 4.1.

Incompressible Navier-Stokes equations in the weak or variational form on the space-time slab n are stated as: Find a velocity-pressure pair $\mathbf{V} = (\mathbf{v}, p) \in \mathcal{V}_n, \mathbf{v} = \mathbf{0}$ on \mathcal{B}_n , such that $\forall \mathbf{W} = (\mathbf{w}, q) \in \mathcal{V}_n, \mathbf{w} = \mathbf{0}$ on \mathcal{B}_n

$$B_n(\mathbf{W}, \mathbf{V}) = F_n(\mathbf{W}) \quad (4.22)$$

where $B_n(\cdot, \cdot)$ is a semi-linear form and $F_n(\cdot)$ is a linear functional defined as

$$\begin{aligned} B_n(\mathbf{W}, \mathbf{V}) &= \left(-\frac{\partial \mathbf{w}}{\partial t}, \rho \mathbf{v}\right)_{\mathcal{Q}_n} + (\mathbf{w}(t_{n+1}^-), \rho \mathbf{v}(t_{n+1}^-))_{\Omega} \\ &- (\nabla^s \mathbf{w}, \rho \mathbf{v} \otimes \mathbf{v} + p \mathbf{I} - \mu \nabla^s \mathbf{v})_{\mathcal{Q}_n} + (q, \nabla \cdot \mathbf{v})_{\mathcal{Q}_n} \end{aligned} \quad (4.23)$$

and

$$F_n(\mathbf{W}) = (\mathbf{w}, \rho \mathbf{f})_{\mathcal{Q}_n} - (\mathbf{w}(t_n^+), \rho \mathbf{v}(t_n^-)). \quad (4.24)$$

In the above equations $\nabla^s(\cdot) = \frac{1}{2}(\nabla(\cdot) + \nabla(\cdot)^T)$ is the symmetric gradient, (\cdot, \cdot) is the L^2 inner product, $\mathbf{f} : \Omega \rightarrow \mathbb{R}^d$ is the body force per unit mass, \mathbf{I} is the identity tensor, and ρ and μ are the density and viscosity of the fluid. Of particular interest is the case of smaller μ that generates “turbulent” solutions, that is, solutions possessing a wide range of spatial and temporal scales. Quantity $\mathbf{v}(t_n^\pm)$ is defined in a standard way as

$$\mathbf{v}(t_n^\pm) = \lim_{\epsilon \rightarrow 0} \mathbf{v}(t_n \pm \epsilon). \quad (4.25)$$

Variational equations (4.22-4.24) imply satisfaction of linear momentum, incompressibility constraint, and initial conditions, namely

$$\mathcal{L}(\mathbf{v}, p) - \rho \mathbf{f} = \mathbf{0} \quad \text{on } \mathcal{Q}_n, \quad (4.26)$$

$$\nabla \cdot \mathbf{v} = 0 \quad \text{on } \mathcal{Q}_n, \quad (4.27)$$

$$\mathbf{v}(t_n^+) - \mathbf{v}(t_n^-) = \mathbf{0} \quad \text{on } \Omega, \quad (4.28)$$

where

$$\mathcal{L}(\mathbf{v}, p) = \rho \frac{\partial \mathbf{v}}{\partial t} + \rho \nabla \cdot (\mathbf{v} \otimes \mathbf{v}) + \nabla p - \nabla \cdot (2\mu \nabla^s \mathbf{v}). \quad (4.29)$$

We also introduce the “advective” form of the above operator

$$\mathcal{L}_{adv}(\mathbf{v}, p) = \rho \frac{\partial \mathbf{v}}{\partial t} + \rho \mathbf{v} \cdot \nabla \mathbf{v} + \nabla p - \mu \Delta \mathbf{v}. \quad (4.30)$$

It is obtained from (4.29) by using the incompressibility constraint in the advective and the viscous stress terms.

Remark 4.2.1. Typically one takes the velocity-pressure function space $\mathcal{V}_n = \mathcal{V}_{n,u} \times \mathcal{V}_{n,p}$, where $\mathcal{V}_{n,u} = H^1(H_0^1(\Omega)^d, (t_n, t_{n+1}))$ and $\mathcal{V}_{n,p} = L^2(L_0^2(\Omega), (t_n, t_{n+1}))$. $L_0^2(\Omega)$ is the space L^2 functions with zero integral average. No-slip boundary conditions imposed on the space of velocities are not necessary for the upcoming developments, the choice was made in the interest of simplicity.

Remark 4.2.2. In the above the INS equations are formulated on a space-time slab, and global in time solutions are defined recursively, that is, problem (4.22) is solved on the n^{th} time slab with the initial condition, imposed weakly, coming from the $n - 1^{\text{st}}$ time slab. Index n is then incremented and the procedure repeats. This variational formulation is non-standard, it is given here so as to elucidate the upcoming developments.

4.2.2 Decomposition of spaces

We define a linear projector $\mathcal{P} = \{\mathcal{P}_v, \mathcal{P}_p\}$ as

$$(\bar{\mathbf{W}}, \mathcal{P}\mathbf{V}) = (\bar{\mathbf{W}}, \mathbf{V}) \quad \forall \bar{\mathbf{W}} \in \bar{\mathcal{V}}_n, \mathbf{V} \in \mathcal{V}_n, \quad (4.31)$$

where (\cdot, \cdot) is a scalar product on \mathcal{V}_n , not necessarily norm-inducing, and

$$(\bar{\mathbf{W}}, \mathcal{P}\mathbf{V}) = (\bar{\mathbf{w}}, \mathcal{P}_v \mathbf{v})_v + (\bar{q}, \mathcal{P}_p p)_p \quad \forall \{\bar{\mathbf{w}}, \bar{q}\} \in \bar{\mathcal{V}}_n, \{\mathbf{v}, p\} \in \mathcal{V}_n \quad (4.32)$$

In (4.32), \mathcal{P}_v and \mathcal{P}_p are the velocity and pressure projectors, and $(\cdot, \cdot)_v$ and $(\cdot, \cdot)_p$ are scalar products on the spaces of velocity and pressure functions. We take the space of coarse scales $\bar{\mathcal{V}}_n$ to be a finite-dimensional subspace of \mathcal{V}_n . As before, the space \mathcal{V}_n admits a decomposition

$$\mathcal{V}_n = \bar{\mathcal{V}}_n \otimes \mathcal{V}'_n, \quad (4.33)$$

where the space of fine scales \mathcal{V}'_n , infinite-dimensional, is the orthogonal complement of $\bar{\mathcal{V}}_n$ in \mathcal{V}_n with respect to the scalar product (\cdot, \cdot) . Decomposition (4.33) splits the problem (4.22) into two sub-problems: Find $\bar{\mathbf{V}} \in \bar{\mathcal{V}}_n, \mathbf{V}' \in \mathcal{V}'_n$, such that

$$B_n(\bar{\mathbf{W}}, \bar{\mathbf{V}} + \mathbf{V}') = F_n(\bar{\mathbf{W}}) \quad \forall \bar{\mathbf{W}} \in \bar{\mathcal{V}}_n, \quad (4.34)$$

and

$$B_n(\mathbf{W}', \bar{\mathbf{V}} + \mathbf{V}') = F_n(\mathbf{W}') \quad \forall \mathbf{W}' \in \mathcal{V}'_n. \quad (4.35)$$

Equations (4.34) are known as the coarse-scale problem, while equations (4.35) define the fine-scale problem. In what follows, we will approximately solve the fine-scale problem for \mathbf{V}' in terms of residual quantities involving $\bar{\mathbf{V}}$. We will then introduce the result into the coarse-scale equations, which depend on the fine-scales \mathbf{V}' . As a result, we will obtain a method which only involves the coarse scales. This approach will yield a class of residual-based discrete formulations for incompressible fluid flow, which are also considered to be models of turbulence in this work.

4.2.3 The fine-scale problem

Equation (4.35) may be rewritten in the following form: Find $\{\mathbf{v}', p'\} \in \mathcal{V}'_n$ such that $\forall \{\mathbf{w}', q'\} \in \mathcal{V}'_n$

$$\begin{aligned} & \langle \mathbf{w}', \mathcal{N}_{\bar{\mathbf{v}}}(\mathbf{v}') + \nabla p' \rangle_{\mathcal{Q}_n} + \langle q', \nabla \cdot \mathbf{v}' \rangle_{\mathcal{Q}_n} \\ & = - \langle \mathbf{w}', \mathbf{r}_M \rangle_{\mathcal{Q}_n} - \langle q', r_C \rangle_{\mathcal{Q}_n}, \end{aligned} \quad (4.36)$$

where

$$\begin{aligned} \langle \mathbf{w}', \mathcal{N}_{\bar{\mathbf{v}}}(\mathbf{v}') + \nabla p' \rangle_{\mathcal{Q}_n} &= (\mathbf{w}', \mathcal{N}_{\bar{\mathbf{v}}}(\mathbf{v}') + \nabla p')_{\tilde{\mathcal{Q}}_n} \\ &+ (\mathbf{w}', \llbracket 2\mu \nabla^s \mathbf{v}' \cdot \mathbf{n} \rrbracket)_{\tilde{\mathcal{P}}_n \setminus \mathcal{P}_n} + (\mathbf{w}'(t_n^+), \rho \mathbf{v}'(t_n^+))_{\Omega}, \end{aligned} \quad (4.37)$$

$$\begin{aligned} \langle \mathbf{w}', \mathbf{r}_M \rangle_{\mathcal{Q}_n} &= (\mathbf{w}', \mathcal{L}_{adv}(\bar{\mathbf{v}}, \bar{p}) - \rho \mathbf{f})_{\tilde{\mathcal{Q}}_n} \\ &+ (\mathbf{w}', \llbracket 2\mu \nabla^s \bar{\mathbf{v}} \cdot \mathbf{n} \rrbracket)_{\tilde{\mathcal{P}}_n \setminus \mathcal{P}_n} + (\mathbf{w}'(t_n^+), \rho(\bar{\mathbf{v}}(t_n^+) - \mathbf{v}(t_n^-)))_{\Omega}, \end{aligned} \quad (4.38)$$

$$\langle q', \nabla \cdot \mathbf{v}' \rangle_{\mathcal{Q}_n} = (q', \nabla \cdot \mathbf{v}')_{\tilde{\mathcal{Q}}_n}, \quad (4.39)$$

$$\langle q', r_C \rangle_{\mathcal{Q}_n} = (q', \nabla \cdot \bar{\mathbf{v}})_{\tilde{\mathcal{Q}}_n}. \quad (4.40)$$

\mathbf{r}_M and r_C are generalized momentum and continuity residuals, and $\mathcal{N}_{\bar{\mathbf{v}}}(\mathbf{v}')$, defined as

$$\mathcal{N}_{\bar{\mathbf{v}}}(\mathbf{v}') = \rho \frac{\partial \mathbf{v}'}{\partial t} + \rho \bar{\mathbf{v}} \cdot \nabla \mathbf{v}' + \rho \mathbf{v}' \cdot \nabla \bar{\mathbf{v}} + \rho \mathbf{v}' \cdot \nabla \mathbf{v}' - \mu \Delta \mathbf{v}', \quad (4.41)$$

is a nonlinear advection-diffusion-reaction operator with coefficients that depend on the coarse-scale solution. Generalized momentum and continuity residuals contain the Navier-Stokes PDE residual on element interiors, the viscous flux jump on element boundaries, and the residual of the initial condition at the bottom of the space-time slab. It is assumed that the space of coarse-scale functions

are of class C^0 . Note that if the continuity of the coarse scales is C^1 or greater, the viscous flux jump term is not present in the definition of the momentum residual.

4.2.4 Derivation of the fine-scale model

Small-scale equations (4.36) are posed over the space of fine scales \mathcal{V}'_n . The space \mathcal{V}'_n is a subspace of \mathcal{V}_n possessing the following characterization:

$$\{\mathbf{v}, p\} \in \mathcal{V}'_n \iff \{\mathcal{P}_v \mathbf{v} = \mathbf{0}, \mathcal{P}_p p = 0\}, \quad (4.42)$$

that is, $\mathcal{V}'_n \in \text{Ker } \mathcal{P}$. As a result, the small-scale equations may be thought of as being posed over a constrained subspace of \mathcal{V}_n . The fine-scale problem may be restated over the full space \mathcal{V}_n with the aid of a Lagrange multiplier approach. Introducing a pair of Lagrange multipliers $\{\boldsymbol{\lambda}_v, \lambda_p\} \in \bar{\mathcal{V}}_n^*$, the dual space of $\bar{\mathcal{V}}_n$, we get the following variational formulation: Find $\{\mathbf{v}', p'\} \in \mathcal{V}_n$, $\{\boldsymbol{\lambda}_v, \lambda_p\} \in \bar{\mathcal{V}}_n^*$, such that $\forall \{\mathbf{w}, q\} \in \mathcal{V}_n$ and $\forall \{\boldsymbol{\mu}_v, \mu_p\} \in \bar{\mathcal{V}}_n^*$

$$\langle \mathbf{w}, \mathcal{N}_{\bar{\mathbf{v}}}(\mathbf{v}') + \nabla p' \rangle_{\mathcal{Q}_n} - \langle \mathcal{P}_v \mathbf{w}, \boldsymbol{\lambda}_v \rangle = - \langle \mathbf{w}, \mathbf{r}_M \rangle_{\mathcal{Q}_n}, \quad (4.43)$$

$$\langle q, \nabla \cdot \mathbf{v}' \rangle_{\mathcal{Q}_n} - \langle \mathcal{P}_p q, \lambda_p \rangle = - \langle q, r_C \rangle_{\mathcal{Q}_n}, \quad (4.44)$$

$$\langle \boldsymbol{\mu}_v, \mathcal{P}_v \mathbf{v}' \rangle = 0, \quad (4.45)$$

$$\langle \mu_p, \mathcal{P}_p p' \rangle = 0. \quad (4.46)$$

In the strong form the above equations are

$$\mathcal{N}_{\bar{\mathbf{v}}}(\mathbf{v}') + \nabla p' - \mathcal{P}_v^T \boldsymbol{\lambda}_v = -\mathbf{r}_M, \quad (4.47)$$

$$\nabla \cdot \mathbf{v}' - \mathcal{P}_p^T \lambda_p = -r_C, \quad (4.48)$$

$$\mathcal{P}_v \mathbf{v}' = \mathbf{0}, \quad (4.49)$$

$$\mathcal{P}_p p' = 0 \quad (4.50)$$

We are going to formally obtain a solution to the above system of PDEs by making use of Green's operators. For this purpose we replace $\mathcal{N}_{\bar{\mathbf{v}}}$ with its linear counterpart $\tilde{\mathcal{N}}_{\bar{\mathbf{v}}}$ by removing the quadratic term, that is

$$\tilde{\mathcal{N}}_{\bar{\mathbf{v}}}(\mathbf{v}') = \rho \frac{\partial \mathbf{v}'}{\partial t} + \rho \bar{\mathbf{v}} \cdot \nabla \mathbf{v}' + \rho \mathbf{v}' \cdot \nabla \bar{\mathbf{v}} - \mu \Delta \mathbf{v}'. \quad (4.51)$$

This is not a bad assumption provided the fine scales are “small”. One way to retain the quadratic term is to expand \mathbf{v}' in perturbation series as shown in Calo [14]. The latter also requires smallness assumption on the fine scales.

The new fine scale momentum equation (4.47) now reads

$$\tilde{\mathcal{N}}_{\tilde{\mathbf{v}}}(\mathbf{v}') + \nabla p' - \mathcal{P}_v^T \boldsymbol{\lambda}_v = -\mathbf{r}_M \quad (4.52)$$

Denoting by \mathcal{G}_v the Green's operator for $\tilde{\mathcal{N}}_{\tilde{\mathbf{v}}}$, equation (4.52) implies

$$\mathbf{v}' + \mathcal{G}_v \nabla p' - \mathcal{G}_v \mathcal{P}_v^T \boldsymbol{\lambda}_v = -\mathcal{G}_v \mathbf{r}_M. \quad (4.53)$$

applying \mathcal{P}_v to the above equation, using (4.49), and solving for $\boldsymbol{\lambda}_v$, we obtain

$$\boldsymbol{\lambda}_v = (\mathcal{P}_v \mathcal{G}_v \mathcal{P}_v^T)^{-1} (\mathcal{P}_v \mathcal{G}_v \mathbf{r}_M + \mathcal{P}_v \mathcal{G}_v \nabla p'). \quad (4.54)$$

Inserting $\boldsymbol{\lambda}_v$ back into (4.53), yields

$$\mathbf{v}' + \mathcal{G}'_v \nabla p' = -\mathcal{G}'_v \mathbf{r}_M, \quad (4.55)$$

where

$$\mathcal{G}'_v = \mathcal{G}_v - \mathcal{G}_v \mathcal{P}_v^T (\mathcal{P}_v \mathcal{G}_v \mathcal{P}_v^T)^{-1} \mathcal{P}_v \mathcal{G}_v \quad (4.56)$$

is now a small-scale Green's operator for $\tilde{\mathcal{N}}_{\tilde{\mathbf{v}}}$ and \mathcal{P}_v . The above expression is form-identical to (4.5). Note that according to (4.55) the small-scale velocity is driven by the momentum residual of large scales as well as the fine-scale pressure gradient. In order to obtain the expression for p' , we apply the divergence operator to (4.55) and make use of (4.48) to obtain

$$\nabla \cdot \mathcal{G}'_v \nabla p' = r_C - \nabla \cdot \mathcal{G}'_v \mathbf{r}_M - \mathcal{P}_p^T \lambda_p. \quad (4.57)$$

Operator $\nabla \cdot \mathcal{G}'_v \nabla$ in the above equation may be thought of as a Shur complement of the small-scale constrained problem. Denoting by \mathcal{S} its inverse ($\mathcal{S} = (\nabla \cdot \mathcal{G}'_v \nabla)^{-1}$), we solve for small-scale pressure as

$$p' = \mathcal{S}(r_C - \nabla \cdot \mathcal{G}'_v \mathbf{r}_M - \mathcal{P}_p^T \lambda_p). \quad (4.58)$$

Applying \mathcal{P}_p to the above equation, making use of (4.50), and solving for λ_p , we get

$$\lambda_p = (\mathcal{P}_p \mathcal{S} \mathcal{P}_p^T)^{-1} \mathcal{P}_p \mathcal{S}(r_C - \nabla \cdot \mathcal{G}'_v \mathbf{r}_M). \quad (4.59)$$

Inserting λ_p from (4.59) into the fine-scale pressure equation (4.58) we obtain

$$p' = \mathcal{S}' r_C - \mathcal{S}' \nabla \cdot \mathcal{G}'_v \mathbf{r}_M, \quad (4.60)$$

where

$$\mathcal{S}' = \mathcal{S} - \mathcal{S} \mathcal{P}_p^T (\mathcal{P}_p \mathcal{S} \mathcal{P}_p^T)^{-1} \mathcal{P}_p \mathcal{S} \quad (4.61)$$

is now a small-scale Green's operator for the pressure. Note that it is also form-identical to (4.5). Combining (4.55) with (4.60) gives the following solution to the fine scale equations

$$\begin{bmatrix} \mathbf{v}' \\ p' \end{bmatrix} = \begin{bmatrix} -\tilde{\mathcal{G}}'_v & -\mathcal{G}'_v \nabla \mathcal{S}' \\ -\mathcal{S}' \nabla \cdot \mathcal{G}'_v & \mathcal{S}' \end{bmatrix} \begin{bmatrix} \mathbf{r}_M \\ r_C \end{bmatrix}, \quad (4.62)$$

with

$$\tilde{\mathcal{G}}'_v = \mathcal{G}'_v - \mathcal{G}'_v \nabla \mathcal{S}' \nabla \cdot \mathcal{G}'_v. \quad (4.63)$$

The second term on the right hand side of the above expression reflects the fine-scale divergence constraint.

Remark 4.2.3. *Note that (4.62) involves only small-scale Green's operators. The corresponding small-scale Green's functions are expected to be highly attenuated, which justifies the use of local residual-based models for the fine scales.*

4.2.5 The coarse-scale problem

Equation (4.34) defines the coarse-scale problem. Direct manipulation of (4.34), assuming the space $\bar{\mathcal{V}}$ is comprised of functions that are at least C^0 —continuous across element boundaries, gives the following formulation of the coarse-scale problem: Find $\{\bar{\mathbf{v}}, \bar{p}\} \in \bar{\mathcal{V}}_n$, such that $\forall \{\bar{\mathbf{w}}, \bar{q}\} \in \bar{\mathcal{V}}_n$

$$\begin{aligned} B_n(\bar{\mathbf{W}}, \bar{\mathbf{V}}) - F_n(\bar{\mathbf{W}}) \\ + \langle \mathcal{L}^*(\bar{\mathbf{w}}, \bar{q}), \mathbf{v}' \rangle_{\mathcal{Q}_n} - (\nabla \cdot \bar{\mathbf{w}}, p')_{\tilde{\mathcal{Q}}_n} \\ - (\rho \bar{\mathbf{v}} \cdot \nabla \bar{\mathbf{w}}^T, \mathbf{v}')_{\tilde{\mathcal{Q}}_n} - (\rho \nabla^s \bar{\mathbf{w}}, \mathbf{v}' \otimes \mathbf{v}')_{\tilde{\mathcal{Q}}_n} = 0 \end{aligned} \quad (4.64)$$

where the third term on the left-hand-side is

$$\begin{aligned} \langle \mathcal{L}^*(\bar{\mathbf{w}}, \bar{q}), \mathbf{v}' \rangle_{\mathcal{Q}_n} = & (-\rho \frac{\partial \bar{\mathbf{w}}}{\partial t} - \rho \bar{\mathbf{v}} \cdot \nabla \bar{\mathbf{w}} - \nabla \bar{q} - \nabla \cdot 2\mu \nabla^s \bar{\mathbf{w}}, \mathbf{v}')_{\tilde{\mathcal{Q}}_n} \\ & + (\llbracket 2\mu \nabla^s \bar{\mathbf{w}} \cdot \mathbf{n} \rrbracket, \mathbf{v}')_{\tilde{\mathcal{P}}_n \setminus \mathcal{P}_n} + (\rho \bar{\mathbf{w}}(t_{n+1}^-), \mathbf{v}'(t_{n+1}^-))_{\Omega}. \end{aligned} \quad (4.65)$$

The above variational form precisely indicates the manner in which unresolved components of the solution influence the large scales.

Remark 4.2.4. *The first two terms on the left-hand-side of (4.64) correspond to the Galerkin part of the formulation. Terms three and five of (4.64) may be identified with the so-called cross stresses, while term six represents the Reynolds stress in the language of classical turbulence modeling.*

Introducing fine-scales (4.62) into the coarse-scale system (4.64), we obtain the formulation: Find $\{\bar{\mathbf{v}}, \bar{p}\} \in \bar{\mathcal{V}}_n$ such that $\forall \{\bar{\mathbf{w}}, \bar{q}\} \in \bar{\mathcal{V}}_n$

$$\begin{aligned} & B_n(\bar{\mathbf{W}}, \bar{\mathbf{V}}) - F_n(\bar{\mathbf{W}}) - \langle \mathcal{L}^*(\bar{\mathbf{w}}, \bar{q}), \tilde{\mathcal{G}}'_v \mathbf{r}_M \rangle_{\mathcal{Q}_n} - \langle \mathcal{L}^*(\bar{\mathbf{w}}, \bar{q}), \mathcal{G}'_v \nabla \mathcal{S}' r_C \rangle_{\mathcal{Q}_n} \\ & + (\nabla \cdot \bar{\mathbf{w}}, \mathcal{S}' \nabla \cdot \mathcal{G}'_v \mathbf{r}_M)_{\tilde{\mathcal{Q}}_n} - (\nabla \cdot \bar{\mathbf{w}}, \mathcal{S}' r_C)_{\tilde{\mathcal{Q}}_n} + (\rho \bar{\mathbf{v}} \cdot \nabla \bar{\mathbf{w}}^T, \tilde{\mathcal{G}}'_v \mathbf{r}_M + \mathcal{G}'_v \nabla \mathcal{S}' r_C)_{\tilde{\mathcal{Q}}_n} \\ & - (\rho \nabla^s \bar{\mathbf{w}}, \{\tilde{\mathcal{G}}'_v \mathbf{r}_M + \mathcal{G}'_v \nabla \mathcal{S}' r_C\} \otimes \{\tilde{\mathcal{G}}'_v \mathbf{r}_M + \mathcal{G}'_v \nabla \mathcal{S}' r_C\})_{\tilde{\mathcal{Q}}_n} = 0. \end{aligned} \quad (4.66)$$

4.2.6 Approximate closures and connection with stabilized methods

Fine scale equations (4.62) appear to be just as complex as the original Navier-Stokes system. Solving them exactly is not a viable option, hence modeling is necessary. For this purpose let (\mathbf{x}, t) , $\mathbf{x} = \{x_\alpha\}_{\alpha=1}^d$, denote the coordinates of a physical space-time element $K \times (t_n, t_{n+1})$, and let $(\boldsymbol{\xi}, \theta)$, $\boldsymbol{\xi} = \{\xi_\alpha\}_{\alpha=1}^d$, denote the coordinates of a parent space-time element $\hat{K} \times (-1, 1)$. Here θ is non-dimensional time. Let $\pi : \hat{K} \rightarrow K$ be a bijection, and let $(-1, 1)$ map onto (t_n, t_{n+1}) by a simple linear mapping.

We will first give an approximation of the action of \mathcal{G}'_v , the small-scale Green's operator for $\tilde{\mathcal{N}}_{\bar{\mathbf{v}}}$, defined in (4.51), and the projector \mathcal{P}_v , on the momentum residual. We assume the following local algebraic model:

$$\mathcal{G}'_v \mathbf{r}_M \approx \boldsymbol{\tau}_M (\mathcal{L}_{adv}(\bar{\mathbf{v}}, \bar{p}) - \rho \mathbf{f}) \text{ on } \tilde{\mathcal{Q}}_n. \quad (4.67)$$

In the above, $\boldsymbol{\tau}_M$ is a $d \times d$ matrix defined as

$$\begin{aligned} \boldsymbol{\tau}_M = & \frac{1}{\rho} \left(\left(\frac{\partial \theta}{\partial t} \right)^2 + \bar{\mathbf{v}}^T \frac{\partial \boldsymbol{\xi}^T}{\partial \mathbf{x}} \frac{\partial \boldsymbol{\xi}}{\partial \mathbf{x}} \bar{\mathbf{v}} + (C_I \frac{\mu}{\rho})^2 \left(\frac{\partial \boldsymbol{\xi}}{\partial \mathbf{x}} \frac{\partial \boldsymbol{\xi}^T}{\partial \mathbf{x}} \right) : \left(\frac{\partial \boldsymbol{\xi}}{\partial \mathbf{x}} \frac{\partial \boldsymbol{\xi}^T}{\partial \mathbf{x}} \right) \right) \mathbf{I} \\ & + \nabla^s \bar{\mathbf{v}} \cdot \nabla^s \bar{\mathbf{v}})^{-1/2}. \end{aligned} \quad (4.68)$$

This definition is inspired by the theory of stabilized methods for reactive-advective-diffusive systems (see, for example, Shakib, Hughes and Johan [88], Hughes and Mallet [47]). Matrix $\boldsymbol{\tau}_M$ is, by construction, symmetric and positive-definite. It incorporates the spatial and temporal scales of the discretization, as well as specific geometrical features by making use of local geometrical mappings.

Remark 4.2.5. Definition (4.68) is non-standard in that it includes the “reaction” contribution $\nabla^s \bar{\mathbf{v}} \cdot \nabla^s \bar{\mathbf{v}}$. This term is present due to the reactive component in the definition of $\tilde{\mathcal{N}}_{\bar{\mathbf{v}}}(\mathbf{v}')$. In contrast to (4.68), most current stabilized methods for incompressible Navier-Stokes equations make use of a simplified definition, which omits the reaction term and renders $\boldsymbol{\tau}_M$ isotropic (diagonal with identical entries), that is

$$\boldsymbol{\tau}_M = \tau_M \mathbf{I} = \frac{1}{\rho} \left\{ \left(\frac{\partial \theta}{\partial t} \right)^2 + \bar{\mathbf{v}}^T \frac{\partial \boldsymbol{\xi}^T}{\partial \mathbf{x}} \frac{\partial \boldsymbol{\xi}}{\partial \mathbf{x}} \bar{\mathbf{v}} + (C_I \frac{\mu}{\rho})^2 \left(\frac{\partial \boldsymbol{\xi}}{\partial \mathbf{x}} \frac{\partial \boldsymbol{\xi}^T}{\partial \mathbf{x}} \right) : \left(\frac{\partial \boldsymbol{\xi}}{\partial \mathbf{x}} \frac{\partial \boldsymbol{\xi}^T}{\partial \mathbf{x}} \right) \right\}^{-1/2} \mathbf{I} \quad (4.69)$$

We also define the local approximation to the gradient operator $\mathbf{g} \approx \nabla$ as

$$\mathbf{g} = \frac{\partial \boldsymbol{\xi}^T}{\partial \mathbf{x}} \mathbf{1}, \quad (4.70)$$

and the divergence operator as $\nabla \cdot \approx -\mathbf{g}^T$. Negative sign is used in order to preserve the transpose property of these operators at the discrete level. In (4.70) $\mathbf{1}$ is a d -dimensional vector of ones.

We approximate the inverse of the small-scale Shur complement operator \mathcal{S}' by a scalar τ_C as follows. Recall that $\mathcal{S} = (\nabla \cdot \mathcal{G}'_v \nabla)^{-1}$, thus, in light of the developments in this section, we define τ_C as

$$\tau_C = (\mathbf{g}^T \boldsymbol{\tau}_M \mathbf{g})^{-1}, \quad (4.71)$$

and the action of \mathcal{S}' on the generalized continuity residual is approximated via

$$\mathcal{S}' r_C \approx -\tau_C \nabla \cdot \bar{\mathbf{v}} \text{ on } \tilde{\mathcal{Q}}_n. \quad (4.72)$$

By virtue of $\boldsymbol{\tau}_M$ being positive-definite, $\tau_C > 0$ if $\|\mathbf{g}\| > 0$.

We approximate the action of $\tilde{\mathcal{G}}'_v = \mathcal{G}'_v - \mathcal{G}'_v \nabla \mathcal{S}' \nabla \cdot \mathcal{G}'_v$ on the generalized momentum residual as

$$\begin{aligned} \tilde{\mathcal{G}}'_v \mathbf{r}_M &\approx \boldsymbol{\tau}'_M (\mathcal{L}_{adv}(\bar{\mathbf{v}}, \bar{\mathbf{p}}) - \rho \mathbf{f}) \\ &= (\boldsymbol{\tau}_M - c_\tau \boldsymbol{\tau}_M \mathbf{g} \tau_C \mathbf{g}^T \boldsymbol{\tau}_M) (\mathcal{L}_{adv}(\bar{\mathbf{v}}, \bar{\mathbf{p}}) - \rho \mathbf{f}) \text{ on } \tilde{\mathcal{Q}}_n, \end{aligned} \quad (4.73)$$

where $0 \leq c_\tau < 1$. The strict inequality on the right renders $\boldsymbol{\tau}'_M$ positive definite, as will be shown later. The latter property is of crucial importance for the overall stability of the numerical method.

Finally, within the proposed framework, the “cross” terms $\mathcal{G}'_v \nabla \mathcal{S}' r_C$ and $\mathcal{S}' \nabla \cdot \mathcal{G}'_v \mathbf{r}_M$ engender the following approximations:

$$\mathcal{G}'_v \nabla \mathcal{S}' r_C \approx -\boldsymbol{\tau}_M \mathbf{g} \tau_C \nabla \cdot \bar{\mathbf{v}} \text{ on } \tilde{\mathcal{Q}}_n, \quad (4.74)$$

and

$$\mathcal{S}' \nabla \cdot \mathcal{G}'_v \mathbf{r}_M \approx \tau_C \mathbf{g}^T \boldsymbol{\tau}_M (\mathcal{L}_{adv}(\bar{\mathbf{v}}, \bar{p}) - \rho \mathbf{f}) \text{ on } \tilde{\mathcal{Q}}_n. \quad (4.75)$$

In summary, the following matrix-vector form, written in the spirit of (4.62), states a local algebraic relationship between fine-scales and residuals of the discrete system:

$$\begin{bmatrix} v' \\ p' \end{bmatrix} \approx \begin{bmatrix} -\boldsymbol{\tau}'_M & \boldsymbol{\tau}_M \mathbf{g} \tau_C \\ -\tau_C \mathbf{g}^T \boldsymbol{\tau}_M & -\tau_C \end{bmatrix} \begin{bmatrix} (\mathcal{L}_{adv}(\bar{\mathbf{v}}, \bar{p}) - \rho \mathbf{f}) \\ \nabla \cdot \bar{\mathbf{v}} \end{bmatrix} \text{ on } \tilde{\mathcal{Q}}_n, \quad (4.76)$$

with

$$\boldsymbol{\tau}'_M = \boldsymbol{\tau}_M - c_\tau \boldsymbol{\tau}_M \mathbf{g} \tau_C \mathbf{g}^T \boldsymbol{\tau}_M \quad (4.77)$$

Note that the model tightly couples the fine-scale velocity and pressure to both momentum and continuity residuals.

Combining (4.76) with the coarse scale variational equations (4.66) gives rise to the formulation of the residual-based turbulence model: Find $\bar{\mathbf{V}} \in \bar{\mathcal{V}}_n$ such that $\forall \bar{\mathbf{W}} \in \bar{\mathcal{V}}_n$

$$\begin{aligned} & B_n(\bar{\mathbf{W}}, \bar{\mathbf{V}})_n - F_n(\bar{\mathbf{W}}) \\ & - (\mathcal{L}^*(\bar{\mathbf{w}}, \bar{q}), \boldsymbol{\tau}'_M (\mathcal{L}_{adv}(\bar{\mathbf{v}}, \bar{p}) - \rho \mathbf{f}))_{\tilde{\mathcal{Q}}_n} - (\mathcal{L}^*(\bar{\mathbf{w}}, \bar{q}), [\boldsymbol{\tau}_M \mathbf{g} \tau_C] \nabla \cdot \bar{\mathbf{v}})_{\tilde{\mathcal{Q}}_n} \\ & + (\nabla \cdot \bar{\mathbf{w}}, [\tau_C \mathbf{g}^T \boldsymbol{\tau}_M] (\mathcal{L}_{adv}(\bar{\mathbf{v}}, \bar{p}) - \rho \mathbf{f}))_{\tilde{\mathcal{Q}}_n} + (\nabla \cdot \bar{\mathbf{w}}, \tau_C \nabla \cdot \bar{\mathbf{v}})_{\tilde{\mathcal{Q}}_n} \\ & + (\rho \bar{\mathbf{v}} \cdot \nabla \bar{\mathbf{w}}^T, \boldsymbol{\tau}'_M (\mathcal{L}_{adv}(\bar{\mathbf{v}}, \bar{p}) - \rho \mathbf{f}) - [\boldsymbol{\tau}_M \mathbf{g} \tau_C] \nabla \cdot \bar{\mathbf{v}})_{\tilde{\mathcal{Q}}_n} \\ & - (\rho \nabla^s \bar{\mathbf{w}}, (\boldsymbol{\tau}'_M (\mathcal{L}_{adv}(\bar{\mathbf{v}}, \bar{p}) - \rho \mathbf{f}) - [\boldsymbol{\tau}_M \mathbf{g} \tau_C] \nabla \cdot \bar{\mathbf{v}}) \\ & \quad \otimes (\boldsymbol{\tau}'_M (\mathcal{L}_{adv}(\bar{\mathbf{v}}, \bar{p}) - \rho \mathbf{f}) - [\boldsymbol{\tau}_M \mathbf{g} \tau_C] \nabla \cdot \bar{\mathbf{v}}))_{\tilde{\mathcal{Q}}_n} = 0. \end{aligned} \quad (4.78)$$

The above model encompasses a whole class of well-known discrete formulations for incompressible fluid flow. In what follows, we demonstrate that various simplifications to (4.76) and (4.78) reproduce existing methods that are well-accepted in the computational mechanics community. Assuming from the outset an element-wise divergence-free velocity field, that is $\nabla \cdot \bar{\mathbf{v}} = 0$, and replacing \mathcal{L}^* with $\rho \bar{\mathbf{v}} \cdot \nabla \bar{\mathbf{w}}$ as in SUPG, simplifies (4.78) to: Find $\bar{\mathbf{V}} \in \bar{\mathcal{V}}_n$ such that $\forall \bar{\mathbf{W}} \in \bar{\mathcal{V}}_n$

$$\begin{aligned} & B_n(\bar{\mathbf{W}}, \bar{\mathbf{V}})_n - F_n(\bar{\mathbf{W}}) \\ & + (\rho \bar{\mathbf{v}} \cdot (\nabla \bar{\mathbf{w}} + \nabla \bar{\mathbf{w}}^T), \boldsymbol{\tau}_M (\mathcal{L}_{adv}(\bar{\mathbf{v}}, \bar{p}) - \rho \mathbf{f}))_{\tilde{\mathcal{Q}}_n} \\ & - (\rho \nabla^s \bar{\mathbf{w}}, \boldsymbol{\tau}_M (\mathcal{L}_{adv}(\bar{\mathbf{v}}, \bar{p}) - \rho \mathbf{f}) \otimes \boldsymbol{\tau}_M (\mathcal{L}_{adv}(\bar{\mathbf{v}}, \bar{p}) - \rho \mathbf{f}))_{\tilde{\mathcal{Q}}_n} = 0. \end{aligned} \quad (4.79)$$

This formulation is given in Calo [14], where the concept of residual-based turbulence modeling was introduced.

One can extract a set of well-known stabilized methods for INS (see, for example Tezduyar and Sathe [101], Codina and Soto [17], and Tejada-Martinez and Jansen [98], as well as references therein) by omitting the last two terms from the left-hand-side of (4.78), and disregarding the “cross” terms, which represent coupling of momentum and continuity residuals in the model for the prime quantities (4.76). With these assumptions we obtain: Find $\bar{V} \in \bar{\mathcal{V}}_n$ such that $\forall \bar{W} \in \bar{\mathcal{V}}_n$

$$B_n(\bar{W}, \bar{V})_n - F_n(\bar{W}) - (\mathcal{L}^*(\bar{w}, \bar{q}), \tau_M(\mathcal{L}_{adv}(\bar{v}, \bar{p}) - \rho \mathbf{f}))_{\tilde{Q}_n} + (\nabla \cdot \bar{w}, \tau_C \nabla \cdot \bar{v})_{\tilde{Q}_n} = 0, \quad (4.80)$$

where τ_M is replaced by its diagonal counterpart $\tau_M \mathbf{I}$, and τ_C takes on alternative definitions, or is often omitted.

Formulations of type (4.80) are ad-hoc extensions of linear stabilized methods to incompressible Navier-Stokes equations, which are nonlinear. On the other hand, formulation (4.78), and its simplified version, (4.79), are a direct consequence of the VMS approach, which accounts for the nonlinearities present in the underlying PDEs. The latter is more consistent with the idea of turbulence modeling that attempts to account for the scales that are missing from the discretization step. Nevertheless, stabilized and residual-based formulations are very similar, and, in this light, stabilized methods can be considered as *partial* models of turbulent fluid flow.

The following lemma establishes symmetry and positivity property of τ'_M . The latter is of crucial importance for the stability of the discrete formulation (4.78).

Lemma 4.2.1. τ'_M is symmetric and positive-definite.

Proof. Symmetry of τ'_M is clear from definition (4.77) while its positivity is shown as follows. Consider the following orthogonal decomposition of \mathbb{R}^d :

$$\mathbb{R}^d = V \oplus V^\perp, \quad (4.81)$$

where

$$V = \{\mathbf{v} \mid \mathbf{v} = \mathbf{g}p, \forall p \in \mathbb{R}\}, \quad (4.82)$$

$$V^\perp = \{\mathbf{w} \mid (\mathbf{w}, \mathbf{v})_{\tau_M} = 0, \forall \mathbf{v} \in V\}, \quad (4.83)$$

where $(\mathbf{w}, \mathbf{v})_{\tau_M} = (\mathbf{w}, \tau_M \mathbf{v})_{l_2(\mathbb{R}^d)}$, is an inner-product on \mathbb{R}^d induced by τ_M . Then, any $\mathbf{v} \in \mathbb{R}^d$

may be decomposed into $\mathbf{v} = \mathbf{v}_1 + \mathbf{v}_2$, $\mathbf{v}_1 = \mathbf{g}p \in V$, $\mathbf{v}_2 \in V^\perp$ and

$$\begin{aligned}
\mathbf{v}^T \boldsymbol{\tau}'_M \mathbf{v} &= (\mathbf{v}_1 + \mathbf{v}_2)^T \boldsymbol{\tau}_M (\mathbf{v}_1 + \mathbf{v}_2) \\
&\quad - c_\tau (\mathbf{v}_1 + \mathbf{v}_2)^T \boldsymbol{\tau}_M \mathbf{g} \tau_C \mathbf{g}^T \boldsymbol{\tau}_M (\mathbf{v}_1 + \mathbf{v}_2) \\
&= \mathbf{v}_1^T \boldsymbol{\tau}_M \mathbf{v}_1 + \mathbf{v}_2^T \boldsymbol{\tau}_M \mathbf{v}_2 \\
&\quad - c_\tau (\mathbf{g}p)^T \boldsymbol{\tau}_M \mathbf{g} \tau_C \mathbf{g}^T \boldsymbol{\tau}_M (\mathbf{g}p + \mathbf{v}_2) \\
&\quad - c_\tau \mathbf{v}_2^T \boldsymbol{\tau}_M \mathbf{g} \tau_C \mathbf{g}^T \boldsymbol{\tau}_M (\mathbf{g}p + \mathbf{v}_2).
\end{aligned} \tag{4.84}$$

The term on the last line of (4.84) is identically zero, as $\mathbf{g} \tau_C \mathbf{g}^T \boldsymbol{\tau}_M (\mathbf{g}p + \mathbf{v}_2) \in V$. The term prior to it may be handled as

$$\begin{aligned}
c_\tau (\mathbf{g}p)^T \boldsymbol{\tau}_M \mathbf{g} \tau_C \mathbf{g}^T \boldsymbol{\tau}_M (\mathbf{g}p + \mathbf{v}_2) &= \\
c_\tau p (\mathbf{g}^T \boldsymbol{\tau}_M \mathbf{g}) (\mathbf{g}^T \boldsymbol{\tau}_M \mathbf{g})^{-1} \mathbf{g}^T \boldsymbol{\tau}_M (\mathbf{g}p + \mathbf{v}_2) &= \\
c_\tau (\mathbf{g}p)^T \boldsymbol{\tau}_M \mathbf{g}p + c_\tau (\mathbf{g}p)^T \boldsymbol{\tau}_M \mathbf{v}_2 &= c_\tau \mathbf{v}_1^T \boldsymbol{\tau}_M \mathbf{v}_1.
\end{aligned} \tag{4.85}$$

Thus, there exists $C > 0$ such that

$$\mathbf{v}^T \boldsymbol{\tau}'_M \mathbf{v} = (1 - c_\tau) \mathbf{v}_1^T \boldsymbol{\tau}_M \mathbf{v}_1 + \mathbf{v}_2^T \boldsymbol{\tau}_M \mathbf{v}_2 \geq C \|\mathbf{v}\|^2, \tag{4.86}$$

provided $0 \leq c_\tau < 1$. Positivity of $\boldsymbol{\tau}'_M$ is established. \square

4.3 Numerical examples

This section presents two turbulent fluid flow examples: a fully developed turbulent flow between two infinite parallel plates, and a flow over a section of an Eppler 387 airfoil. In all cases residual-based turbulence modeling approach is used. Time discretization makes use of a generalized- α algorithm (see Chung and Hulbert [15] for details). Parallel implementation using MPI [73] as a programming paradigm is employed. Test cases were run on a 1024 compute node Cray-Dell Linux cluster “lonestar”, maintained by the Texas Advanced Computing Center (TACC) [96].

4.3.1 Turbulent channel flow at $Re_\tau = 395$

In this numerical example a fully developed turbulent flow between two parallel plates is considered. Reynolds number of the flow, defined in terms of friction velocity u_τ and channel half-width δ as $Re_\tau = \frac{u_\tau \delta}{\nu}$, is 395, which is a standard benchmark test cases for newly emerging numerical methods for turbulent fluid flow. Here $u_\tau = \sqrt{\tau_w}$ is the friction velocity, and τ_w is the average wall shear stress. $\nu = \mu/\rho$ is the dynamic viscosity of the fluid. Infinite domain is simulated by means of a

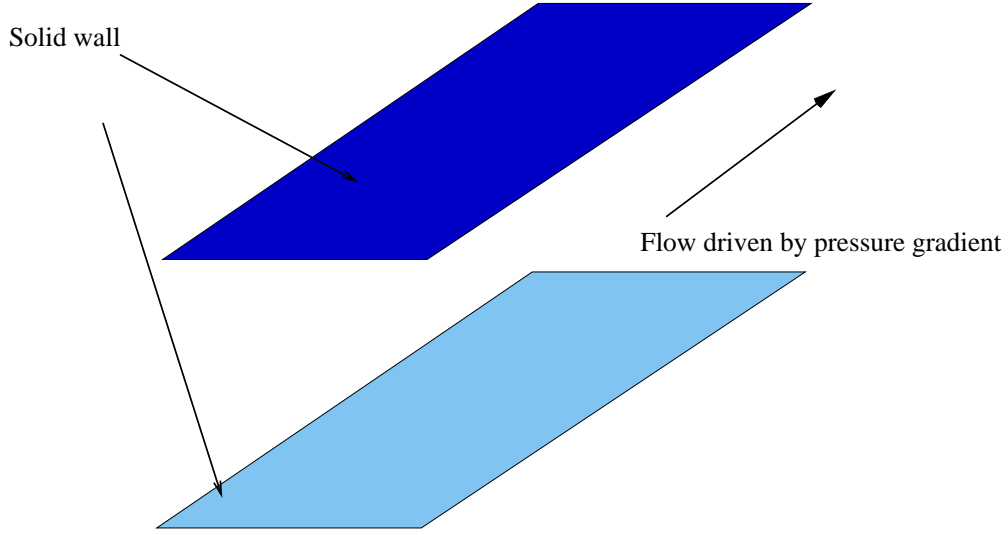


Figure 4.2: Turbulent channel. Problem setup.

finite rectangular domain of dimension $2\pi \times 2 \times 4/3\pi$ in the stream-wise, wall-normal, and span-wise directions, respectively. The flow is driven by a constant pressure gradient, as illustrated in Figure 4.2. Periodic boundary conditions are imposed in the stream-wise and span-wise directions, while wall-normal direction inherits a zero velocity Dirichlet boundary condition.

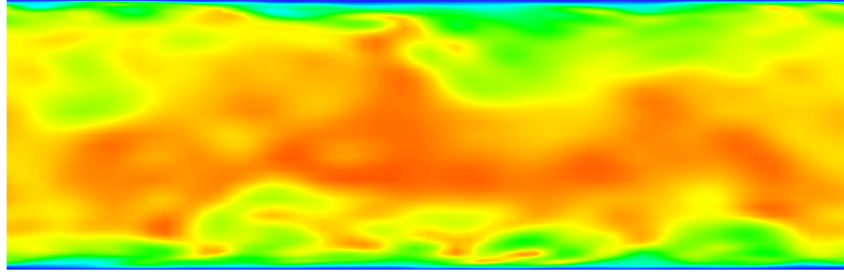
Meshes of 16^3 , 32^3 , and 64^3 rectangular elements, with uniform spacing in the periodic directions, and stretched in the wall-normal direction by a hyperbolic tangent function, are used in this study. B-spline bases of order one, two, and three are constructed on these meshes to generate discrete solution spaces for velocity and pressure, assumed to be equal order. For B-splines of order p , C^{p-1} -continuity of the basis functions is enforced, leading to k -refinement on every fixed mesh. This construction, for a mesh of n^3 elements, generates $(n+1) \times (n+p) \times (n+1)$ basis functions for a discretization of order p . Due to no-slip boundary conditions, the open-knot vector construct generates $n+p$ univariate spline basis functions in the wall-normal direction. Periodic boundary conditions in the remaining directions give rise to a univariate basis which is comprised of $n+1$ periodic splines. This number is independent of the polynomial order of the discretization.. Note that linear splines are equivalent to tri-linear hexahedral finite elements.

Figure 4.3 shows stream-wise velocity contours at an instant in time for a medium cubic simulation. The flow is characterized by a very thin boundary layer where turbulent structures are generated, and later propagate into the core region, which is fully turbulent.

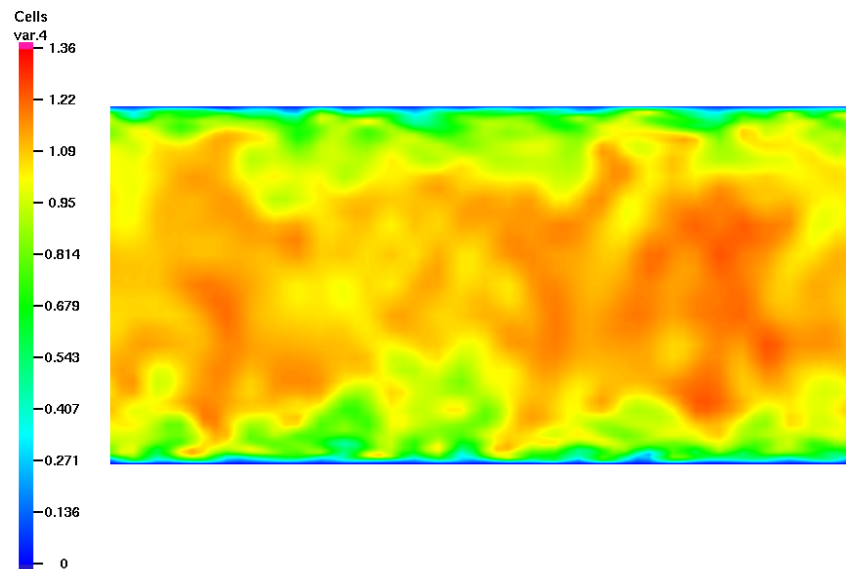
Statistics of the mean flow, or primary statistics, and fluctuations, or secondary statistics, are computed by means of averaging the solution fields in time and periodic flow directions. To

asses performance of the method, results are compared with a benchmark DNS computation of [72], which is taken as an “exact solution”, and which made use of a spectral method with 256^3 points. Results are reported in Figures 4.4-4.6. On all plots mean stream-wise velocity is scaled by the friction velocity u_τ and is denoted by u^+ . The root-mean-square deviations of the three velocity components, u_{rms} , v_{rms} , and w_{rms} , also appear in the non-dimensional form scaled by the friction velocity. These quantities are plotted against $y^+ = yu_\tau/\nu$, the non-dimensional distance from the wall in so-called “wall units”. The following observation can be made about the results of this computational study:

- Convergence of all statistics, primary and secondary, to the DNS results is apparent in all cases. As expected, mean quantities converge faster to the DNS than the fluctuations.
- Higher order simulations outperform their linear counterparts on the basis of the number of degrees of freedom used in computations. Mean quantities are much more accurate in the case of higher order discretizations. Most dramatic increase in accuracy is observed when going from a linear to a quadratic discretization, which adds only one extra layer of control variables in the wall-normal direction. Note the remarkable accuracy in predicting the mean stream-wise velocity for the case of a medium cubic spline simulation, especially considering how few degrees of freedom are employed.
- In some cases secondary statistics curves appear to be non-smooth, which suggests that the flow may need to be advanced for a longer time period and/or a larger sample size needs to be used for the computation of statistical quantities. In particular, 64^3 cubics need additional simulation time in order to reach a statistically stationary state.
- Results appear to be competitive with, if not superior to, computations with standard methods making use of turbulence models based on eddy viscosities.



a) Stream-wise view



b) Span-wise view

Figure 4.3: Turbulent channel flow. Stream-wise velocity contours in different views.

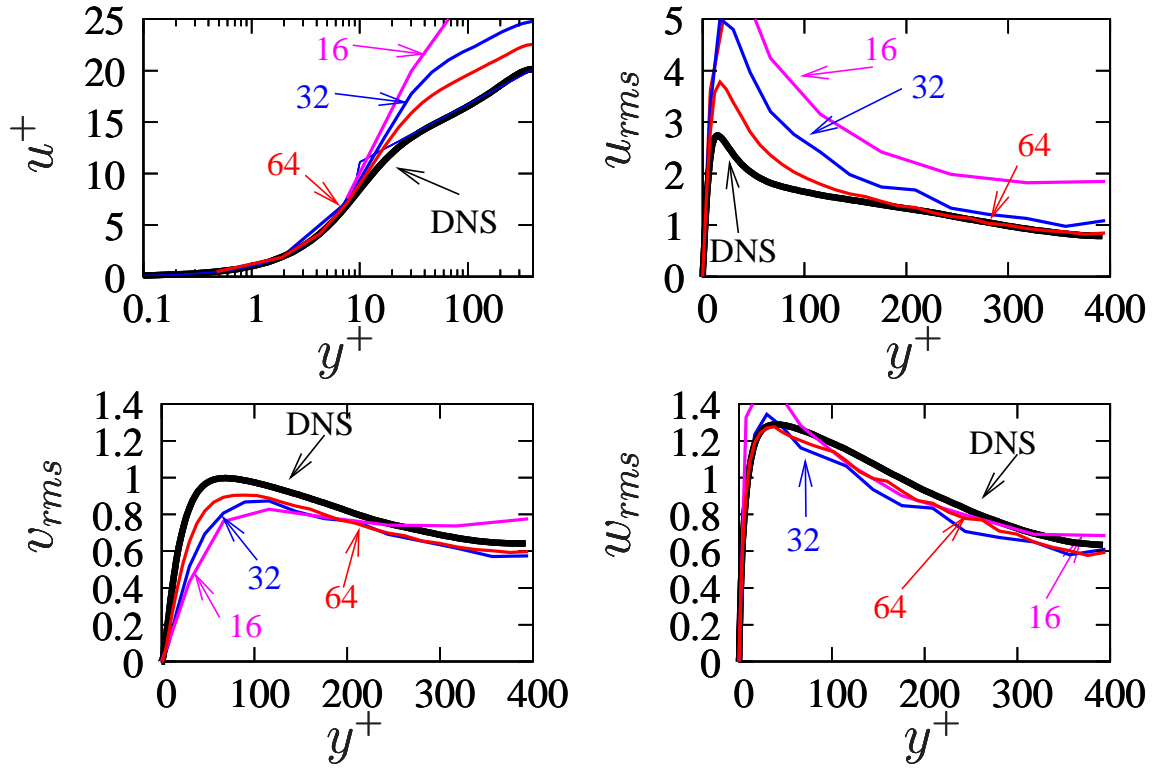


Figure 4.4: Turbulent channel flow, results using linear elements. Top left: convergence of the mean flow, top right: convergence of u_{rms} , bottom left: convergence of v_{rms} , bottom right: convergence of w_{rms} .

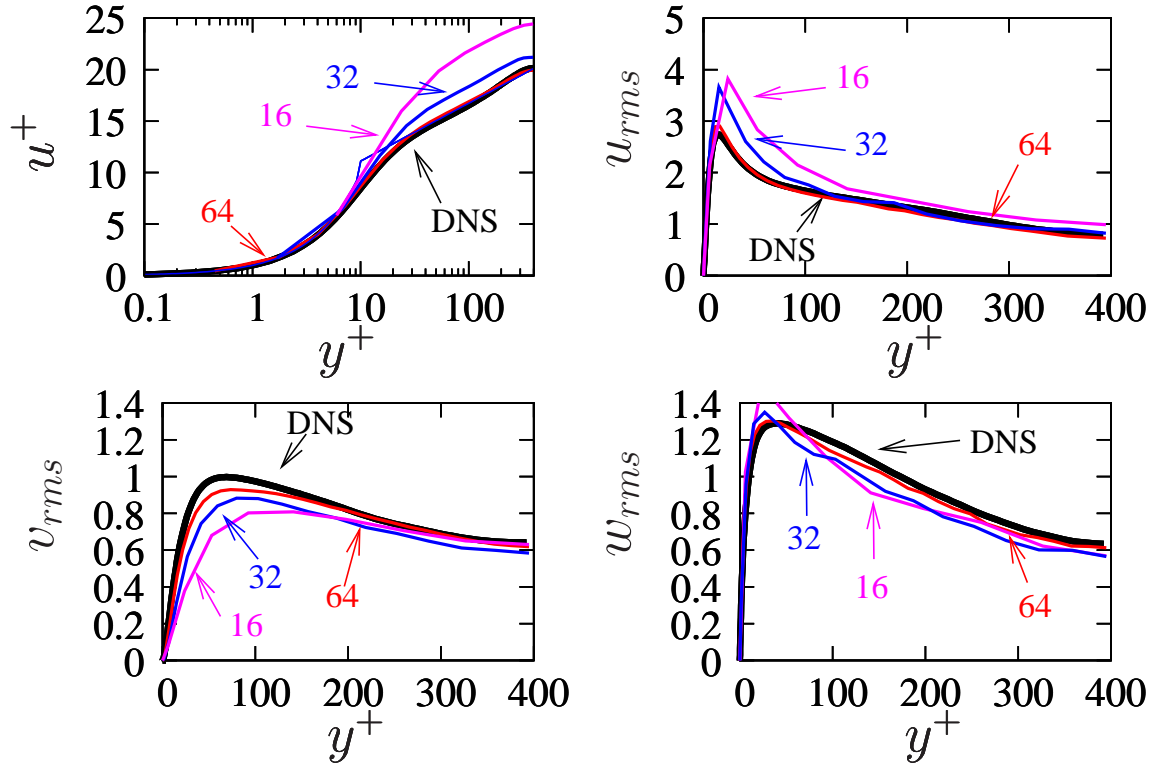


Figure 4.5: Turbulent channel flow, results using quadratic splines. Top left: convergence of the mean flow, top right: convergence of u_{rms} , bottom left: convergence of v_{rms} , bottom right: convergence of w_{rms} .

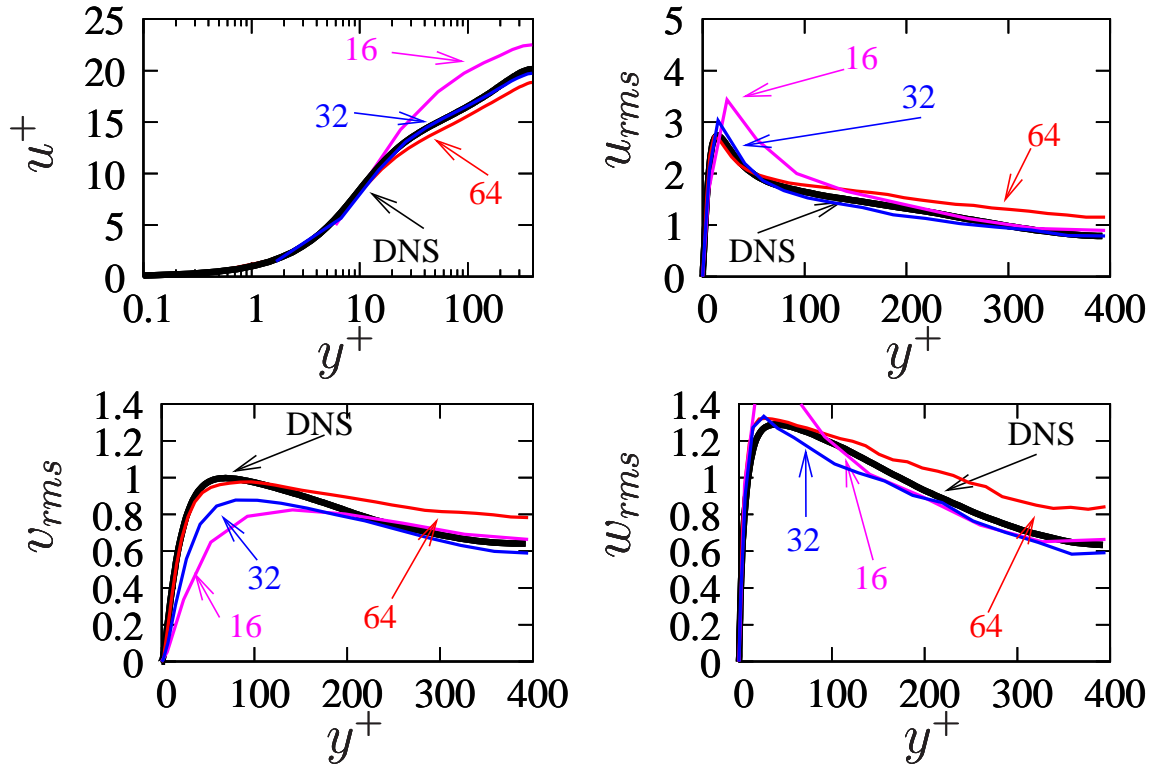


Figure 4.6: Turbulent channel flow, results using quartic splines. Top left: convergence of the mean flow, top right: convergence of u_{rms} , bottom left: convergence of v_{rms} , bottom right: convergence of w_{rms} .

4.3.2 Flow over Eppler 387 airfoil

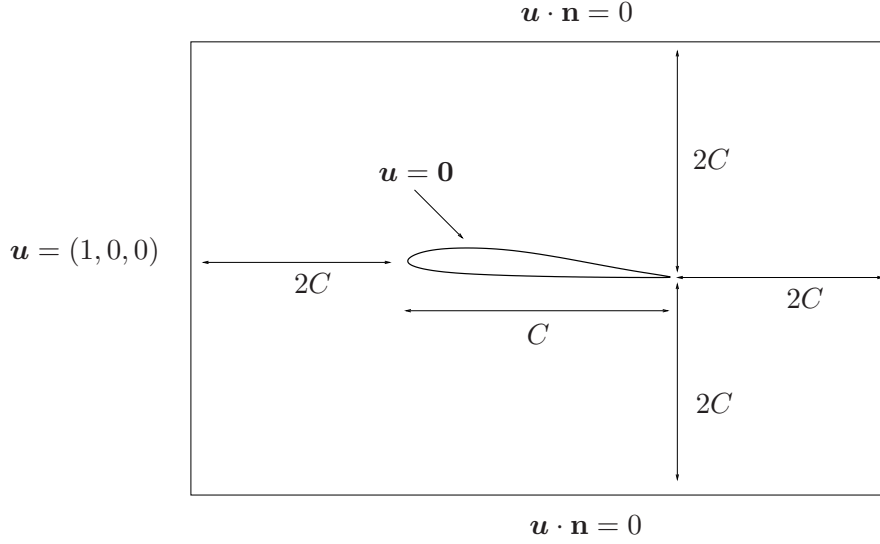
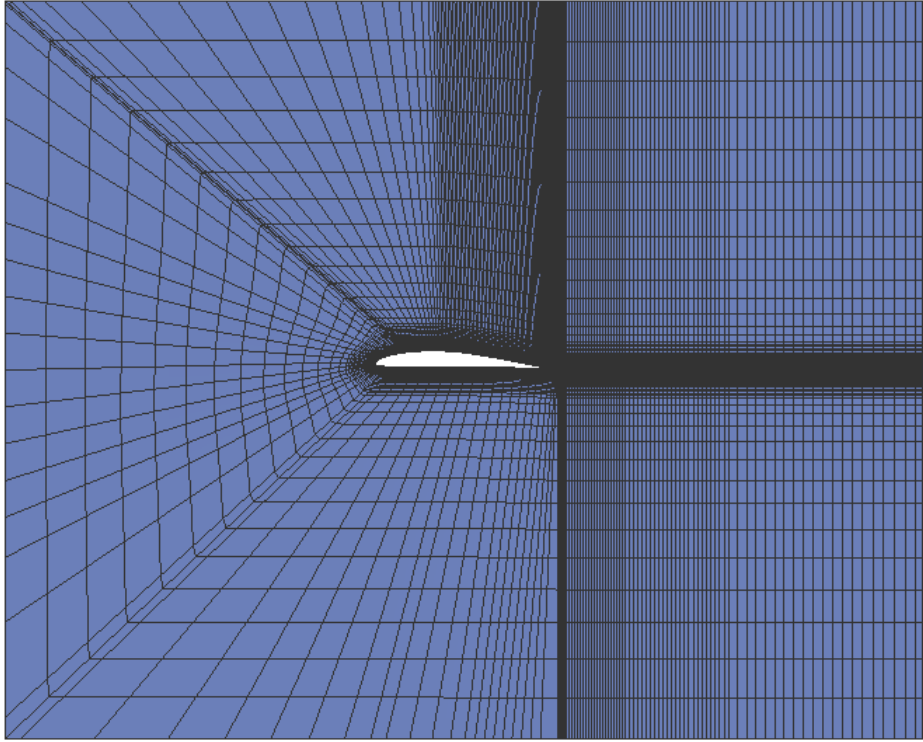


Figure 4.7: Flow over Eppler airfoil problem setup. Computational domain and boundary conditions.

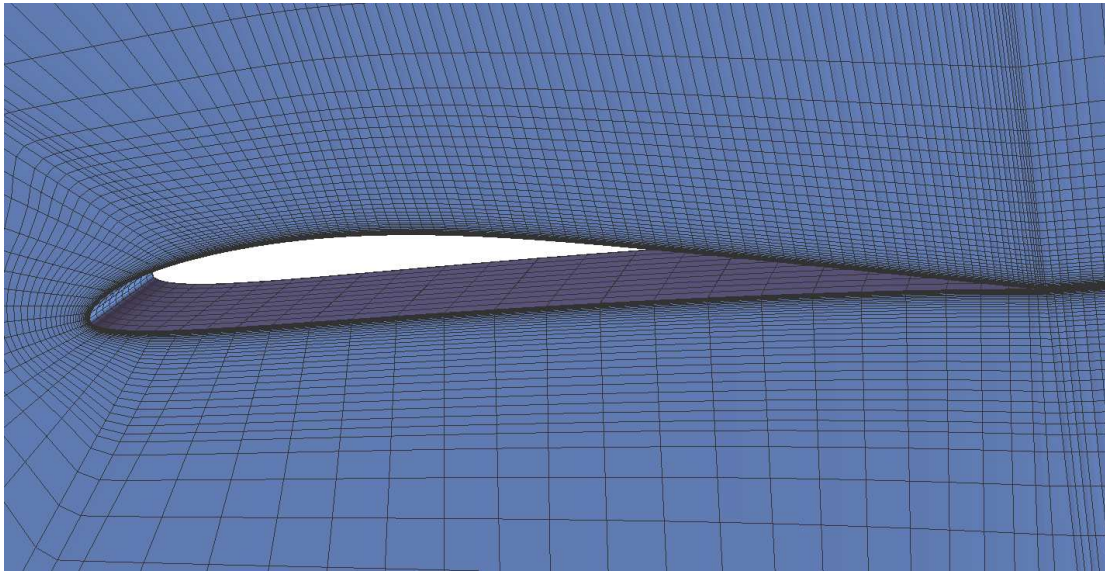
Computations of a fully-developed flow over Eppler 387 airfoil at Reynolds number $Re = 100,000$, based on the cord length C , and $\alpha = 2^\circ$ angle of attack are presented in this example. The flow is at low Mach number, hence the incompressibility assumption is valid in this situation. Problem setup and boundary conditions are given in Figure 4.7. Two- and three-dimensional simulations are performed. In the three-dimensional case the domain was given a thickness of $0.12C$ and periodic boundary conditions were applied in the span-wise direction.

Figure 4.8 shows the mesh, comprised of 12,690 and 126,900 cubic NURBS elements used in the two- and three-dimensional simulations, respectively. It was generated in the spirit a C -grid. Basis functions used are C^2 -continuous in the direction normal to the airfoil surface and C^0 -continuous in the span-wise direction. Mixed order of continuity, that is both C^0 and C^2 , is employed in the direction tangential to the airfoil.

Figure 4.9 shows a snapshot of stream-wise velocity and pressure contours for a two-dimensional simulation. Results are in good agreement with those of Oberai, Roknaldin and Hughes [76, 77]. Note the coherence of the vortical structures shown on the stream-wise velocity plot 4.9a. These structures are a consequence of a two-dimensional description of the flow. In three-dimensions these structures break up into smaller eddies, which is a fundamental turbulence mechanism. Also note the smoothness of the pressure contours shown on 4.9b.

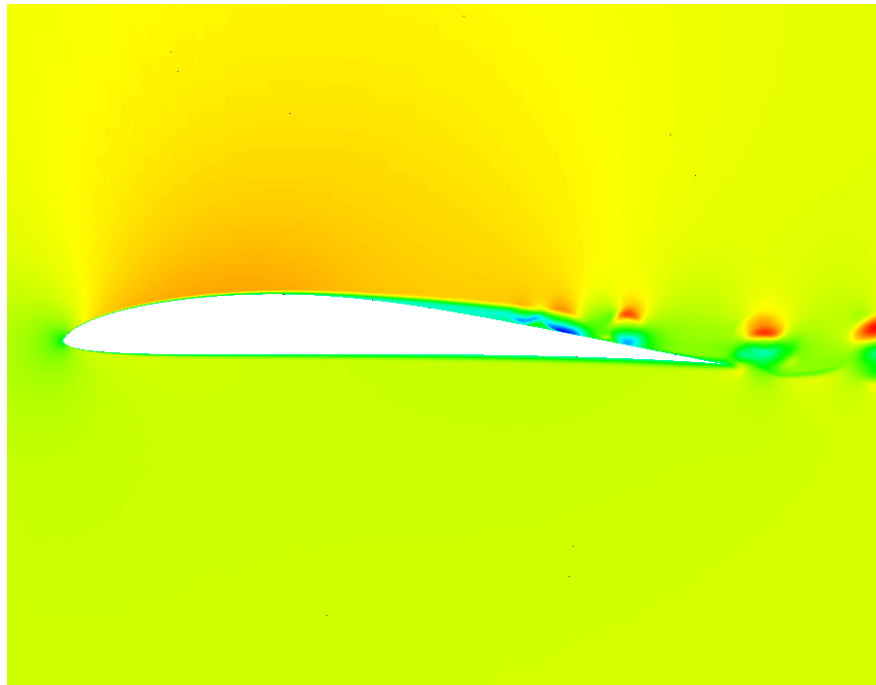


a) Full mesh

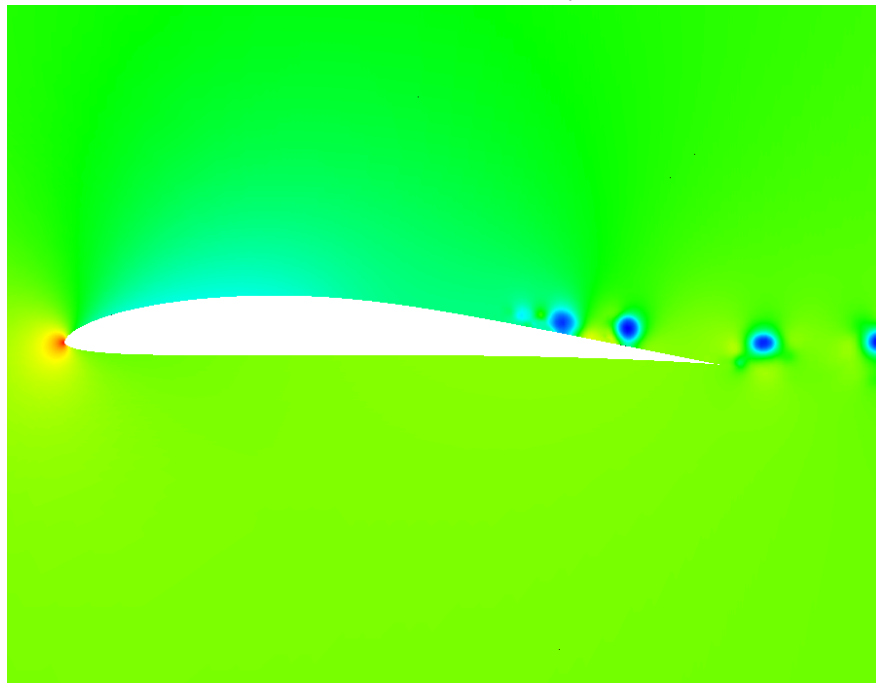


b) Zoom on the boundary layer mesh

Figure 4.8: Flow over Eppler airfoil. NURBS mesh for both two-dimensional and three-dimensional calculations. Span-wise resolution was reduced to one linear element for a two-dimensional calculation.



a) Stream-wise velocity

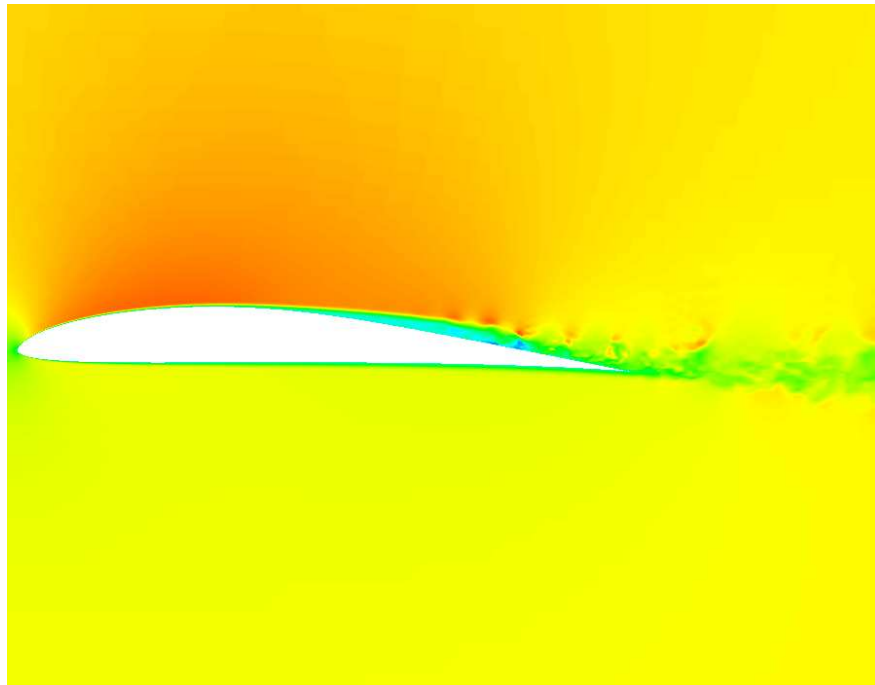


b) Pressure

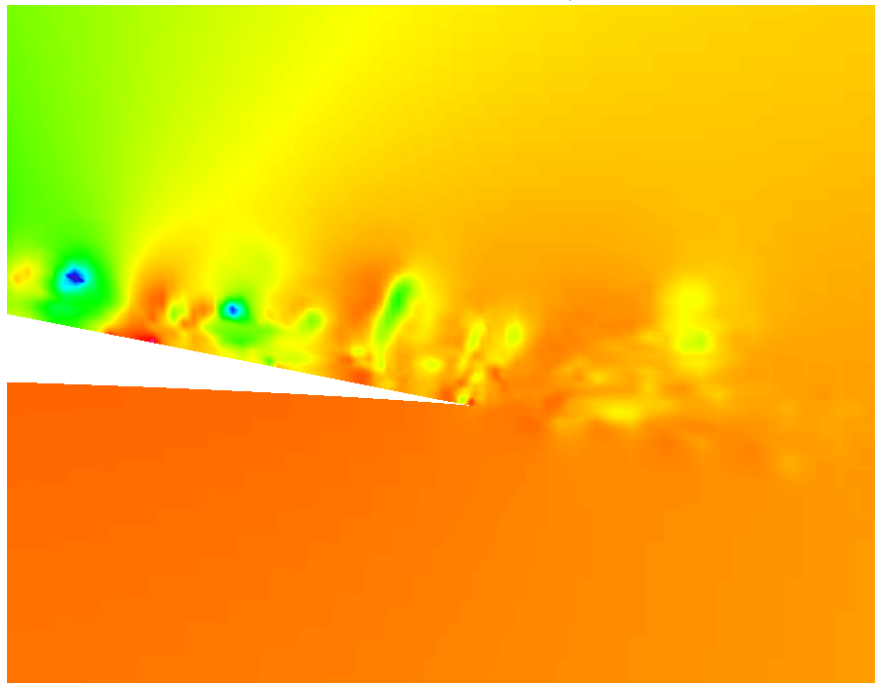
Figure 4.9: Flow over Eppler airfoil. Snapshots of stream-wise velocity and pressure fields for a two-dimensional calculation. Note the coherence of the vortical structures and smoothness of pressure contours.

In designing airfoils, quantities such lift and drag are of great importance to aeronautical engineers as they define airfoil performance characteristics. These are functionals of the flow fields and their values change dramatically when the flow undergoes transition from laminar to turbulent. Predicting these quantities of interest accurately behooves one to go to a full three-dimensional description of the flow, wherein lies a great computational challenge. Figure 4.10 shows the stream-wise velocity and the trailing-edge pressure contours on a span-wise slice of the computational domain. Note that the coherent structures, characteristic of the two-dimensional description, are no longer present. Instead, the flow possesses a multitude of spatial and temporal scales, and appears chaotic. To further illustrate the point Figure 4.11 depicts isosurfaces of span-wise velocity fluctuations. Fine-grained solution structures occur in parts of the domain where the flow is highly turbulent, namely the trailing edge of the airfoil and its wake. In other parts of the domain the flow is nearly two-dimensional. Situations like this present a great modeling challenge: a “good” turbulence model must be able to identify various flow regimes and adapt accordingly.

Figure 4.12 shows the plot of the pressure coefficient distribution along the airfoil upper and lower surfaces. It is defined as $C_p = \frac{1}{2} \frac{p - p_\infty}{\rho u_\infty^2}$. p_∞ , the reference pressure, is set equal to zero, and u_∞ , the reference velocity is set equal to the magnitude of the velocity vector at the inflow of the computational domain. Results of the three-dimensional computation are in excellent agreement with the experimental findings of [71].



a) Stream-wise velocity



b) Pressure

Figure 4.10: Flow over Eppler airfoil. Snapshots of stream-wise velocity and trailing edge pressure fields for a three-dimensional calculation. Pressure fluctuations are a source of hydrodynamically generated noise.

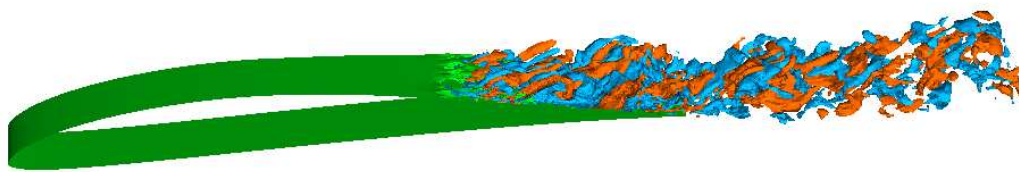


Figure 4.11: Flow over Eppler airfoil. Span-wise velocity isosurfaces for a three-dimensional calculation.

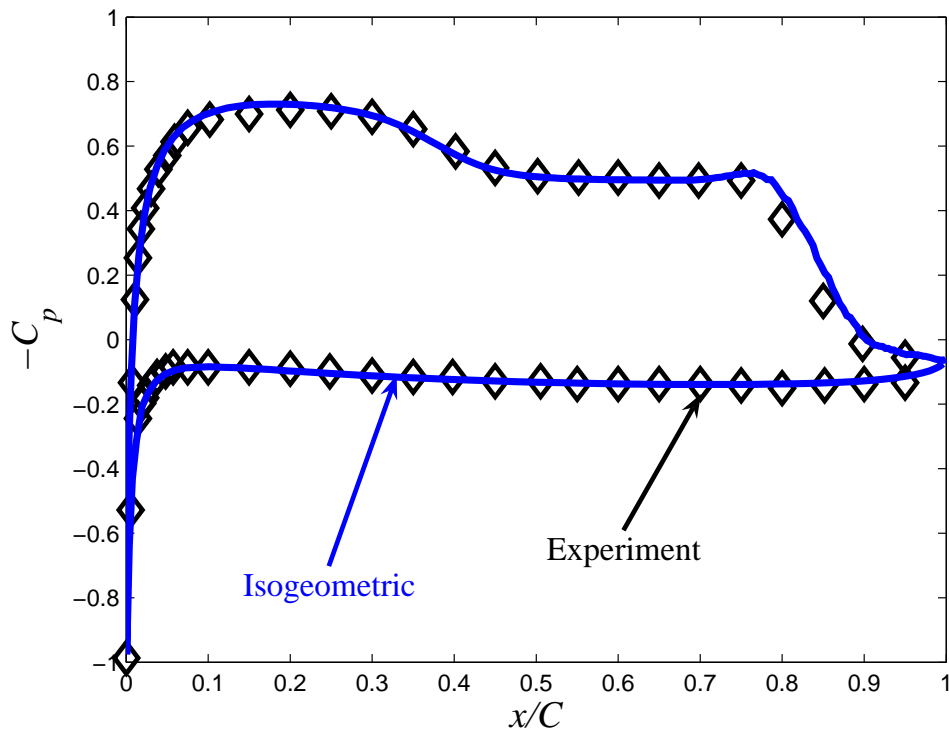


Figure 4.12: Flow over Eppler airfoil. Plot of the pressure coefficient $C_p = \frac{1}{2} \frac{p - p_\infty}{\rho u_\infty^2}$. Excellent agreement between a three-dimensional computation and experimental data is observed.

Chapter 5

Isogeometric Fluid-Structure Interaction Analysis with Applications to Arterial Blood Flow

5.1 Formulation of the fluid-structure interaction problem

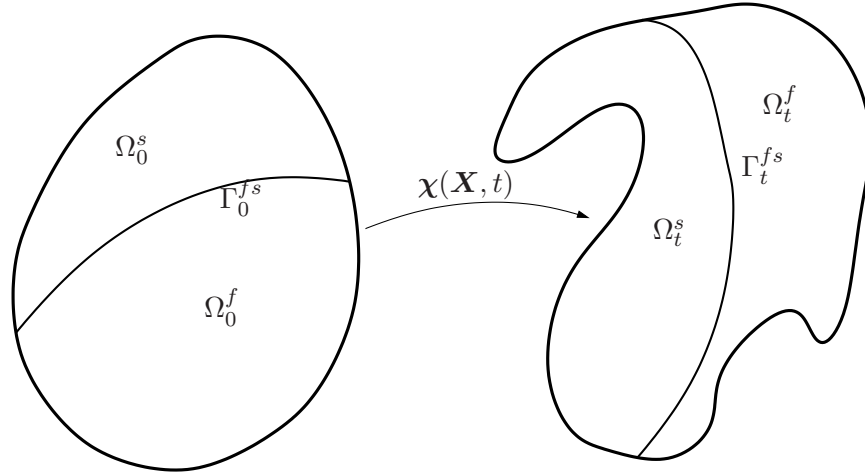


Figure 5.1: Abstract setting for the fluid-structure interaction problem. Depiction of the initial and the current configurations related through the ALE mapping. The initial configuration also serves as the reference configuration.

In this section we present the formulation of the fluid-structure interaction problem. We begin by introducing notation. Let $\Omega_0 \in \mathbb{R}^d$, $d = 2, 3$, open and bounded, be the initial or the

reference configuration. Let $\Omega_t \in \mathbb{R}^d$, open and bounded, represent the current configuration, namely Ω_t is the image of Ω_0 under the motion $\mathbf{x} = \chi(\mathbf{X}, t)$ with $\mathbf{x} \in \Omega_t$, $\mathbf{X} \in \Omega_0$, and $t \in (0, T)$, the time interval of interest. In what follows, \mathbf{x} will be referred to as current coordinates, and \mathbf{X} as reference coordinates. Note that $\chi(\mathbf{X}, 0) = \mathbf{X}$. The domain Ω_0 admits a decomposition

$$\Omega_0 = \Omega_0^f \cup \Omega_0^s, \quad (5.1)$$

where Ω_0^f is a subset of Ω_0 occupied by the fluid, and Ω_0^s is a subset of Ω_0 occupied by the solid. The decomposition is non-overlapping, that is

$$\Omega_0^f \cap \Omega_0^s = \emptyset. \quad (5.2)$$

Likewise,

$$\Omega_t = \Omega_t^f \cup \Omega_t^s, \quad (5.3)$$

with

$$\Omega_t^f \cap \Omega_t^s = \emptyset. \quad (5.4)$$

Let Γ_0^{fs} denote the boundary between the fluid and the solid regions in the initial configuration, and, analogously, let Γ_t^{fs} be its counterpart in the current configuration. The above setup is illustrated in Figure 5.1. It is important to emphasize that the motion of the fluid domain is not the particle motion of the fluid. It does, however, conform to the particle motion of the arterial wall. The Lagrangian description is adopted for the artery wall.

5.1.1 The solid problem

This section gives a weak formulation of the hyperelastic nonlinear solid in the Lagrangian description. Let $\mathcal{V}^s = \mathcal{V}^s(\Omega_0^s)$ denote the trial solution space for displacements and let $\mathcal{W}^s = \mathcal{W}^s(\Omega_0^s)$ denote the trial weighting space for the linear momentum equations. Let \mathbf{u} denote the displacement of the solid body with respect to the initial configuration and let \mathbf{w}^s be the weighting function for the momentum equation. We also assume that the displacement satisfies the boundary condition, $\mathbf{u} = \mathbf{g}^s$ on $\Gamma_0^{s,D}$, the Dirichlet part of the solid domain boundary. The variational formulation is stated as follows: Find $\mathbf{u} \in \mathcal{V}^s$ such that $\forall \mathbf{w}^s \in \mathcal{W}^s$,

$$B^s(\mathbf{w}^s, \mathbf{u}) = F^s(\mathbf{w}^s) \quad (5.5)$$

where

$$B^s(\mathbf{w}^s, \mathbf{u}) = \left(\mathbf{w}^s, \rho_0^s \frac{\partial^2 \mathbf{u}}{\partial t^2} \right)_{\Omega_0^s} + (\nabla_X \mathbf{w}^s, \mathbf{F} \mathbf{S})_{\Omega_0^s}, \quad (5.6)$$

and

$$F^s(\mathbf{w}^s) = (\mathbf{w}^s, \rho_0^s \mathbf{f}^s)_{\Omega_0^s} + (\mathbf{w}^s, \mathbf{h}^s)_{\Gamma_0^{s,N}}. \quad (5.7)$$

The above relations are written over the reference configuration. The subscript X on the partial derivative operators indicates that the derivatives are taken with respect to the material coordinates \mathbf{X} . $\Gamma_0^{s,N}$ is the Neumann part of the solid boundary, \mathbf{h}^s is the boundary traction vector, ρ_s^0 is the density of the solid in the initial configuration, and \mathbf{f}^s is the body force per unit mass. The displacement \mathbf{u} is defined as

$$\mathbf{u}(\mathbf{X}, t) = \chi(\mathbf{X}, t) - \mathbf{X}, \quad (5.8)$$

\mathbf{F} is the deformation gradient

$$\mathbf{F} = \frac{\partial \chi}{\partial \mathbf{X}} = \mathbf{I} + \frac{\partial \mathbf{u}}{\partial \mathbf{X}}, \quad (5.9)$$

and \mathbf{S} is the second Piola-Kirchhoff stress tensor. We consider the following constitutive models:

Case 1 The St.Venant-Kirchhoff constitutive relation:

$$\mathbf{S} = \mathcal{C} : \mathbf{E}, \quad (5.10)$$

where

$$\mathbf{E} = \frac{1}{2}(\mathbf{F}^T \mathbf{F} - \mathbf{I}), \quad (5.11)$$

$$\mathcal{C} = \lambda^s \mathbf{I} \otimes \mathbf{I} + 2\mu^s \left(\mathbb{I} - \frac{1}{3} \mathbf{I} \otimes \mathbf{I} \right), \quad (5.12)$$

$$\mathbb{I}_{IJKL} = \frac{1}{2}(\delta_{IK}\delta_{JL} + \delta_{IL}\delta_{JK}), \quad (5.13)$$

\mathbf{E} is the Green-Lagrange strain tensor, δ_{IJ} is the Kronecker delta, and λ^s and μ^s are the Lamé constants. Note that the fourth-order elastic tensor \mathcal{C} is assumed constant in this model.

The St. Venant-Kirchhoff model is not without shortcomings. It exhibits a seemingly spuri-

ous material instability under states of strong compression. However this is not felt to be important in the present applications. The essential point is that it represents an objective generalization of the linear isotropic theory to the nonlinear case. Of course, there is no physical justification of the model beyond the linear strain regime.

Case 2 Material model treated in Simo and Hughes [90]. Here \mathbf{S} comes from the gradient of the elastic potential ϕ , namely

$$\mathbf{S} = 2 \frac{\partial \phi}{\partial \mathbf{C}}, \quad (5.14)$$

where \mathbf{C} is the Cauchy-Green strain tensor defined as

$$\mathbf{C} = \mathbf{F}^T \mathbf{F}. \quad (5.15)$$

The elastic potential engenders a sum decomposition

$$\phi = \phi_{iso} + \phi_{dil}, \quad (5.16)$$

where ϕ_{iso} is the energy associated with the volume-preserving or isochoric part of the motion, while ϕ_{dil} reflects the volume-changing or dilatational component of the deformation. This decomposition is due to the fact that materials respond differently in bulk and in shear. We assume three-dimensional elastic medium and perform the following multiplicative decomposition of the deformation gradient \mathbf{F} :

$$\mathbf{F} = J^{1/3} \overline{\mathbf{F}}, \quad (5.17)$$

where $J = \det \mathbf{F}$, the determinant of \mathbf{F} , and $\overline{\mathbf{F}} = J^{-1/3} \mathbf{F}$. Note that $\det \overline{\mathbf{F}} = 1$, hence $\overline{\mathbf{F}}$ is associated with the volume-preserving part of the motion, while $J^{1/3}$ is the volume-changing component.

Let

$$\overline{\mathbf{C}} = \overline{\mathbf{F}}^T \overline{\mathbf{F}}, \quad (5.18)$$

in direct analogy with (5.15). Then

$$\phi_{iso} = \frac{1}{2} \mu^s (\text{tr} \overline{\mathbf{C}} - 3), \quad (5.19)$$

and

$$\phi_{dil} = \frac{1}{2} \kappa^s \left(\frac{1}{2} (J^2 - 1) - \ln J \right). \quad (5.20)$$

Note that this model, as opposed to St. Venant-Kirchhoff, satisfies all the necessary normalization conditions. In particular, the $\ln J$ term in the definition of ϕ_{dil} precludes material instabilities for states of strong compression.

For the above definition of elastic potential, second Piola-Kirchhoff stress tensor becomes

$$\mathbf{S} = \mu^s J^{-2/3} (\mathbf{I} - \frac{1}{3} \text{tr} \mathbf{C} \mathbf{C}^{-1}) + \frac{1}{2} \kappa^s (J^2 - 1) \mathbf{C}^{-1}, \quad (5.21)$$

and the fourth-order tensor of elastic moduli is

$$\begin{aligned} \mathcal{C} = 4 \frac{\partial^2 \phi}{\partial \mathbf{C} \partial \mathbf{C}} = & \left(\frac{2}{9} \mu^s J^{-2/3} \text{tr} \mathbf{C} + \kappa^s J^2 \right) \mathbf{C}^{-1} \otimes \mathbf{C}^{-1} \\ & + \left(\frac{2}{3} \mu^s J^{-2/3} \text{tr} \mathbf{C} - \kappa^s (J^2 - 1) \right) \mathbf{C}^{-1} \odot \mathbf{C}^{-1} \\ & - \frac{2}{3} \mu^s J^{-2/3} (\mathbf{I} \otimes \mathbf{C}^{-1} + \mathbf{C}^{-1} \otimes \mathbf{I}). \end{aligned} \quad (5.22)$$

In (5.22) the \otimes symbol is used to denote an outer product of two second-rank tensors, and

$$(\mathbf{C}^{-1} \odot \mathbf{C}^{-1})_{IJKL} = \frac{(\mathbf{C}^{-1})_{IK}(\mathbf{C}^{-1})_{JL} + (\mathbf{C}^{-1})_{IL}(\mathbf{C}^{-1})_{JK}}{2} \quad (5.23)$$

Parameters μ^s and κ^s may be identified with Lamé constants of the linear elastic model, denoted μ^l and λ^l , by considering the case when the current and the reference configurations coincide. Then the elastic tensor (5.22) reduces to the form given in (5.12), and, by inspection,

$$\mu^s = \mu^l \quad (5.24)$$

$$\kappa^s = \lambda^l + \frac{2}{3} \mu^l. \quad (5.25)$$

5.1.2 Motion of the fluid subdomain problem and the ALE mapping

This section gives a weak formulation of the motion of the fluid subdomain. Partial differential equations of linear elastostatics subject to Dirichlet boundary conditions coming from the displacements of the solid region define the ALE mapping $\chi(\mathbf{X}, t)$ on the fluid domain. This construction, which is by no means unique, imposes sufficient regularity on the ALE mapping so as to make the fluid problem (5.35) well-posed. For precise conditions on the regularity of the ALE map, see Nobile [74]. In the discrete setting, the fluid subdomain motion problem is referred to as “mesh moving.”

Let δ denote the displacement of the fluid domain from its initial configuration

$$\delta(\mathbf{X}, t) = \chi(\mathbf{X}, t) - \mathbf{X} \quad (5.26)$$

and let $\frac{\partial \delta}{\partial t}$ be its velocity in the reference configuration. We also define the displacement and the velocity of the fluid subdomain in the current configuration as a push-forward of the respective quantities in the reference domain, that is,

$$\gamma(\mathbf{x}, t) = \delta \circ \chi^{-1}(\mathbf{x}, t) = \delta(\chi^{-1}(\mathbf{x}, t), t) \quad (5.27)$$

$$\beta(\mathbf{x}, t) = \frac{\partial \delta}{\partial t} \circ \chi^{-1}(\mathbf{x}, t) = \frac{\partial \delta}{\partial t}(\chi^{-1}(\mathbf{x}, t), t) \quad (5.28)$$

Let $\Omega_{\tilde{t}}$ be the configuration of Ω_0 at $\tilde{t} < t$. We think of this as a “nearby” configuration that in numerical computations will typically represent the final configuration of the previous time step. Then, let $\tilde{\gamma}$ be the displacement of the reference domain at time \tilde{t} . Let $\mathcal{V}^m = \mathcal{V}^m(\Omega_t^f)$ denote the trial solution space of displacements and let $\mathcal{W}^m = \mathcal{W}^m(\Omega_t^f)$ denote the weighting space for the “elastic equilibrium” equations. The variational formulation of the problem is stated as follows: Find $\gamma \in \mathcal{V}^m$ such that $\forall \mathbf{w}^m \in \mathcal{W}^m$,

$$B^m(\mathbf{w}^m, \gamma) = 0, \quad (5.29)$$

subject to

$$\gamma|_{\Gamma_t^{fs}} = \mathbf{u} \circ \chi^{-1}|_{\Gamma_t^{fs}}, \quad (5.30)$$

and

$$\mathbf{w}^m|_{\Gamma_t^{fs}} = \mathbf{0}, \quad (5.31)$$

where

$$B^m(\mathbf{w}^m, \gamma) = (\nabla_x^s \mathbf{w}^m, 2\mu^m \nabla_x^s (\gamma - \tilde{\gamma}) + \lambda^m \nabla_x \cdot (\gamma - \tilde{\gamma}))_{\Omega_t^f}. \quad (5.32)$$

The above relations are written over the current configuration. The subscript x on the partial derivative operators indicates that the derivatives are taken with respect to the current coordinates \mathbf{x} . Constants μ^m and λ^m are the Lamé parameters of the linear elastic model characterizing the motion of the fluid region. Their choice at the continuous level should be such that the problem (5.29) is well-posed. In the discrete setting they should be selected such that the fluid mesh quality is preserved for as long as possible. In particular, mesh quality can be preserved by dividing the elastic coefficients by the Jacobian of the element mapping, effectively increasing the stiffness of the smaller elements [103], which are typically placed at fluid-solid interfaces. For advanced mesh moving techniques see [92, 93]. Parts of the boundary of the fluid region may also have motion

prescribed to them independent of the motion of the solid region. This is handled in a standard way as a Dirichlet boundary condition. The remainder of the fluid region boundary is subjected to a “zero stress” boundary condition.

As a result of the above construction, the ALE mapping for the entire domain may be defined in a piece-wise fashion, namely:

$$\chi(\mathbf{X}, t) = \begin{cases} \mathbf{u}(\mathbf{X}, t) + \mathbf{X} & \forall \mathbf{X} \in \Omega_0^s \\ \boldsymbol{\delta}(\mathbf{X}, t) + \mathbf{X} & \forall \mathbf{X} \in \Omega_0^f \end{cases}. \quad (5.33)$$

Note that (5.27) together with (5.30) imply

$$\boldsymbol{\delta} = \boldsymbol{\gamma} \circ \chi = \mathbf{u} \text{ on } \Gamma_0^{fs}, \quad (5.34)$$

which makes the ALE map (5.33) continuous on the fluid-solid boundary.

5.1.3 The fluid problem

In this section we give a weak formulation of the incompressible Navier-Stokes fluid on a moving domain in the ALE description. Motion of the fluid domain was constructed in the previous section, and is given by (5.33). Let $\mathcal{V}^f = \mathcal{V}^f(\Omega_t^f)$ denote the trial solution space of velocities and pressures and let $\mathcal{W}^f = \mathcal{W}^f(\Omega_t^f)$ denote the trial weighting space for the momentum and continuity equations. Let $\{\mathbf{v}, p\}$ denote the particle velocity-pressure pair and $\{\mathbf{w}^f, q^f\}$ the weighting functions for the momentum and continuity equations. We also assume that the fluid particle velocity field satisfies the boundary condition, $\mathbf{v} = \mathbf{g}^f$ on $\Gamma_t^{f,D}$, the Dirichlet part of the fluid boundary. The variational formulation is stated as follows: Find $\{\mathbf{v}, p\} \in \mathcal{V}^f$ such that $\forall \{\mathbf{w}^f, q^f\} \in \mathcal{W}^f$,

$$B^f(\{\mathbf{w}^f, q^f\}, \{\mathbf{v}, p\}; \boldsymbol{\beta}) = F^f(\{\mathbf{w}^f, q^f\}) \quad (5.35)$$

where

$$\begin{aligned} B^f(\{\mathbf{w}^f, q^f\}, \{\mathbf{v}, p\}; \boldsymbol{\beta}) = & \left(\mathbf{w}^f, \rho^f \frac{\partial \mathbf{v}}{\partial t} \right)_{\Omega_t^f} + \left(\mathbf{w}^f, \rho^f (\mathbf{v} - \boldsymbol{\beta}) \cdot \nabla_x \mathbf{v} \right)_{\Omega_t^f} \\ & + (q^f, \nabla_x \cdot \mathbf{v})_{\Omega_t^f} - (\nabla_x \cdot \mathbf{w}^f, p)_{\Omega_t^f} + \left(\nabla_x^s \mathbf{w}^f, 2\mu^f \nabla_x^s \mathbf{v} \right)_{\Omega_t^f}, \end{aligned} \quad (5.36)$$

and

$$F^f(\{\mathbf{w}^f, q^f\}) = (\mathbf{w}^f, \rho^f \mathbf{f}^f)_{\Omega_t^f} + (\mathbf{w}^f, \mathbf{h}^f)_{\Gamma_t^{f,N}}. \quad (5.37)$$

The above equations are written over the current configuration and (\cdot, \cdot) defines the corresponding L^2 inner product. The subscript x on the partial derivative operators indicates that the derivatives are taken with respect to the current coordinates \mathbf{x} . $\Gamma_t^{f,N}$ is the Neumann part of the fluid domain boundary, \mathbf{h}^f is the boundary traction vector, \mathbf{f}^f is the body force per unit mass, and ρ^f and μ^f are the density and the dynamic viscosity of the fluid, respectively. β is the velocity of the fluid subdomain defined in (5.28).

Remark 5.1.1. *Note that the quantity $\frac{\partial \mathbf{v}}{\partial t}$ is not the spatial particle acceleration, instead it is a push-forward of the material particle acceleration defined as*

$$\frac{\partial \mathbf{v}}{\partial t} = \frac{\partial \hat{\mathbf{v}}}{\partial t} \circ \chi^{-1}, \quad (5.38)$$

where $\hat{\mathbf{v}} = \mathbf{v} \circ \chi$.

Remark 5.1.2. *Also note that, unless the Lagrangian description is utilized in the fluid domain, $\beta \neq \mathbf{v}$.*

5.1.4 The coupled problem

In this section we present the coupled FSI problem, which is based on the individual subproblems introduced in previous sections of this chapter. The variational formulation for the coupled problem is stated as: Find $\{\mathbf{v}, p\} \in \mathcal{V}^f$, $\mathbf{u} \in \mathcal{V}^s$, and $\gamma \in \mathcal{V}^m$ such that $\forall \{\mathbf{w}^f, q^f\} \in \mathcal{W}^f$, $\forall \mathbf{w}^s \in \mathcal{W}^s$, and $\forall \mathbf{w}^m \in \mathcal{W}^m$,

$$\begin{aligned} B^f(\{\mathbf{w}^f, q^f\}, \{\mathbf{v}, p\}; \beta) - F^f(\{\mathbf{w}^f, q^f\}) + \\ B^s(\mathbf{w}^s, \mathbf{u}) - F^s(\mathbf{w}^s) + B^m(\mathbf{w}^m, \gamma) = 0. \end{aligned} \quad (5.39)$$

with the following auxiliary relations holding in the sense of traces:

$$\mathbf{v}|_{\Gamma_t^{fs}} = \frac{\partial \mathbf{u}}{\partial t} \circ \chi^{-1}|_{\Gamma_t^{fs}}, \quad (5.40)$$

$$\mathbf{w}^f|_{\Gamma_t^{fs}} = \mathbf{w}^s \circ \chi^{-1}|_{\Gamma_t^{fs}}, \quad (5.41)$$

as well as equations (5.30) and (5.31).

Relationship (5.40), the kinematic constraint, equates the fluid velocity with that of the solid at the fluid-solid boundary. Equation (5.41) leads to the compatibility of the Cauchy stresses at the fluid-solid interface. Indeed, integrating by parts, setting $\mathbf{w}^m = \mathbf{0}$, and assuming sufficient

regularity of the solution fields in (5.39), gives

$$\begin{aligned}
0 = & \left\langle \mathbf{w}^f, \mathcal{L}^f(\mathbf{v}, p; \beta) - \rho^f \mathbf{f}^f \right\rangle_{\Omega_t^f} \\
& + \left\langle q^f, \nabla_x \cdot \mathbf{v} \right\rangle_{\Omega_t^f} \\
& + \left\langle \mathbf{w}^f, \boldsymbol{\sigma}^f \mathbf{n}_t^f - \mathbf{h}^f \right\rangle_{\Gamma_t^{f,N}} \\
& + \left\langle \mathbf{w}^f, \boldsymbol{\sigma}^f \mathbf{n}_t^f \right\rangle_{\Gamma_t^{fs}} \\
& + \left\langle \mathbf{w}^s, \mathcal{L}^s(\mathbf{u}) - \rho_0^s \mathbf{f}^s \right\rangle_{\Omega_0^s} \\
& + \left\langle \mathbf{w}^s, \mathbf{P} \mathbf{n}_0^s - \mathbf{h}^s \right\rangle_{\Gamma_0^{s,N}} \\
& + \left\langle \mathbf{w}^s, \mathbf{P} \mathbf{n}_0^s \right\rangle_{\Gamma_0^{fs}}, \tag{5.42}
\end{aligned}$$

where $\langle \cdot, \cdot \rangle_{\Omega}$ and $\langle \cdot, \cdot \rangle_{\Gamma}$ denote volume and surface integrals, respectively. In (5.42) the following definitions apply:

$$\mathcal{L}^f(\mathbf{v}, p; \beta) = \rho^f \frac{\partial \mathbf{v}}{\partial t} + \rho^f (\mathbf{v} - \beta) \cdot \nabla_x \mathbf{v} - \nabla_x \cdot \boldsymbol{\sigma}^f, \tag{5.43}$$

$$\boldsymbol{\sigma}^f = -\nabla_x p \mathbf{I} + 2\mu^f \nabla_x^s \mathbf{v}, \tag{5.44}$$

$$\mathcal{L}^s(\mathbf{u}) = \rho_0^s \frac{\partial^2 \mathbf{u}}{\partial t^2} - \nabla_X \cdot \mathbf{P}, \tag{5.45}$$

$$\mathbf{P} = \mathbf{F} \mathbf{S}, \tag{5.46}$$

and \mathbf{n}_t^f and \mathbf{n}_0^s are the unit outward normal vectors to the fluid domain in the current, and the solid domain in the reference configurations, respectively. Standard arguments of distribution theory for (5.42) imply that the fluid and the solid PDEs hold in the interior of their respective domains, and the Neumann boundary conditions are satisfied on the appropriate parts of the fluid and solid domain boundaries. Selecting test functions that vanish everywhere in the domain except at the fluid-solid interface in (5.42) gives

$$\left\langle \mathbf{w}^f, \boldsymbol{\sigma}^f \mathbf{n}_t^f \right\rangle_{\Gamma_t^{fs}} + \left\langle \mathbf{w}^s, \mathbf{P} \mathbf{n}_0^s \right\rangle_{\Gamma_0^{fs}} = 0. \tag{5.47}$$

Transporting the second term in (5.47) to the current configuration, yields

$$\left\langle \mathbf{w}^f, \boldsymbol{\sigma}^f \mathbf{n}_t^f \right\rangle_{\Gamma_t^{fs}} + \left\langle \mathbf{w}^s \circ \chi^{-1}, \boldsymbol{\sigma}^s \mathbf{n}_t^s \right\rangle_{\Gamma_t^{fs}} = 0, \tag{5.48}$$

where $\boldsymbol{\sigma}^s$ is the Cauchy or true stress tensor. It is symmetric and is related to the first Piola-Kirchhoff

stress tensor \boldsymbol{P} through the Piola identity (see, e.g., [43])

$$\boldsymbol{\sigma}^s = J^{-1} \boldsymbol{P} \boldsymbol{F}^T. \quad (5.49)$$

Finally, using relationship (5.41) we arrive at the weak compatibility of surface tractions on the fluid-solid interface in the current configuration:

$$\left\langle \boldsymbol{w}^f, \boldsymbol{\sigma}^f \boldsymbol{n}_t^f + \boldsymbol{\sigma}^s \boldsymbol{n}_t^s \right\rangle_{\Gamma_t^{fs}} = 0. \quad (5.50)$$

5.2 Formulation of the fluid-structure interaction problem at the discrete level

In this section we give a formulation of the FSI equations (5.39) in the discrete setting. We begin by defining spatial discretization of the problem. Our only requirement on the trial weighting and solution spaces is that they are H^1 -conforming. Although we will only show examples which make use of the isogeometric approach, formulation presented here may be employed in conjunction with standard finite elements. Having defined the semi-discrete forms, we present the time advancement algorithm, which is the generalized- α method introduced in Chung and Hulbert [15].

5.2.1 Approximation spaces for ALE formulations and enforcement of kinematic compatibility conditions

We begin by considering the discretization of the reference domain Ω_0 . Here, and in what follows, we will use the same notation for discrete objects as for their continuous counterparts to simplify presentation. Let

$$\{\hat{N}_A(\boldsymbol{X})\}_{A \in I_t}, \quad \boldsymbol{X} \in \Omega_0 \quad (5.51)$$

denote a set of basis functions defined on Ω_0 , and let I_t denote the index set of all basis functions defined on Ω_0 . These functions do not depend on time, they are “fixed” in space on the reference domain. Consider a discrete ALE mapping $\boldsymbol{\chi}(\boldsymbol{X}, t)$, which maps Ω_0 onto Ω_t , the current configuration, and which can be expressed as a linear combination of basis functions in (5.51), and control points $\boldsymbol{\chi}_A \in \mathbb{R}^3$ (or nodal coordinates in standard finite elements) as

$$\boldsymbol{\chi}(\boldsymbol{X}, t) = \sum_{A \in I_t} \boldsymbol{\chi}_A(t) \hat{N}_A(\boldsymbol{X}) \quad (5.52)$$

We also choose to approximate the displacement field of the solid problem (5.5) in the same basis, that is

$$\mathbf{u}(\mathbf{X}, t) = \sum_{A \in I_s} U_A(t) \hat{N}_A(\mathbf{X}), \quad (5.53)$$

where $I_s \subset I_t$ is the index set of basis functions supported on the solid domain. This approach amounts to an isoparametric description. We assume that all basis functions in the reference configuration are at least C^0 -continuous, which automatically makes them H^1 -conforming. We also require \hat{N}_A 's with support in both fluid and solid subdomains to be C^0 -continuous across Γ_0^{fs} .

In contrast to the solid problem, the fluid subdomain motion (5.29) and the fluid (5.35) problems are posed over the current configuration with unknown fields being functions of the spatial coordinates \mathbf{x} . In order to approximate the unknown fields in the current domain, we define another set of basis functions, $\{N_A(\mathbf{x}, t)\}_{A \in I_f}$, as a push-forward of (5.51) to the current domain by the discrete ALE map (5.52), that is

$$N_A(\mathbf{x}, t) = \hat{N}_A \circ \chi^{-1}(\mathbf{x}, t) = \hat{N}_A(\chi^{-1}(\mathbf{x}, t)) \quad \forall A \in I_f, \mathbf{x} \in \Omega_t, \quad (5.54)$$

where $I_f \subset I_t$ is the index set of basis functions supported on the fluid domain. The above basis is used to approximate fluid velocity and pressure, and the fluid region displacement as

$$\mathbf{v}(\mathbf{x}, t) = \sum_{A \in I_f} \mathbf{V}_A(t) N_A(\mathbf{x}, t), \quad (5.55)$$

$$p(\mathbf{x}, t) = \sum_{A \in I_f} P_A(t) N_A(\mathbf{x}, t), \quad (5.56)$$

$$\gamma(\mathbf{x}, t) = \sum_{A \in I_f} \Upsilon_A(t) N_A(\mathbf{x}, t). \quad (5.57)$$

Note that due to the motion of the fluid domain, the basis functions in (5.54) are time-dependent.

Kinematic compatibility conditions (5.30) and (5.40), as well as conditions on the weighting spaces, (5.31) and (5.41), are essential for the continuous FSI problem (5.39) to ensure proper coupling. In the discrete setting there is a variety of ways of incorporating them into the formulation. For example, condition (5.40) may be imposed weakly (see, e.g., Bazilevs and Hughes [7]) by constructing additional terms on the fluid-solid interface using ideas of discontinuous Galerkin methods. As a result, incompatible fluid and solid discretizations may be employed. This approach is not adopted here. Instead, in our discrete formulation, we choose to satisfy the above mentioned conditions strongly as shown in the following.

Continuity of the discrete ALE mapping at the fluid-solid interface is ensured as follows. Let

$I_{fs} = I_f \cap I_s$ denote the indexed set of basis functions (and the associated geometry and solution degrees of freedom) supported on the fluid-solid boundary. Then, setting $\Upsilon_A = U_A \forall A \in I_{fs}$ gives

$$\mathbf{u}|_{\Gamma_0^{fs}} = \sum_{A \in I_{fs}} U_A \hat{N}_A|_{\Gamma_0^{fs}} = \sum_{A \in I_{fs}} \Upsilon_A (N_A \circ \chi)|_{\Gamma_0^{fs}} = \gamma \circ \chi|_{\Gamma_0^{fs}}, \quad (5.58)$$

which is precisely (5.30). Continuity of the ALE map together with continuity of the basis in the reference configuration assures that the basis functions in the current configuration are at least C^0 -continuous, and thus H^1 -conforming.

Kinematic compatibility condition (5.40), which ensures that the fluid particles adhere to the fluid-solid boundary, is satisfied by setting $\mathbf{V}_A = \partial U_A / \partial t \forall A \in I_{fs}$. Indeed,

$$\frac{\partial \mathbf{u}}{\partial t}|_{\Gamma_0^{fs}} = \sum_{A \in I_{fs}} \frac{\partial U_A}{\partial t} \hat{N}_A|_{\Gamma_0^{fs}} = \sum_{A \in I_{fs}} \mathbf{V}_A (N_A \circ \chi)|_{\Gamma_0^{fs}} = \mathbf{v} \circ \chi|_{\Gamma_0^{fs}}, \quad (5.59)$$

which is exactly (5.40).

Condition (5.31) is satisfied by setting to zero the weighting functions for the mesh motion problem supported on the fluid-solid interface, while a unique set of basis functions at the fluid-solid interface guarantees (5.41).

Finally, we demonstrate the following result:

Lemma 5.2.1. *Let $\mathbf{v} = \sum_{A \in I_f} \mathbf{V}_A N_A$. Then $\frac{\partial \mathbf{v}}{\partial t} = \sum_{A \in I_f} \partial \mathbf{V}_A / \partial t N_A$, where $\frac{\partial \mathbf{v}}{\partial t}$ is defined as in (5.38).*

Proof. Recall that $\frac{\partial \mathbf{v}}{\partial t}$ is the push-forward of the material fluid acceleration defined as $\frac{\partial \mathbf{v}}{\partial t} = \frac{\partial \hat{\mathbf{v}}}{\partial t} \circ \chi^{-1}$, where $\hat{\mathbf{v}} = \mathbf{v} \circ \chi$. Then

$$\begin{aligned} \hat{\mathbf{v}} &= \mathbf{v} \circ \chi = \left(\sum_{A \in I_f} \mathbf{V}_A N_A \right) \circ \chi \\ &= \sum_{A \in I_f} \mathbf{V}_A (N_A \circ \chi) = \sum_{A \in I_f} \mathbf{V}_A \hat{N}_A \end{aligned} \quad (5.60)$$

Taking a partial time derivative and composing with χ^{-1} , we obtain

$$\frac{\partial \mathbf{v}}{\partial t} = \frac{\partial \hat{\mathbf{v}}}{\partial t} \circ \chi^{-1} = \left(\sum_{A \in I_f} \frac{\partial \mathbf{V}_A}{\partial t} \hat{N}_A \right) \circ \chi^{-1} = \sum_{A \in I_f} \frac{\partial \mathbf{V}_A}{\partial t} N_A, \quad (5.61)$$

which is the desired result. \square

The interpretation of the above lemma is that the coefficients $\partial \mathbf{V}_A / \partial t$ are the control

variables for the material acceleration. Setting $\mathbf{V}_A = \partial \mathbf{U}_A / \partial t \forall A \in I_{fs}$ implies $\partial \mathbf{V}_A / \partial t = \partial^2 \mathbf{U}_A / \partial t^2 \forall A \in I_{fs}$, which, in turn, leads to the continuity of the material acceleration across the fluid-solid boundary.

Remark 5.2.1. *Same basis functions are used for the pressure as for the fluid particle velocity and the displacement of the fluid region. This is not necessary. One may use a different basis for pressure in order to satisfy the discrete BB condition. See, for example, Nobile [74] for use of mixed interpolations in the ALE setting.*

5.2.2 The semi-discrete problem

Let $\mathcal{V}_h^f, \mathcal{V}_h^s, \mathcal{V}_h^m$ and $\mathcal{W}_h^f, \mathcal{W}_h^s, \mathcal{W}_h^m$ be the finite dimensional subspaces of their infinite dimensional counterparts. We approximate the coupled fluid-structure interaction problem (5.39) as follows: Find $\{\mathbf{v}, p\} \in \mathcal{V}_h^f$, $\mathbf{u} \in \mathcal{V}_h^s$, and $\boldsymbol{\gamma} \in \mathcal{V}_h^m$ such that $\forall \{\mathbf{w}^f, q^f\} \in \mathcal{W}_h^f$, $\forall \mathbf{w}^s \in \mathcal{W}_h^s$, and $\forall \mathbf{w}^m \in \mathcal{W}_h^m$,

$$\begin{aligned} & B^f(\{\mathbf{w}^f, q^f\}, \{\mathbf{v}, p\}; \boldsymbol{\beta}) - F^f(\{\mathbf{w}^f, q^f\}) + \\ & ((\mathbf{v} - \boldsymbol{\beta}) \cdot \nabla_x \mathbf{w}^f, \mathbf{v}')_{\tilde{\Omega}_t^f} + (\nabla_x q^f, \frac{1}{\rho^f} \mathbf{v}')_{\tilde{\Omega}_t^f} + \\ & (\nabla_x \cdot \mathbf{w}^f \rho^f \tau_C, \nabla_x \cdot \mathbf{v})_{\tilde{\Omega}_t^f} - (\mathbf{w}^f, \mathbf{v}' \cdot \nabla_x \mathbf{v})_{\tilde{\Omega}_t^f} - \\ & (\nabla_x \mathbf{w}^f, \frac{1}{\rho^f} \mathbf{v}' \otimes \mathbf{v}')_{\tilde{\Omega}_t^f} + (\mathbf{v}' \cdot \nabla_x \mathbf{w}^f \bar{\tau}, \mathbf{v}' \cdot \nabla_x \mathbf{v})_{\tilde{\Omega}_t^f} + \\ & B^s(\mathbf{w}^s, \mathbf{u}) - F^s(\mathbf{w}^s) + B^m(\mathbf{w}^m, \boldsymbol{\gamma}) = 0, \end{aligned} \quad (5.62)$$

with the following definition of terms:

$$\mathbf{v}' = \tau_M(\mathcal{L}^f(\mathbf{v}, p; \boldsymbol{\beta}) - \rho^f \mathbf{f}^f), \quad (5.63)$$

$$\tau_M = (\frac{C_t}{\Delta t^2} + (\mathbf{v} - \boldsymbol{\beta}) \cdot \mathbf{G}(\mathbf{v} - \boldsymbol{\beta}) + C_I(\frac{\mu^f}{\rho^f})^2 \mathbf{G} : \mathbf{G})^{-1/2}, \quad (5.64)$$

$$\tau_C = (\mathbf{g} \cdot \tau_M \mathbf{g})^{-1}, \quad (5.65)$$

and

$$\bar{\tau} = (\mathbf{v}' \cdot \mathbf{G} \mathbf{v}')^{-1/2}. \quad (5.66)$$

In expressions (5.64-5.66) \mathbf{G} is a second rank metric tensor

$$\mathbf{G} = \frac{\partial \boldsymbol{\xi}}{\partial \mathbf{x}}^T \frac{\partial \boldsymbol{\xi}}{\partial \mathbf{x}}, \quad (5.67)$$

\mathbf{g} is a vector obtained by contracting \mathbf{G} on its first index as

$$\mathbf{g} = (\mathbf{g})_i = \sum_{j=1}^d (\mathbf{G})_{ji}, \quad (5.68)$$

and $\frac{\partial \boldsymbol{\xi}}{\partial \mathbf{x}}$ is the inverse Jacobian of the mapping between the elements in the parent and physical domains. In (5.62) the symbol $\tilde{\Omega}_t^f$ is used to denote the fact that integrals are taken over element interiors.

The first eight terms of (5.62) pertain to the fluid description. The formulation originates from the multiscale residual-based turbulence modeling paradigm proposed in Calo [14], and Hughes, Calo, and Scovazzi [51], and treated in detail in the previous chapter. Residual-based formulation of fluid flow may be viewed as an extension of well-known stabilized methods to the nonlinear realm. Terms on the first line emanate from Galerkin's method. Terms three, four, and five represent the standard SUPG stabilization for INS extended to the ALE description. Terms six and seven model the second cross-stress and the Reynolds stress contributions. The eighth term is not motivated by multiscale arguments, it merely provides additional residual-based stabilization for term six, which is advection-like (see Taylor, Hughes, and Zarins for details [97]). Terms nine and ten of (5.62) pertain to the description of the nonlinear solid, while the last term represents the mesh motion. Galerkin's method is employed for both as it is optimal for strongly elliptic problems.

5.2.3 Time integration of the FSI system

In this section we present the time integration algorithm for semi-discrete equations (5.62). The method is an application of generalized- α algorithm proposed by Chung and Hulbert [15] for the equations of structural dynamics, and extended to the equations of fluid mechanics by Jansen, Whiting, and Hulbert [56]. In the context of fluid-structure interaction, generalized- α method was applied to coupling of the linearized Euler equations with the nonlinear structure in one spatial dimension by Kuhl, Hulshoff, and de Borst [64]. In this section we give details of the method as it applies to the semi-discrete formulation (5.62).

We begin by making the following observations. In the solid region, where the basis functions are independent of time, solution coefficients of the displacement, velocity, and acceleration

fields are related through time derivatives. That is, for every basis function A ,

$$\mathbf{A}_A = \frac{\partial \mathbf{V}_A}{\partial t} = \frac{\partial^2 \mathbf{U}_A}{\partial t^2}, \forall A \in I_s, \quad (5.69)$$

where \mathbf{A}_A 's are acceleration coefficients. Denoting by $(\dot{\cdot})$ and $(\ddot{\cdot})$ the first and second time derivatives, we set $\mathbf{A}_A = \ddot{\mathbf{U}}_A$ and $\mathbf{V}_A = \dot{\mathbf{U}}_A$, $\forall A \in I_s$.

In the fluid region the situation is similar. Thanks to lemma 5.2.1, coefficients of the fluid velocity and material acceleration are also related through time derivatives despite the fact that the basis functions used in the expansion of these fields are time-dependent. As a result, we also set $\mathbf{A}_A = \ddot{\mathbf{U}}_A$ and $\mathbf{V}_A = \dot{\mathbf{U}}_A$, $\forall A \in I_f$. Note that there is no “fluid displacement” in our formulation, $\dot{\mathbf{U}}_A$ and $\ddot{\mathbf{U}}_A$ are simply labels that we chose for fluid velocity and acceleration coefficients in the interest of a concise presentation of the time integration algorithm.

The above observations, together with the the discrete kinematic compatibility conditions, allow one to have a unique set of degrees of freedom representing displacement, velocity, and acceleration for the coupled fluid-structure system. Likewise, let Υ_A , $\dot{\Upsilon}_A$, and $\ddot{\Upsilon}_A$, $\forall A \in I_f$ represent the coefficients of the mesh displacement, velocity, and acceleration, respectively. We define three discrete nonlinear residuals as:

$$\begin{aligned} R_{A,i}^{mom}(\mathbf{U}, \dot{\mathbf{U}}, \ddot{\mathbf{U}}, \mathbf{P}, \Upsilon, \dot{\Upsilon}, \ddot{\Upsilon}) = & \\ & (N_A \mathbf{e}_i, \rho^f \frac{\partial \mathbf{v}}{\partial t} + \rho^f (\mathbf{v} - \boldsymbol{\beta}) \cdot \nabla_x \mathbf{v} - \rho^f \mathbf{f}^f)_{\Omega_t^f} + \\ & (\nabla_x N_A \mathbf{e}_i, -p \mathbf{I} + 2\mu^f \nabla_x^s \mathbf{v})_{\Omega_t^f} - (N_A \mathbf{e}_i, \mathbf{h}^f)_{\Gamma_t^{f,N}} + \\ & ((\mathbf{v} - \boldsymbol{\beta}) \cdot \nabla_x N_A \mathbf{e}_i, \mathbf{v}')_{\tilde{\Omega}_t^f} + (\nabla_x \cdot N_A \mathbf{e}_i, \rho^f \tau_C \nabla_x \cdot \mathbf{v})_{\tilde{\Omega}_t^f} - \\ & (N_A \mathbf{e}_i, \mathbf{v}' \cdot \nabla_x \mathbf{v})_{\tilde{\Omega}_t^f} - (\nabla_x N_A \mathbf{e}_i, \frac{1}{\rho^f} \mathbf{v}' \otimes \mathbf{v}')_{\tilde{\Omega}_t^f} + \\ & (\mathbf{v}' \cdot \nabla_x N_A \mathbf{e}_i \bar{\tau}, \mathbf{v}' \cdot \nabla_x \mathbf{v})_{\tilde{\Omega}_t^f} + (\hat{N}_A \mathbf{e}_i, \rho_0^s \frac{\partial^2 \mathbf{u}}{\partial t^2} - \rho_0^s \mathbf{f}^s)_{\Omega_0^s} + \\ & (\nabla_X \hat{N}_A \mathbf{e}_i, \mathbf{F}(\mathbf{u}) \mathbf{S}(\mathbf{u}))_{\Omega_0^s} - (\hat{N}_A \mathbf{e}_i, \mathbf{h}^s)_{\Gamma_t^{s,N}}. \end{aligned} \quad (5.70)$$

$$\begin{aligned} R_A^{cont}(\mathbf{U}, \dot{\mathbf{U}}, \ddot{\mathbf{U}}, \mathbf{P}, \Upsilon, \dot{\Upsilon}, \ddot{\Upsilon}) = & \\ & (N_A, \nabla_x \cdot \mathbf{v})_{\Omega_t^f} + (\nabla_x N_A, \frac{1}{\rho^f} \mathbf{v}')_{\tilde{\Omega}_t^f} \end{aligned} \quad (5.71)$$

and

$$R_{A,i}^{mesh}(\mathbf{U}, \dot{\mathbf{U}}, \ddot{\mathbf{U}}, \mathbf{P}, \boldsymbol{\Upsilon}, \dot{\boldsymbol{\Upsilon}}, \ddot{\boldsymbol{\Upsilon}}) = (\nabla_x N_A \mathbf{e}_i, 2\mu^m \nabla_x^s (\boldsymbol{\gamma} - \tilde{\boldsymbol{\gamma}}) + \lambda^m \nabla_x \cdot (\boldsymbol{\gamma} - \tilde{\boldsymbol{\gamma}}))_{\Omega_i^f}. \quad (5.72)$$

In the above \mathbf{e}_i be the i^{th} Cartesian basis vector, and \mathbf{U} , \mathbf{P} , $\boldsymbol{\Upsilon}$, and their time derivatives, collect the discrete solution coefficients into a single vector of unknowns. $R_{A,i}^{mom}$ is the combined fluid and solid residual of the linear momentum equations for the A^{th} basis function in the spatial direction i , R_A^{cont} is the residual of the fluid continuity equation for the A^{th} basis function, and $R_{A,i}^{mesh}$ is the residual of the mesh motion equations for the A^{th} basis function in the i^{th} spatial direction. Note that in contrast to more traditional presentations, no distinction is made between the fluid and solid momentum residuals. Coupled PDEs are treated as one physical system. This presentation foreshadows the implementation of the method in which the fluid and solid partitions contribute to a global nonlinear equation system according to their designation.

Generalized- α time integration algorithm consists of the following: given the solution at time level t^n , find the solution at time level t^{n+1} , such that

$$\begin{aligned} R_{A,i}^{mom}(\mathbf{U}_{n+\alpha_f}, \dot{\mathbf{U}}_{n+\alpha_f}, \ddot{\mathbf{U}}_{n+\alpha_m}, \mathbf{P}_{n+1}, \boldsymbol{\Upsilon}_{n+\alpha_f}, \dot{\boldsymbol{\Upsilon}}_{n+\alpha_f}, \ddot{\boldsymbol{\Upsilon}}_{n+\alpha_m}) &= 0_{A,i}, \\ R_A^{cont}(\mathbf{U}_{n+\alpha_f}, \dot{\mathbf{U}}_{n+\alpha_f}, \ddot{\mathbf{U}}_{n+\alpha_m}, \mathbf{P}_{n+1}, \boldsymbol{\Upsilon}_{n+\alpha_f}, \dot{\boldsymbol{\Upsilon}}_{n+\alpha_f}, \ddot{\boldsymbol{\Upsilon}}_{n+\alpha_m}) &= 0_A, \\ R_{A,i}^{mesh}(\mathbf{U}_{n+\alpha_f}, \dot{\mathbf{U}}_{n+\alpha_f}, \ddot{\mathbf{U}}_{n+\alpha_m}, \mathbf{P}_{n+1}, \boldsymbol{\Upsilon}_{n+\alpha_f}, \dot{\boldsymbol{\Upsilon}}_{n+\alpha_f}, \ddot{\boldsymbol{\Upsilon}}_{n+\alpha_m}) &= 0_{A,i}. \end{aligned} \quad (5.73)$$

Generalized- α method forces nonlinear residuals, evaluated at two temporal locations $n + \alpha_m$ and $n + \alpha_f$ defined as

$$(\cdot)_{n+\alpha_m} = (\cdot)_n + \alpha_m ((\cdot)_{n+1} - (\cdot)_n) \quad (5.74)$$

$$(\cdot)_{n+\alpha_f} = (\cdot)_n + \alpha_f ((\cdot)_{n+1} - (\cdot)_n), \quad (5.75)$$

to vanish identically. Fluid and solid displacement, velocity, and acceleration solution coefficients are now related through the Newmark formulas (see, e.g., [44])

$$\dot{\mathbf{U}}_{n+1} = \dot{\mathbf{U}}_n + \Delta t((1 - \gamma)\ddot{\mathbf{U}}_n + \gamma\ddot{\mathbf{U}}_{n+1}), \quad (5.76)$$

$$\mathbf{U}_{n+1} = \mathbf{U}_n + \Delta t\dot{\mathbf{U}}_n + \frac{\Delta t^2}{2}((1 - 2\beta)\ddot{\mathbf{U}}_n + 2\beta\ddot{\mathbf{U}}_{n+1}). \quad (5.77)$$

Mesh motion coefficients engender the same relationships. Parametrs α_m and α_f are selected so as to ensure second order accuracy and unconditional stability of the time integrator. For a second

order linear ODE system with constant coefficients, which is related to the solid and the mesh parts of the FSI problem, Chung and Hulbert [15] showed that second order accuracy is ensured if

$$\gamma = \frac{1}{2} - \alpha_f + \alpha_m, \quad (5.78)$$

and

$$\beta = \frac{1}{4}(1 - \alpha_f + \alpha_m)^2, \quad (5.79)$$

while unconditional stability is guaranteed if

$$\alpha_m \geq \alpha_f \geq \frac{1}{2}. \quad (5.80)$$

Results (5.78) and (5.80) were also shown by Jansen, Whiting, and Hulbert [56] to hold true for a first order linear ODE system with constant coefficients, which is related to the fluid part of the FSI system. Condition (5.79) is only applicable to the second order case. In order to have strict control over high frequency damping, both sources parametrize α_m and α_f with ρ_∞ , the spectral radius of the amplification matrix at an infinitely large time step. Optimal high frequency damping occurs when all the eigenvalues of the amplification matrix take on the same value, and are equal to $-\rho_\infty$. In this case, for the second order system, Chung and Hulbert [15] derive

$$\begin{aligned} \alpha_m^h &= \frac{2 - \rho_\infty^h}{1 + \rho_\infty^h}, \\ \alpha_f^h &= \frac{1}{1 + \rho_\infty^h}, \end{aligned} \quad (5.81)$$

while for the first order system Jansen *et al.* [56] give

$$\begin{aligned} \alpha_m^j &= \frac{1}{2} \left(\frac{3 - \rho_\infty^j}{1 + \rho_\infty^j} \right), \\ \alpha_f^j &= \frac{1}{1 + \rho_\infty^j}, \end{aligned} \quad (5.82)$$

where superscripts distinguish the quantities coming from two different methods. The above equations show that for the same values of ρ_∞ (that is, $\rho_\infty^h = \rho_\infty^j$) there is an implied mismatch between the acceleration levels for the fluid and the solid, while for different values of ρ_∞ (that is, $\rho_\infty^h \neq \rho_\infty^j$) there is an implied mismatch in the velocity levels for both systems. Both inconsistencies are eliminated for $\rho_\infty^h = \rho_\infty^j = 1$, the case of zero high frequency damping which also corresponds to the midpoint rule. This fact was also noted in Kuhl, Hulshoff, and de Borst [64]. In this work, we adopt

expressions (5.82), thus making the fluid part of the problem optimally damped, and examine the eigenvalues of the amplification matrix for a second order linear ODE system at an infinitely large time step:

$$\lim_{\Delta t \rightarrow \infty} \lambda = \left\{ \frac{-1 + (\alpha_m^j - \alpha_f^j)}{1 + (\alpha_m^j - \alpha_f^j)}, \frac{-1 + (\alpha_m^j - \alpha_f^j)}{1 + (\alpha_m^j - \alpha_f^j)}, 1 - \frac{1}{\alpha_f^j} \right\}. \quad (5.83)$$

Inserting (5.82) into the expression above, we get

$$\lim_{\Delta t \rightarrow \infty} \lambda = \left\{ \frac{-1 - 3\rho_\infty^j}{3 + \rho_\infty^j}, \frac{-1 - 3\rho_\infty^j}{3 + \rho_\infty^j}, -\rho_\infty^j \right\}. \quad (5.84)$$

While the third eigenvalue remains unchanged, the first two are different, but it is a simple matter to show that they are monotone decreasing functions of ρ_∞^j and

$$\frac{1}{3} \leq \left| \frac{-1 - 3\rho_\infty^j}{3 + \rho_\infty^j} \right| \leq 1 \quad \forall |\rho_\infty^j| \leq 1, \quad (5.85)$$

which means that the spectral radius of the amplification matrix never exceeds unity in magnitude and no instabilities are incurred in a second order system. Note that this choice of parameters does not upset second order accuracy and unconditional stability of the method because conditions (5.78 -5.80) are preserved.

Remark 5.2.2. *It should be noted that Newmark relationships (5.76) constitute an approximation to time derivatives. They are used directly on the solution coefficients of the discrete FSI problem. This approximation is valid due to the fact that our discrete FSI problem was formulated in a way that solution coefficients are truly related through time derivatives.*

5.3 Linearization of the discrete FSI system: a methodology for computing shape derivatives

Fully discrete system (5.73) constitutes a set of nonlinear algebraic equations to be solved at each time step of the generalized- α time integrator. Inside the time integration loop Newton's method is used as the main driver. The latter requires an appropriate linearization of (5.73). We will work with acceleration and pressure increments, thus we define the following quantities. Let $\ddot{U}_{B,j}$ collect acceleration degrees of freedom for every basis function B and every Cartesian direction j . Note that the kinematic constraint (5.40) implies that there is a unique set of acceleration degrees of freedom at the fluid-solid interface. Let P_B collect the fluid pressure degrees of freedom for every basis function B , and let $\ddot{\Upsilon}_{B,j}$ denote the mesh accelerations degrees of freedom. Newton iteration

for the discrete FSI system (5.73) is

$$\begin{aligned}
R_{A,i}^{mom,\nu} + \frac{\partial R_{A,i}^{mom,\nu}}{\partial \ddot{U}_{B,j}^{n+1}} \Delta \ddot{U}_{B,j}^{n+1,\nu} + \\
\frac{\partial R_{A,i}^{mom,\nu}}{\partial P_B^{n+1}} \Delta P_B^{n+1,\nu} + \frac{\partial R_{A,i}^{mom,\nu}}{\partial \ddot{\Upsilon}_{B,j}^{n+1}} \Delta \ddot{\Upsilon}_{B,j}^{n+1,\nu} = 0, \\
R_A^{cont,\nu} + \frac{\partial R_A^{cont,\nu}}{\partial \ddot{U}_{B,j}^{n+1}} \Delta \ddot{U}_{B,j}^{n+1,\nu} + \\
\frac{\partial R_A^{cont,\nu}}{\partial P_B^{n+1}} \Delta P_B^{n+1,\nu} + \frac{\partial R_A^{cont,\nu}}{\partial \ddot{\Upsilon}_{B,j}^{n+1}} \Delta \ddot{\Upsilon}_{B,j}^{n+1,\nu} = 0, \\
R_{A,i}^{mesh,\nu} + \frac{\partial R_{A,i}^{mesh,\nu}}{\partial \ddot{U}_{B,j}^{n+1}} \Delta \ddot{U}_{B,j}^{n+1,\nu} + \\
\frac{\partial R_{A,i}^{mesh,\nu}}{\partial P_B^{n+1}} \Delta P_B^{n+1,\nu} + \frac{\partial R_{A,i}^{mesh,\nu}}{\partial \ddot{\Upsilon}_{B,j}^{n+1}} \Delta \ddot{\Upsilon}_{B,j}^{n+1,\nu} = 0,
\end{aligned} \tag{5.86}$$

supplemented with the update formulas

$$\ddot{U}_{B,j}^{n+1,\nu+1} = \ddot{U}_{B,j}^{n+1,\nu} + \Delta \ddot{U}_{B,j}^{n+1,\nu}, \tag{5.87}$$

$$\dot{U}_{B,j}^{n+1,\nu+1} = \dot{U}_{B,j}^{n+1,\nu} + \gamma \Delta t \Delta \ddot{U}_{B,j}^{n+1,\nu}, \tag{5.88}$$

$$U_{B,j}^{n+1,\nu+1} = U_{B,j}^{n+1,\nu} + \beta (\Delta t)^2 \Delta \ddot{U}_{B,j}^{n+1,\nu}, \tag{5.89}$$

$$\ddot{\Upsilon}_{B,j}^{n+1,\nu+1} = \ddot{\Upsilon}_{B,j}^{n+1,\nu} + \Delta \ddot{\Upsilon}_{B,j}^{n+1,\nu}, \tag{5.90}$$

$$\dot{\Upsilon}_{B,j}^{n+1,\nu+1} = \dot{\Upsilon}_{B,j}^{n+1,\nu} + \gamma \Delta t \Delta \ddot{\Upsilon}_{B,j}^{n+1,\nu}, \tag{5.91}$$

$$\Upsilon_{B,j}^{n+1,\nu+1} = \Upsilon_{B,j}^{n+1,\nu} + \beta (\Delta t)^2 \Delta \ddot{\Upsilon}_{B,j}^{n+1,\nu}, \tag{5.92}$$

$$P_B^{n+1,\nu+1} = P_B^{n+1,\nu} + \Delta P_B^{n+1,\nu}, \tag{5.93}$$

where ν is the Newton iteration index. Residuals in equations (5.86) are taken at the intermediate time levels $t_{n+\alpha_m}$ and $t_{n+\alpha_f}$, while partial derivatives are taken with respect to the solution variables at time level t_{n+1} as indicated by the superscripts. The resulting scheme falls in the class of predictor-multicorrector algorithms (see, e.g., Brooks and Hughes [12]).

Derivatives of the momentum, continuity, and mesh motion residuals with respect to solution variables define the so-called *tangent matrices*. In particular, derivatives of the momentum and continuity residuals with respect to the mesh motion variables are referred to as *shape derivatives*. Computation of shape derivatives is required for consistent linearization of the discrete FSI system. To the authors' knowledge, the only reference in which this issue is addressed is [26], where shape

derivative operators based on space-continuous ALE formulation of incompressible Navier-Stokes equations are derived. It is advocated in this work that the relevant object in nonlinear analysis is not the “continuum tangent”, which is a discretization of a derivative operator of the continuous formulation, but the “algorithmic tangent”, which is a tangent matrix that is derived from a given discrete formulation. It is precisely the latter that gives quadratic convergence of the Newton iteration, and is most robust in practice.

In this section we focus on presenting a methodology for deriving shape derivatives and provide explicit expressions for these tangent matrices coming from our discrete formulation of the FSI problem. These results are new and comprise one of the main contributions of this dissertation. This methodology is applicable to other FSI formulations, including the space-time approach advocated in [99, 100, 102].

5.3.1 Shape derivatives

We begin by introducing notation. Let $\mathbf{x} = \mathbf{x}(\boldsymbol{\xi})$ denote the mapping between the elements in the parent and the physical domains defined on each element. Let $\frac{\partial \mathbf{x}}{\partial \boldsymbol{\xi}}$ be the Jacobian of this mapping, let $\frac{\partial \boldsymbol{\xi}}{\partial \mathbf{x}} = \frac{\partial \mathbf{x}}{\partial \boldsymbol{\xi}}^{-1}$ be its inverse, and let $J_{\boldsymbol{\xi}} = \det \frac{\partial \mathbf{x}}{\partial \boldsymbol{\xi}}$ be its determinant. Cartesian basis will be used throughout and, in what follows, operations on vectors and tensors will be expressed through operations on their components in the Cartesian basis. Let x_i and ξ_i denote the i^{th} component of \mathbf{x} and $\boldsymbol{\xi}$, respectively, and let $(\frac{\partial \mathbf{x}}{\partial \boldsymbol{\xi}})_{ij} = \frac{\partial x_i}{\partial \xi_j}$, and $(\frac{\partial \boldsymbol{\xi}}{\partial \mathbf{x}})_{ij} = \frac{\partial \xi_i}{\partial x_j}$ be the components of the Jacobian and its inverse.

The following identities, standard in nonlinear continuum mechanics (see, e.g., Holzapfel [43]) will be used in the sequel:

$$\mathcal{D}\left(\frac{\partial \xi_i}{\partial x_j}\right) = -\frac{\partial \xi_i}{\partial x_l} \mathcal{D}\left(\frac{\partial x_l}{\partial \xi_k}\right) \frac{\partial \xi_k}{\partial x_j}, \quad (5.94)$$

and

$$\mathcal{D}J_{\boldsymbol{\xi}} = J_{\boldsymbol{\xi}} \frac{\partial \xi_j}{\partial x_i} \mathcal{D}\left(\frac{\partial x_i}{\partial \xi_j}\right), \quad (5.95)$$

where \mathcal{D} denotes a general derivative operator. Summation convention on repeated indices is used throughout. Making use of equations (5.94 - 5.95) and the chain rule of differentiation, we obtain

$$\mathcal{D}\left(J_{\boldsymbol{\xi}} \frac{\partial \xi_i}{\partial x_j}\right) = J_{\boldsymbol{\xi}} \left(\frac{\partial \xi_l}{\partial x_k} \mathcal{D}\left(\frac{\partial x_k}{\partial \xi_l}\right) \frac{\partial \xi_i}{\partial x_j} - \frac{\partial \xi_i}{\partial x_l} \mathcal{D}\left(\frac{\partial x_l}{\partial \xi_k}\right) \frac{\partial \xi_k}{\partial x_j} \right), \quad (5.96)$$

and, furthermore,

$$\begin{aligned} \mathcal{D}(J_\xi \frac{\partial \xi_i}{\partial x_j} \frac{\partial \xi_m}{\partial x_n}) = \\ J_\xi \{ \frac{\partial \xi_l}{\partial x_k} \mathcal{D}(\frac{\partial x_k}{\partial \xi_l}) \frac{\partial \xi_i}{\partial x_j} - \frac{\partial \xi_i}{\partial x_l} \mathcal{D}(\frac{\partial x_l}{\partial \xi_k}) \frac{\partial \xi_k}{\partial x_j} \} \frac{\partial \xi_m}{\partial x_n} - J_\xi \frac{\partial \xi_i}{\partial x_j} \frac{\partial \xi_m}{\partial x_l} \mathcal{D}(\frac{\partial x_l}{\partial \xi_k}) \frac{\partial \xi_k}{\partial x_n}. \end{aligned} \quad (5.97)$$

Our task is to derive expressions for shape derivatives in a term-by-term fashion. We will treat several terms in detail so as to make the underlying procedures clear. Results for the rest of the terms will be stated without derivation.

Consider the expression

$$\frac{\partial R_{A,i}^{mom}}{\partial \ddot{\Upsilon}_{B,j}}. \quad (5.98)$$

This is a derivative of the discrete residual of momentum equation with respect to mesh acceleration degrees of freedom. In (5.98), temporal as well as iteration superscripts are omitted in the interest of a concise exposition. This derivative is active in the fluid region only, so we consider just the Navier-Stokes contributions to the discrete residual.

Acceleration term

We begin with the acceleration contribution to the shape derivative matrix, that is

$$\frac{\partial \sum_{e=1}^{N_{el}} \int_{\Omega_e} N_{A,\underline{i}} \rho^f \frac{\partial v_i}{\partial t} d\Omega_e}{\partial \ddot{\Upsilon}_{B,j}}. \quad (5.99)$$

In (5.99) N_{el} is the number of elements in the fluid mesh, Ω_e is the domain of the spatial element, and the underlined index indicates that no sum is taken over it. Subscript \underline{i} on the basis function N_A is used to denote a Cartesian direction and index the resultant matrix contribution. Otherwise, no distinction is made between basis functions approximating different components of the solution vector.

Taking the partial derivative operator inside the sum over the elements, for a given element e we obtain

$$\frac{\partial \int_{\Omega_e} N_{A,\underline{i}} \rho^f \frac{\partial v_i}{\partial t} d\Omega_e}{\partial \ddot{\Upsilon}_{B,j}}. \quad (5.100)$$

In (5.100) we cannot take the partial derivative operator inside the integral, as the region of integration directly depends on the mesh motion. In order to circumvent this difficulty, we change variables

under the integral, $x \rightarrow \xi$. With this change of variables expression (5.100) becomes

$$\int_{\hat{\Omega}_e} \hat{N}_{A,\underline{i}} \hat{\rho}^f \frac{\partial \hat{v}_{\underline{i}}}{\partial t} \frac{\partial J_\xi}{\partial \ddot{\Upsilon}_{B,j}} d\hat{\Omega}_e, \quad (5.101)$$

where $\hat{(\cdot)}$ is used to denote the fact that the quantity is a function of the parent domain variable ξ . Note that basis functions, and particle density and acceleration in the parent domain are independent of the mesh motion variables, hence the partial derivative only affects the Jacobian determinant. Using expression (5.95) in (5.101) gives

$$\int_{\hat{\Omega}_e} \hat{N}_{A,\underline{i}} \hat{\rho}^f \frac{\partial \hat{v}_{\underline{i}}}{\partial t} \frac{\partial(\frac{\partial x_k}{\partial \xi_l})}{\partial \ddot{\Upsilon}_{B,j}} \frac{\partial \xi_l}{\partial x_k} J_\xi d\hat{\Omega}_e \quad (5.102)$$

The term $\frac{\partial(\frac{\partial x_k}{\partial \xi_l})}{\partial \ddot{\Upsilon}_{B,j}} \frac{\partial \xi_l}{\partial x_k}$ is analyzed as follows. Recall the definition of x_k

$$x_k(\xi) = \chi_k(\xi) = \delta_k(\xi) + X_k(\xi), \quad (5.103)$$

where X_k are components of a local geometrical mapping and δ_k are components of the local mesh displacement in the reference domain. Then,

$$\frac{\partial x_k}{\partial \xi_l} = \frac{\partial \delta_k}{\partial \xi_l} + \frac{\partial X_k}{\partial \xi_l}, \quad (5.104)$$

which implies

$$\frac{\partial(\frac{\partial x_k}{\partial \xi_l})}{\partial \ddot{\Upsilon}_j^B} = \frac{\partial(\frac{\partial \delta_k}{\partial \xi_l})}{\partial \ddot{\Upsilon}_j^B}, \quad (5.105)$$

as the second term in (5.104) is independent of the mesh motion. Mesh displacement $\delta_k(\xi)$ is defined as a linear combination of mesh displacement coefficients and basis functions, that is

$$\delta_{\underline{k}}(\xi) = \sum_{A=1}^{N_{shl}} \Upsilon_{A,\underline{k}} \hat{N}_{A,\underline{k}}(\xi), \quad (5.106)$$

where N_{shl} is the number of element basis functions. The above implies

$$\frac{\partial(\frac{\partial x_k}{\partial \xi_l})}{\partial \ddot{\Upsilon}_{B,j}} \frac{\partial \xi_l}{\partial x_k} = \alpha_f \beta \Delta t^2 \frac{\partial \hat{N}_{B,\underline{j}}}{\partial \xi_l} \frac{\partial \xi_l}{\partial x_{\underline{j}}}. \quad (5.107)$$

In (5.107) we made use of Newmark update formulas (5.76) the relationship between displacements

at time levels t_{n+1} and $t_{n+\alpha_f}$. Inserting (5.107) into (5.102), changing variables back to the physical domain, and summing over the elements of the fluid mesh, we finally get

$$\sum_{e=1}^{N_{el}} \alpha_f \beta \Delta t^2 \int_{\Omega_e} N_{A,\underline{i}} \rho^f \frac{\partial v_{\underline{i}}}{\partial t} \frac{\partial N_{B,j}}{\partial x_{\underline{j}}} d\Omega_e. \quad (5.108)$$

Matrix (5.108) is the contribution to the shape derivative matrix (5.98) from the acceleration term present in the discrete momentum equations of the INS system. It appears to be form-identical to the matrices that contribute to the tangents in the analysis of fluids and solids, and its implementation in a finite element and isogeometric codes is standard.

Advection term

In the acceleration term the coupling between the momentum residual and the mesh motion variables occurs exclusively through the determinant Jacobian of the ALE mapping. Other terms of the discrete INS system exhibit more complex coupling. For instance, consider the advective contribution to the momentum residual

$$\begin{aligned} \sum_{e=1}^{N_{el}} \int_{\Omega_e} N_{A,\underline{i}} \rho^f (v_k - \beta_k) \frac{\partial v_{\underline{i}}}{\partial x_k} d\Omega_e = \\ \sum_{e=1}^{N_{el}} \int_{\Omega_e} N_{A,\underline{i}} \rho^f v_k \frac{\partial v_{\underline{i}}}{\partial x_k} d\Omega_e - \sum_{e=1}^{N_{el}} \int_{\Omega_e} N_{A,\underline{i}} \rho^f \beta_k \frac{\partial v_{\underline{i}}}{\partial x_k} d\Omega_e. \end{aligned} \quad (5.109)$$

Restricting the sum to a single element, changing variables to the parent domain, and taking the derivative with respect to the mesh acceleration degrees of freedom gives

$$\int_{\hat{\Omega}_e} \hat{N}_{A,\underline{i}} \hat{\rho}^f (\hat{v}_k - \hat{\beta}_k) \frac{\partial \hat{v}_{\underline{i}}}{\partial \hat{\xi}_l} \frac{\partial (\frac{\partial \hat{\xi}_l}{\partial x_k} J_{\xi})}{\partial \hat{\Upsilon}_{B,j}} d\hat{\Omega}_e - \int_{\hat{\Omega}_e} \hat{N}_{A,\underline{i}} \hat{\rho}^f \frac{\partial \hat{v}_{\underline{i}}}{\partial \hat{\xi}_l} \frac{\partial \hat{\xi}_l}{\partial x_k} \frac{\partial \hat{\beta}_k}{\partial \hat{\Upsilon}_{B,j}} J_{\xi} d\hat{\Omega}_e \quad (5.110)$$

Using relation (5.96) in the first term of (5.110) gives

$$\begin{aligned} \int_{\hat{\Omega}_e} \hat{N}_{A,\underline{i}} \hat{\rho}^f (\hat{v}_k - \hat{\beta}_k) \frac{\partial \hat{v}_{\underline{i}}}{\partial \hat{\xi}_l} \left(\frac{\partial \xi_m}{\partial x_n} \frac{\partial (\frac{\partial x_n}{\partial \xi_m})}{\partial \hat{\Upsilon}_{B,j}} \frac{\partial \hat{\xi}_l}{\partial x_k} - \right. \\ \left. \frac{\partial \hat{\xi}_l}{\partial x_n} \frac{\partial (\frac{\partial x_n}{\partial \xi_m})}{\partial \hat{\Upsilon}_{B,j}} \frac{\partial \xi_m}{\partial x_k} \right) J_{\xi} d\hat{\Omega}_e \end{aligned} \quad (5.111)$$

Changing variables back to the physical domain, taking the sum over the elements in the fluid mesh,

and accounting for the second term of (5.110), we get

$$\begin{aligned}
& \sum_{e=1}^{N_{el}} \alpha_f \beta \Delta t^2 \int_{\Omega_e} N_{A,\underline{i}} \rho^f (v_k - \beta_k) \frac{\partial v_{\underline{i}}}{\partial x_k} \frac{\partial N_{B,\underline{j}}}{\partial x_{\underline{j}}} d\Omega_e - \\
& \sum_{e=1}^{N_{el}} \alpha_f \beta \Delta t^2 \int_{\Omega_e} N_{A,\underline{i}} \rho^f (v_k - \beta_k) \frac{\partial v_{\underline{i}}}{\partial x_{\underline{j}}} \frac{\partial N_{B,\underline{j}}}{\partial x_k} d\Omega_e - \\
& \sum_{e=1}^{N_{el}} \alpha_f \gamma \Delta t \int_{\Omega_e} N_{A,\underline{i}} \rho^f \frac{\partial v_{\underline{i}}}{\partial x_{\underline{j}}} N_{B,\underline{j}} d\Omega_e.
\end{aligned} \tag{5.112}$$

Matrix (5.112) is the contribution to the shape derivative matrix (5.98) from the advection term present in the momentum equations of the INS system. It also appears to be form-identical to the matrices that contribute to the tangents in the analysis of fluids and solids, but contains more terms than its acceleration counterpart. Implementation is also standard in this case.

Pressure stabilization term

As a final example we present the derivation of the contribution to the shape derivative from the discrete continuity equation, that is

$$\frac{\partial R_A^{cont}}{\partial \ddot{\Upsilon}_{B,j}}. \tag{5.113}$$

Consider the pressure contribution from the stabilizing terms, that is

$$\sum_{e=1}^{N_{el}} \int_{\Omega_e} \frac{\partial N_A}{\partial x_i} \frac{\tau_M}{\rho^f} \frac{\partial p}{\partial x_i} d\Omega_e. \tag{5.114}$$

As before, restricting to a single element and changing variables gives

$$\int_{\hat{\Omega}_e} \frac{\partial \hat{N}_A}{\partial \xi_k} \frac{\partial \xi_k}{\partial x_i} \frac{\hat{\tau}_M}{\hat{\rho}^f} \frac{\partial \hat{p}}{\partial \xi_l} \frac{\partial \xi_l}{\partial x_i} J_\xi d\hat{\Omega}_e. \tag{5.115}$$

Taking the derivative with respect to the acceleration degrees of freedom and isolating terms independent of the mesh motion we get

$$\begin{aligned}
\int_{\hat{\Omega}_e} \frac{\partial \hat{N}_A}{\partial \xi_k} \frac{1}{\hat{\rho}^f} \frac{\partial \hat{p}}{\partial \xi_l} \frac{\partial (\hat{\tau}_M \frac{\partial \xi_k}{\partial x_i} \frac{\partial \xi_l}{\partial x_i} J_\xi)}{\partial \ddot{\Upsilon}_{B,j}} d\hat{\Omega}_e &= \int_{\hat{\Omega}_e} \frac{\partial \hat{N}_A}{\partial \xi_k} \frac{\hat{\tau}_M}{\hat{\rho}^f} \frac{\partial \hat{p}}{\partial \xi_l} \frac{\partial (\frac{\partial \xi_k}{\partial x_i} \frac{\partial \xi_l}{\partial x_i} J_\xi)}{\partial \ddot{\Upsilon}_{B,j}} d\hat{\Omega}_e + \\
&\int_{\hat{\Omega}_e} \frac{\partial \hat{N}_A}{\partial \xi_k} \frac{1}{\hat{\rho}^f} \frac{\partial \hat{p}}{\partial \xi_l} \frac{\partial \xi_k}{\partial x_i} \frac{\partial \xi_l}{\partial x_i} J_\xi \frac{\partial \hat{\tau}_M}{\partial \ddot{\Upsilon}_{B,j}} d\hat{\Omega}_e.
\end{aligned} \tag{5.116}$$

The last term on the right-hand-side of the above expression involves the derivative of $\hat{\tau}_M$ with

respect to the mesh acceleration degrees of freedom. It is, in principle, present in the tangent matrix and is computable, but in this work it is omitted. In order to handle the first term on the right-hand-side of (5.116) we employ relation (5.97) to obtain

$$\begin{aligned} \int_{\hat{\Omega}_e} \frac{\partial \hat{N}_A}{\partial \xi_k} \frac{\hat{\tau}_M}{\hat{\rho}^f} \frac{\partial \hat{p}}{\partial \xi_l} & \left(\frac{\partial \xi_m}{\partial x_n} \frac{\partial(\frac{\partial x_n}{\partial \xi_m})}{\partial \ddot{\Upsilon}_{B,j}} \frac{\partial \xi_k}{\partial x_i} \frac{\partial \xi_l}{\partial x_i} - \right. \\ & \frac{\partial \xi_l}{\partial x_n} \frac{\partial(\frac{\partial x_n}{\partial \xi_m})}{\partial \ddot{\Upsilon}_{B,j}} \frac{\partial \xi_m}{\partial x_i} \frac{\partial \xi_k}{\partial x_i} - \\ & \left. \frac{\partial \xi_k}{\partial x_n} \frac{\partial(\frac{\partial x_n}{\partial \xi_m})}{\partial \ddot{\Upsilon}_{B,j}} \frac{\partial \xi_m}{\partial x_i} \frac{\partial \xi_l}{\partial x_i} \right) J_\xi d\hat{\Omega}_e. \end{aligned} \quad (5.117)$$

Changing variables back to the physical domain and summing over the fluid domain elements gives the following contribution to the shape derivative

$$\begin{aligned} \sum_{e=1}^{N_{el}} \alpha_f \beta \Delta t^2 \int_{\Omega_e} \frac{\partial N_A}{\partial x_i} \frac{\tau_M}{\rho^f} \frac{\partial p}{\partial x_i} \frac{\partial N_{B,j}}{\partial x_j} d\Omega_e - \\ \sum_{e=1}^{N_{el}} \alpha_f \beta \Delta t^2 \int_{\Omega_e} \frac{\partial N_A}{\partial x_i} \frac{\tau_M}{\rho^f} \frac{\partial p}{\partial x_j} \frac{\partial N_{B,j}}{\partial x_i} d\Omega_e - \\ \sum_{e=1}^{N_{el}} \alpha_f \beta \Delta t^2 \int_{\Omega_e} \frac{\partial N_A}{\partial x_j} \frac{\tau_M}{\rho^f} \frac{\partial p}{\partial x_i} \frac{\partial N_{B,j}}{\partial x_i} d\Omega_e. \end{aligned} \quad (5.118)$$

As before, these matrices and their implementation in a finite element FSI solver are standard. In what follows we give, without derivation, expressions for shape derivative contributions from some of the remaining terms in the formulation.

Pressure gradient term

$$\begin{aligned} - \frac{\partial \sum_{e=1}^{N_{el}} \int_{\Omega_e} \frac{\partial N_{A,i}}{\partial x_i} p d\Omega_e}{\partial \ddot{\Upsilon}_{B,j}} = \\ - \sum_{e=1}^{N_{el}} \alpha_f \beta \Delta t^2 \int_{\Omega_e} \frac{\partial N_{A,i}}{\partial x_i} p \frac{\partial N_{B,j}}{\partial x_j} - \frac{\partial N_{A,i}}{\partial x_j} p \frac{\partial N_{B,j}}{\partial x_i} d\Omega_e. \end{aligned} \quad (5.119)$$

Viscous stress term

$$\frac{\partial \sum_{e=1}^{N_{el}} \int_{\Omega_e} \frac{\partial N_{A,\underline{i}}}{\partial x_k} \mu^f \left(\frac{\partial v_{\underline{i}}}{\partial x_k} + \frac{\partial v_k}{\partial x_{\underline{i}}} \right) d\Omega_e}{\partial \ddot{\Upsilon}_{B,j}} = \quad (5.120)$$

$$\sum_{e=1}^{N_{el}} \alpha_f \beta \Delta t^2 \int_{\Omega_e} \frac{\partial N_{A,\underline{i}}}{\partial x_k} \mu^f \left(\frac{\partial v_{\underline{i}}}{\partial x_k} + \frac{\partial v_k}{\partial x_{\underline{i}}} \right) \frac{\partial N_{B,\underline{j}}}{\partial x_{\underline{j}}} -$$

$$\frac{\partial N_{A,\underline{i}}}{\partial x_{\underline{j}}} \mu^f \left(\frac{\partial v_{\underline{i}}}{\partial x_k} + \frac{\partial v_k}{\partial x_{\underline{i}}} \right) \frac{\partial N_{B,\underline{j}}}{\partial x_k} -$$

$$\frac{\partial N_{A,\underline{i}}}{\partial x_k} \mu^f \frac{\partial v_{\underline{i}}}{\partial x_{\underline{j}}} \frac{\partial N_{B,\underline{j}}}{\partial x_k} - \frac{\partial N_{A,\underline{i}}}{\partial x_k} \mu^f \frac{\partial v_k}{\partial x_{\underline{j}}} \frac{\partial N_{B,\underline{j}}}{\partial x_{\underline{i}}} d\Omega_e.$$

Body force term

$$\frac{\partial \sum_{e=1}^{N_{el}} \int_{\Omega_e} N_{A,\underline{i}} \rho^f f_{\underline{i}}^f d\Omega_e}{\partial \ddot{\Upsilon}_{B,j}} = \sum_{e=1}^{N_{el}} \int_{\Omega_e} N_{A,\underline{i}} \rho^f \frac{\partial f_{\underline{i}}^f}{\partial \ddot{\Upsilon}_{B,j}} + \alpha_f \beta \Delta t^2 N_{A,\underline{i}} \rho^f f_{\underline{i}}^f \frac{\partial N_{B,\underline{j}}}{\partial x_{\underline{j}}} d\Omega_e. \quad (5.121)$$

Continuity constraint term

$$\frac{\partial \sum_{e=1}^{N_{el}} \int_{\Omega_e} N_A \frac{\partial v_i}{\partial x_i} d\Omega_e}{\partial \ddot{\Upsilon}_{B,j}} = \sum_{e=1}^{N_{el}} \alpha_f \beta \Delta t^2 \int_{\Omega_e} N_A \left(\frac{\partial v_i}{\partial x_i} \frac{\partial N_{B,\underline{j}}}{\partial x_{\underline{j}}} - \frac{\partial v_i}{\partial x_{\underline{j}}} \frac{\partial N_{B,\underline{j}}}{\partial x_i} \right) d\Omega_e. \quad (5.122)$$

Continuity least-squares term

$$\frac{\partial \sum_{e=1}^{N_{el}} \int_{\Omega_e} \frac{\partial N_{A,\underline{i}}}{\partial x_{\underline{i}}} \tau_C \frac{\partial v_k}{\partial x_k} d\Omega_e}{\partial \ddot{\Upsilon}_{B,j}} = \quad (5.123)$$

$$\sum_{e=1}^{N_{el}} \alpha_f \beta \Delta t^2 \int_{\Omega_e} \frac{\partial N_{A,\underline{i}}}{\partial x_{\underline{i}}} \tau_C \frac{\partial v_k}{\partial x_k} \frac{\partial N_{B,\underline{j}}}{\partial x_{\underline{j}}} -$$

$$\frac{\partial N_{A,\underline{i}}}{\partial x_{\underline{j}}} \tau_C \frac{\partial v_k}{\partial x_k} \frac{\partial N_{B,\underline{j}}}{\partial x_{\underline{i}}} -$$

$$\frac{\partial N_{A,\underline{i}}}{\partial x_{\underline{i}}} \tau_C \frac{\partial v_k}{\partial x_{\underline{j}}} \frac{\partial N_{B,\underline{j}}}{\partial x_k} d\Omega_e.$$

Streamline diffusion stabilization term

$$\begin{aligned}
& \frac{\partial \sum_{e=1}^{N_{el}} \int_{\Omega_e} (v_k - \beta_k) \frac{\partial N_{A,\underline{i}}}{\partial x_k} \tau_M (v_l - \beta_l) \frac{\partial v_{\underline{i}}}{\partial x_l} d\Omega_e}{\partial \ddot{\Upsilon}_{B,j}} = \\
& - \sum_{e=1}^{N_{el}} \alpha_f \gamma \Delta t \int_{\Omega_e} \frac{\partial N_{A,\underline{i}}}{\partial x_{\underline{j}}} \tau_M (v_k - \beta_k) \frac{\partial v_{\underline{i}}}{\partial x_k} N_{B,\underline{j}} + \frac{\partial N_{A,\underline{i}}}{\partial x_k} \tau_M (v_k - \beta_k) \frac{\partial v_{\underline{i}}}{\partial x_{\underline{j}}} N_{B,\underline{j}} d\Omega_e \\
& + \\
& \sum_{e=1}^{N_{el}} \alpha_f \beta \Delta t^2 \int_{\Omega_e} (v_l - \beta_l) \frac{\partial N_{A,\underline{i}}}{\partial x_l} \tau_M (v_k - \beta_k) \frac{\partial v_{\underline{i}}}{\partial x_k} \frac{\partial N_{B,\underline{j}}}{\partial x_{\underline{j}}} - \\
& \frac{\partial N_{A,\underline{i}}}{\partial x_{\underline{j}}} \tau_M (v_l - \beta_l) \frac{\partial v_{\underline{i}}}{\partial x_l} (v_k - \beta_k) \frac{\partial N_{B,\underline{j}}}{\partial x_k} - \\
& (v_l - \beta_l) \frac{\partial N_{A,\underline{i}}}{\partial x_l} \tau_M \frac{\partial v_{\underline{i}}}{\partial x_{\underline{j}}} (v_k - \beta_k) \frac{\partial N_{B,\underline{j}}}{\partial x_k} d\Omega_e
\end{aligned} \tag{5.124}$$

Contributions to the shape derivative matrix given in this section are implemented in our software used to compute numerical examples presented in the sequel. With these contributions to the tangent matrix we observed satisfactory nonlinear convergence of the FSI system within the time step. It is possible that including additional terms in the tangent matrix may lead to a better performance of the nonlinear solver for other problem classes.

5.4 Numerical examples

In all the examples, the wall is modeled by two elements and four C^1 -continuous second order basis functions through the thickness. See [52] for further details regarding modeling of shell-like structures as solids.

5.4.1 Wave propagation in an elastic tube

Our first test case, taken from Greenshields and Weller [38], deals with wave propagation in a fluid-filled elastic tube. In this example the tube length is $L = 10$ cm, its inner radius is $R_i = 1$ cm, and its outer radius is $R_o = 1.2$ cm. The solid region is enclosed between R_i and R_o while the fluid occupies the rest of the tube. The problem setup and boundary conditions are illustrated in Figure 5.2. Material properties representative of blood flow in arteries are defined as follows: the density of the solid is $\rho^s = 1 \frac{\text{g}}{\text{cm}^3}$, and Young's modulus and Poisson's ratio are $E = 10^7 \frac{\text{dyn}}{\text{cm}^2}$ and $\nu = 0.3$, respectively. The fluid density is also $\rho^f = 1 \frac{\text{g}}{\text{cm}^3}$, and its viscosity is $\mu^f = 0.04 \frac{\text{g}}{\text{cm s}}$.

The computational mesh, consisting of 6,080 quadratic NURBS elements, is shown in Fig-

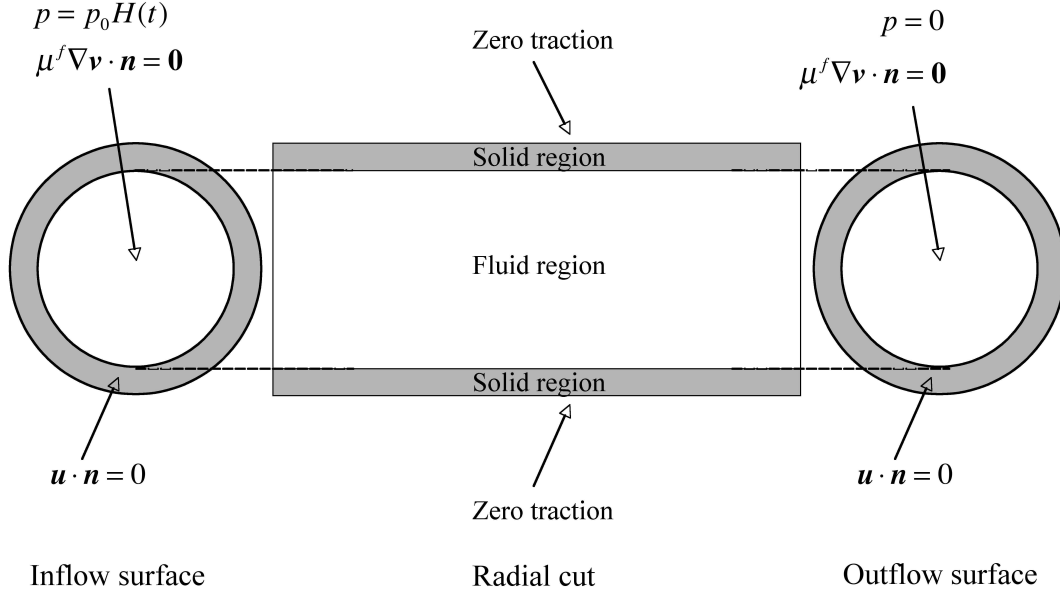


Figure 5.2: Wave propagation in a fluid-filled elastic tube problem setup. $H(t)$ is the Heaviside function.

ure 5.3. At $t = 0$ a step change in pressure is applied at the fluid inflow boundary to the system that is initially at rest (all initial fields are zero). The pulse causes a pressure wave to propagate down the tube. Figure 5.4 presents snapshots of fluid pressure at various times. Four radial cuts are shown on each of the plots to demonstrate that the computed solution is pointwise axisymmetric. For visualization purposes, pressure in the solid region is set to zero to create a sharp contrast at the fluid-solid interface. As a result, radial wall displacement, which is on the order of 5%, is visible in the figure.

Figure 5.5a shows the outer wall displacement, while Figure 5.5b shows the centerline fluid pressure at various times. Isogeometric results are compared with reference computations of Greenshields and Weller [38], who employed a small-strain, small-displacement formulation of the solid. Discrepancies between results are assumed attributable to the fully nonlinear model used in the present study versus the linear model utilized in [38]. Nevertheless, results are in fairly good agreement with the reference computations, as well as with the Joukowsky solution (see Greenshields and Weller [38] for details). These observations provide tentative confirmation that the coupled momentum method for hemodynamics, proposed by Figueroa *et al.* [28], in which the fluid and the structure exhibit strong coupling, but the geometry stays fixed at a reference configuration, is an adequate description for blood flow calculations.

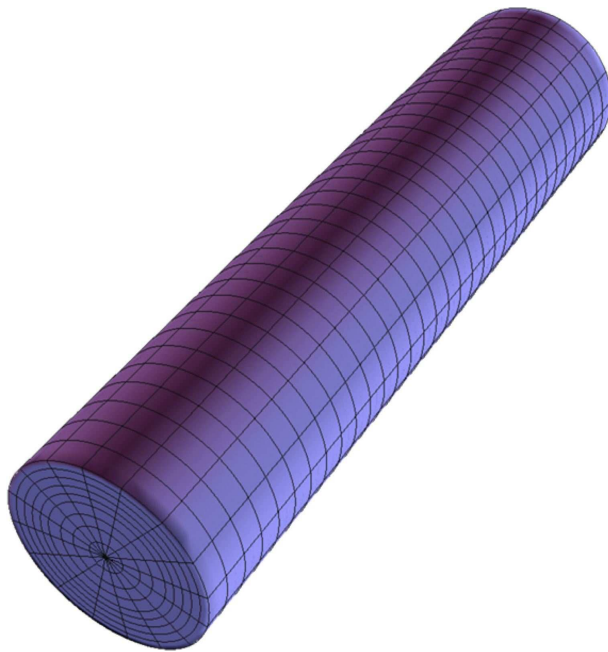


Figure 5.3: Wave propagation in a fluid-filled elastic tube mesh consisting of 6,080 NURBS elements.

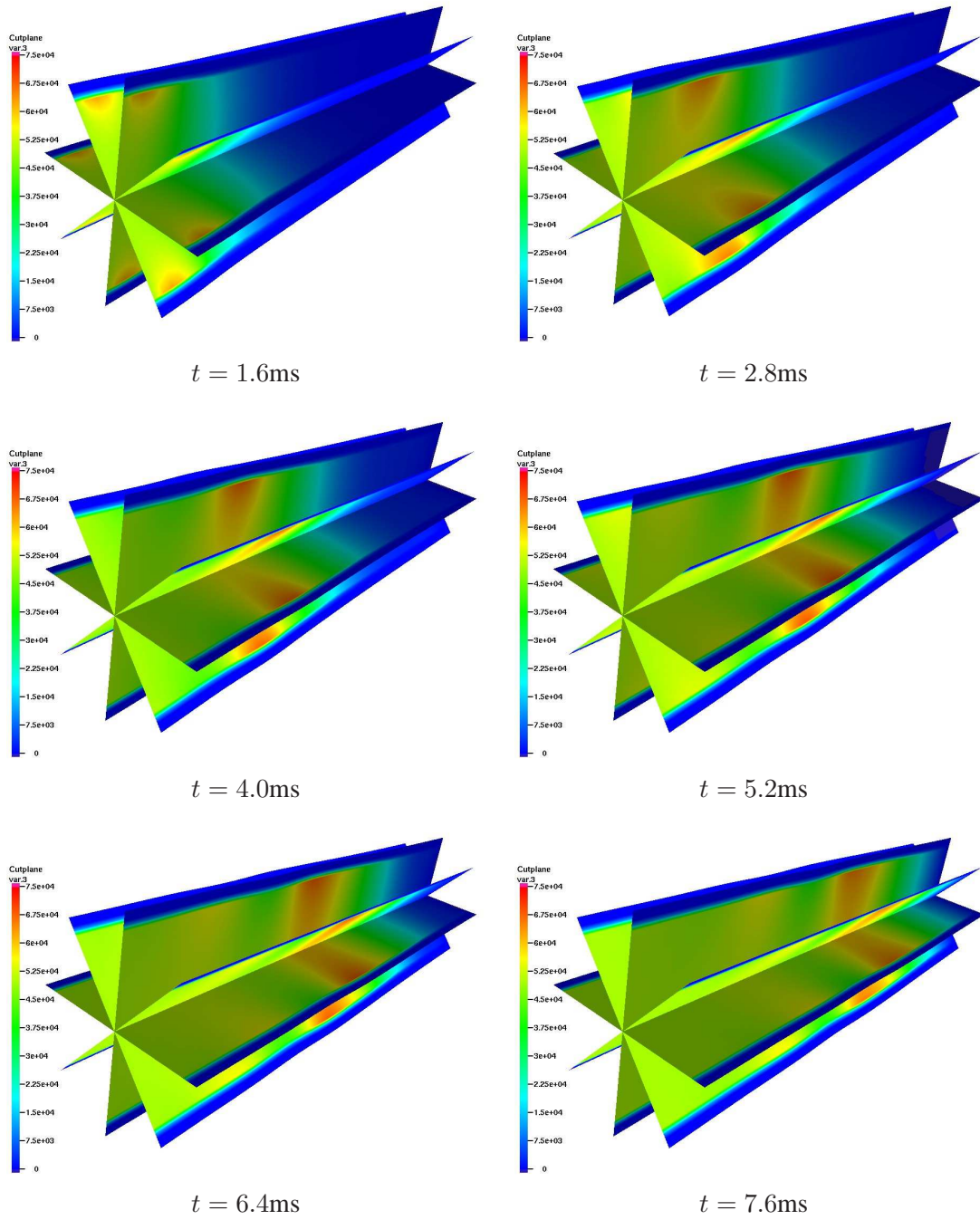
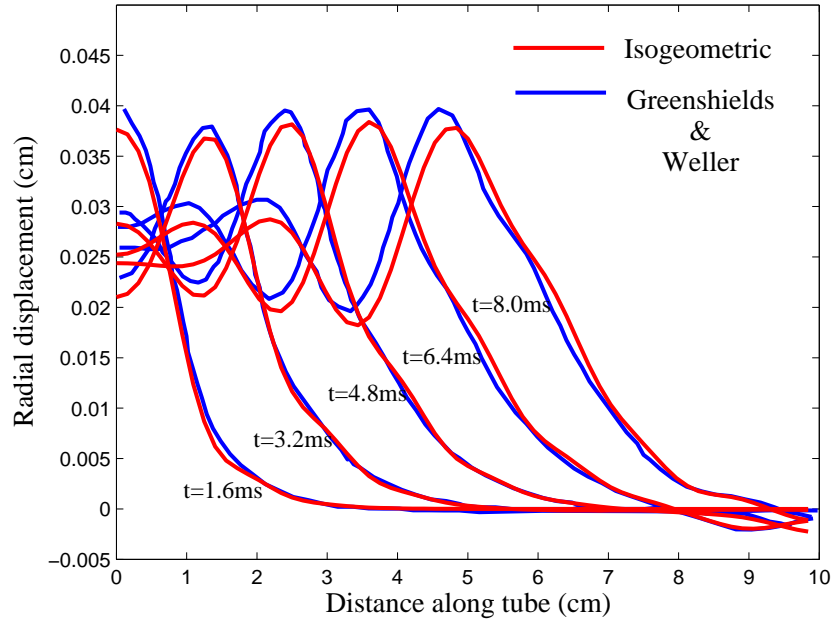
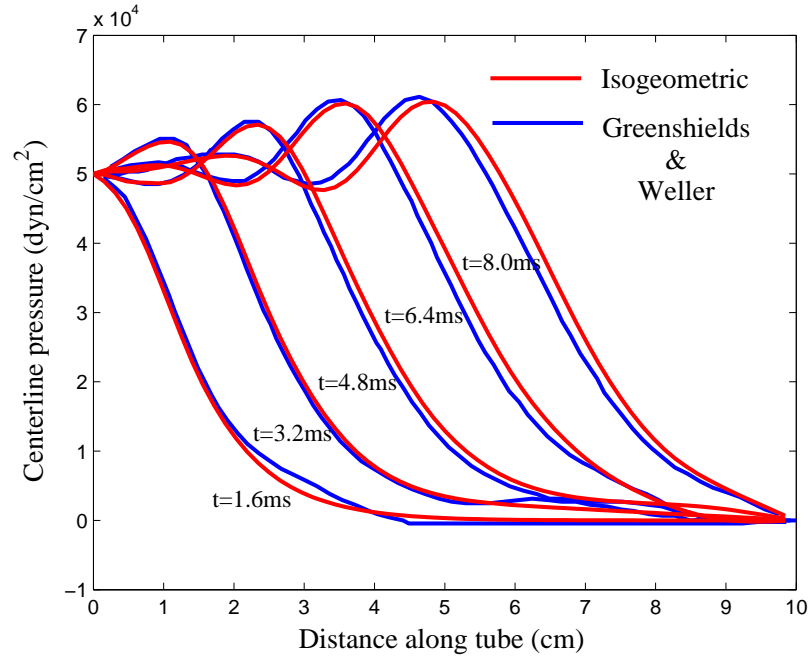


Figure 5.4: Wave propagation in a fluid-filled elastic tube. Contours of fluid pressure at various radial slices. Solution remains pointwise axisymmetric



(a)



(b)

Figure 5.5: Wave propagation in a fluid-filled elastic tube. (a) Outer wall radial displacement. (b) Centerline pressure. Computational results of Greenshields and Weller [38] are plotted for comparison.

5.4.2 Blood flow in an idealized aneurysm

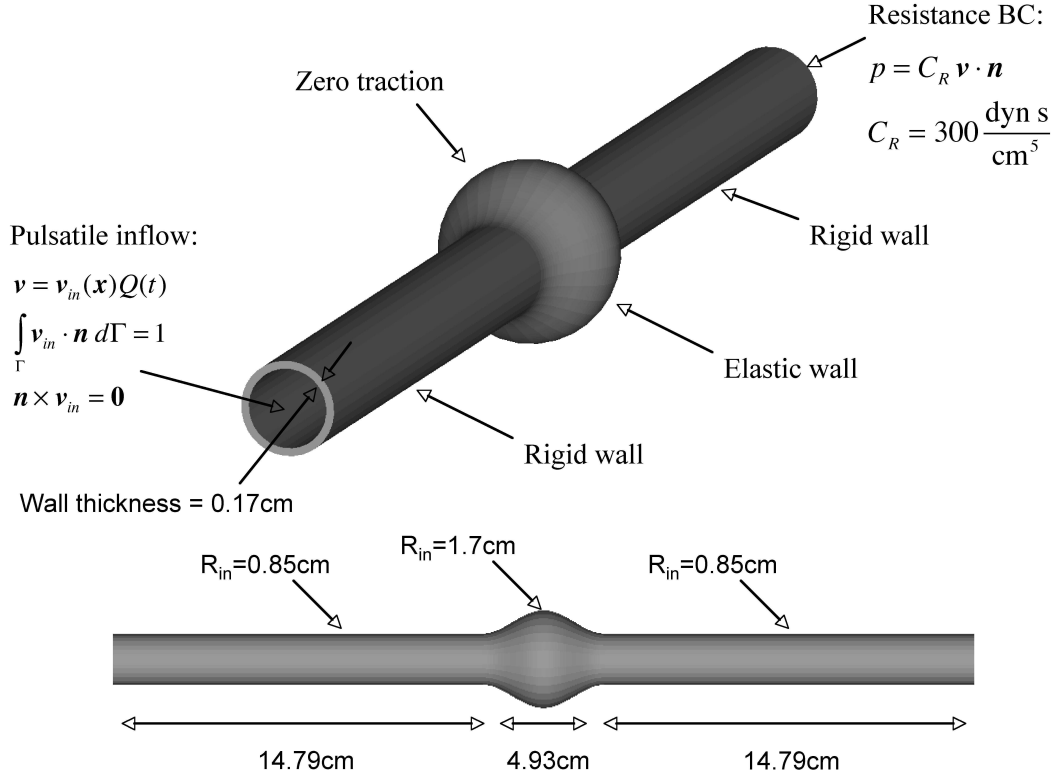


Figure 5.6: Idealized aneurysm problem setup.

In this test case, taken from [27, 86], we examine pulsatile flow in an idealized aneurysm. The problem setup is shown in Figure 5.6. A time-periodic velocity waveform, specified at the inflow plane, is parabolically distributed over the circular surface. The period of the wave, T , is 0.84s. The domains proximal and distal to the aneurysm region are assumed to have rigid walls, while the aneurysm wall is elastic. The density of the solid, its Young's modulus, and Poisson's ratio are $\rho^s = 1.2 \frac{\text{g}}{\text{cm}^3}$, $E = 6 \times 10^6 \frac{\text{dyn}}{\text{cm}^2}$, and $\nu = 0.3$, respectively. The fluid density and dynamic viscosity are $\rho^f = 1.012 \frac{\text{g}}{\text{cm}^3}$ and $\mu^f = 0.035 \frac{\text{g}}{\text{cm s}}$, respectively. A resistance boundary condition is applied at the outflow. The value of the resistance constant is $C_R = 300 \frac{\text{dyn s}}{\text{cm}^5}$. For implementation of boundary conditions employing various pressure-flow relationships, see Heywood *et al.* [41] and Vignon *et al.* [110]. The mesh, consisting of 14,630 quadratic NURBS elements, is shown in Figure 5.7.

Figure 5.8 shows velocity vectors superimposed on the axial velocity contours in the aneurysm region at different times. A 135° “pie” slice was cut out of the domain in order to exhibit the flow



Figure 5.7: Idealized aneurysm mesh consisting of 14,630 NURBS elements.

features. Distensibility of the wall contributes significantly to the unsteadiness of the flow. Nevertheless, the flow remains axisymmetric, as may be discerned from symmetry of the velocity vectors. As in the previous example, no axisymmetry in the solution is assumed at the outset. It should be noted that the peak Reynolds number, estimated to be about 1,400-1,500 based on the largest diameter, is close to the transitional value for circular pipe flow (see, e.g., White [112]). Thus, relatively small perturbations in the geometry and/or flow conditions may lead to much more complex, unsteady solutions. Figure 5.9 shows the inflow and outflow waveforms. Note the outflow lags the inflow due to the distensibility of the aneurysm wall. This well-known phenomenon was also observed in the computations of Figueroa *et al.* [28]. Figure 5.9 also shows reference results from [27, 86]. The agreement is excellent despite the differences in the wall models (a nonlinear shell was used in [27, 86]).

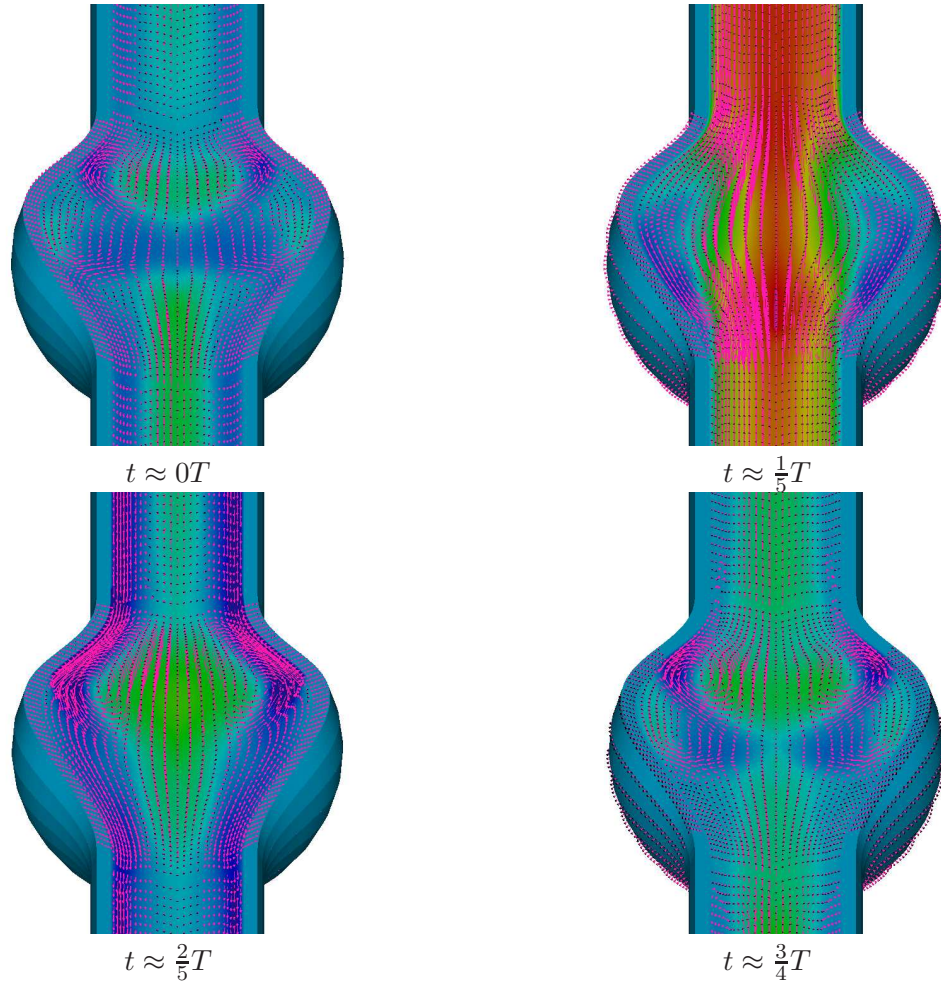


Figure 5.8: Idealized aneurysm. Velocity vectors superimposed on axial velocity contours at various times. Top right and bottom left correspond to the systolic and diastolic phases, respectively. Note that the flow is axisymmetric.

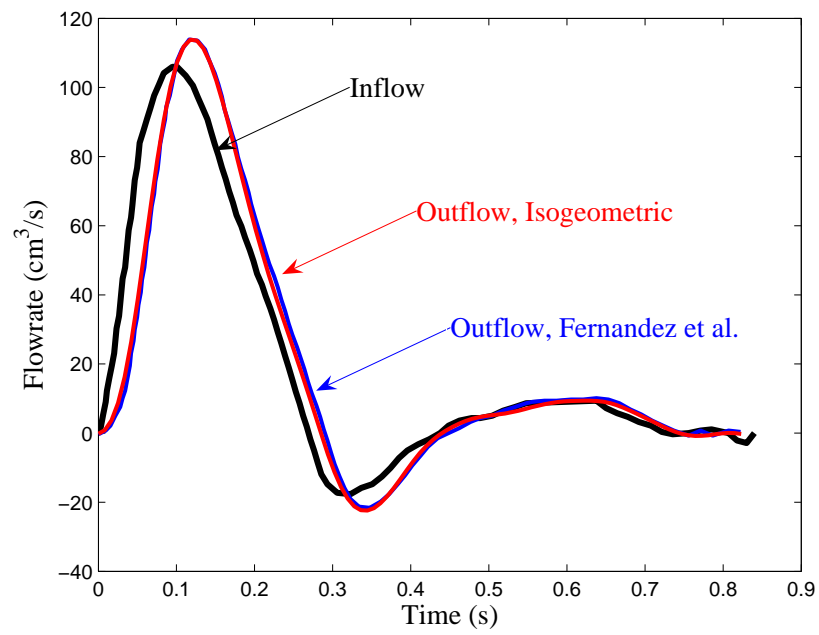


Figure 5.9: Idealized aneurysm. Inflow and outflow waveforms. Notice the time lag attributable to the distensibility of the wall.

5.4.3 Patient-specific abdominal aorta

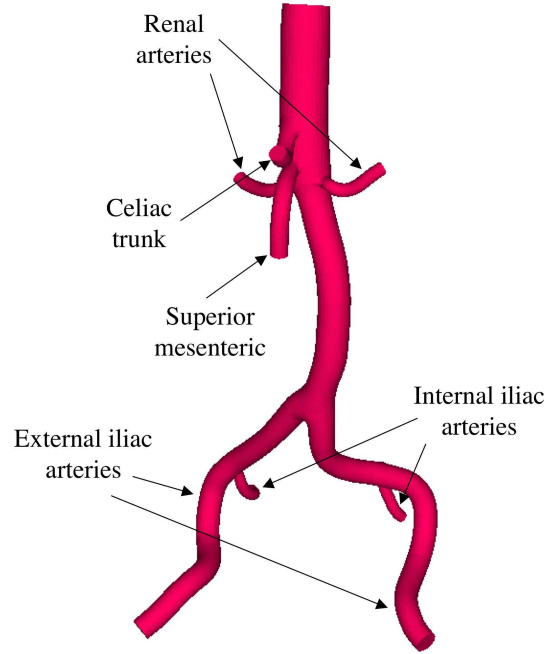


Figure 5.10: Patient-specific abdominal aorta geometry.

We present fluid-structure interaction calculations of a patient-specific abdominal aorta for a healthy over-55 volunteer obtained from 64-slice CT angiography. The geometrical model, which contains most major branches of a typical abdominal aorta, is shown in Figure 5.10. The inferior mesenteric artery was not clearly captured in the imaging and was omitted in the geometrical model. The fluid properties are: $\rho^f = 1.06 \frac{\text{g}}{\text{cm}^3}$, $\mu^f = 0.04 \frac{\text{g}}{\text{cm s}}$. The solid is characterized by the density $\rho^s = 1 \frac{\text{g}}{\text{cm}^3}$, Young's modulus, $E = 4.144 \times 10^6 \frac{\text{dyn}}{\text{cm}^2}$, and Poisson's ratio, $\nu = 0.4$. A periodic flow waveform, with period $T = 1.05\text{s}$, is applied at the inlet of the aorta, while resistance boundary conditions are applied at all outlets. The solid is fixed at the inlet and at all outlets. Material and flow rate data, as well as resistance values are taken from Figueroa *et al.* [28], with the following exception. Poisson's ratio is taken to be 0.4, not 0.5 as in [28], as the latter is not allowed in the pure displacement formulation of an elastic solid. Wall thickness for this model is taken to be 15% of the nominal radius of each cross-section of the fluid domain model. The computational mesh, consisting of 52,420 quadratic NURBS elements, is shown in Figure 5.11.

Figure 5.12 shows velocity isosurfaces plotted on the current configuration of the geometry at various times during the cardiac cycle. The flow appears to be fully three-dimensional and unsteady, with most of the unsteadiness occurring in late diastole. Figure 5.13 shows the distribution



Figure 5.11: Patient-specific abdominal aorta mesh consisting of 52,420 quadratic NURBS elements.

of flow among the branches. As in the previous example, the outflow lags the inflow due to the distensibility of the arterial wall. Although perfect matching with [28] cannot be expected because the geometry and analysis models are different, the overall flow distribution and the time lag are in qualitative agreement.

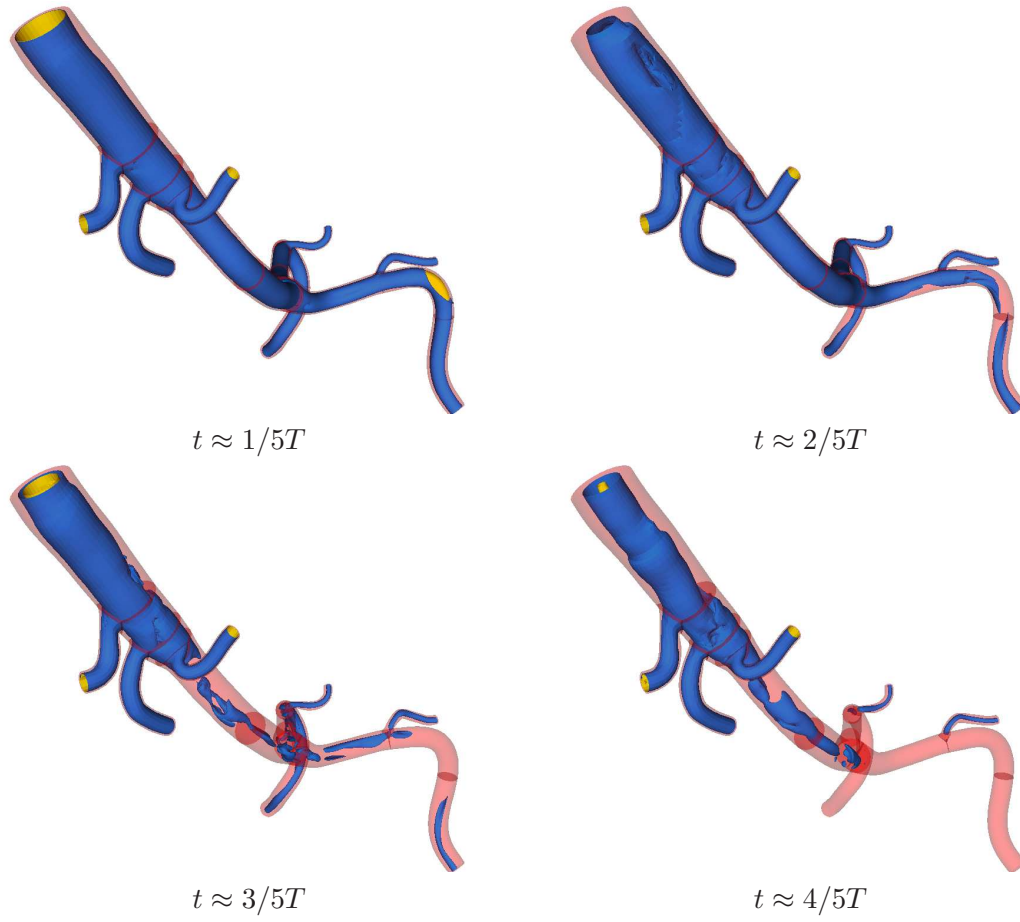


Figure 5.12: Patient-specific abdominal aorta. Isosurfaces of the velocity magnitude plotted on the deformed geometry at various times.

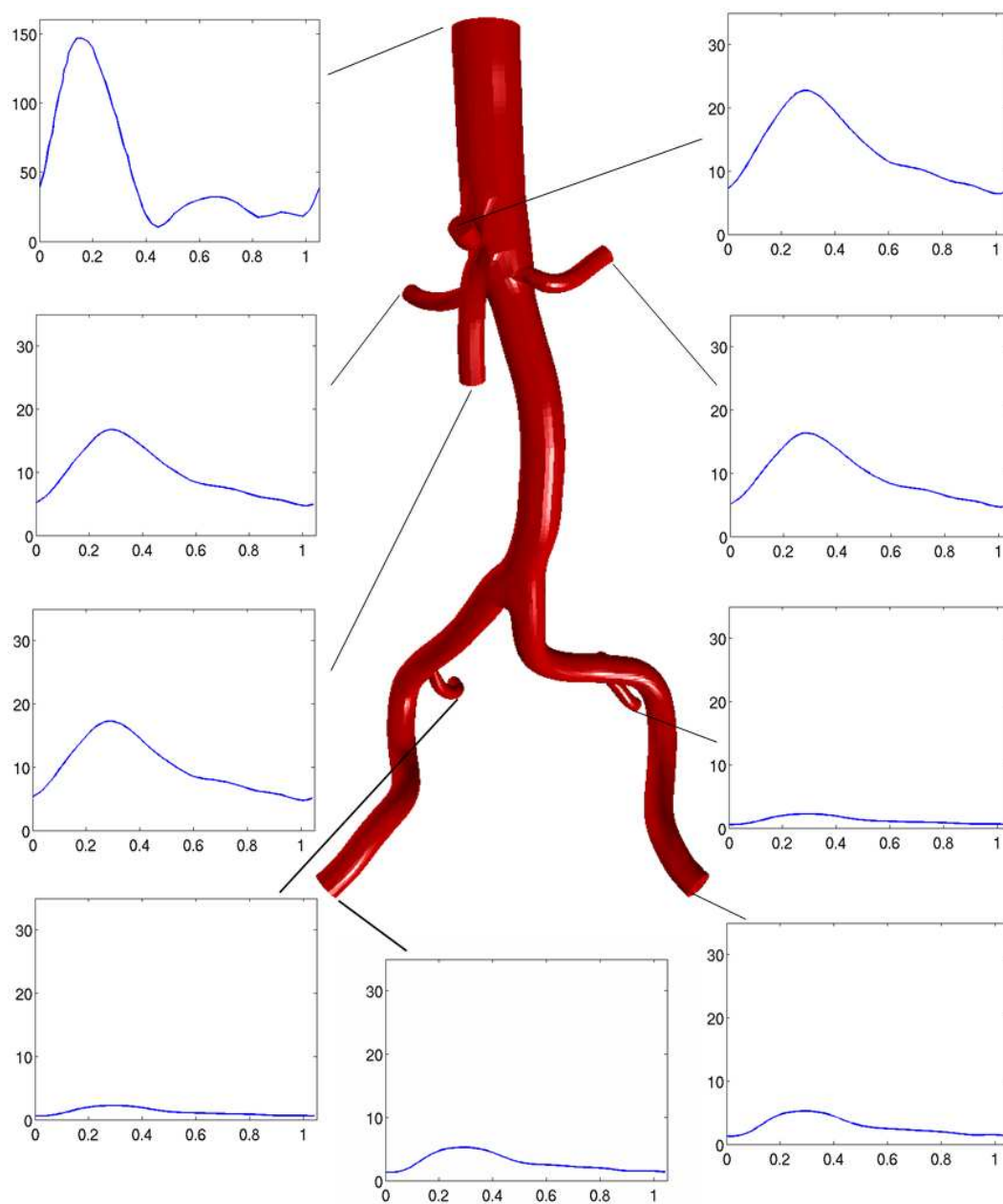


Figure 5.13: Patient-specific abdominal aorta. Inlet and outlet flow waveforms. Flowrates (cm^3/s) versus time (s).

Chapter 6

Conclusions and Future Work

In this thesis the mathematical study of Isogeometric Analysis based on NURBS, an extension of classical finite element analysis, was initiated. We developed approximation properties based on a new Bramble-Hilbert lemma and new inverse estimates for the cases at hand. Our study focused on h -refinement and did not treat order-elevation methods such as p - or k -refinement, which will be a subject of future research. We applied the method to several cases of physical interest, namely, elasticity, isotropic incompressible elasticity and Stokes flow, and advection-diffusion. These serve as linear model problems for applications such as turbulent fluid flow and fluid-structure interaction, also treated in this dissertation. We considered standard primal and mixed Galerkin methods as well as stabilized methods. All of our numerical results were consistent with our theoretical predictions. We also performed some numerical tests involving singularities and unresolved layers that went beyond the limits of the hypotheses of our mathematical results. These tests suggest that we have barely scratched the surface in that many other interesting mathematical properties, yet to be rigorously established, are possessed by Isogeometric Analysis.

We have developed a class of discrete formulations for incompressible fluid flow based on the multiscale paradigm and the concept of fine-scale Green's function. These residual-based formulations are considered to be models of turbulence in this work. New methods were tested in the parallel isogeometric unsteady flow solver, developed as a part of this thesis. Results appear to be competitive with, and often superior to state-of-the-art, eddy-viscosity based formulations. Increased accuracy was noted for high-order, high-continuity discretizations native to Isogeometric Analysis. Future research efforts will be focused on improving accuracy of local fine-scale approximations which are embedded in the VMS methodology. Additional benchmark test cases, as well as flows of industrial complexity need to be computed to obtain a fuller understanding of the performance of newly proposed methods.

We have developed a NURBS-based isogeometric fluid-structure interaction capability cou-

pling incompressible fluids with nonlinear elastic solids and allowing for large structural displacements, and applied it to problems of arterial blood flow. We have also developed a set of procedures allowing us to construct analysis-suitable NURBS geometries directly from patient-specific imaging data. The new approach is evaluated on two benchmark problems and applied to the fluid-structure interaction of a patient-specific abdominal aorta. Very good results are obtained for the benchmark computations and the results for our patient-specific model are in qualitative agreement with the results of other researchers using similar models. Future developments will address extensions to hyperelastic materials with anisotropy and viscoelasticity, which are capable of representing more physically realistic behavior of the arterial wall. Solid incompressibility and near-incompressibility will be dealt with by means of a mixed formulation employing displacement and pressure. Comparisons with standard finite elements are also planned.

Bibliography

- [1] R.A. Adams. *Sobolev Spaces*. Academic Press, New York, 1975.
- [2] J. E. Akin and T. E. Tezduyar. Calculation of the advective limit of the SUPG stabilization parameter for linear and higher-order elements. *Computer Methods in Applied Mechanics and Engineering*, 193:1909–1922, 2004.
- [3] D.N. Arnold, F. Brezzi, B. Cockburn, and L.D. Marini. Unified analysis of Discontinuous Galerkin methods for elliptic problems. *SIAM Journal of Numerical Analysis*, 39:1749–1779, 2002.
- [4] F. Auricchio, L. Beirao da Veiga, C. Lovadina, and A. Reali. Triangular enhanced strain elements for plain linear elasticity. *Computer Methods in Applied Mechanics and Engineering*, to appear, 2005. Preprint IMATI-CNR.
- [5] C. Bajaj, Q. Wu, and G. Xu. Level set based volumetric anisotropic diffusion. 2003. ICES Report 03-10, UT Austin.
- [6] Y. Bazilevs, L. Beirao da Veiga, J.A. Cottrell, T.J.R. Hughes, and G. Sangalli. Isogeometric analysis: Approximation, stability and error estimates for h -refined meshes. *Mathematical Models and Methods in Applied Sciences*, 2006. In press, available as ICES Report 06-04, UT Austin.
- [7] Y. Bazilevs and T.J.R. Hughes. Weak imposition of Dirichlet boundary conditions in fluid mechanics. *Computers and Fluids*, 2006. In press, published online.
- [8] M. Bischoff and K.-U. Bletzinger. Improving stability and accuracy of Reissner-Mindlin plate finite elements via algebraic subgrid scale stabilization. *Computer Methods in Applied Mechanics and Engineering*, 193:1491–1516, 2004.
- [9] P. B. Bochev, M. D. Gunzburger, and J. N. Shadid. On inf-sup stabilized finite element methods for transient problems. *Computer Methods in Applied Mechanics and Engineering*, 193:1471–1489, 2004.

- [10] J.H. Bramble and S.R. Hilbert. Estimation of linear functionals on Sobolev spaces with application to Fourier transforms and spline interpolation. *SIAM Journal of Numerical Analysis*, 7:112–124, 1970.
- [11] F. Brezzi and M. Fortin. *Mixed and Hybrid Finite Element Methods*. Springer-Verlag, Berlin, 1991.
- [12] A. N. Brooks and T. J. R. Hughes. Streamline upwind / Petrov-Galerkin formulations for convection dominated flows with particular emphasis on the incompressible Navier-Stokes equations. *Computer Methods in Applied Mechanics and Engineering*, 32:199–259, 1982.
- [13] E. Burman and P. Hansbo. Edge stabilization for Galerkin approximations of convection-diffusion-reaction problems. *Computer Methods in Applied Mechanics and Engineering*, 193:1437–1453, 2004.
- [14] V.M. Calo. *Residual-based Multiscale Turbulence Modeling: Finite Volume Simulation of Bypass Transistion*. PhD thesis, Department of Civil and Environmental Engineering, Stanford University, 2004.
- [15] J. Chung and G. M. Hulbert. A time integration algorithm for structural dynamics with improved numerical dissipation: The generalized- α method. *Journal of Applied Mechanics*, 60:371–75, 1993.
- [16] P.G. Ciarlet and P.A. Raviart. Interpolation theory over curved elements with applications to finite element methods. *Computer Methods in Applied Mechanics and Engineering*, 1:217–249, 1972.
- [17] R. Codina and O. Soto. Approximation of the incompressible Navier-Stokes equations using orthogonal subscale stabilization and pressure segregation on anisotropic finite element meshes. *Computer Methods in Applied Mechanics and Engineering*, 193:1403–1419, 2004.
- [18] J.A. Cottrell, A. Reali, Y. Bazilevs, and T.J.R. Hughes. Isogeometric analysis of structural vibrations. *Computer Methods in Applied Mechanics and Engineering*, 2005. In press, available as ICES Report 05-27, UT Austin.
- [19] A. L. G. A. Coutinho, C. M. Diaz, J. L. D. Alvez, L. Landau, A. F. D. Loula, S. M. C. Malta, R. G. S. Castro, and E. L. M. Garcia. Stabilized methods and post-processing techniques for miscible displacements. *Computer Methods in Applied Mechanics and Engineering*, 193:1421–1436, 2004.

- [20] J. Donea, S. Giuliani, and J. P. Halleux. An arbitrary Lagrangian-Eulerian finite element method for transient dynamics fluid-structure interactions. *Computer Methods in Applied Mechanics and Engineering*, 33:689–723, 1982.
- [21] J. Douglas and J. Wang. An absolutely stabilized finite element method for the Stokes problem. *Mathematics of Computation*, 52:495–508, 1989.
- [22] C. Farhat and P. Geuzaine. Design and analysis of robust ALE time-integrators for the solution of unsteady flow problems on moving grids. *Computer Methods in Applied Mechanics and Engineering*, 193:4073–4095, 2004.
- [23] C. Farhat, P. Geuzaine, and C. Grandmont. The discrete geometric conservation law and the nonlinear stability of ALE schemes for the solution of flow problems on moving grids. *Journal of Computational Physics*, 174(2):669–694, 2001.
- [24] C. Farhat and B. Koobus. Finite volume discretization on unstructured meshes of the multi-scale formulation of large eddy simulations. In F.G. Rammerstorfer, H.A. Mang, and J. Eberhardsteiner, editors, *In Proceedings of the Fifth World Congress on Computational Mechanics (WCCM V)*. Vienna University of Technology, Austria, July 7-12, 2002.
- [25] G.E. Farin. *NURBS Curves and Surfaces: From Projective Geometry to Practical Use*. A. K. Peters, Ltd., Natick, MA, 1995.
- [26] M.A. Fernandez and M. Moubachir. A Newton method using exact jacobians for solving fluid-structure coupling. *Computers and Structures*, 83:127–142, 2005.
- [27] M.A. Fernandez and A.-V. Salsac. Numerical investigation of the effects of the wall compliance on the wall shear stress distribution in abdominal aortic aneurisms. 2006. In preparation.
- [28] A. Figueroa, I.E. Vignon-Clementel, K.E. Jansen, T.J.R. Hughes, and C.A. Taylor. A coupled momentum method for modeling blood flow in three-dimensional deformable arteries. *Computer Methods in Applied Mechanics and Engineering*, 2005. In press.
- [29] C. Foias, O. Manley, R. Rosa, and R. Temam. *Navier-Stokes Equations and Turbulence*. Cambridge University Press, Cambridge, 2001.
- [30] L. Formaggia, J.-F. Gerbeau, F. Nobile, and A. Quarteroni. On the coupling of 3D and 1D Navier-Stokes equations for flow problems in compliant vessels. *Computer Methods in Applied Mechanics and Engineering*, 191:561–582, 2001.

- [31] L. P. Franca, S. Frey, and T.J.R. Hughes. Stabilized finite element methods: I. Application to the advective-diffusive model. *Computer Methods in Applied Mechanics and Engineering*, 95:253–276, 1992.
- [32] L.P. Franca and R. Stenberg. Error analysis of some galerkin least squares methods for the elasticity problem. *SIAM Journal of Numerical Analysis*, 28(6):1680–1697, 1991.
- [33] J.-F. Gerbeau, M. Vidrascu, and P. Frey. Fluid-structure interaction in blood flows on geometries based on medical images. *Computers and Structures*, 83:155–165, 2005.
- [34] M. Germano, U. Piomelli, P. Moin, and W. H. Cabot. A dynamic subgrid-scale eddy viscosity model. *Physics of Fluids*, 3:1760, 1991.
- [35] S. Goswami, T. K. Dey, and C. L. Bajaj. Identifying planar and cylindrical regions of a shape by unstable manifold. 2006. In preparation.
- [36] P. L. Gould. *Introduction to Linear Elasticity*. Springer Verlag, Berlin, 1999.
- [37] V. Gravemeier, W. A. Wall, and E. Ramm. A three-level finite element method for the stationary incompressible Navier-Stokes equations. *Computer Methods in Applied Mechanics and Engineering*, 193:1323–1366, 2004.
- [38] C.J. Greenshields and H.G. Weller. A unified formulation for continuum mechanics applied to fluid-structure interaction in flexible tubes. *International Journal of Numerical Methods in Engineering*, 64:1575–1593, 2005.
- [39] I. Harari. Stability of semidiscrete formulations for parabolic problems at small time steps. *Computer Methods in Applied Mechanics and Engineering*, 193:1491–1516, 2004.
- [40] G. Hauke and L. Valiño. Computing reactive flows with a field Monte Carlo formulation and multi-scale methods. *Computer Methods in Applied Mechanics and Engineering*, 193:1455–1470, 2004.
- [41] J.G. Heywood, R. Rannacher, and S. Turek. Artificial boundaries and flux and pressure conditions for the incompressible navier-stokes equations. *International Journal of Numerical Methods in Fluids*, 22:325–352, 1996.
- [42] J. Holmen, T.J.R. Hughes, A.A. Oberai, and G.N. Wells. Sensitivity of the scale partition for variational multiscale LES of channel flow. *Physics of Fluids*, 16(3):824–827, 2004.
- [43] G.A. Holzapfel. *Nonlinear Solid Mechanics, a Continuum Approach for Engineering*. Wiley, Chichester, 2000.

- [44] T. J. R. Hughes. *The Finite Element Method: Linear Static and Dynamic Finite Element Analysis*. Dover Publications, Mineola, NY, 2000.
- [45] T. J. R. Hughes, L. P. Franca, and M. Balestra. A new finite element formulation for fluid dynamics: V. A stable Petrov-Galerkin formulation of the Stokes problem accommodating equal-order interpolations. *Computer Methods in Applied Mechanics and Engineering*, 59:85–99, 1986.
- [46] T. J. R. Hughes, W. K. Liu, and T. K. Zimmermann. Lagrangian-Eulerian finite element formulation for incompressible viscous flows. *Computer Methods in Applied Mechanics and Engineering*, 29:329–349, 1981.
- [47] T. J. R. Hughes and M. Mallet. A new finite element formulation for fluid dynamics: III. The generalized streamline operator for multidimensional advective-diffusive systems. *Computer Methods in Applied Mechanics and Engineering*, 58:305–328, 1986.
- [48] T. J. R. Hughes, L. Mazzei, and K. E. Jansen. Large-eddy simulation and the variational multiscale method. *Computing and Visualization in Science*, 3:47–59, 2000.
- [49] T. J. R. Hughes, L. Mazzei, A. A. Oberai, and A.A. Wray. The multiscale formulation of large eddy simulation: Decay of homogenous isotropic turbulence. *Physics of Fluids*, 13(2):505–512, 2001.
- [50] T. J. R. Hughes, A. A. Oberai, and L. Mazzei. Large-eddy simulation of turbulent channel flows by the variational multiscale method. *Physics of Fluids*, 13(6):1784–1799, 2001.
- [51] T.J.R. Hughes, V.M. Calo, and G. Scovazzi. Variational and multiscale methods in turbulence. In W. Gutkowski and T.A. Kowalewski, editors, *In Proceedings of the XXI International Congress of Theoretical and Applied Mechanics (IUTAM)*. Kluwer, 2004.
- [52] T.J.R. Hughes, J.A. Cottrell, and Y. Bazilevs. Isogeometric analysis: CAD, finite elements, NURBS, exact geometry, and mesh refinement. *Computer Methods in Applied Mechanics and Engineering*, 194:4135–4195, 2005.
- [53] T.J.R. Hughes and L. P. Franca. A new finite element formulation for fluid dynamics: VII. The Stokes problem with various well-posed boundary conditions: Symmetric formulations that converge for all velocity/pressure spaces. *Computer Methods in Applied Mechanics and Engineering*, 65:85–96, 1987.
- [54] T.J.R. Hughes and G. Sangalli. Variational multiscale analysis: the fine-scale Green’s function, projection, optimization, localization, and stabilized methods. *SIAM Journal of Numerical Analysis*, 2005. Submitted, available as ICES Report 05-46, UT Austin.

- [55] T.J.R. Hughes, G.N. Wells, and A.A. Wray. Energy transfers and spectral eddy viscosity of homogeneous isotropic turbulence: comparison of dynamic Smagorinsky and multiscale models over a range of discretizations. Technical report, ICES, The University of Texas at Austin, 2004.
- [56] K. E. Jansen, C. H. Whiting, and G. M. Hulbert. A generalized- α method for integrating the filtered Navier-Stokes equations with a stabilized finite element method. *Computer Methods in Applied Mechanics and Engineering*, 190:305–319, 1999.
- [57] K.E. Jansen and A.E. Tejada-Martinez. An evaluation of the variational multiscale model for large-eddy simulation while using a hierarchical basis. In *AIAA Paper 2002-0283*, 2002.
- [58] A. A. Johnson and T. E. Tezduyar. Mesh update strategies in parallel finite element computations of flow problems with moving boundaries and interfaces. *Computer Methods in Applied Mechanics and Engineering*, 119:73–94, 1994.
- [59] C. Johnson, U. Nävert, and J. Pitkäranta. Finite element methods for linear hyperbolic problems. *Computer Methods in Applied Mechanics and Engineering*, 45:285–312, 1984.
- [60] T. Ju, F. Losasso, S. Schaefer, and J. Warren. Dual contouring of hermite data. In *Proceedings of SIGGRAPH*, pages 339–346, 2002.
- [61] B. Koobus and C. Farhat. A variational multiscale method for the large eddy simulation of compressible turbulent flows on unstructured meshes – application to vortex shedding. *Computer Methods in Applied Mechanics and Engineering*, 193:1367–1383, 2004.
- [62] A. G. Kravchenko, P. Moin, and R. Moser. Zonal embedded grids for numerical simulation of wall-bounded turbulent flows. *Journal of Computational Physics*, 127:412–423, 1996.
- [63] A. G. Kravchenko, P. Moin, and K. Shariff. B-spline method and zonal grids for simulation of complex turbulent flows. *Journal of Computational Physics*, 151:757–789, 1999.
- [64] E. Kuhl, S. Hulshoff, and R. de Borst. An arbitrary Lagrangian Eulerian finite element approach for fluid-structure interaction phenomena. *International Journal of Numerical Methods in Engineering*, 57:117–142, 2003.
- [65] W. Y. Kwok, R. D. Moser, and J. Jiménez. A critical evaluation of the resolution properties of B-spline and compact finite difference methods. *Journal of Computational Physics*, 174:510–551, 2001.
- [66] P. Le Tallec and J. Mouro. Fluid structure interaction with large structural displacements. *Computer Methods in Applied Mechanics and Engineering*, 190:3039–3068, 2001.

- [67] A. Leonard. Energy cascade in large-eddy simulations of turbulent fluid flows. *Adv. Geophys.*, 18A:237–248, 1974.
- [68] W. Lorensen and H. Cline. Marching cubes: A high resolution 3d surface construction algorithm. In *SIGGRAPH*, pages 163–169, 1987.
- [69] Y. Maday, A.T. Patera, and E.M. Ronquist. The $P_N \times P_{N-2}$ method for the approximation of the Stokes problem. Technical report, Department of Mechanical Engineering, Massachusetts Institute of Technology, 1992.
- [70] A. Masud and R. A. Khurram. A multiscale/stabilized finite element method for the advection-diffusion equation. *Computer Methods in Applied Mechanics and Engineering*, 193:1997–2018, 2004.
- [71] R.J. McGhee, B.S. Walker, and B.F. Millard. Experimental results for the Eppler 387 airfoil at low Reynolds numbers in Langley low-turbulence pressure tunnel. Technical report, NASA Langley, October 1988.
- [72] R. Moser, J. Kim, and R. Mansour. DNS of turbulent channel flow up to $Re=590$. *Physics of Fluids*, 11:943–945, 1999.
- [73] Message Passing Interface (MPI). <http://www.mpi-forum.org>.
- [74] F. Nobile. *Numerical Approximation of Fluid-Structure Interaction Problems with Application to Haemodynamics*. PhD thesis, EPFL, 2001.
- [75] A.A. Oberai and T.J.R. Hughes. The variational multiscale formulation of LES: channel flow at $Re_\tau = 590$. *40th AIAA Ann. Mtg.*, Reno, NV, 2002. AIAA 2002-1056.
- [76] A.A. Oberai, F. Roknaldin, and T.J.R. Hughes. Computational procedures for determining structural acoustic response due to hydrodynamic sources. *Computer Methods in Applied Mechanics and Engineering*, 190(3-4):345–361, 2000.
- [77] A.A. Oberai, F. Roknaldin, and T.J.R. Hughes. Trailing-edge noise from a finite chord airfoil. *AIAA Journal*, 40(11):2206–2216, 2002.
- [78] J. T. Oden, I. Babuška, and C. E. Baumann. A discontinuous hp finite element method for diffusion problems. *Journal of Computational Physics*, 146:491–519, 1998.
- [79] L. Piegl and W. Tiller. *The NURBS Book (Monographs in Visual Communication)*, 2nd ed. Springer-Verlag, New York, 1997.

- [80] S. B. Pope. *Turbulent Flows*. Cambridge University Press, Cambridge, 2000.
- [81] S. Ramakrishnan and S.S. Collis. Variational multiscale modeling for turbulence control. *AIAA 1st Flow Control Conference*, St. Louis, MO, June 2002. AIAA 2002-3280.
- [82] S. Ramakrishnan and S.S. Collis. Multiscale modeling for turbulence simulation in complex geometries. *40th AIAA Aerospace Sciences Meeting and Exhibit*, Reno, NV, Jan. 2004. AIAA 2004-0241.
- [83] S. Ramakrishnan and S.S. Collis. Partition selection in multiscale turbulence modeling. *Preprint*, 2004.
- [84] S. Ramakrishnan and S.S. Collis. Turbulence control simulation using the variational multiscale method. *AIAA Journal*, 42(4):745–753, 2004.
- [85] D. F. Rogers. *An Introduction to NURBS With Historical Perspective*. Academic Press, San Diego, CA, 2001.
- [86] A.-V. Salsac, M.A. Fernandez, J.-M. Chomaz, and P. Le Tallec. Effects of the flexibility of the arterial wall on the wall shear stress and wall tension in abdominal aortic aneurysms. In *Proceedings of 58th Annual Meeting of the Division of Fluid Dynamics*, Chicago, IL, November 2005.
- [87] L.L. Schumaker. *Spline Functions: Basic Theory*. Krieger, 1993.
- [88] F. Shakib, T. J. R. Hughes, and Z. Johan. A new finite element formulation for computational fluid dynamics: X. The compressible Euler and Navier-Stokes equations. *Computer Methods in Applied Mechanics and Engineering*, 89:141–219, 1991.
- [89] K. Shariff and R. D. Moser. Two-dimensional mesh embedding for B-spline methods. *Journal of Computational Physics*, 145:471–488, 1998.
- [90] J.C. Simo and T.J.R. Hughes. *Computational Inelasticity*. Springer-Verlag, New York, 1998.
- [91] J. Smagorinsky. General circulation experiments with the primitive equations, I. The basic experiment. *Monthly Weather Review*, 91:99–152, 1963.
- [92] K. Stein, T. Tezduyar, and R. Benney. Mesh moving techniques for fluid-structure interactions with large displacements. *Journal of Applied Mechanics*, 70:58–63, 2003.
- [93] K. Stein, T.E. Tezduyar, and R. Benney. Automatic mesh update with the solid-extension mesh moving technique. *Computer Methods in Applied Mechanics and Engineering*, 193:2019–2032, 2004.

- [94] R. Stenberg. Error analysis of some finite element methods for the stokes problem. *Mathematics of Computation*, 54:495–508, 1990.
- [95] R. Stenberg. A technique for analyzing finite element methods for viscous incompressible flow. *International Journal of Numerical Methods in Fluids*, 11:934–948, 1990.
- [96] Texas Advanced Computing Center (TACC). <http://www.tacc.utexas.edu>.
- [97] C. A. Taylor, T. J. R. Hughes, and C. K. Zarins. Finite element modeling of blood flow in arteries. *Computer Methods in Applied Mechanics and Engineering*, 158:155–196, 1998.
- [98] A.E. Tejada-Martinez and K.E. Jansen. On the interaction between dynamic model dissipation and numerical dissipation due to streamline upwind/Petrov-Galerkin stabilization. *Computer Methods in Applied Mechanics and Engineering*, 194:1225–1248, 2005.
- [99] T. E. Tezduyar, M. Behr, and J. Liou. New strategy for finite element computations involving moving boundaries and interfaces. The deforming-spatial-domain/space-time procedure. I. the concept and the preliminary numerical tests. *Computer Methods in Applied Mechanics and Engineering*, 94:339–351, 1992.
- [100] T. E. Tezduyar, M. Behr, and J. Liou. New strategy for finite element computations involving moving boundaries and interfaces. The deforming-spatial-domain/space-time procedure. II. Computation of free-surface flows, two-liquid flows, and flows with drifting cylinders. *Computer Methods in Applied Mechanics and Engineering*, 94:353–371, 1992.
- [101] T. E. Tezduyar and S. Sathe. Enhanced-discretization space-time technique (EDSTT). *Computer Methods in Applied Mechanics and Engineering*, 193:1385–1401, 2004.
- [102] T.E. Tezduyar. Computation of moving boundaries and interfaces and stabilization parameters. *International Journal of Numerical Methods in Fluids*, 43:555–575, 2003.
- [103] T.E. Tezduyar, M. Behr, S. Mittal, and A.A. Johnson. Computation of unsteady incompressible flows with the stabilized finite element methods – space-time formulations, iterative strategies and massively parallel implementations. In *New Methods in Transient Analysis*, PVP-Vol. 246/ AMD-Vol. 143, pages 7–24. ASME, New York, 1992.
- [104] C. Tomasi and R. Madcuchi. Bilateral filtering for gray and color images. In *IEEE International Conference on Computer Vision*, page 839, 1998.
- [105] R. Torii, M. Oshima, T. Kobayashi, K. Takagi, and T.E. Tezduyar. Influence of wall elasticity on image-based blood flow simulation. *Japan Society of Mechanical Engineers Journal Series A*, 70:1224–1231, 2004.

- [106] R. Torii, M. Oshima, T. Kobayashi, K. Takagi, and T.E. Tezduyar. Computer modeling of cardiovascular fluid-structure interactions with the deforming-spatial-domain/stabilized space-time formulation. *Computer Methods in Applied Mechanics and Engineering*, 195:1885–1895, 2006.
- [107] R. Torii, M. Oshima, T. Kobayashi, K. Takagi, and T.E. Tezduyar. Fluid-structure interaction modeling of aneurysmal conditions with high and normal blood pressures. *Computational Mechanics*, 2006. In press.
- [108] R. Torii, M. Oshima, T. Kobayashi, K. Takagi, and T.E. Tezduyar. Influence of the wall elasticity in patient-specific hemodynamic simulations. *Computers and Fluids*, 2006. In press, published online.
- [109] R. Verfürth. Error estimates for a mixed finite element approximation of the Stokes problem. *RAIRO Anal. Numer.*, 18(175–182), 1984.
- [110] I.E. Vignon-Clementel, C.A. Figueroa, K.E. Jansen, and C.A. Taylor. Outflow boundary conditions for three-dimensional finite element modeling of blood flow and pressure in arteries. *Computer Methods in Applied Mechanics and Engineering*, 2005. In press.
- [111] L. B. Wahlbin. Local behavior in finite element methods. In P. G. Ciarlet and J. L. Lions, editors, *Finite Element Methods (Part 1)*, volume 2 of *Handbook of Numerical Analysis*, pages 353–522. North-Holland, 1991.
- [112] F. White. *Viscous Flow*. McGraw Hill, New York, 1974.
- [113] David C. Wilcox. *Turbulence Modeling for CFD*. DCW Industries, La Canada, CA, 1998.
- [114] Z. Yu and C. Bajaj. Image segmentation using gradient vector diffusion and region merging. In *16th International Conference on Pattern Recognition*, volume 2, pages 941–944, 2002.
- [115] Z. Yu and C. Bajaj. A fast and adaptive algorithm for image contrast enhancement. In *IEEE International Conference on Image Processing (ICIP'04)*, volume 2, pages 1001–1004, 2004.
- [116] L.T. Zhang, A. Gerstenberger, X. Wang, and W. K. Liu. Immersed finite element method. *Computer Methods in Applied Mechanics and Engineering*, 193:2051–2067, 2004.
- [117] Y. Zhang, Y. Bazilevs, C. Bajaj, and T. J.R. Hughes. Patient-specific vascular geometric modeling. 2006. In preparation.

Vita

Jurij Sergeevitch Bazilev, son of Sergey Bazilev and Jelena Bazileva, was born on August 1st in the year 1978, in Riga, Latvia. After graduating from Riga High School 40 in 1996, he enrolled at Rensselaer Polytechnic Institute, Troy, NY. In December 2000, he received the degree of Bachelor of Science in Mechanical Engineering, and, subsequently, the degree of Master of Science in December 2001 in the same field. After a few months of PhD work at Stanford University, Stanford, CA, he moved to the University of Texas at Austin in September 2002, along with his doctorate adviser, to pursue a PhD degree in Computational and Applied Mathematics at the Institute for Computational Engineering and Sciences.

Permanent Address: 1951 Old FM 306, apt. 1202
New Braunfels, Texas 78130

This dissertation was typeset with $\text{\LaTeX 2}_{\epsilon}$ ¹ by the author.

¹ $\text{\LaTeX 2}_{\epsilon}$ is an extension of \LaTeX . \LaTeX is a collection of macros for \TeX . \TeX is a trademark of the American Mathematical Society. The macros used in formatting this dissertation were written by Dinesh Das, Department of Computer Sciences, The University of Texas at Austin, and extended by Bert Kay, James A. Bednar, and Ayman El-Khashab.